

**DEVELOPMENT AND ASSESSMENT OF INTEGRATED ENERGY SYSTEMS
WITH AMMONIA SYNTHESIS AND FUEL CELLS**

By

OSAMAH SIDDIQUI

A Thesis Submitted in Partial Fulfillment
of the Requirements for the degree of Doctor of Philosophy

in

Mechanical Engineering

University of Ontario Institute of Technology
(Ontario Tech University)
Faculty of Engineering and Applied Science

Oshawa, Ontario, Canada

December 2020

© Osamah Siddiqui, 2020

THESIS EXAMINATION INFORMATION

Submitted by: **Osamah Siddiqui**

Doctor of Philosophy in Mechanical Engineering

Thesis title: Development and Assessment of Integrated Energy Systems with Ammonia Synthesis and Fuel Cells

An oral defense of this thesis took place on December 4, 2020 in front of the following examining committee:

Examining Committee:

Chair of Examining Committee	Dr. Amirkianoosh Kiani
Research Supervisor	Dr. Ibrahim Dincer
Examining Committee Member	Dr. Yuping He
Examining Committee Member	Dr. Dipal Patel
University Examiner	Dr. Matthew Kaye
External Examiner	Dr. Meng Ni, Hong Kong Polytechnic University

The above committee determined that the thesis is acceptable in form and content and that a satisfactory knowledge of the field covered by the thesis was demonstrated by the candidate during an oral examination. A signed copy of the Certificate of Approval is available from the School of Graduate and Postdoctoral Studies.

ABSTRACT

Hydrogen and ammonia comprise two important clean fuels, which are expected to play a vital role in the development of clean energy production and utilization. Currently, their production relies heavily on fossil fuel-based resources that entail considerable environmental detriments. The utilization of renewable energy such as solar and wind energy resources for the production of these important commodities can address the current challenges associated with conventional production methods. However, their intermittent nature have hindered their usage in such applications. Nevertheless, ammonia entails several favorable properties that make it a promising candidate to be utilized as an energy storage medium. In this thesis, integrated solar and wind energy-based energy systems are developed for clean production of electricity, hydrogen and ammonia. Three new integrated energy systems are developed utilizing ammonia as a medium to store energy. Direct ammonia fuel cells are utilized for clean power generation via electrochemical ammonia oxidation through the utilization of alkaline electrolytes. A new multi-bed catalyst reactor was developed and investigated experimentally for ammonia synthesis. Performance improvement in comparison with a conventional catalyst-based reactor is determined. Comprehensive thermodynamic, electrochemical, exergoeconomic and multi-objective optimization studies are also performed on the developed systems to assess their performances. The peak daily ammonia and hydrogen production amounts are found to reach 98045.8 kg and 19887.6 kg, respectively. The peak overall energy and exergy efficiencies of 57.8% and 60.5% are attained. Multi-objective optimization results provided optimal operational points entailing overall exergy efficiencies of 51% and 44.6% at total cost rates of \$4503.3 per hour and \$6007.2 per hour, respectively. These correspond to different combinations of solar intensity and wind speed levels. The direct ammonia fuel cell stack is found to have an open circuit voltage of 1399 mV and a peak power density of 13.4 W/m² that entailed an increasing trend with rising humidification temperatures. Various sensitivity analyses are also performed to determine system performances under varying operating conditions and system parameters.

Keywords: Hydrogen, Ammonia, Solar, Wind, Ammonia fuel cell, energy, exergy, efficiency

AUTHOR'S DECLARATION

I hereby declare that this thesis consists of original work of which I have authored. This is a true copy of the thesis, including any required final revisions, as accepted by my examiners.

I authorize the University of Ontario Institute of Technology (Ontario Tech University) to lend this thesis to other institutions or individuals for the purpose of scholarly research. I further authorize University of Ontario Institute of Technology (Ontario Tech University) to reproduce this thesis by photocopying or by other means, in total or in part, at the request of other institutions or individuals for the purpose of scholarly research. I understand that my thesis will be made electronically available to the public.



Osamah Siddiqui

ACKNOWLEDGEMENTS

I express my earnest gratitude, respect, appreciation and love for my supervisor, mentor and teacher Professor Dr. Ibrahim Dincer. Professor Dincer's stellar support, confidence, energy and exergy kept me motivated and inspired throughout my degree. Working under his supervision helped me comprehend the difference between a person's energy and exergy. His continuous support and guidance were significant for the successful completion of this thesis. His outstanding comprehension and experience helped me overcome various obstacles during my research. Through his wise supervision, he trained and educated me about various technical and non-technical aspects and instilled in me the immense passion he entails.

I am also grateful to all my colleagues and friends at the Clean Energy Research Laboratory and ACE3030 for providing me with cherishable memories. Moreover, I am thankful to Professor Bekir Sami Yilbas for his support. Also, I express my gratitude towards all roommates and friends.

I am thankful to my relatives for their continuous assistance and support throughout my stay in Canada.

The most sincere and honest relation in this world comprises of parents. I express my utmost appreciation, love and thankfulness for my beloved parents Mr. Abdul Bari Siddiqui and Ms. Nusrat Sultana for their continuous prayers, support, help, guidance and supervision. I am also thankful to my siblings Abdul Jabbar, Abdul Qadeer, Abdul Basith and Sumayya Sultana for their continuous support and motivation. I hope to serve them all with the best of my abilities.

Statement of Contributions

The content covered in this thesis is partially taken from the following published work:

O. Siddiqui and I. Dincer, Development of a sustainable energy system utilizing a new molten-salt based hybrid thermal energy storage and electrochemical energy conversion technique, *Sustainable Energy Technologies and Assessment* 42 (2020) 100866.

O. Siddiqui and I. Dincer, A new solar energy system for ammonia production and utilization in fuel cells, *Energy Conversion and Management* 208 (2020) 112590.

O. Siddiqui and I. Dincer, Experimental investigation of a sustainable integrated ammonia synthesis and fuel cell system, *Fuel* 278 (2020) 118300.

O. Siddiqui and I. Dincer, Design and transient analyses of a new renewable energy system for multigeneration of power, heat, hydrogen and ammonia, *Journal of Cleaner Production* 270 (2020) 112502.

O. Siddiqui and I. Dincer, Experimental investigation of improvement capability of ammonia fuel cell performance with addition of hydrogen, *Energy Conversion and Management* 205 (2020) 112372.

O. Siddiqui and I. Dincer, Development and performance evaluation of a direct ammonia fuel cell stack, *Chemical Engineering Science* 200 (2019) 285-293.

O. Siddiqui and I. Dincer, Design and analysis of a novel solar-wind based integrated energy system utilizing ammonia for energy storage, *Energy Conversion and Management* 195 (2019) 866-884.

O. Siddiqui and I. Dincer, Development of a novel renewable energy system integrated with biomass gasification combined cycle for cleaner production purposes, *Journal of Cleaner Production* 241 (2019) 118345.

O. Siddiqui and I. Dincer, A novel hybrid ammonia fuel cell and thermal energy storage system, *International Journal of Energy Research* 43 (2019) 3006-2010.

O. Siddiqui and I. Dincer, Experimental investigation and assessment of direct ammonia fuel cells utilizing alkaline molten and solid electrolytes, *Energy* 169 (2019) 914-923.

Table of Contents

Thesis Examination Information	ii
Abstract	iii
Author’s Declaration	iv
Acknowledgements	v
Statement of Contributions	vi
Table of Contents	vii
List of Figures	x
List of Tables	xvii
Nomenclature	xviii
Chapter 1 : Introduction	1
1.1 Fossil fuels and importance of renewable energy resources	1
1.2 Hydrogen as a clean fuel	5
1.3 Ammonia as a sustainable fuel	9
1.4 Conventional fossil fuel-based ammonia production.....	12
1.5 Ammonia utilization.....	15
1.6 Thesis outline	16
Chapter 2 : Background and literature review	18
2.1 Integrated energy systems for clean hydrogen and ammonia synthesis.....	18
2.2 Ammonia for energy storage and power generation	28
2.3 Ammonia fuel cells	31
2.3.1 Ammonia-based solid oxide fuel cells.....	32
2.3.2 Ammonia fuel cells utilizing alkaline electrolytes	36
2.4 Main gaps in the literature.....	38
2.5 Motivation, objectives and novelties.....	39
2.5.1 Objectives	40
2.5.2 Novelties	41
Chapter 3 : System development	43
3.1 System 1	43
3.2 System 2	46
3.3 System 3	49
Chapter 4 : Experimental apparatus and procedure	52

4.1 System components and measurement devices.....	52
4.1.1 Potentiostat	52
4.1.2 Flow meters	53
4.1.3 Temperature measurement	54
4.1.4 Ammonia synthesis catalysts.....	54
4.1.5 Ammonia synthesis reactor	55
4.1.6 Alkaline membranes.....	57
4.1.7 Gas diffusion layers	58
4.1.8 Bipolar flow channel plates	59
4.1.9 Gaskets.....	60
4.1.10 End plates	61
4.1.11 Fuel cell oxidant humidifier	61
4.1.12 Assembling the ammonia fuel cell stack	61
4.2 Experimental setup for the integrated ammonia synthesis and fuel cell system.....	63
4.2.1 Ammonia fuel cell utilizing molten electrolyte.....	64
Chapter 5 : Analysis and modeling	66
5.1 System 1	66
5.1.1 Solar-based power generation	66
5.1.2 Wind-based power generation	68
5.1.3 Hydrogen production via water splitting	69
5.1.4 Nitrogen production via air separation	72
5.1.5 Clean ammonia synthesis	73
5.1.6 Anion exchange membrane-based ammonia fuel cell	77
5.1.7 Algorithm for system 1 modeling and analysis	79
5.2 System 2	82
5.2.1 Solar and wind-based power generation.....	82
5.2.2 Electrochemical synthesis of ammonia	85
5.2.3 Molten alkaline electrolyte-based ammonia fuel cell subsystem	88
5.2.4 Algorithm for system 2 modelling and analysis.....	89
5.3 System 3	92
5.3.1 Solar and wind-based power generation.....	92
5.3.2 Ammonia synthesis and dissociation subsystems	94

5.3.3 Algorithm for system 3 modelling and analysis.....	95
5.4 System efficiencies.....	97
5.5 Exergoeconomic analysis.....	102
5.6 Multi-objective optimization.....	104
5.7 Scale-up analysis.....	106
5.8 Experimental uncertainty analysis	107
Chapter 6 : Results and discussion.....	110
6.1 Experimental results.....	110
6.1.1. Ammonia synthesis results	110
6.1.2 Ammonia fuel cell results.....	126
6.2 System 1 analysis and modelling results.....	136
6.3 System 2 analysis and modelling results.....	157
6.4 System 3 analysis and modelling results.....	168
6.5 Exergoeconomic analysis results	175
6.5.1 System 1 exergoeconomic analysis results.....	175
6.5.2 System 2 exergoeconomic analysis results.....	187
6.5.3 System 3 exergoeconomic analysis results.....	202
6.6 Multi-objective optimization results	214
6.6.1 System 1 multi-objective optimization results	215
6.6.2 System 2 multi-objective optimization results	219
6.6.3 System 3 multi-objective optimization results	223
Chapter 7 : Conclusions and recommendations	228
7.1 Conclusions.....	228
7.2 Recommendations	230

LIST OF FIGURES

Fig. 1.1 Global historical consumption of fossil fuel resources (Data from [1]).....	2
Fig. 1.2 Global percentage change in energy demand between the years 2010 and 2019 (Data from [2]).....	2
Fig. 1.3 Percentages of resources utilized for primary energy supply globally (Data from [3]).....	3
Fig. 1.4 Global carbon dioxide emissions arising from fossil fuel usage for energy related activities (Data from [4])	4
Fig. 1.5 Temporal change in global hydrogen demand for different applications (Data from [5]).....	5
Fig. 1.6 Schematic representing different routes of hydrogen production (Adapted from [6]).....	6
Fig. 1.7 Comparison of various energy storage methods (Data from [7]).....	10
Fig. 1.8 Global usage of fossil fuel resources for ammonia synthesis (Data from [12-13])	12
Fig. 1.9 Different routes of ammonia production via electricity and natural gas usage (Adapted from [9]).....	13
Fig. 1.10 Different stages in conventional natural gas-based ammonia synthesis (Adapted from [9])	15
Fig. 1.11 Percentage of ammonia utilization in different industries (Data from [12])	15
Fig. 1.12 Different possible applications of ammonia fuel.....	16
Fig. 2.1 Schematic representing clean ammonia synthesis through different renewable energy sources (Adapted from [6]).....	18
Fig. 2.2 Schematic representing different electrochemical routes of ammonia synthesis (Adapted from [9]).....	25
Fig. 2.3 Schematic representing the classification of ammonia power generation methods (Adapted from [17]).....	29
Fig. 2.4 Schematic representing different types of ammonia fuel cells (Adapted from [103]).....	32
Fig. 3.1 Schematic representing system 1 utilizing solar and wind energy resources for clean ammonia, hydrogen and electricity	45
Fig. 3.2 Schematic representing system 2 utilizing solar and wind energy resources for clean ammonia, hydrogen and electricity	48
Fig. 3.3 Schematic representing system 3 utilizing solar and wind energy resources for clean ammonia, hydrogen and electricity	51
Fig. 4.1 Gamry Reference 3000 potentiostat used in the present system	52
Fig. 4.2 FMA-1600A mass flow meter utilized in the present system	53
Fig. 4.3 Ammonia synthesis reactor developed in the present study utilizing single-bed conventional iron oxide catalyst and multi-layer catalyst bed.....	56
Fig. 4.4 Ammonia fuel cell stack showing (a) components in exploded view and (b) assembled five cell stack.....	62
Fig. 4.5 Experimental setup of the ammonia synthesis and fuel cell system.....	63
Fig. 5.1 Schematic representing the algorithm for system 1 modelling and analysis.....	80

Fig. 5.2 Schematic representing the algorithm for system 2 modelling and analysis.....	90
Fig. 5.3 Schematic representing the algorithm for system 3 modelling and analysis.....	96
Fig. 5.4 Steps associated with a genetic algorithm cycle (Reproduced from [86])	104
Fig. 6.1 Comparison of nitrogen conversion in the ammonia synthesis reactor at an operating pressure of 800 kPa and 700 kPa	112
Fig. 6.2 Comparison of energy efficiencies at operating pressures of 800 kPa and 700 kPa	112
Fig. 6.3 Comparison of exergy efficiencies at operating pressures of 800 kPa and 700 kPa	113
Fig. 6.4 Ammonia synthesis reaction energy and exergy efficiencies.....	114
Fig. 6.5 Comparison of nitrogen conversion in the ammonia synthesis reactor at an operating pressure of 800 kPa.....	115
Fig. 6.6 Comparison of energy and exergy efficiencies at an operating pressure of 800 kPa.....	116
Fig. 6.7 Comparison of energy and exergy efficiencies at an operating pressure of 700 kPa.....	117
Fig. 6.8 Adsorption-desorption plot for conventional iron oxide catalyst depicting volume adsorbed vs relative pressure	118
Fig. 6.9 BET surface area plot for conventional iron oxide catalyst	118
Fig. 6.10 Adsorption-desorption plot for ruthenium-based catalyst depicting volume adsorbed vs relative pressure	120
Fig. 6.11 BET surface area plot for ruthenium-based catalyst	120
Fig. 6.12 Adsorption-desorption plot for wustite-based catalyst depicting volume adsorbed vs relative pressure	121
Fig. 6.13 BET surface area plot for wustite-based catalyst	121
Fig. 6.14 SEM characterization and EDS results of conventional iron oxide-based catalyst	123
Fig. 6.15 SEM characterization and EDS results of ruthenium-based catalyst	124
Fig. 6.16 SEM characterization and EDS results of wustite-based catalyst	125
Fig. 6.17 SEM characterization and EDS results of wustite-based catalyst with cobalt	126
Fig. 6.18 Voltage vs current density results obtained for the single cell ammonia fuel cell	127
Fig. 6.19 Power density vs current density results obtained for the single cell ammonia fuel cell.....	128
Fig. 6.20 Voltage vs current density results obtained for the single cell ammonia fuel cell with aqueous ammonia	130
Fig. 6.21 Power density vs current density results obtained for the single cell ammonia fuel cell.....	130
Fig. 6.22 Voltage vs current density results obtained for the 5-cell ammonia fuel cell stack	132
Fig. 6.23 Power density vs current density results obtained for the 5-cell ammonia fuel cell stack.....	132

Fig. 6.24 Voltage vs current density results obtained for the molten alkaline electrolyte fuel cell.....	134
Fig. 6.25 Power density vs current density results obtained for the molten alkaline electrolyte fuel cell.....	134
Fig. 6.26 Energy and exergy efficiency results obtained for the five-cell ammonia fuel cell stack utilizing anion exchange membrane electrolyte	136
Fig. 6.27 Solar PV power generation results on monthly average days	137
Fig. 6.28 Hydrogen production rate results for the monthly average days.....	138
Fig. 6.29 Nitrogen production rate results for the monthly average days.....	138
Fig. 6.30 Ammonia production rate results for the monthly average days.....	139
Fig. 6.31 Daily hydrogen and ammonia production rate results for the monthly average days	140
Fig. 6.32 Daily AFC energy output capacity results for the monthly average days	141
Fig. 6.33 Daily ASR and PEM exergy destruction results for the monthly average days of each month	143
Fig. 6.34 Daily exergy destruction results for the monthly average days for the compression subsystem.....	145
Fig. 6.35 Daily energy and exergy efficiency results for the monthly average days for system 1 considering only solar PV-based operation	146
Fig. 6.36 Results of PV output electricity for the monthly average days of January to March for system 1 considering both solar PV and wind farm operation	147
Fig. 6.37 Results of PV output electricity for the monthly average days of April to June for system 1 considering both solar PV and wind farm operation.....	147
Fig. 6.38 Results of PV output electricity for the monthly average days of April to June for system 1 considering both solar PV and wind farm operation.....	148
Fig. 6.39 Results of PV output electricity for the monthly average days of April to June for system 1 considering both solar PV and wind farm operation.....	149
Fig. 6.40 Results of wind-based output electricity for the monthly average days of January to March for system 1 considering both solar PV and wind farm operation.....	150
Fig. 6.41 Results of wind-based output electricity for the monthly average days of April to June for system 1 considering both solar PV and wind farm operation	150
Fig. 6.42 Results of wind-based output electricity for the monthly average days of July to September for system 1 considering both solar PV and wind farm operation.....	151
Fig. 6.43 Results of wind-based output electricity for the monthly average days of October to December for system 1 considering both solar PV and wind farm operation	152
Fig. 6.44 Results of daily ammonia production for the monthly average days for system 1 considering both solar PV and wind farm operation	153
Fig. 6.45 Results of daily hydrogen production and PEM exergy destruction for the monthly average days for system 1 considering both solar PV and wind farm operation	154
Fig. 6.46 Results of daily hydrogen production and PEM exergy destruction on monthly average days for system 1 considering both solar PV and wind farm operation.....	155

Fig. 6.47 Results of daily AFC energy discharge capacity on the monthly average days for system 1 considering both solar PV and wind farm operation.....	156
Fig. 6.48 Results of energy and exergy efficiencies of System 1 considering both solar PV and wind farm operation	157
Fig. 6.49 Results of power generation cycle output for the monthly average days of January to March for system 2.....	158
Fig. 6.50 Results of power generation cycle output for the monthly average days of April to June for system 2	158
Fig. 6.51 Results of power generation cycle output for the monthly average days of July to September for system 2.....	159
Fig. 6.52 Results of power generation cycle output for the monthly average days of October to December for system 2	160
Fig. 6.53 Results of daily ammonia production for the monthly average days for system 2	161
Fig. 6.54 Results of daily MEAFC energy discharge capacities on the monthly average days for system 2	162
Fig. 6.55 Results of daily hydrogen production amounts on the monthly average days for system 2	163
Fig. 6.56 Results of daily heating outputs on the monthly average days for system 2...	164
Fig. 6.57 Results of daily energy output capacities from the power generation cycle on the monthly average days.....	165
Fig. 6.58 Results of daily T1 exergy destructions on the monthly average days	166
Fig. 6.59 Results of daily T2 exergy destructions on monthly average days	166
Fig. 6.60 Results of daily T3 exergy destructions on monthly average days	167
Fig. 6.61 Results of daily energy and exergy efficiencies of system 2 on monthly average days	168
Fig. 6.62 Results of solar-based power output for system 3 on monthly average days of January to June.....	169
Fig. 6.63 Results of solar-based power output for system 3 on monthly average days for July to December	170
Fig. 6.64 Results of daily hydrogen production on the monthly average days for system 3	170
Fig. 6.65 Results of daily ammonia production on the monthly average days for system 3	171
Fig. 6.66 Results of daily useful heating outputs on monthly average days for system 3	172
Fig. 6.67 Results of daily ADR thermal energy input requirement on monthly average days	173
Fig. 6.68 Results of daily FC energy discharge capacities on monthly average days	173
Fig. 6.69 Results of daily RC energy discharge capacities on monthly average days....	173
Fig. 6.70 Results of daily overall energy and exergy efficiencies of System 3 on monthly average days.....	175

Fig. 6.71 Effects of changes in the ambient temperature on the exergoeconomic performance of System 1	176
Fig. 6.72 Effects of changes in the solar intensity on the exergoeconomic performance of the ASR and PV subsystems.....	177
Fig. 6.73 Effects of changes in the solar intensity on the overall exergoeconomic performance of System 1	178
Fig. 6.74 Effects of changes in the PV efficiency on the exergoeconomic performances of the ASR, PEM and PV subsystems	179
Fig. 6.75 Effects of changes in the PV efficiency on the overall exergoeconomic performance of System 1	180
Fig. 6.76 Effects of interest rate on the exergoeconomic performance of major subsystems of System 1	180
Fig. 6.77 Effects of changes in the interest rate on the overall exergoeconomic performance of System 1	181
Fig. 6.78 Effects of changes in the system lifetime on the exergoeconomic performances of different subsystems of System 1	182
Fig. 6.79 Effects of changes in the system lifetime on the overall exergoeconomic performance of System 1	183
Fig. 6.80 Effects of varying wind speeds on the exergoeconomic performance of different subsystems of System 1	184
Fig. 6.81 Effects of varying wind speeds on the overall exergoeconomic performance of System 1	185
Fig. 6.82 Effects of PEM temperature on the exergoeconomic performances of different subsystems of System 1	185
Fig. 6.83 Effects of PEM temperature on the overall exergoeconomic performance of System 1	186
Fig. 6.84 Effects of isentropic efficiency of compressors on the overall exergoeconomic performance of System 1	187
Fig. 6.85 Effects of changes in the ambient temperature on the exergoeconomic performance of MEAFC and PEM subsystems of System 2.....	188
Fig. 6.86 Effects of changes in the ambient temperature on the exergoeconomic performance of different subsystems of System 2.....	189
Fig. 6.87 Effects of changes in the ambient temperature on the overall exergoeconomic performance of System 2	189
Fig. 6.88 Effects of changes in the solar intensity on the exergoeconomic performances of different subsystems of System 2	190
Fig. 6.89 Effects of changes in the solar intensity on the exergoeconomic performances of turbines T1-T3 of System 2	191
Fig. 6.90 Effects of changes in the solar intensity on the overall exergoeconomic performance of System 2	192
Fig. 6.91 Effect of interest rate on the exergoeconomic performance of different subsystems of System 2	193

Fig. 6.92 Effect of interest rate on the exergoeconomic performance of steam turbines in System 2.....	194
Fig. 6.93 Effect of interest rate on the overall exergoeconomic performance of System 2	194
Fig. 6.94 Effect of system lifetime on the exergoeconomic performance of different subsystems of System 2	195
Fig. 6.95 Effect of system lifetime on the exergoeconomic performance of solar-based power generation subsystem in System 2	196
Fig. 6.96 Effect of system lifetime on the overall exergoeconomic performance of System 2.....	196
Fig. 6.97 Effect of wind speed on the exergoeconomic performance of PEM, EAS and MEAFC subsystems of System 2	197
Fig. 6.98 Effect of wind speed on the exergoeconomic performance of PSA subsystem in System 2.....	198
Fig. 6.99 Effect of wind speed on the overall exergoeconomic performance of System 2	198
Fig. 6.100 Effect of PEM temperature on the exergoeconomic performances of different subsystems of System 2	199
Fig. 6.101 Effect of PEM temperature on the overall exergoeconomic performances of System 2.....	200
Fig. 6.102 Effect of isentropic efficiency on the exergoeconomic performances of PSA and HX1 in System 2	201
Fig. 6.103 Effect of isentropic efficiency on the exergoeconomic performances of steam turbines in System 2.....	201
Fig. 6.104 Effect of ambient temperature on the exergoeconomic performances of ADR and REC subsystems in System 3	203
Fig. 6.105 Effect of ambient temperature on the exergoeconomic performances of different subsystems in System 3.....	203
Fig. 6.106 Effect of ambient temperature on the overall exergoeconomic performance of System 3.....	204
Fig. 6.107 Effect of solar intensity on the exergoeconomic performance of different subsystems of System 3	205
Fig. 6.108 Effect of solar intensity on overall exergoeconomic performance of System 3	205
Fig. 6.109 Effect of heliostat efficiency on the exergoeconomic performance of major subsystems of System 3	206
Fig. 6.110 Effect of heliostat efficiency on the overall exergoeconomic performance of System 3.....	207
Fig. 6.111 Effect of interest rate on the exergoeconomic performance of different subsystems of System 3	208
Fig. 6.112 Effect of interest rate on the exergoeconomic performance of solar-based subsystems of System 3	209

Fig. 6.113 Effect of interest rate on total investment and exergy destruction cost rates of System 3	209
Fig. 6.114 Effect of system lifetime on the exergoeconomic performance of different subsystems of System 3	210
Fig. 6.115 Effect of system lifetime on the exergoeconomic performance of solar-based subsystems of System 3	210
Fig. 6.116 Effect of system lifetime on the overall exergoeconomic performance of System 3	211
Fig. 6.117 Effect of wind speed on the exergoeconomic performance of PEM, ASR and FC subsystems of System 3	212
Fig. 6.118 Effect of wind speed on the exergoeconomic performance of PSA and ADR subsystems of System 3	212
Fig. 6.119 Effect of wind speed on the overall exergoeconomic performance of System 3	213
Fig. 6.120 Effect of PEM temperature on the overall exergoeconomic performance of System 3	214
Fig. 6.121 Effect of isentropic efficiency on exergoeconomic performance of major subsystems	214
Fig. 6.122 Pareto frontier for System 1 under high solar radiation and high wind speed ($H_{sol}H_{wn}$) configuration	215
Fig. 6.123 Pareto frontier for System 1 under high solar radiation and low wind speed ($H_{sol}L_{wn}$) configuration	217
Fig. 6.124 Pareto frontier for System 1 under low solar radiation and high wind speed ($L_{sol}H_{wn}$) configuration	218
Fig. 6.125 Pareto frontier for System 1 under medium solar radiation and medium wind speed ($M_{sol}M_{wn}$) configuration	218
Fig. 6.126 Pareto frontier for System 2 under high solar radiation and high wind speed ($H_{sol}H_{wn}$) configuration	220
Fig. 6.127 Pareto frontier for System 2 under high solar radiation and low wind speed ($H_{sol}L_{wn}$) configuration	221
Fig. 6.128 Pareto frontier for System 2 under low solar radiation and high wind speed ($L_{sol}H_{wn}$) configuration	221
Fig. 6.129 Pareto frontier for System 2 under medium solar radiation and medium wind speed ($M_{sol}M_{wn}$) configuration	222
Fig. 6.130 Pareto frontier for System 3 under high solar radiation and high wind speed ($H_{sol}H_{wn}$) configuration	224
Fig. 6.131 Pareto frontier for System 3 under high solar radiation and low wind speed ($H_{sol}L_{wn}$) configuration	225
Fig. 6.132 Pareto frontier for System 3 under low solar radiation and high wind speed ($L_{sol}H_{wn}$) configuration	225
Fig. 6.133 Pareto frontier for System 3 under medium solar radiation and medium wind speed ($M_{sol}M_{wn}$) configuration	226

LIST OF TABLES

Table 1.1 Comparison of energy storage properties of ammonia and hydrogen	10
Table 4.1 Specifications of FMA mass flow meters.....	54
Table 4.2 Specifications of the temperature measurement systems	54
Table 4.3 Specifications of the gas diffusion layer.....	59
Table 5.1 Input parameters utilized for modelling and analysis of system 1	81
Table 5.2 Input parameters utilized for modelling and analysis of system 2	91
Table 5.3 Input parameters utilized for modelling and analysis of system 3	97
Table 5.4 Decision variables and associated constraints utilized for multi-objective optimization of system 1	105
Table 5.5 Decision variables and associated constraints utilized for multi-objective optimization of system 2.....	106
Table 5.6 Decision variables and associated constraints utilized for multi-objective optimization of system 3.....	106
Table 5.7 Measurement devices and corresponding range and accuracies.....	108
Table 5.8 List of the bias and precision errors of experimental equipment utilized.....	108
Table 6.1 Ammonia synthesis results obtained via boric acid trap with single-bed iron-oxide based catalyst	111
Table 6.2 Ammonia synthesis results obtained via boric acid trap at operating pressures of 700 kPa and 800 kPa with the multi-bed catalyst reactor.....	114
Table 6.3 Values of decision variables and objective functions for system 1	218
Table 6.4 Values of decision variables and objective functions for system 2	222
Table 6.5 Values of decision variables and objective functions for system 3	226
Table 6.6 Comparison of overall exergy efficiencies and associated costs of the developed systems	227

NOMENCLATURE

A	area (m ²)
C	concentration (M)
C_p	specific heat capacity (kJ/kgK)
en	specific energy (kJ/kg)
ex	specific exergy (kJ/kg)
E	potential (V)
En	energy (kJ)
$\dot{E}n$	energy rate (kW)
Ex	exergy (kJ)
$\dot{E}x$	exergy rate (kW)
F	Faraday constant (96485.3 C/mol)
g	gravitational acceleration (m/s ²)
G	Gibbs free energy (kJ)
h	specific enthalpy (kJ/kg)
I	current (A)
J	current density (A/m ²)
J_L	limiting current density (A/m ²)
J_0	exchange current density (A/m ²)
k	thermal conductivity (kW/m ² K)
m	mass (kg)
\dot{m}	mass flow rate (kg/s)
M	molar mass (kg/kmol)
\dot{M}_i''	molar diffusion rate flux (mol/m ² s)
n	number of cells
\dot{N}	molar flow rate (mol/s)
P	pressure (kPa)
\dot{Q}	heat rate (kW)
R	resistance (ohm)
R	universal gas constant (8.314 kJ/kmolK)
R_e	random error (%)
s	specific entropy (kJ/kgK)
S	entropy (kJ/K)
\dot{S}	entropy rate (kW/K)
S_e	systematic error (%)
Sh	Sherwood number (-)
t	time (s)
T	temperature (°C)
U	uncertainty (%)
V	voltage (V)
\dot{V}	volume flow rate (m ³ /s)
w	specific work (kJ/kg)
W	work (kJ)
\dot{W}	work rate (kW)
x	mole fraction (-)

\bar{y}	statistical mean
Y	scale-up factor
Z	elevation (m)

Greek letters

α	transfer coefficient
δ	declination angle ($^{\circ}$)
Δ	change
η	efficiency
ϕ	phase angle ($^{\circ}$)
σ	membrane conductivity ($1/\Omega\text{cm}$)
μ	kinematic viscosity (m^2/s)
ρ	density (kg/m^3)
ψ	shape factor
ω	angular frequency (rad/s)

Subscripts

0	ambient condition
a	anode
act	activation
c	cathode
conc	concentration
ch	chemical
dest	destroyed
eff	effective
en	energy
ex	exergy
FC	fuel cell
gen	generation
hf	heliostat field
imag	imaginary part
in	input
L	inductance
ohm	Ohmic
out	outlet
ov	overall
rev	reversible
R	resistance
sc	short circuit
sol	solar
sw	sea water
tn	thermonuetral
tot	total
wn	wind
z	zenith

Acronyms

ADR	ammonia dissociation reactor
AFC	ammonia fuel cell
AP	acidification potential
ASR	ammonia synthesis reactor
BCE	barium cerate
BCG	Gadolinium-doped barium cerate
BCGE	Europium doped barium cerate
BCGO	$\text{BaCe}_{0.8}\text{Gd}_{0.2}\text{O}_{2.9}$
BCGP	Gadolinium and Praseodymium-doped barium Cerate
BCNO	$\text{BaCe}_{0.9}\text{Nd}_{0.1}\text{O}_{3-\delta}$
BSCF	$\text{Ba}_{0.5}\text{Sr}_{0.5}\text{Co}_{0.8}\text{Fe}_{0.2}\text{O}_{3-\delta}$
BZCY	$\text{BaZr}_{0.1}\text{Ce}_{0.7}\text{Y}_{0.2}\text{O}_{3-\delta}$
CDN/C	Chromium decorated nickel/carbon
CON	condenser
CPPO	Chloroacetyl poly (2, 6-dimethyl-1, 4-phenylene oxide)
CPR	compression subsystem
CT	cold tank
DAFC	direct ammonia fuel cell
DC	direct current
DMC	dimethyl carbonate
EAS	electrochemical ammonia synthesis
FC	fuel cell
GHG	greenhouse gas emissions
HH	high solar and high wind configuration
HHV	higher heating value
HL	high solar and low wind configuration
HT	hot tank
HX	heat exchanger
LH	low solar and high wind configuration
LHV	lower heating value
LSCO	$\text{La}_{0.5}\text{Sr}_{0.5}\text{CoO}_{3-\delta}$
LSM	$\text{La}_{0.67}\text{Sr}_{0.33}\text{MnO}_{3-\delta}$
MEAFC	molten electrolyte ammonia fuel cell
MM	medium solar and medium wind configuration
Mtoe	mega tonnes of oil equivalent
NI	national instruments
OCV	open circuit voltage
OTEC	ocean thermal energy conversion
PEC	photoelectrochemical
PEM	proton exchange membrane
PSA	pressure swing adsorption
PV	photovoltaic
PVA	polyvinyl alcohol
PV/T	photovoltaic-thermal
SDC	Samarium doped ceria

SEP	separator
SMR	steam methane reforming
SOFC	solid oxide fuel cell
SSAS	solid-state ammonia synthesis
SSC	$\text{Sm}_{0.5} \text{Sr}_{0.5} \text{CoO}_{3-\delta}$
T	turbine
TC	thermochemical
TV	throttle valve
TB	Triple phase boundary
WES	water electrolysis
YSZ	Yittria stabilized zirconia

CHAPTER 1 : INTRODUCTION

In this chapter, the considerable use of fossil fuels globally and their continuous rise is discussed highlighting the importance of renewable energy resources and their significance in the future of clean energy production. The importance of hydrogen as well as ammonia fuels is presented and their potentials to be utilized as effective energy storage mediums are discussed. Finally, the potential for using ammonia fuel in various applications and its importance as a carbon-free fuel is described.

1.1 Fossil fuels and importance of renewable energy resources

Primary energy production is reliant on fossil fuel-based energy sources. Although fossil fuels are widely utilized in different mature technologies, their usage has been proven to be associated with harmful emissions that are detrimental to both the environment as well as human health. However, the consumption of fossil fuels has been observed to have a continuously increasing trend in recent decades as shown in Fig. 1.1. As can be observed from the figure, the total consumption of oil, natural gas and coal has increased by nearly 30% in the last two decades. The consumption of coal has risen by nearly 65% since the year 2000. The consumption was reported to be 2300 Mtoe in 2000, which increased to 3800 Mtoe in 2018. Natural gas consumption across the globe has increased from nearly 2000 Mtoe to 3340 Mtoe between the years 2000 and 2018, signifying an increase of nearly 67%. Similarly, oil consumption has risen by 25% during this time period.

This continuous rise in the consumption of fossil fuels can be attributed to the incessant rise in energy demands. Fig. 1.2 depicts the annual change in energy demands every year since 2010. As can be observed from the figure, a positive increment in the global energy demand occurs every year. Although the rise in 2019 had a value of 0.9% as compared to the previous year, in 2018, there was a sharp rise of 2.9% in the global energy demands. The continuous rise in energy demands can be attributed primarily to the increased industrial activity as well as infrastructural and technological development across the globe. Although industrial and technological development is being enhanced, the energy resources powering these developments are not completely favorable.

Fig. 1.3 depicts the breakdown of energy resources utilized globally. Nearly 80% of the total energy consumed is derived from carbon-based fossil fuels where oil constitutes the highest portion of 32%. Coal and natural gas constitute nearly 27% and 22%, respectively.

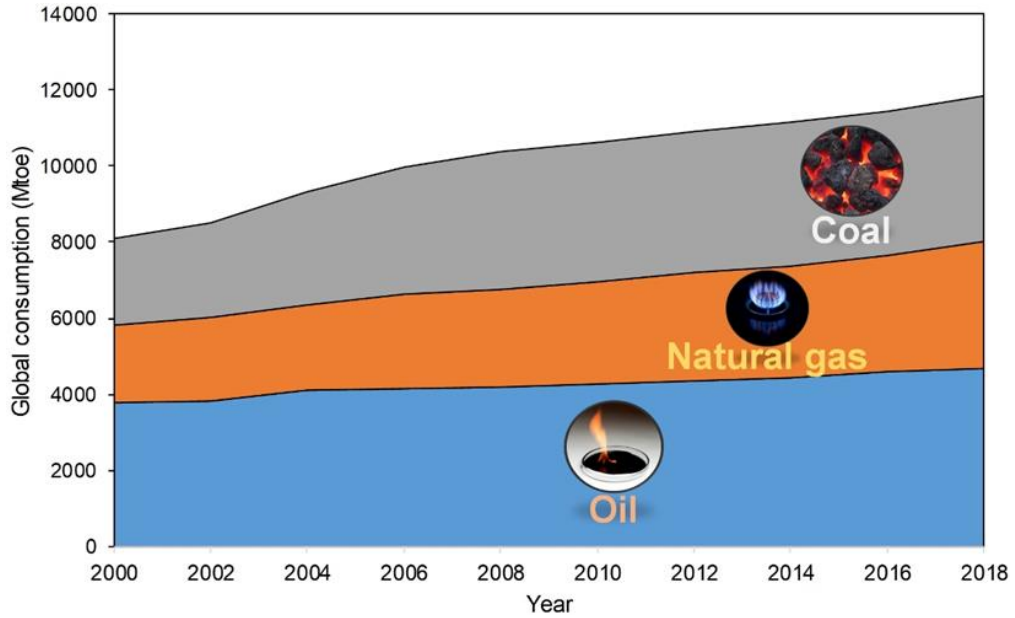


Fig. 1.1 Global historical consumption of fossil fuel resources (Data from [1])

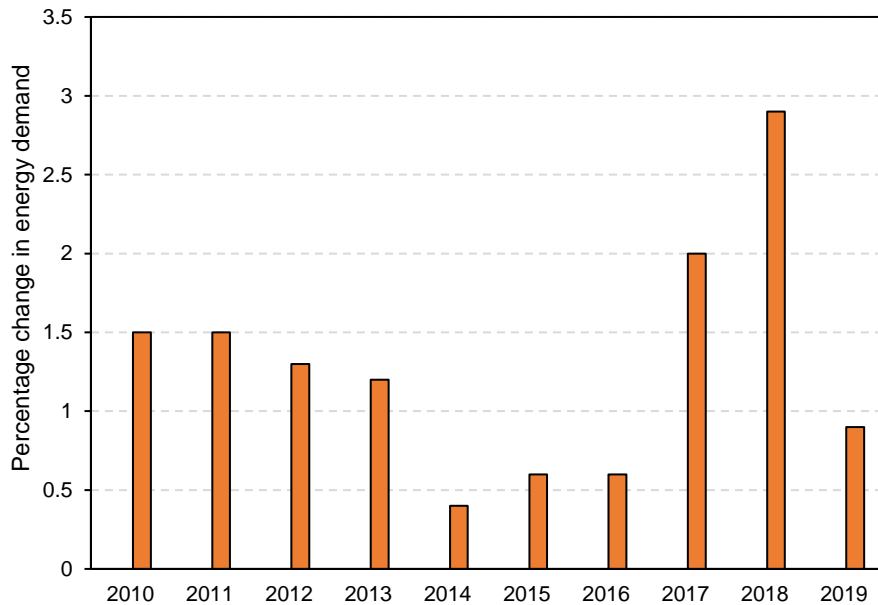


Fig. 1.2 Global percentage change in energy demand between the years 2010 and 2019 (Data from [2])

However, renewable energy resources such as solar, wind, geothermal, *etc.* comprised a mere 2% of the total energy resources. Nevertheless, biofuels as well as waste were reported as a 10% share in the total primary energy supply. Hence, the colossal usage of fossil fuels as well as continuous increase in the amount of their usage has led to various environmental detriments, which have raised global concerns about energy sustainability and security.

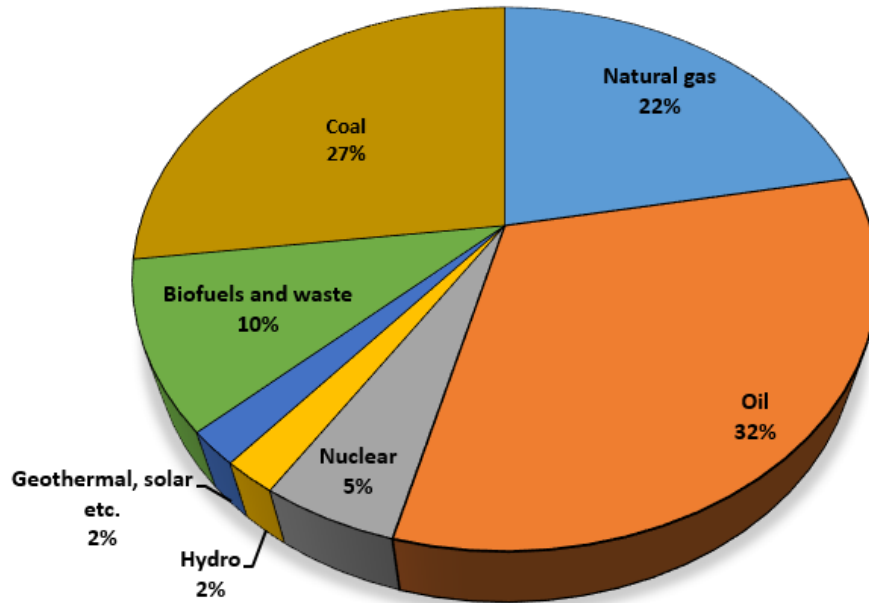


Fig. 1.3 Percentages of resources utilized for primary energy supply globally (Data from [3])

Fig. 1.4 shows the increase in global CO₂ emissions associated with energy related applications. As can be observed, the CO₂ emissions have been continuously rising for the past 2 decades. An increase of 48.7% is observed in these emissions since the year 1999. The last decade is observed to have an increase of 20.5% in global CO₂ emissions. Substantial amounts of CO₂ emissions (33.3 GTONne) have been reported for the year 2019. These emissions have been proved to be have detrimental effects on the environment, human health and are causing climate change. The usage of fossil fuels is associated with the harmful emissions of nitrogen oxides and sulphur oxides.

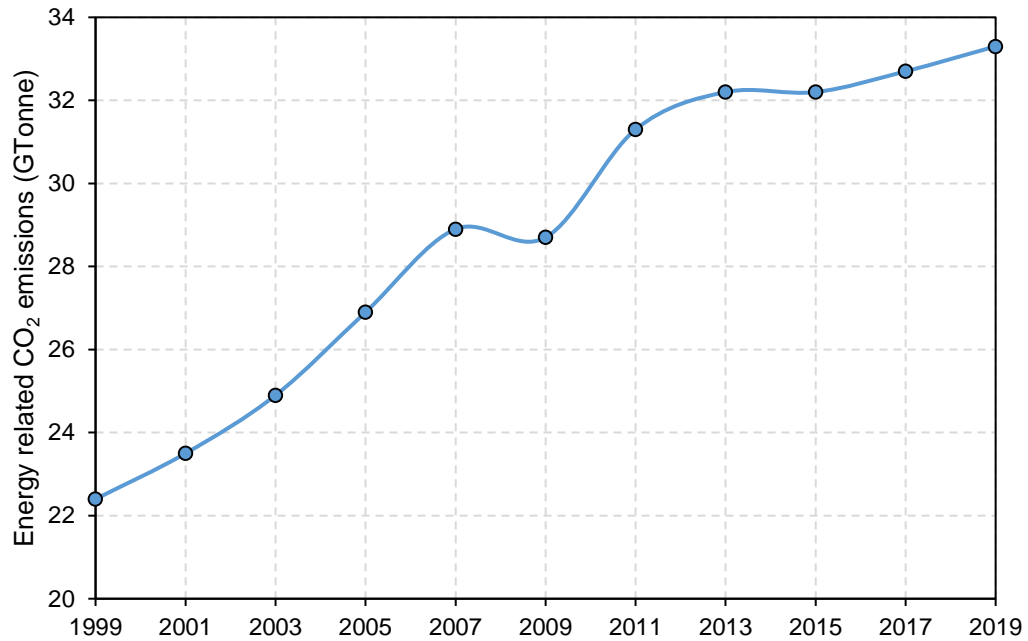


Fig. 1.4 Global carbon dioxide emissions arising from fossil fuel usage for energy related activities (Data from [4])

Hence, owing to various detriments associated with the usage of fossil fuels, efforts across the globe have been initiated that aim at decreasing the dependency on fossil fuels and increasing the usage of clean and environmentally benign energy resources. Different types of renewable energy resources are being investigated and their usage is being increased in various countries. Primarily, solar and wind energy resources have been observed to be adopted more heavily than other renewable resources in recent years. However, the intermittent and fluctuant nature of these energy resources has been a major challenge.

Different techniques that include chemical, electrical, mechanical and thermal methods of storing excess energy are being implemented. The usage of carbon-free and environmentally benign fuels is considered an integral solution to the problems associated with fossil fuels. Fuels that have high energy contents and do not result in harmful emissions when utilized for energy production are being investigated. Hydrogen is one such carbon-free fuel that is considered a promising option that can decrease the dependency on fossil fuels and increase the usage of clean fuels. However, challenges, such as low volumetric density and high flammability have hindered its implementation and deployment.

1.2 Hydrogen as a clean fuel

Hydrogen is a carbon-free fuel that has a high energy density per unit mass of fuel and does not emit harmful emissions upon usage. When combined with oxygen molecules for combustion or electrochemical oxidation, water vapour is the reaction product that can be recycled in the overall lifecycle. Being a constituent element of numerous naturally occurring compounds, hydrogen is the most abundant elements on earth.

Conventional techniques of producing hydrogen utilize considerable amounts of fossil fuels and emit significant environmental emissions. Hydrogen has been utilized in different industries for several decades. Primarily it has been used in refineries as well as in ammonia production plants. The usage of hydrogen has seen a sharp rise in the past few decades as depicted in Fig. 1.5. Between the years 1975 and 2018, the global hydrogen usage has seen an increase of nearly 300% from 18.2 MTonne to 73.9 MTonne.

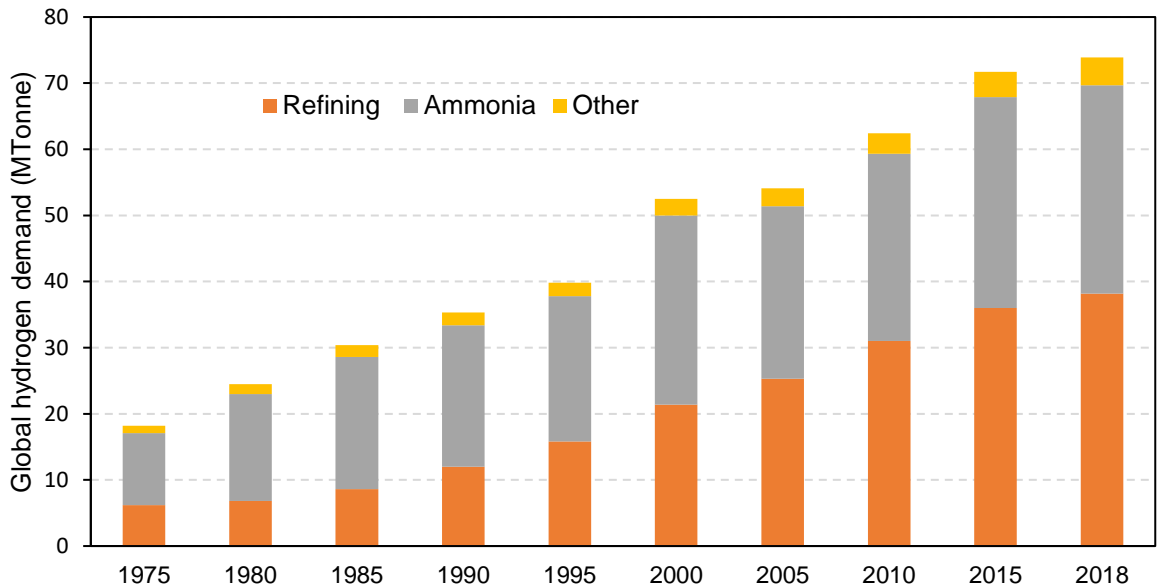


Fig. 1.5 Temporal change in global hydrogen demand for different applications (Data from [5])

The hydrogen demand for refining industries also had a considerable rise from 6.2 MTonne to 38.2 MTonne that signifies a rise of 5.2 times. The global hydrogen demand for ammonia synthesis has risen from 10.9 MTonne to 31.5 MTonne between the years 1975 and 2018, which corresponds to an increase of nearly 200%. Nevertheless, the continuous rise in hydrogen production targeted towards meeting the increasing demands has been reliant on

fossil fuels. Significant usage of fossil fuels is associated with hydrogen production that has led to colossal amounts of detrimental environmental emissions. Nearly 6% of global natural gas usage is attributed to hydrogen production and approximately 2% of coal consumption across the globe is associated with hydrogen production. These have been estimated to result in 830 MTONne of CO₂ emissions every year [5].

The production of clean hydrogen that is independent of fossil fuel usage is crucial for the development of a sustainable infrastructure. Although the usage of hydrogen does not result in significant amounts of emissions, the production of hydrogen is attributed to considerable environmental emissions and detriments. There are various methods of producing hydrogen as depicted in Fig. 1.6. The solar-based hydrogen production techniques include photoelectrochemical (PEC), photocatalytic (PC), artificial photosynthesis (AP) and thermochemical (TC). The electricity generated via various types of renewable energy resources can be utilized to produce hydrogen through water electrolysis.

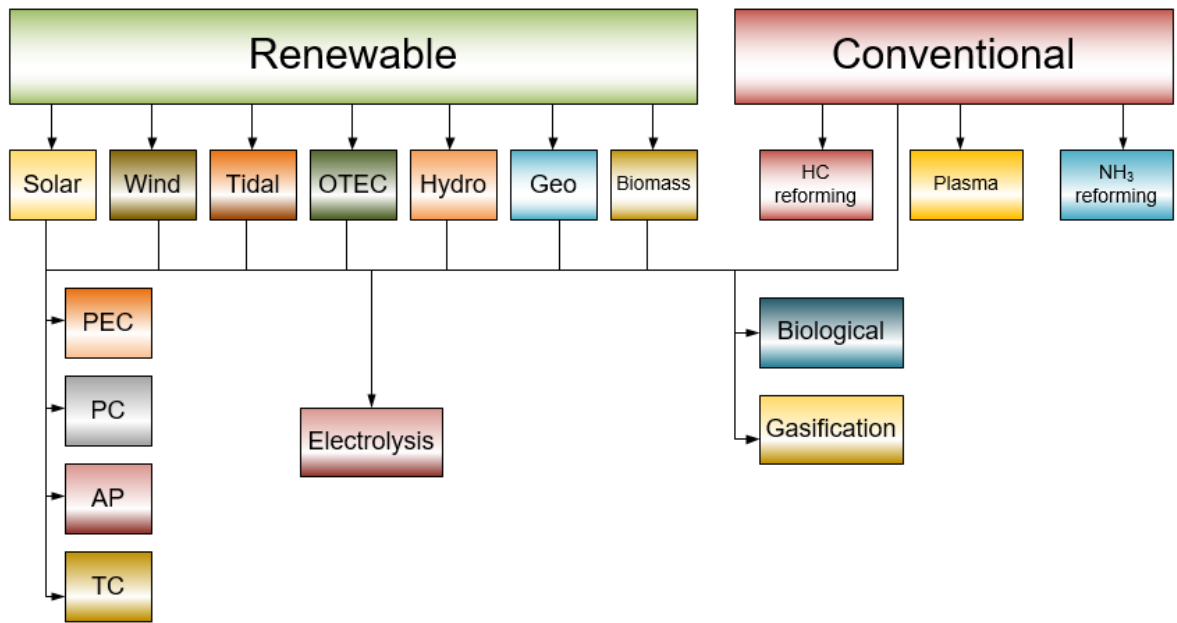
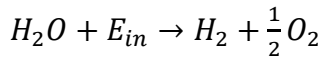


Fig. 1.6 Schematic representing different routes of hydrogen production (Adapted from [6])

Other techniques of producing renewable hydrogen include the usage of biomass resources. Both biological as well as gasification biomass conversion processes are utilized to produce renewable hydrogen. On the other hand, the conventional method of hydrogen production

that is primarily utilized includes the reforming of hydrocarbons. Specifically, steam methane reforming (SMR) is utilized extensively in most hydrogen production plants where natural gas or methane is reformed in the presence of steam to produce carbon monoxide and hydrogen. The carbon monoxide is further converted into CO₂ and H₂ through the water gas shift reaction. The water electrolysis method of hydrogen production includes the dissociation of water into hydrogen and oxygen through the usage of input electrical power. This overall dissociation process can be written as



The energy input needed for the above reaction can be obtained through different renewable energy resources, hence, providing a clean production method for hydrogen. On the other hand, the SMR process of producing hydrogen includes an endothermic reaction of steam and methane to produce hydrogen. The energy input needed for the reaction is also obtained through the combustion of natural gas. The operating conditions of this process are generally pressures of 3-25 bar and temperatures of 700-850°C. A secondary reformer is also utilized to achieve higher overall conversions.

Hydrogen is also obtained from coal through two main processes. Firstly, the process of underground coal gasification is utilized that includes gasifying coal beneath the surface of the earth. Secondly, the conventional coal gasification process includes gasifying coal in specialized reactors. Gasification of coal comprises the second most widely utilized process for producing hydrogen. Several types of gasifiers exist that include entrained flow, fluidized bed or fixed bed configurations.

Entrained flow configurations having high temperatures are known to provide effective conversion of carbon to gas. This also prevents the formation of excess phenols, tar and char. However, since the process is endothermic, heat input is required to undertake the conversion process. The underground method of gasifying coal has the advantage that unprocessed reserves of coal can be directly utilized to produce hydrogen. Coal reserves that cannot be reached for extraction can be utilized through underground coal gasification processes to obtain hydrogen. The underground gasification techniques are also known to be capable of avoiding environmental as well as hazardous impacts that are generally

associated with conventional coal mining processes. The product of gasification includes primarily syngas that can be either used to produce hydrogen or can be combusted after post processing to generate power.

Partial oxidation is another technique that is utilized to convert heavy feedstock into useful products including hydrogen. High-viscosity plastic waste as well as hydrocarbon compounds can also be utilized through this conversion process. The oxygen needed for the process is obtained via air separation units. Pure nitrogen streams are also used to obtain lower concentrations on contaminants in the syngas produced. However, this type of oxidation process is non-catalytic that is undertaken at high pressures exceeding 5000 kPa and high temperatures of nearly 1400°C. Different types of biomass are also utilized to produce hydrogen.

These include animal biomass resources, agricultural wastes and byproducts, and industrial as well as municipal wastes. Commonly utilized biomass-based hydrogen production methods employ biochemical, thermochemical and gasification processes. The product of biomass conversion is also syngas, similar to the coal conversion process, which constitutes specific ratios of hydrogen depending on the biomass composition. The chemical reactions associated with the process of biomass conversion to hydrogen are similar to the reactions that are associated with the fossil fuel gasification processes. The processes of pyrolysis as well as gasification have been identified as two key methods that can be implemented to convert different biomass resources into useful hydrogen at commercial scale.

The hydrogen production method of water electrolysis provides the opportunity to utilize different renewable energy resources to produce environmentally benign and emission-free hydrogen. For instance, wind turbines can be utilized to convert the kinetic energy of wind into mechanical energy, which can be further converted into electrical power. The generated electrical power is then used to operate the water electrolysis subsystem that dissociates water molecules to produce hydrogen. However, the power generated from wind turbines requires control and regulation before it is sent to the electrolyser based upon its specifications. Solar energy can also be used to produce environmentally benign hydrogen through different methods. These include electrolysis, photoelectrochemical splitting of water, thermochemical techniques, and artificial photosynthesis. Each method

has its own advantages and challenges, however, both provide a clean route of producing hydrogen. The solar-based electrolysis route generally includes power generation via solar thermal or photovoltaic (PV) methods followed by water dissociation. The photoelectrochemical route also includes the common step of solar-based power generation, however, it also includes the usage of photosensitive materials to utilize photonic energy to enhance the rates of hydrogen production. Other renewable energy resources including geothermal, ocean thermal energy conversion and wave energy can also be integrated with water electrolysis to produce clean hydrogen.

Although hydrogen provides the potential to produce clean and environmentally benign energy, there are several challenges that need to be addressed. Firstly, the conventional methods of producing hydrogen are heavily reliant of carbon intensive fossil fuels as described earlier. These methods are associated with considerable environmental detriments. Hence, if hydrogen is to be utilized as a clean fuel, conventional fossil-based hydrogen production methods need to be replaced with renewable energy-based techniques. Secondly, comparatively higher storage costs as well as safety hazards are associated with hydrogen usage. Due to its low volumetric density, sufficient amounts of hydrogen cannot be stored in a given volume unless pressurized to high levels of pressure. Being odorless and highly flammable, hydrogen poses major safety hazards at the locations of storage as well as usage. These challenges associated with hydrogen can be addressed through different techniques. Ammonia has been identified as an important chemical that can be utilized to address these challenges.

1.3 Ammonia as a sustainable fuel

Ammonia has favourable properties in comparison with hydrogen, which make it suitable for energy storage. Table 1 provides a comparison of various energy storage characteristics of hydrogen and ammonia at low as well as high pressures. At a pressure of 100 kPa, hydrogen has a density of 0.08127 kg/m³. Ammonia, on the other hand has a significantly higher density of 0.6942 kg/m³. In 1 m³ of hydrogen, there is an energy content of 9750 kJ. In 1 m³ of ammonia at atmospheric pressure, there is an energy content of 12945 kJ and hydrogen content of 0.245 kg H₂. At higher pressures these values are significantly higher for ammonia as compared to hydrogen. For instance, at 10 atmospheres, ammonia has

nearly 50% higher energy density than hydrogen at the same pressure. At this pressure, there is more mass content of hydrogen in 1 m³ of ammonia than in 1 m³ of hydrogen. For example, 1 m³ of ammonia at 1000 kPa contains 2.745 kg of hydrogen compared to 0.8085 kg at the same pressure for pure hydrogen. Hence, these depict the advantageous characteristics of ammonia as compared to hydrogen in terms of volumetric density, energy density and hydrogen content.

Table 1.1 Comparison of energy storage properties of ammonia and hydrogen

Fuel	Pressure (kPa)	Volumetric density (kg/m ³)	Energy density (kJ/m ³)	Hydrogen content (kg H ₂ /m ³)
Hydrogen	100	0.08127	9750	0.08127
Ammonia	100	0.6942	12945	0.245
Hydrogen	1000	0.8085	96983	0.8085
Ammonia	1000	7.778	145029	2.745

Source: Ref. [6]

In terms of storage properties, ammonia has been identified as a promising fuel as compared to other energy storage methods. Fig. 1.7 depicts a comparison of output capacity of different technologies with their viable discharge times considering available methods as well as under development technologies.

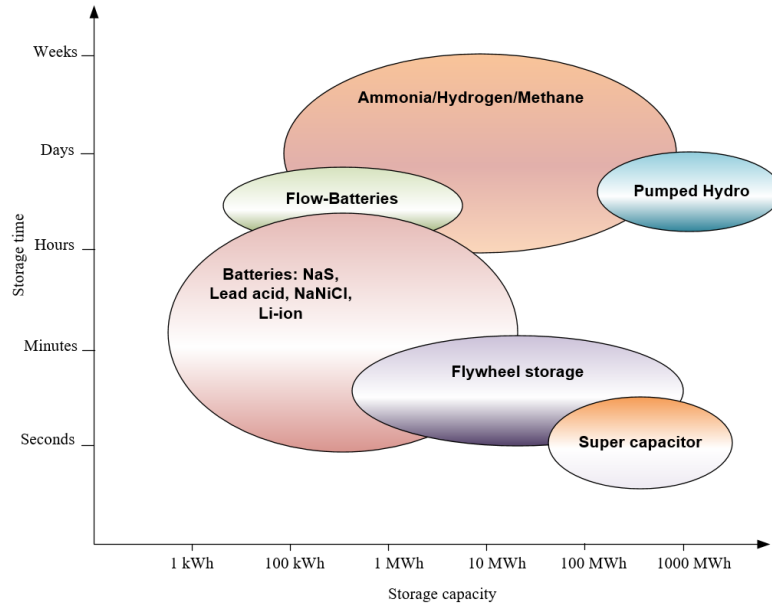


Fig. 1.7 Comparison of various energy storage methods (Data from [7])

From Fig. 1.7 it can be seen that chemical storage through fuels such as ammonia, hydrogen and methane have better characteristics comparatively. A wide range of output power for such energy methods exists depending on the amount of fuel stored and produced, and the storage times are higher for these methods. Thus, fuels such as ammonia can be produced during periods of excess power and stored for long periods of time before being used for power generation. Current ammonia synthesis methods, such as the Haber-Bosch process, rely heavily on the consumption of fossil fuels.

Massive production of ammonia is carried out across the globe every year with this method. For example, the global ammonia production using the Haber-Bosch process increased from nearly 160 million tonnes in 2010 to about 180 million tonnes in 2015 [8]. Conventional ammonia synthesis plants emit considerable amounts of environmentally detrimental emissions. Nearly 2 tonnes of carbon dioxide (CO_2) is emitted for every 1 tonne of ammonia produced with the current synthesis technique used in the ammonia industry [9]. The conventional ammonia synthesis technique used today was introduced in the beginning of the 20th century. The significant amounts of environmental emissions associated with this method can be attributed to the consumption of fossils for obtaining the required hydrogen.

Steam methane reforming process is employed in majority of the ammonia synthesis plants. In this process, methane (CH_4) is reacted with steam (H_2O) to produce hydrogen. However, for every mole of CH_4 used, 1 mole of carbon monoxide (CO) or carbon dioxide (CO_2) is produced. Thus, considerable amounts of these carbon emissions are emitted everyday owing to the colossal production of ammonia worldwide. For example, ammonia production plants emit nearly 7.5 million tonnes of CO_2 emissions every year [10]. Hence, environmentally benign systems that can produce ammonia and utilize it for power generation need to be developed. Such systems have the potential to overcome various challenges associated with energy production, storage and distribution. The environmental challenges associated with current conventional ammonia synthesis can be mitigated through such systems and the considerable amounts of harmful emissions produced during ammonia production can be avoided.

1.4 Conventional fossil fuel-based ammonia production

Fig. 1.8 shows the global production of ammonia from fossil fuel-based methods that have significant environmental detriments. Fig. 1.8 depicts the usage of different feedstock that are employed in ammonia synthesis plants. Natural gas is the primary source of feedstock utilized in nearly 72% of ammonia synthesis plants. This includes the SMR process (described earlier) that reforms natural gas using steam. Other fossil fuels including coal and fuel oil the next two largest sources and account for 22% and 4% of the total feedstock provided respectively.

The feedstock utilized is dependent upon the resource availability for a given location. For instance, owing to the easier availability of coal in China, coal is the primary feedstock for synthesizing ammonia. This is why China has higher greenhouse gas emissions as well as energy consumption related to ammonia synthesis, as compared to other countries. However, in the U.S., natural gas comprises the main resource utilized as feedstock for ammonia synthesis plants constituting nearly 98% of national production [11]. The significant reliance on natural gas has also made ammonia prices dependent on the fluctuations in gas prices.

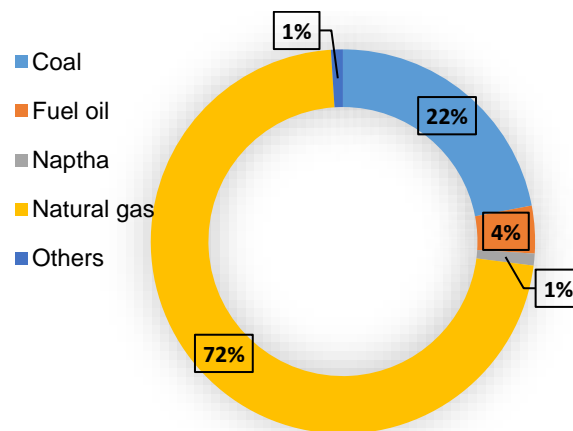
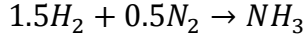


Fig. 1.8 Global usage of fossil fuel resources for ammonia synthesis (Data from [12-13])

There are several routes that can be utilized to synthesize ammonia as depicted in Fig. 1.9. The Haber-Bosch process is the technique that is most commonly employed. In this process, the exothermic combination of hydrogen and nitrogen in the presence of a catalyst is undertaken to produce ammonia according to the following chemical reaction:



For each mol of ammonia produced through the above reaction, 45.2 kJ of energy is released due to the exothermic reaction. The Haber-Bosch process was introduced in the twentieth century and has been the most widely used process since then. In this process, the molecular bonds of nitrogen and hydrogen molecules are broken followed by atomic adsorption on catalyst surface to form ammonia molecules. As the chemical reaction is exothermic, high reaction pressures and low reaction temperatures favour higher rates of ammonia synthesis.

As depicted in Fig. 1.9, the pure stream of nitrogen required is obtained via air separation units. Generally, these comprise of either cryogenic or adsorption-based air separation processes. In cryogenic systems, nitrogen and oxygen are separated from air through cryogenic refrigeration. In adsorption-based systems, selective adsorption of nitrogen molecules allow their separation from other gases contained in air. During ammonia synthesis, a portion of the input stream remains unreacted that is recycled back into the synthesis reactor. An iron-based catalyst comprises an integral part of the overall process that enhances the rate of ammonia synthesis reaction.

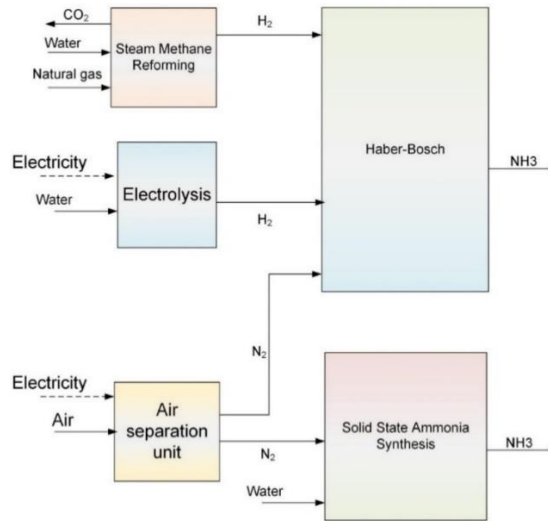


Fig. 1.9 Different routes of ammonia production via electricity and natural gas usage (Adapted from [9])

Apart from the renewable energy based-water electrolysis technique, solid-state ammonia synthesis (SSAS) processes are also being investigated. In this type of ammonia synthesis

technique, electricity, nitrogen, and water inputs are converted into ammonia molecules through a series of electrochemical reactions. The SSAS is considered to be another alternative for clean ammonia production. Primary use of ammonia is for fertilizer production. As the demand for global food supply increases every year, the demand for fertilizers and thus ammonia also rises proportionally. Hence, if the dependence on fossil fuels for synthesizing ammonia were not decreased, the continuous rise in ammonia production would mean a continuous rise in greenhouse gas (GHG) emissions as well as detrimental environmental impacts.

A comparison of GHG emissions associated with ammonia synthesis globally is provided in Table 1.2. Owing to the heavy consumption of coal in ammonia synthesis plants in India and China, comparatively higher GHG emissions of 5.21 kgCO_{2eq} result for every 1 kg of NH₃ produced. The global average is estimated to be nearly 3.45 kgCO_{2eq}/kg NH₃. These emission values, as well as the continuously rising trends in ammonia production, demonstrate the significance in decreasing the dependency on fossil fuels.

Table 1.2 Regional breakdown of GHG emissions associated with ammonia production

Region	GHG emissions (kg CO_{2eq}/kgNH₃)
India and China	5.21
Russia and Central Europe	3.31
North America	2.55
Western Europe	2.34
Rest of the world	2.45
World average	3.45

Source: Ref. [14]

The conventional ammonia synthesis process is associated with different sub-processes that are needed due to the usage of fossil fuel-based resources as shown in Fig. 1.10. When natural gas is used as the feedstock, the desulfurization process is undertaken to separate the constituent sulfur atoms. This is carried out through a catalytic process that reacts hydrogen with sulfur to form sulfide compounds. Removing sulfur is essential as it deteriorates the catalyst activity. The desulfurized natural gas is sent to the SMR process described earlier. The CO₂ content in the SMR outlet is lowered via the CO₂ removal process. Either this process includes a physical absorption or pressure swing adsorption

based process to separate carbon based emissions. The next process includes methanation that involves further elimination of CO₂ and CO through chemical reactions with hydrogen to form methane and water. Finally, the clean hydrogen stream exiting the methanation process is sent for ammonia synthesis where nitrogen obtained via cryogenic air separation also enters the subsystem.

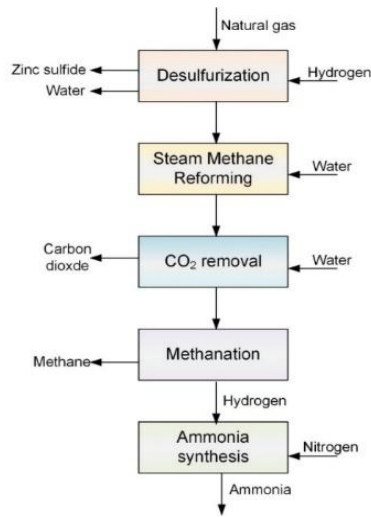


Fig. 1.10 Different stages in conventional natural gas-based ammonia synthesis (Adapted from [9])

1.5 Ammonia utilization

Conventional ammonia utilization breakdown is shown in Fig. 1.11. Nearly half of the ammonia produced globally is used for urea production constituting about 48% of the total usage. Ammonia is also utilized in non-fertilizer related chemical industries that constitute nearly 19% of the usage and nearly 14% of ammonia use is in the production of other fertilizers apart from urea. Another 7% and 8% of the total usage is attributed to ammonium phosphate and ammonium nitrate respectively.

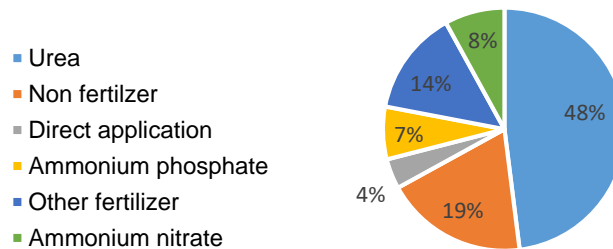


Fig. 1.11 Percentage of ammonia utilization in different industries (Data from [12])

However, favourable properties of ammonia make it suitable for use in a variety of applications as depicted in Fig. 1.12. Firstly, ammonia is used as the working fluid in refrigeration systems.

Specifically, absorption chillers utilize ammonia-water mixtures to provide cooling. The usage of ammonia in compression-based refrigeration cycles has also been investigated. Ammonia can be used in different energy production systems, ranging from spark ignition to compression ignition engines, ammonia can be utilized to power vehicle engines. Ammonia can also be combusted to release thermal energy in ammonia gas turbines as well as stationary power generators. Boilers and furnaces can also combust ammonia to produce thermal energy, or ammonia fuel cells can generate power through electrochemical conversion processes. Having favorable properties in comparison with hydrogen such as higher volumetric densities and lower safety hazards, ammonia has been proposed to be a promising candidate for fuel cell applications.

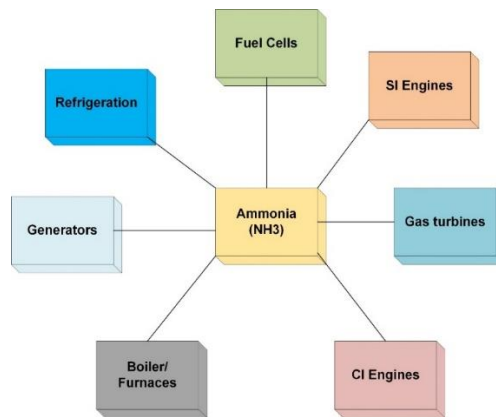


Fig. 1.12 Different possible applications of ammonia fuel

1.6 Thesis outline

This thesis consists of seven chapters. The first chapter covers the introduction and background information where the significant use of fossil fuels is discussed highlighting the importance of renewable energy resources and their significance in the future of clean energy production. The usage of ammonia fuel in various applications and its importance as a carbon-free fuel is described. The second chapter is a literature review where relevant studies performed in the present research area are surveyed and described. Their main contributions are highlighted and the need for improvements are suggested. The main gaps

in the literature that are found though the survey are also described. The motivation of the present study considering these gaps is highlighted. The original contributions as well as specific objectives of the study are discussed. The third chapter describes the integrated solar and wind-based energy systems. Three different systems developed are described along with the details of each subsystem utilized. The fourth chapter covers the experimental apparatus and procedures. The experimental apparatus utilized as well as different components constituting the ammonia fuel cell and synthesis systems are described and their specific details are provided. The fifth chapter discusses the methodology utilized for the comprehensive thermodynamic, exergoeconomic and multi-objective optimization studies of the developed systems. The sixth chapter presents the results obtained. The experimental results obtained are described followed by the thermodynamic analysis results of each system. The results of the transient analysis performed considering the variations in the solar intensities as well as wind speeds are described. The peak and minimum daily production capacities of useful commodities across the year are described for each system. This is followed by the exergoeconomic analysis results that present the total cost rate of the energy systems developed as well as the associated cost rates of different subsystems included. Various sensitivity analyses that are performed are described to depict the system performance through integrated exergetic and economic analyses. The results obtained for the multi-objective optimization of each system maximizing the efficiencies and minimizing the total cost rates are discussed. Finally, in chapter 7, conclusions with main findings as well as several recommendations for future studies are presented.

CHAPTER 2 : BACKGROUND AND LITERATURE REVIEW

In this chapter, a literature survey of studies that have developed or investigated similar subsystems is presented. Solar and wind energy-based integrated energy systems for producing clean hydrogen and ammonia are covered first. These are followed by studies incorporating ammonia as the energy storage medium in either direct or indirect ammonia fuel cell systems.

2.1 Integrated energy systems for clean hydrogen and ammonia synthesis

Clean ammonia production methods can be divided into two main categories. The chemical method of synthesizing ammonia reacts hydrogen and nitrogen gases at temperatures in the range of 200°C to 400°C and high pressures of 100-300 bar. These methods include the production of hydrogen and nitrogen from different renewable energy sources as shown in Fig. 2.1. Although there are several types of renewable energy sources that can be used for this purpose, solar and wind comprise the primary technologies that have been investigated. This can be attributed to the current rise in the consumption of these renewable energy resources. Solar and wind energy-based clean ammonia synthesis options have also been investigated due to the potential of utilizing excess energy which is available during periods of high solar intensity or excess wind speeds.

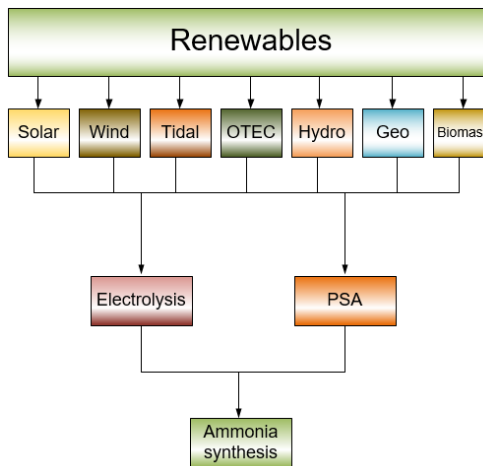


Fig. 2.1 Schematic representing clean ammonia synthesis through different renewable energy sources (Adapted from [6])

Several studies have considered this clean ammonia synthesis route. Wang *et al.* [15] investigated the integration of solar energy in a conventional ammonia synthesis plant. In

this system termed a solar ammonia refinery, solar electricity, heat and photons produced the hydrogen and nitrogen required for the synthesis. However, the system also relied on steam methane reforming for hydrogen production. Solar collectors generated heat and electricity, which provide the necessary heat and power for various subsystems found in conventional ammonia synthesis plants.

Hasan and Dincer [16] studied a renewable energy based system for cogeneration of ammonia power. Solar and wind energy operated the system. Proton exchange membrane (PEM) water electrolysis was considered and a multistage ammonia production system was incorporated. The waste heat from the ammonia synthesis system was used to operate a Rankine cycle for power generation. The overall system efficiency was found to be 75.8% in terms of energetic performance and 73.6% in terms of exergetic performance.

Bicer and Dincer [17] investigated a solar based electrochemical ammonia synthesis system that operated with photoelectrochemical hydrogen. Water electrolysis powered by solar PV was used with photo-sensitive electrodes that permitted incoming solar radiation to enhance the hydrogen production rates. The molten electrolyte based electrochemical route was taken for synthesizing ammonia. A eutectic mixture of sodium and potassium hydroxide was used as the molten salt electrolyte. The operating temperatures varied from 180 °C to 260 °C. The electrodes were fabricated from nickel meshes, and had an area of 25 cm². The ammonia synthesis rate was found to be 4.41×10^{-9} mol/s cm² and the coulombic efficiency was reported to be 14.2%.

Sanchez and Martin [18] investigated a clean ammonia production system from air and water. Solar PV and wind energy resources were considered. The nitrogen was produced from a Linde's double column and the hydrogen from water electrolysis. The study focused on modelling and optimizing the parameters of each subsystem including water splitting and air separation.

Matzen *et al.* [19] investigated a renewable ammonia and methanol production system that operated with wind power. The ammonia production capacity was 1202.6 mTonne/day. However, the hydrogen requirement for this production was reported to be 217.72 mTonne/day. The nitrogen production capacity required was evaluated to be 1009.15

mTonne/day. For such plants, the primary constraint in terms of cost was described to be the production of hydrogen.

Pfromm [20] studied the production of clean ammonia for sustainable agriculture. The study was focused on environmental and economic aspects of such systems. The energy price of producing ammonia without the consumption of fossil fuels was reported to be \$0.2/kg. The amount of CO₂ emissions that could be avoided through this clean synthesis of ammonia was reported to be 1.5 tonnes. The development of new ammonia production systems that can eliminate the use of fossil fuels was suggested.

Al-Zareer *et al.* [21] developed and investigated a new ammonia production system for the application of hydrogen storage. The system included a multistage ammonia production methodology and an ammonia electrolyser for dissociation. A tanker truck equipped with an ammonia storage tank at high pressure was considered. The input hydrogen was converted into ammonia and stored at high pressures. When hydrogen was required, the stored ammonia in the tank was passed through an ammonia electrolyser to produce constituent nitrogen and hydrogen gases. The ammonia synthesis subsystem was incorporated with a steam turbine for power generation. The energy efficiency of the overall system was found to be 72.3% and the overall exergy efficiency of the system was reported to be 71.8%. The ammonia storage capacity considered was 21 m³ at a pressure of 61 atmospheres.

Ye *et al.* [22] summarized various possible technologies for clean ammonia synthesis and discussed the techno-economic aspects. The primary methods of producing clean ammonia described were carbon capturing methods, water electrolysis for hydrogen production, and electrochemical ammonia synthesis techniques. The carbon capturing methods were found to be unfavorable. The water electrolysis route posed significant challenges because the low hydrogen production pressures were unsuitable for ammonia synthesis. The primary challenge was identified to be the electrochemical reduction of nitrogen. Diatomic (N₂) nitrogen is highly inert nature and is difficult to reduce. High power inputs would be required to dissociate the nitrogen bonds and form negatively charged anions.

Shahid *et al.* [23] investigated a new renewable energy based system for multigeneration, which produced clean ammonia and used it as a hydrogen storage medium. The hydrogen

required for ammonia synthesis was obtained from electrolysis of desalinated water. The required nitrogen was supplied from an external source. The multigeneration system incorporated an organic Rankine cycle as well as steam Rankine cycle for power generation, and an absorption cooling cycle provided cooling through the available waste heat. PEM water electrolysis was used for hydrogen production. The energy efficiency was reported to be 28% for the overall system and the exergy efficiency was found to be 18.9%.

Gordon [24] designed an ammonia synthesis system that operated with non-carbon based hydrogen production. The nitrogen production technique was employed in a way to provide de-centralized nitrogen generation. The water electrolysis hydrogen production method was used and the pressure swing adsorption based nitrogen generation method was utilized. While the proposed system was presented, the output capacities were not reported.

Javaid and Nanba [25] studied clean ammonia synthesis over Ru/CeO₂ catalysts. Ammonia synthesis was observed to be higher values at 375°C and 2.5 MPa. It was observed that the ratio of hydrogen and nitrogen had a significant effect on the synthesis rates. Higher temperatures were observed to favour higher synthesis rates at higher hydrogen to nitrogen ratios. Lower hydrogen to nitrogen ratios were reported to be suitable for enhancing ammonia synthesis rates at lower temperatures and a pressure of 2.5 MPa. Finally, the synthesis activity was also found to rise with increasing pressures at high temperatures, which was attributed to the high dispersion of Ru particles.

Armijo and Philibert [26] investigated the flexible production of clean ammonia and hydrogen using wind and solar energy. Technoeconomic modelling of the solar and wind-based energy system was performed. The hybridization of solar and wind energy resources was found to result in a reduction of hydrogen production costs. The hybridization technique was reported to promote favourable outcomes for ammonia production. For instance, the variability in power outputs was observed to decrease leading to lower operational costs. The near-term production cost of hydrogen was estimated to be \$2/kg while the ammonia production cost was evaluated as \$500/Tonne.

Esteves *et al.* [27] studied the potential of producing clean ammonia via solar and wind energy. The proposed system used water electrolysis-based hydrogen production that was powered via renewable solar and wind energy. The ammonia synthesis process considered

was the Haber-Bosch process. The study focused upon mapping potentials of utilizing solar and wind energy in different locations to produce clean hydrogen and thus ammonia. The feasibility of developing such systems was also investigated.

Mohammed and Bicer [28] proposed a solar-based clean ammonia production system that utilized liquefied natural gas. Solar energy was used for thermal cracking that was integrated with the ammonia synthesizer. The designed system produced a pure stream of CO₂ suitable for urea synthesis. The optimal temperature for the thermocatalytic cracking was found to be 900°C and the optimal pressure for hydrogen production was reported to be 23.8 bar. The efficiencies of the system were found to be 35.8% energetically and 37.4% exergetically, and had a production capacity of 974 Tonnes per day.

Verleysen *et al.* [29] performed optimization of a wind energy-based clean ammonia synthesis system to investigate its robustness under operational uncertainties. It was reported that a trade-off exists between the robustness and ammonia production. For instance, the productive design provided 3.2 times higher productivity albeit a 2.6 times lower robustness. However, it was also found that the productive design had an effect of 75.4% and 22.5% on the ammonia production, due to speed measurement error and temperature variation respectively. Nevertheless, the robustness was reported to increase with a decrease in load size.

Guerra *et al.* [30] performed a technoeconomic analysis of a clean ammonia synthesis plant. The system investigated used water electrolysis for producing hydrogen. An optimized electrolyser stack input of 164.2 MW was studied and the economic analysis provided a payback period of 7.62 years. The net present value was 76.1% positive occurrence considering the capital costs as well as various operational and maintenance costs.

Sanchez and Martin *et al.* [31] investigated the scale up and scale down issue associated with clean ammonia synthesis plants utilizing renewable energy. A modular design was considered to evaluate the performance. The nitrogen production techniques considered included the membrane-based separation, PSA based air separation and Linde's double column technique. The hydrogen production was considered via solar and wind powered water electrolysis. It was found that the membrane-based separation technique is more

favourable for low production rates while the PSA technique is more favourable for medium capacities of ammonia synthesis.

Allman and Daoutidis [32] performed an optimization study on a wind-powered ammonia production system and investigated the effects of key design parameters. A 48-hour receding horizon optimization was proposed for optimizing the schedule set points that provide minimum costs. The results obtained were utilized to develop correlations between the operating costs and capacity ratios. The dependency on location was mitigated through scaling optimization. The study was focused on optimizing the overall supply chain of ammonia by keeping the overall costs as low as possible.

Osman *et al.* [33] performed a techno-economic optimization of a renewable energy-based ammonia production plant. The hydrogen needed for ammonia synthesis was obtained via water electrolysis of desalinated seawater, while the nitrogen required was acquired through an air separation unit. The energy consumption of the developed system was reported to be 10.43 kWh/kg-NH₃ while the efficiency of the system was reported to be 37.4%. The optimization study performed, determined the optimal configuration of generation and storage.

Tallaksen *et al.* [34] studied a community-scale ammonia production plant powered by wind energy. The study focused on determining the GHG emissions as well as energy balances. A cradle-to-gate life cycle assessment was performed. The study examined two distinct cases considering the effect of location and dependence on the local energy system as well as the balance of system for the ammonia production. It was found that the renewable energy-based ammonia production system leads to a significant decrease in emissions, however, the source of regional electricity generation was found to be a significant contribution to the overall life cycle environmental impacts.

Morgan *et al.* [35] investigated a wind-powered ammonia synthesis system targeting isolated islands. Air and water were converted into ammonia. A traditional air separation unit was used to generate the required nitrogen while hydrogen was produced using alkaline electrolyzers. The mechanical vapor compression-based desalination unit was also utilized to produce a clean stream of water while ammonia was produced via Haber-Bosch. Wind data for a specific island were utilized to analyse the system. Although the wind-

based system entailed higher cost as compared to the conventional diesel-based system, the breakeven diesel price that makes the wind-powered system competitive was also determined.

Palys *et al.* [36] proposed a wind powered system for both sustainable energy and agriculture using clean ammonia. The design capacity of the system was considered according to a demand of 40.3 Tonne/year while the power demand was 985 kW. The system was reported to provide an emission reduction cost of \$17.6 per tonne of CO₂ and also used hydrogen and ammonia as energy storage mediums.

Usman *et al.* [37] performed a thermodynamic assessment of a multigeneration system that stored hydrogen in the form of clean ammonia. Along with clean ammonia, the system produced hydrogen, heating, electricity and cooling. A phase change material was used as the energy storage medium. The system was investigated via first and second laws of thermodynamics. Several parametric analyses were also performed to investigate how environmental as well as other parameters effect the performance. The energy efficiency of the system was reported to be 18.9%, while the exergetic performance was 28%. An exergy destruction rate of 32 MW was calculated for the steam Rankine cycle.

The second method of producing clean ammonia uses the electrochemical method of ammonia synthesis and produces ammonia through electrical input, electrodes, and electrolyte. In this method, high pressures are not required and the synthesis process can be performed at ambient conditions. Fig. 2.2 depicts different types of electrochemical ammonia synthesis routes [9].

As can be observed from the figure, the major classification is based on the type of electrolyte used. The liquid state electrolyte based electrochemical ammonia synthesis employs different types of solutions and can be operated at ambient temperatures. Molten electrolyte based electrochemical ammonia synthesis includes the utilization of eutectic mixtures of molten salts such as potassium or sodium hydroxide. Membrane electrolyte based ammonia synthesis are comprised of composite membrane electrolytes of different materials such as potassium or calcium phosphate and yttria decorated chromium. Finally, solid oxide based electrochemical methods of ammonia synthesis have also been investigated.

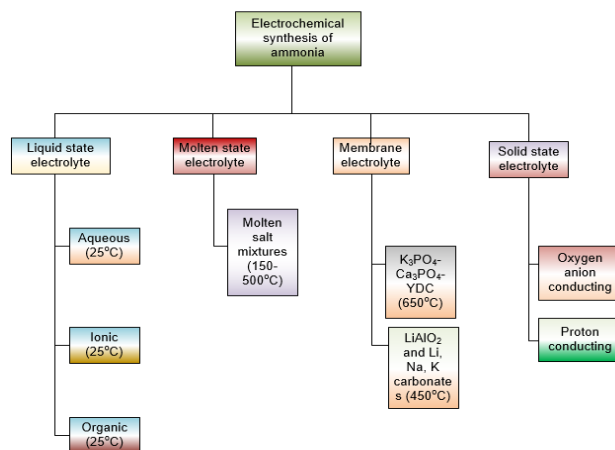


Fig. 2.2 Schematic representing different electrochemical routes of ammonia synthesis (Adapted from [9])

The operating pressures for electrochemical synthesis routes are generally near ambient pressure and high pressures are not necessary. However, operating temperatures vary according to the type of electrolyte. Typically, molten electrolytes have operating temperatures ranging from 150 to 500°C while composite membranes require temperatures from 450°C to 650°C. Recently, attention has been directed towards clean and green ammonia synthesis.

Several studies have investigated the electrochemical route of ammonia synthesis. Bicer and Dincer [38] investigated a solar-based electrochemical ammonia production system using photoelectrochemical hydrogen. The study was focused on performing exergoeconomic as well as optimization studies. The study considered a solar concentrator as well as spectrum-splitting mirrors to produce photoelectrochemical hydrogen. The solar PV-based system energy input was considered to operate the electrochemical ammonia synthesis system. The performance parameters obtained were then optimized to maximize the efficiencies and minimize the costs. The optimal exergetic efficiency of the system was found to vary between 5% and 9.6%. Optimal efficiencies of the hydrogen production and ammonia synthesis subsystems were found to be 8.7% and 5% respectively.

Licht *et al.* [39] studied clean synthesis of ammonia from the electrochemical route. Ammonia was produced from water and nitrogen. The electrolyte was composed of a molten salt and nano-size iron oxide catalyst. The coulombic efficiency of the ammonia

synthesizer was reported to be 35%, at operating conditions of 250°C and a steam pressure of 25 bar.

Kim *et al.* [40] studied ammonia synthesis from electrical power via the electrochemical route. They employed lithium-potassium-caesium chloride based electrolyte and utilized iron oxide as well as cobalt oxide catalysts. The ammonia production rate was reported to be 3×10^{-10} mol/cm²s. The reactants used for the synthesis included nitrogen and water.

Utilizing molten salt alkaline hydroxide electrolytes provides various opportunities of implementation in several applications. These operate at comparatively lower temperatures than chloride salts and also entail lower corrosiveness. Yang *et al.* [41] reviewed various types of molten salt based electrochemical methods of ammonia synthesis. They summarized the factors for selecting sources of hydrogen in these processes, and characterization of the reaction was performed for all associated reactions. The Faradaic efficiency of molten salt based ammonia synthesis was reported to be as high as 80% and the formation rate was also reported to be higher than solid state or aqueous electrolytes for the nano-size iron oxide catalyst.

Bicer *et al.* [42] investigated a wind powered electrochemical ammonia synthesis system using a molten salt electrolyte. To assess the system performance, wind speeds associated with a given location were considered. A wind turbine with a rated power output of 6 MW was considered. Electrochemical modelling of the ammonia synthesis system was performed. The results obtained showed that the two parameters that mainly influenced the low-frequency region were the electrolyte capacitance and the capacitance of the electrode. Finally, different electrochemical impedance spectroscopy models were developed and validated.

Zhao *et al.* [43] also conducted a review of the recent advances in electrochemical ammonia synthesis at atmospheric pressure. New electrocatalysts developed for the reduction reaction on the nitrogen molecule, which is essential in electrochemical ammonia synthesis were discussed. The types of catalysts investigated in the literature include precious metal based catalysts, which primarily are fabricated from ruthenium, gold, or palladium. Other non-noble metal based electro-catalysts studied include catalysts synthesized from

molybdenum, titanium, and iron based materials. Other non-metal comprising catalysts have also been investigated which include carbon and phosphorous based synthesis.

Gomez *et al.* [44] performed a techno-economic and life cycle assessment study of electrochemical ammonia production utilizing proton conducting membranes. Near ambient operating pressure was considered for the synthesis process utilizing a feed rate of 32 Tonnes/day of hydrogen and 135 Tonnes/day of nitrogen. Several pathways utilizing different hydrogen and nitrogen production techniques were investigated. The electrochemical synthesis of ammonia using hydrogen from the water electrolysis subsystem and nitrogen from the cryogenic air separation unit was found to be a viable pathway. The discounted cash flow return from the system was found to be 8%.

Wahedi and Bicer [45] proposed an off-grid charging station for electrical vehicles. The system included hybridization with renewable energy sources as well as multiple energy storage units, and was designed to fast-charge 80 electric vehicles. Hybridization of concentrated photovoltaic/thermal (PV/T), wind turbines and biomass with several energy storage units was considered. Both hydrogen and ammonia fuel cells were also utilized for clean power generation. The absorption cooling cycle was employed to produce cooling needed for battery cooling as well as ammonia liquefaction.

Casallas and Dincer [46] assessed an integrated solar-powered electrochemical ammonia synthesis system. An experimental system was built and designed considering lab-scale operation. Nano-size iron catalysts were utilized for the synthesis process. The ammonia concentration in the output stream was found to be 950 ppm. By increasing nitrogen flow rates as well as decreasing steam flow rates, higher output concentrations were possible. The optimum current and voltage for the developed electrochemical system was found to be 650 mA at 1.7 V. The proposed system was suggested to be investigated with an integration to fuel cell systems to attain higher efficiencies.

Sanchez *et al.* [47] investigated a sustainable dimethyl carbonate (DMC) production system utilizing CO₂ as well as renewable ammonia and methanol. The proposed system entailed the synthesis of urea followed by DMC production. The production cost of DMC was found to be \$665/Tonne. The associated subsystems were also investigated including the synthesis of urea from ammonia. A simple sustainability model was also used to

determine the environmental performance of the developed system. Kyriakou *et al.* [48] proposed and investigated an electrochemical Haber-Bosch process. The proposed electrochemical cell placed methane and steam at one electrode, and nitrogen at the other. The anode included electrochemical interaction of methane and steam to form CO₂ and H⁺ ions. The H⁺ ions formed were then transported to the cathode via a proton conducting membrane. At the cathode, nitrogen molecules react electrochemically with positively charged H⁺ ions to form ammonia. The cathode included the electrochemical reduction of H⁺ ions to hydrogen gas. It was reported that the extraction of hydrogen from the reforming compartment improves the overall performance. The percentage conversion of H⁺ ions to ammonia was found to range between 5% and 14%.

Chisalita *et al.* [49] performed an environmental evaluation of different ammonia synthesis routes including the renewable hydrogen based route. The cradle-to-gate life cycle assessment methodology was used and the environmental impact assessment method of ReCIpe was considered. It was reported that the route of producing hydrogen via steam methane reforming integrated with chemical hydrogen looping entailed comparatively higher reduction in the global warming potentials. However, this method was found to entail higher environmental impacts considering other impact categories. The electrolysis-based hydrogen production route was reported to be environmentally benign if undertaken through renewable energy resources.

Zhang *et al.* [50] conducted a comparative technoeconomic study of different types of green ammonia production methods. The reference production capacity was considered to be 50 kTonne/year. The study found that tradeoffs existed between the overall system efficiencies and the production costs. The power-to-ammonia route was reported to have comparatively higher efficiencies than the biomass-to-ammonia and methane-to-ammonia routes. An overall theoretical efficiency of 74% was obtained for the power-to-ammonia route. However, the feasibility of this route was reported to be dependent on the increased use of renewable energy resources as well as mass production of solid oxide electrolytes.

2.2 Ammonia for energy storage and power generation

Once clean ammonia is synthesized, it can be used for power generation through various methodologies. Ammonia based power generation methods can be broadly classified into

thermochemical and electrochemical methods. The thermochemical methods include the conversion of chemical energy into thermal energy that is further converted into electrical energy. However, electrochemical method of power generation includes direct conversion of chemical energy into electrical energy. Different technologies under each type of category are summarized in Fig. 2.3 [17]. The thermochemical methods include ammonia gas turbines, spark ignition engines, compression ignition engines, and ammonia boilers which include the conversion of chemical energy to thermal energy for applications where thermal energy is required.

The electrochemical methods of power generation from ammonia fuel include different types of ammonia fuel cells. Membrane based direct ammonia fuel cell (DAFC) use anion exchange membranes that act as alkaline electrolytes for the operation of an electrochemical cell. Molten electrolyte cells use a molten salt electrolyte in a DAFC. Ammonia fed solid oxide fuel cells (SOFC) use ammonia fuel in a high temperature fuel cell where the ammonia is partially dissociated into constituent hydrogen, which reacts electrochemically to produce power. Ammonia cracking followed by fuel cell operation is another technique that involves dissociating ammonia into hydrogen and nitrogen followed by a hydrogen fuel cell that generates electrical power. Along with these ammonia based power generation methods, cyclic ammonia synthesis and dissociation based energy storage methods have been investigated.

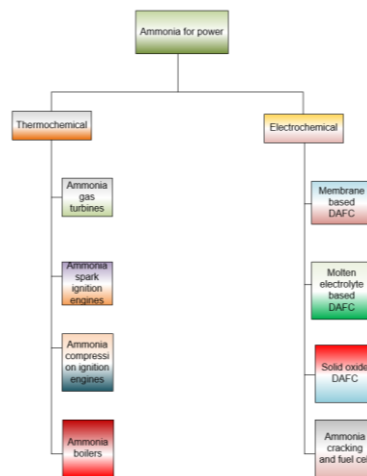


Fig. 2.3 Schematic representing the classification of ammonia power generation methods (Adapted from [17])

Chen *et al.* [51] investigated the ammonia based solar thermochemical energy storage method with a conical reactor for the dissociation reaction. In this system, concentrated solar energy is used to dissociate ammonia into nitrogen and hydrogen, which are stored. When energy is required, these stored gases are allowed to react in the ammonia synthesis reactor which produces thermal energy because the reaction is exothermic. The thermal energy output resulting from the exothermic ammonia synthesis reaction is used to operate a power cycle. This process is repeated in a cyclic manner, where the ammonia produced is reused in the solar based dissociation reactor during periods of surplus power. The study was focused on investigating the effects of the geometrical designs of the dissociation reactor.

Lovegrove *et al.* [52] developed and investigated solar dish based thermochemical energy storage with ammonia. The system included 20 tubes of reactors, where each tube was filled with an iron based catalyst for ammonia synthesis. The solar dish comprised of an area of 20 m² to provide thermal energy to the ammonia dissociation reactor. The energy storage efficiency of the developed system was found to be nearly 53%.

Zhou *et al.* [53] investigated ammonia for energy storage as an energy storage medium to store hydrogen, which could be utilized for renewable and clean power generation. The energy storage system proposed included the utilization of solar, wind and biomass energy resources with a water electrolysis and air separation unit for hydrogen and nitrogen production. The produced hydrogen and nitrogen were then used to synthesize ammonia, which was considered to be a raw material for various applications such as fertilizer production and power generation.

Wang *et al.* [54] investigated an ammonia based energy storage system for a large scale solar PV power plant. The proposed system also considered the water electrolysis route to produce hydrogen during periods of surplus energy availability. An air separation unit to produce nitrogen from air was considered that operated with an electrical power input. These were followed by ammonia synthesis and storage. This method of energy storage was found to be more favourable than lithium ion batteries. A comparative study showed that lithium ion batteries have 10 times lower energy density per volume than ammonia. Ammonia based energy storage is associated with significantly higher storage times than

batteries. For instance, the ammonia energy storage system was reported to have a storage time range of 10 to 10000 hours whereas the lithium battery had a maximum storage time of 10 hours.

Wang *et al.* [55] investigated a new ammonia based energy storage system. The conceptual system comprised of cyclic ammonia synthesis and power generation with a reversible SOFC. The SOFC was used reversibly to generate power electrochemically or dissociate water into hydrogen and oxygen. A refrigeration cycle was incorporated to liquefy the ammonia and water produced during operation. The conceptual system was studied for a 100 MW capacity. The round trip efficiency of the energy storage system was reported to be 72%.

Ikaheimo *et al.* [56] investigated a power to ammonia route for the European case to achieve a complete renewable power generation and heat system. The power to ammonia route was described as having the primary advantages of clean ammonia for the fertilizer industry, energy storage, and production according to demand. The proposed system included a combination of renewable energy resources such as solar, wind, and hydropower. The electricity grid was interconnected to the ammonia synthesis system to produce ammonia during periods of surplus energy. The system produced heat along with electricity. The study found that the water electrolysis route for hydrogen production has the highest energy input and is thus associated with the highest cost in the system.

2.3 Ammonia fuel cells

Ammonia fuel cells provide an environmentally benign method to produce electrical power from ammonia fuel. Hence, once clean ammonia is synthesized during periods of surplus energy, it can be used in ammonia fuel cells to produce clean energy. Several types of ammonia fuel cells have been investigated recently. Fig. 2.4 summarizes these ammonia fuel cell types. The type of ammonia fuel cells can be broadly classified into direct and indirect types of cells. The direct type of cells include the direct input of ammonia fuel without dissociation into constituent nitrogen and hydrogen molecules.

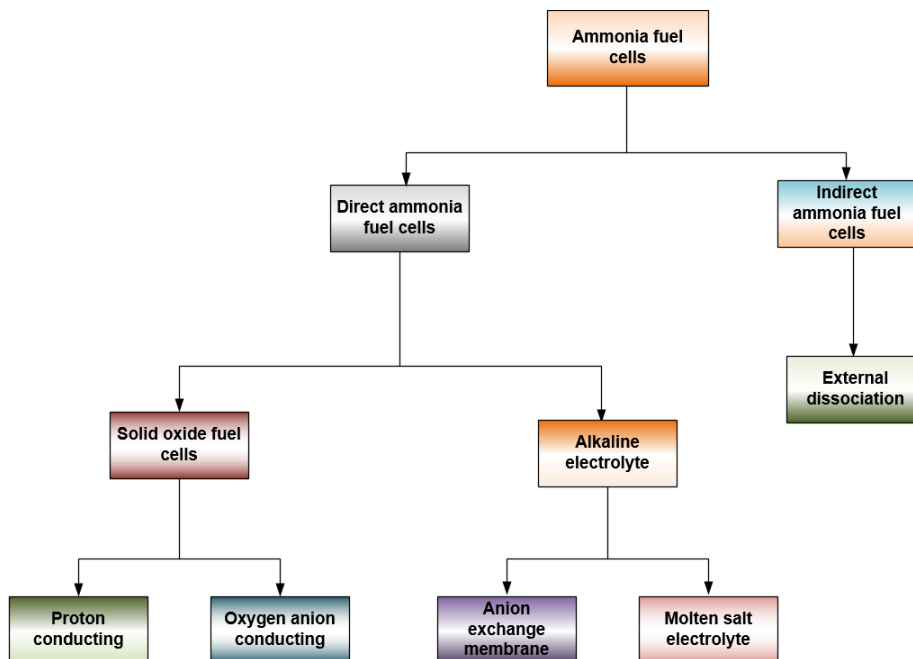


Fig. 2.4 Schematic representing different types of ammonia fuel cells (Adapted from [103])

On the other hand, indirect ammonia fuel cell systems include an external ammonia storage and dissociation unit. The stored ammonia is first dissociated externally to form hydrogen molecules that are allowed to enter the fuel cell and react electrochemically for power generation.

Several studies have been conducted on direct ammonia fuel cells. These can be classified into ammonia fed SOFC and direct ammonia alkaline electrolyte fuel cells. Each of these categories can be further divided into subcategories. The ammonia fed SOFC can be divided further into proton conducting and oxygen anion conducting electrolyte cells. The direct ammonia alkaline cells can be further classified into membrane or molten electrolyte cells. In the following sections, previous studies under each of these categories are summarized.

2.3.1 Ammonia-based solid oxide fuel cells

Solid oxide fuel cells for direct utilization of ammonia as a fuel have been developed and investigated. These can be divided primarily into two categories: (i) Oxygen anion conducting and (ii) Proton conducting. This classification is based upon the type of electrolyte used where the type of ions transferred through the ion conducting solid oxide

electrolyte determines the category of SOFC. In these type of ammonia fuel cells, there is a high operating temperature between 500°C and 1000°C. Ammonia is fed to the anodic compartment of the cell where owing to the high cell temperature, it is dissociated in H₂ and N₂ molecules. In the first category of ammonia-based SOFC (also referred to as SOFC-O), commonly used electrolytes include samarium doped ceria (SDC) and yttria stabilized zirconia (YSZ) materials. An SOFC-O with an SDC electrolyte was investigated and a power output density of 168.1 mW/cm² was obtained. The thickness of the electrolyte was 50 μm. To decrease the cell cost, nickel was used as the anodic material, while the cathode was fabricated from samarium-cobalt oxide-strontium-based material. The developed SOFC-O was reported to provide higher performances at elevated temperatures [57]. A similar ammonia-based SOFC-O was investigated with the same electrolyte and anodic material. In this case, barium-cobalt oxide-strontium-iron oxide based cathodic material was used and it was found to provide better performances at higher temperatures. However, this electrolyte thickness that was five times lower allowed to attain a considerably higher power output of 1190 mW/cm². The operating temperature corresponding to this output was reported to be 650°C. Increased hydrogen utilization rates were also reported to provide higher performances reaching up to an increase of approximately 682 mW/cm² [58].

Another ammonia-based SOFC-O was developed utilizing SDC electrolyte [59]. A low-cost nickel oxide was used as the cathode with a low electrolyte thickness of 50 μm. A samarium-cobalt oxide-strontium was used as the cathode. The performance of the developed cell provided a power output density of 467 mW/cm², observed at a temperature of 650°C, corresponding to the peak power density.

The next category of SOFC-O includes the utilization of the YSZ electrolyte. The comparative performance of these ammonia-based cells were lower as compared to the SDC-based fuel cells. A maximum output density for power, for example, was found to be 202 mW/cm² for an YSZ-based ammonia fueled SOFC [60]. Although the electrolyte thickness was comparatively lower (15 μm), the cell performance was lower as compared to the SDC-based cells. The nickel-based anode was utilized along with a lanthanum-

strontium-manganese oxide cathode. The peak power found corresponded to a temperature of 800°C.

Another study investigated a similar ammonia-based SOFC-O with similar electrolyte composition, anodic as well as cathodic materials. However, the electrolyte thickness considered was twice as compared to the previous study. A power density of 299 mW/cm² was measured at 750°C and a rise of approximately 227 mW/cm² was found at 850°C [61]. A 400 µm thick YSZ electrolyte-based ammonia fuel cell was investigated with nickel oxide and silver as the anodic and cathodic materials respectively [62]. A low cell performance was reported with a power output of 60 mW/cm² at 800°C. The lower performance of the cell was attributed to the high electrolyte thickness, as higher electrolyte thicknesses are associated with higher resistances to ionic currents.

Another ammonia-based SOFC-O with a 200 µm thick YSZ electrolyte was investigated [63]. Here a nickel anode and a lanthanum-strontium-manganese oxide cathode generated a power output of 88 mW/cm², which is comparatively low considering that it was operating at a temperature of 900°C. The power output was reported to drop by 50 mW/cm² when the cell operated at 700°C.

Thus, several parameters of the SOFC-O effect the output cell performances. Higher temperatures allow faster dissociation of ammonia molecules, leading to higher power outputs. Platinum has been proposed as an alternative anodic material that was investigated in an YSZ-based ammonia fueled SOFC-O [64]. Here the cathode was a silver-based alloy/material. The cell performances were not found to be considerably better than the nickel anode-based cells. The power output, for instance, was found to be 50 mW/cm² at 800°C, and 125 mW/cm² at 1000°C.

The next category of ammonia-based SOFC use proton conducting electrolytes, and are known as SOFC-H. In these type of cells, the electrolyte allows the ionic current of H⁺ ions. A platinum-based SOFC-H was investigated with ammonia fuel utilizing BCGP electrolyte [65]. The electrolyte thickness considered was 1300 µm that was primarily responsible for lowering the cell performances. The power output, for example, was reported to reach a maximum value of 35 mW/cm² at 700°C. An open circuit voltage of

0.85 V was reported. Another similar study investigated the performance of an ammonia-based SOFC-H. Similar platinum electrodes were used, however, the electrolyte was composed of BCG materials. Although similar open circuit voltages were observed for both types of cells, the power density was found to be lower for the BCG-based cell. A difference of 10 mW/cm² was observed between the power densities of these two ammonia-based SOFC-H cells.

Another BCG-based SOFC-H was investigated for electrochemical ammonia conversion [66]. The power output of the cell was observed to have a peak value of 32 mW/cm² in an electrolyte that was 1000 μm thick at 700°C. The no-load voltage, however, was found to be 0.66 V, which was lower as compared to other similar ammonia-based SOFC-H cells at this temperature. Similar platinum electrodes were used in conjunction with a BCG electrolyte. Although a lower-thickness electrolyte was employed, comparatively lower power densities were reported. These variations, however, could be attributed to other factors such as experimental uncertainties and differences in equipment precision.

Another study with BCGP electrolyte at a thickness of 1000 μm was reported [67]. The BCGP-based ammonia fuel cell provided a power output value of 23 mW/cm² at an operating temperature of 600°C. Because of the lower operating temperature, a lower power density was observed as compared to other similar ammonia-based cells.

Along with platinum-based electrodes, nickel-based materials have also been investigated for ammonia-based SOFC-H. A nickel-BCE anode was studied in conjunction with a platinum cathode for an ammonia-based cell. The electrolyte comprised a 1000 μm thick BCG material. The no-load voltage was reported to be 0.92 V, and the temperature varied between 500°C and 600°C. Elevated temperatures provided higher power outputs as well as better overall performances. At 500°C, for example, the output power density was 15 mW/cm². This was observed to rise to 18 mW/cm² and 28 mW/cm² at respective elevated temperatures of 550°C and 600°C, respectively.

The studies performed for the developed cells hinted at better cell performances in comparison with cells containing only platinum materials. Another ammonia-based SOFC-H was investigated with an LSCO cathode and a nickel-based anode [68]. Similar BCGO material was used for the electrolyte material. The electrolyte thickness was designed to

function at a low value of 50 μm . The operating temperatures of 600°C to 750°C were investigated. In this type of cell, the no-load voltage was found to be 1.1 V at 600°C. However, at a higher temperature of 650°C, the no-load voltage decreased to 1.09 V. At 750°C, the no-load voltage reduced to 0.985 V. Although the no-load voltages were observed to decrease, the power densities were reported to increase. For example, a power output of 96 mW/cm^2 was observed at 600°C, which rises by 265 mW/cm^2 and 288 mW/cm^2 for temperature increases of 100°C and 150°C, respectively.

A BCGO-based electrolyte has been investigated for ammonia-based SOFC-H. Different materials for electrodes were also considered. The thickness of the BCGO electrolyte was 30 μm and the anodic materials investigated included nickel, cerium, strontium and iron oxides. Similar to the previous study, the no-load voltage was observed to decrease with rising temperatures. For example, a no-load voltage of 1.12 V was associated with 600°C that was observed to drop to 1.1 V at 650°C. At the same time, the power density was reported to increase from 147 mW/cm^2 at 600°C to nearly 200 mW/cm^2 at 650°C [69].

2.3.2 Ammonia fuel cells utilizing alkaline electrolytes

Ammonia fuel cells containing alkaline electrolytes operate with ionic currents of hydroxyl (OH^-) ions through the electrolyte. Previous studies investigating this route of power generation have been reported in the literature. These type of ammonia-based cells can also be divided into molten and membrane electrolytic cells. The molten electrolytic cells utilize mixtures of different types of molten salts. Most studies have investigated the usage of potassium and sodium hydroxide salts, which generally operate at temperatures of 200°C to 500°C. At 200°C, a power density of 16 mW/cm^2 was attained utilizing nickel electrodes and molten alkaline electrolyte [70]. The power density was reported to increase with temperature. For example, power densities of 40, 31, and 21 mW/cm^2 were observed at temperatures of 450, 400, and 300°C, respectively.

Elevated temperatures resulting in better performances can be attributed to both higher electronic, ionic and chemical activities. The rate of ionic currents rises at high temperatures due to the higher rates of electrochemical oxidation of ammonia molecules. The higher ionic conductivity of the molten electrolyte also results in lower voltage losses

due to ionic current resistance. It has also been suggested that at elevated temperatures, ammonia molecules partially convert into constituent hydrogen molecules that provide considerably higher electrochemical performances. The losses in voltage due to ionic and electric current resistances are also reduced at elevated temperatures owing higher electrolyte conductivities. The activation losses that occur during the initial electrochemical interaction also decrease owing to higher reaction kinetics.

The diffusion of reactants as well as products also plays an important role in determining the concentration losses in voltage. As the temperature is raised, the diffusion coefficients of different species also rises. This leads to lower performance losses that could occur due to mass transport limitations. Platinum electrodes have also been investigated in molten electrolyte ammonia-based cells [71]. A similar mixture of potassium and sodium hydroxide was employed for the alkaline electrolyte. The usage of these electrodes did not provide considerable improvements. The voltage under no output load, for instance, was found to be 0.82 V at 200°C with nickel electrodes that decreased to 0.76 V for platinum electrodes. The power density was also observed to be 10.5 mW/cm² that is 5.5 mW/cm² lower than power output obtained via nickel electrodes. However, the difference in cell performances can also be attributed to the difference in cell design and fabrication.

The next type of alkaline ammonia fuel includes the membrane-based configuration that utilizes an electrolyte constituting of polymeric material that allows the ionic transport of OH⁻ ions. A chloroacetyl polydimethyl polyvinyl alcohol (CPPO-PVA)-based material was utilized for the membrane constituting the ammonia fuel cell developed [72]. The developed ammonia fuel cell also constituted a chromium anode, which was deposited on a nickel substrate and carbon support. The composition of the cathode included the usage of manganese oxide on a carbon support. The primary advantage of the developed cell was the possibility of operating at room temperature. Although lower operating temperatures were considered, the performance of the ammonia fuel cell was comparable to the molten electrolyte cell. For example, 0.85 V were obtained under no-load for the membrane-based ammonia fuel cell. The maximum power output was also reported as 16 mW/cm². The results reported were comparable to the molten electrolyte-based ammonia fuel cells that produced an output voltage and power of 0.82 V and 16 mW/cm², respectively at 200°C.

The comparable results obtained can be due to several reasons. In membrane-based cells, the key advantage is the minimal distances between the electrodes. This leads to a significant drop in the Ohmic resistance as compared to the molten electrolyte ammonia fuel cells that have greater distances between the anode and cathode. When the distance of ionic flow increases, the polarization loss also increases. Nevertheless, in membrane-based cells as the distance between electrodes is minimized owing to thin electrolyte usage, these losses are also inherently decreased. Hence, this trade-off between high temperatures of molten electrolytic cells and low electrodes distances in membrane-based cells need to be considered. The membrane type as well as electrocatalysts play a key role in determining the cell performances. A membrane-based ammonia fuel cell, for example, was investigated with the usage of platinum on carbon cathode while the anode comprised of platinum and ruthenium on carbon [73]. Although noble metal catalysts were employed, a comparatively lower no-load voltage of 0.42 V was observed.

2.4 Main gaps in the literature

The literature survey performed results in the identification of several gaps that need to be addressed. There exists a gap in the literature in the area of multi-bed catalyst reactors for synthesizing ammonia. Such reactors have not been investigated through the utilization of multiple beds comprising of different types noble as well as non-noble catalysts. The thermodynamic performance of such experimental ammonia synthesis systems has not been performed. Most studies were focused on analyzing the theoretical performance through thermodynamic approaches. However, to determine the experimental performance, it is essential to investigate the energetic as well as exergetic performance.

There exists a gap in the literature in the area of thermodynamic simulation of hydrogen, ammonia, and electricity production through the utilization of solar and wind-based energy sources considering the transient variations in the solar intensities as well as wind speeds. Specifically, efforts have not been directed towards investigating the transient thermodynamic performances of such systems.

Studies were not found in the literature that consider integrated ammonia synthesis and fuel cell systems to utilize ammonia as an energy storage medium as well as a carbon-free fuel.

Specifically, intermittent renewable energy resources such as solar and wind-based plants have not been investigated through such systems that utilize ammonia as an energy storage medium.

Ammonia as one of the major useful chemicals relies heavily on fossil fuels and requires major efforts to be directed towards shifting its production from fossil fuel-based resources to renewable energy based resources. When intermittent sources such as solar or wind are utilized for such applications, excess availability of energy can be utilized to synthesize clean ammonia that can be electrochemically oxidized via direct ammonia fuel cells to produce electrical power during periods of low solar activity or wind availability. Thus, efforts have not been directed towards the development and investigation of such energy systems.

Limited experimental investigations were found in the literature in the area of direct ammonia fuel cells. Few studies have considered the direct electrochemical route of oxidation of ammonia via alkaline membrane electrolytes as well as molten alkaline electrolytes. Thus, there is a need to develop and investigate such direct ammonia fuel cell stacks to determine their output potentials. Since limited studies have been performed on such types of energy systems, there exists a gap in the literature associated with the exergoeconomic performances of such systems. Exergoeconomic performance investigations are essential to determine how the exergetic performances relate to the corresponding economic performances. Hence, efforts are required to investigate the exergoeconomic performance of clean hydrogen, ammonia, and electricity production through the utilization of solar and wind energy sources. Efforts have not been directed towards determining the optimal performances of clean ammonia, hydrogen, and electricity generation systems under different combinations of solar intensities as well as wind speeds.

2.5 Motivation, objectives and novelties

There is a global necessity to reduce the environmental burden caused by power generation, hydrogen production, and ammonia synthesis. The consumption of fossil fuels needs to be decreased to attain an environment friendly infrastructure. This can be achieved by developing new energy systems that use efficient and environmentally benign

methodologies and configurations. In this study, new solar and wind energy-based energy systems will be developed and investigated with the motivation of mitigating the problems and challenges associated with current synthesis of ammonia and hydrogen as well as clean energy production and storage. Renewable energy resources such as solar and wind are intermittent in nature and require energy storage methods. Efforts have not been directed towards investigating energy storage in the form of fuels such as ammonia. With a high density, ammonia can act as a promising energy storage medium as compared to other fuels such as hydrogen, which have significantly low densities and require large storage volumes and pressures. The stored fuel can be used in ammonia fuel cells to produce carbon-free energy.

2.5.1 Objectives

The specific objectives of the present thesis are described as follows:

- To develop three new integrated solar and wind energy-based systems for clean ammonia, hydrogen, electricity and heating incorporating a new integrated clean ammonia synthesis and fuel cell system;
- To analyse the developed systems and associated subsystems thermodynamically;
 - Analysing the developed systems using electrochemical as well as thermodynamic energy and exergy approaches;
 - Evaluating the energy and exergy efficiencies of the developed systems as well as associated subsystems;
 - Conducting a parametric study to evaluate the system behavior under varying operating conditions and system parameters;
- To perform a transient simulation of the developed systems considering the variations in the solar intensities as well as wind speeds;
 - Simulating the system operation on the monthly average days considering the transient variations in the solar intensities as well as wind speeds;
 - Determining the daily potentials of producing clean hydrogen, ammonia, electricity and heating;

- Analysing the energy output capacities of the ammonia fuel cell subsystems considering the daily production of ammonia during excess solar and wind energy;
- Evaluating the daily performances of the developed systems through energy and exergy efficiencies considering transient operation;
- To perform an exergoeconomic analysis of the developed systems;
 - Performing exergoeconomic analysis to investigate the exergetic and economic performances of the developed systems;
 - Determining exergy efficiencies, investment cost rates, exergy destruction cost rates and exergoeconomic factors of the overall systems as well as associated subsystems;
 - Conducting parametric studies to investigate how the exergoeconomic performances vary with changing operating conditions and system parameters;
- To perform multi-objective optimization of the developed systems;
 - Using objective functions of exergy efficiency and total cost rates to maximize the efficiencies and minimize the costs;
 - Using genetic algorithm technique to determine the optimal operating points under varying combinations of solar intensities as well as wind speeds;
- To develop and investigate a multi-bed catalyst reactor for ammonia synthesis;
 - Building a lab scale experimental multi-bed reactor utilizing both conventional iron oxide catalyst as well as non-conventional wustite and ruthenium-based catalysts;
 - Performing an experimental investigation of the developed multi-bed reactor to determine the nitrogen conversion, energy efficiencies and exergy efficiencies;

2.5.2 Novelties

The original work in the present study is described below:

- Three new integrated solar and wind energy-based systems for clean ammonia, hydrogen, electricity and heating are developed utilizing a new integrated clean ammonia synthesis and fuel cell system

- A new ammonia-based integration technique is developed that effectively utilizes excess energy from solar and wind power plants
- A new integrated thermal energy storage, electrochemical ammonia synthesis and direct ammonia fuel cell technique is developed that utilizes an alkaline molten electrolyte for integrated storage of thermal energy, electrochemical production of ammonia and power generation through direct electrochemical ammonia oxidation
- A new multi-bed ammonia synthesis reactor is introduced that incorporates the utilization of a combination of conventional iron oxide-based catalyst as well as non-conventional ruthenium and wustite-based catalysts
- A five-cell direct ammonia fuel cell stack is developed and investigated under varying operating conditions utilizing the anion exchange-membrane electrolyte
- A new waste heat utilization technique is developed during ammonia synthesis that stores the released thermal energy, which is used when required for ammonia dissociation

CHAPTER 3 : SYSTEM DEVELOPMENT

This chapter describes the three energy systems and associated subsystems developed as part of this work. Each stream input and output to different subsystems are discussed. The primary inputs considered are solar and wind energy sources. Three new systems are developed in the present study to harness solar and wind energy for the production of useful commodities. Specifically, the clean production of hydrogen and ammonia is targeted. Currently, the conventional methods of producing these valuable commodities are highly dependent on fossil fuels and have significant environmental impacts. The developed systems synthesize hydrogen and ammonia during periods of excess available solar or wind energy.

3.1 System 1

In the present study, the first integrated energy system is designed for producing clean hydrogen, ammonia, and electricity. Solar and wind provide the input energy as it is shown in Fig. 3.1. The solar PV panels produce clean electrical power. Wind turbines transfer the kinetic energy of air currents to produce electricity. The electricity produced by solar panels and wind turbines provides energy to the grid, produces clean hydrogen, and environmentally benign ammonia.

The water electrolysis subsystem (WES) includes a proton exchange membrane (PEM)-based water electrolyser. Water stream at state 1 (state points indicated on Fig. 3.1) enters and is converted into oxygen and hydrogen. The PEM electrolyser stack exchanges positively charged H^+ ions across the membrane electrolyte. Water enters the electrolyser stack at the anodic side and is dissociated into oxygen (O_2) and H^+ ions. The H^+ ions produced at the interface of the anode and membrane travel to the cathodic side through the membrane electrolyte. At the cathode, the H^+ ions accept electrons to form hydrogen (H_2) gas that exits the stack at state 2.

The oxygen molecules formed at the anode exit the WES subsystem at state 3. The air separation unit utilizing the pressure swing adsorption (PSA) technique is utilized to generate the needed nitrogen for synthesizing ammonia. Air at state 4 enters the air separation unit and the generated nitrogen leaves at state 5. The oxygen produced during air separation is used as an oxidant in ammonia fuel cell (AFC). The PSA subsystem separates air into nitrogen and oxygen through the selective adsorption process. Selective adsorbents placed in packed beds adsorb oxygen or nitrogen molecules while the remaining

stream is allowed to exit the system. The adsorbed molecules are then released to generate a pure stream of nitrogen that can be utilized for ammonia synthesis.

Nitrogen and hydrogen gases are mixed and compressed to ammonia synthesis pressures. The reactant mixture stream is delivered to the compressor and the reactor (ASR) with a molar ratio of 3 mol H₂ to 1 mol N₂. The mixture is delivered to the ASR at state 8 while the ammonia produced as well as unreacted gases, leave through stream 9. State 9 is passed through HX-1 to condense the ammonia contained in stream 9. Next, state 10 is passed through the separator (SEP) that separates the produced ammonia at state 11 and unreacted gases at state 14. The unreacted stream at state 14 is delivered to C-2 to reach the ASR pressure at state 20. A partial amount of hydrogen synthesized is used for ammonia synthesis while the unused hydrogen comprises a useful output of the system. Similarly, synthesized ammonia is partly utilized for generating electricity while the remaining is considered as a useful output of the system. Ammonia exiting the SEP at state 11 is stored to be utilized for power generation when required.

During low wind speeds and solar intensities, the stored ammonia is used for electricity generation with the AFC through direct electrochemical ammonia oxidation as described earlier. Thus, clean electrical power, ammonia, and hydrogen are produced through the developed system utilizing environmentally benign solar and wind energy.

System 1 targets these three important commodities of electricity, hydrogen, and ammonia to address the current challenges associated with their conventional production methods. Electricity production using fossil fuels has led to significant environmental pollution, which has made clean energy an imperative. Solar and wind energy sources are considered to be promising alternatives that can aid in decreasing fossil fuel dependency across the globe. However, the intermittent nature of these energy sources is a serious disadvantage. Thus, the system developed in the present study has an integrated approach of synthesizing clean ammonia and using it as an energy storage medium.

The AFC operates through direct electrochemical ammonia oxidation and provides clean electricity during low solar or wind availability. There are multiple advantages of utilizing this energy storage technique. It entails considerably long storage times as compared to other energy storage methods that are associated with limited storage times. It also entails lower storage costs as compared to hydrogen fuel cell systems.

Owing to several safety hazards, hydrogen storage is costly and necessitates additional measures and precautions as compared to storage of ammonia. The low volumetric density

of hydrogen requires high storage pressures. On the other hand, ammonia can be liquefied at low pressures and sufficient amounts can be stored safely with lower space requirements as well as costs.

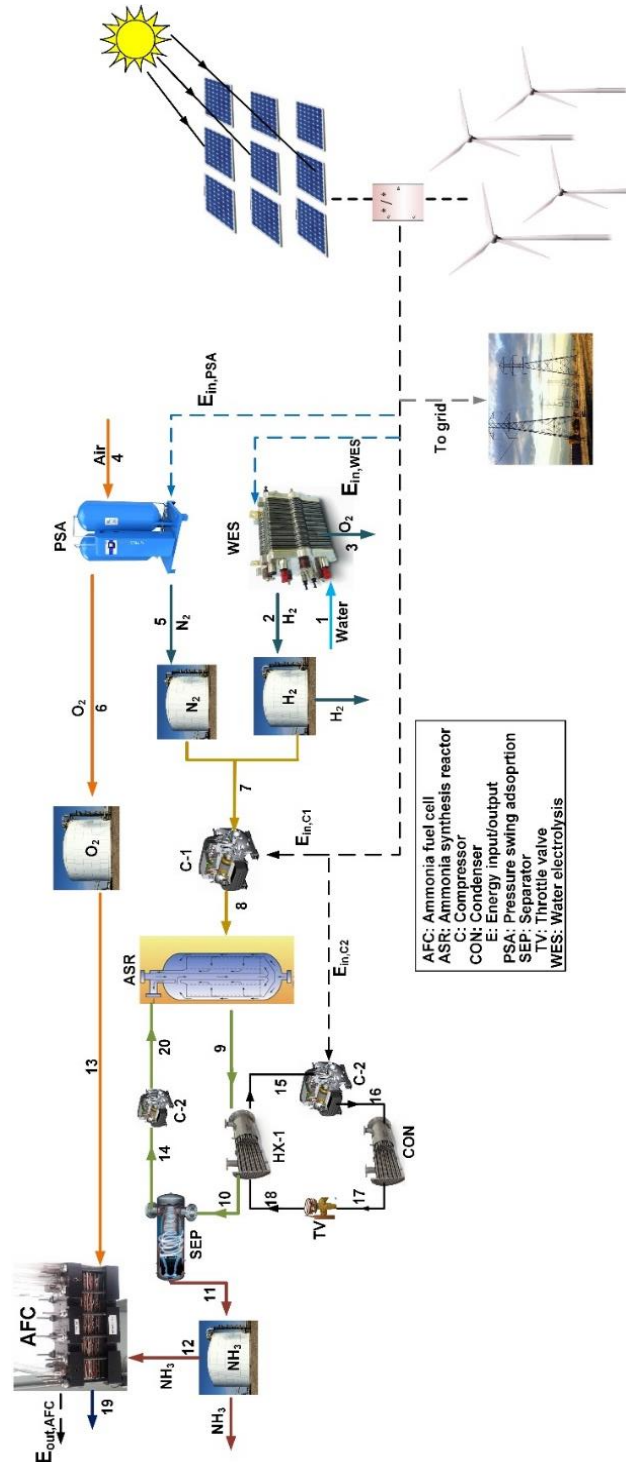


Fig. 3.1 Schematic representing system 1 utilizing solar and wind energy resources for clean ammonia, hydrogen and electricity

3.2 System 2

The second energy system developed in the present study is shown in Fig. 3.2. The primary energy inputs are solar and wind energy. A solar tower receives incoming solar radiation, which is concentrated onto the central receiver by heliostat mirrors. Alkaline molten salt is sent to the solar tower at state 17, which absorbs incoming solar energy and leaves the solar tower at state 18 to enter the hot tank (HT).

Heat exchanger-1 (HX-1) transfers heat to the reheat Rankine power generation cycle. High-pressure water enters HX-1 at state 22 and is converted into superheated vapour at state 23. Turbine T1 receives the input stream at state 23 and produces the output stream at state 24. Since the pressure at state 23 is a maximum, T1 denotes the high-pressure turbine in the cycle.

Once stream 24 leaves T1, it is reheated to state 25 prior to entering T2 that is the medium-pressure turbine of the cycle. Stream 26 exits T2 and is reheated prior to entering the low-pressure turbine T3. The high pressure and temperature of steam at the inlet of each turbine is harnessed to generate mechanical power in the turbine, which is converted into useful electrical power.

The final turbine exit stream leaves T3 at state 28 and enters the condenser (CON) where heat is rejected to return the steam to the initial state 21. The rejected heat is utilized as a useful system output in the present study.

Pump P2 increases the pressure of state 21 to the highest cycle pressure at state 22. The hot molten salt enters HX1 at state 19 and exits at state 20 after delivering thermal energy to the power generation cycle. At state 20, the molten salt enters the cold tank (CT) where it is stored for later use as either a thermal energy storage medium or as an electrolyte for electrochemical processes.

The electrochemical ammonia synthesis (EAS) system is used in the present system to produce environmentally clean ammonia. This subsystem has an input stream (state 7) that is comprised of a mixture of hydrogen and nitrogen in a mole ratio of 3:1.

When excess wind energy is available, it is used to operate the water splitting, air separation and EAS processes. Hydrogen is produced via the PEM electrolysis process described earlier. A portion of the hydrogen is used as a useful system output while the remaining

hydrogen is used to synthesize clean ammonia. The PSA subsystem separates the air input stream at state 4 into nitrogen at state 5 as well as oxygen at state 6. The EAS subsystem is capable of synthesizing ammonia at low pressures. Thus, the present system does not require compression of the reactant mixture prior to the ammonia synthesis process.

The synthesized ammonia as well as unreacted gases exit the EAS at state 8. Here, the ammonia is separated from the unreacted gases in a manner similar to system 1. The ammonia is stored for later usage in the molten electrolyte ammonia fuel cell (MEAFC). When there is a shortage of wind energy, the stored ammonia is used to generate clean electrical power via the MEAFC. The remaining stream exiting the PSA subsystem after air separation is used as the oxidant input to the MEAFC subsystem. An electrolyte is used for the EAS as well as the MEAFC subsystems (alkaline molten salt).

During electrochemical ammonia synthesis, diatomic nitrogen molecules are reduced to negatively charged N^{3-} ions through the acceptance of electrons at the cathode. The ionic current of N^{3-} ions produced at the cathode reaches the anodic side of the EAS through the alkaline electrolyte. The anodic half-cell reaction at the EAS combines these negatively charged ions and hydrogen molecules to form ammonia (NH_3) and releases electrons due to electrochemical oxidation.

The electrical power input to the EAS reduces the nitrogen molecules at the cathode and produces ammonia molecules at the anode via oxidation. As the power input is varied, the current densities across the electrodes and the ammonia synthesis rates vary accordingly. At higher current densities, higher ammonia synthesis rates can be obtained. In the present study, when excess wind energy is available, the EAS is operated and the ammonia synthesis rates are thus a function of the available surplus wind energy.

The MEAFC subsystem uses the principle of direct electrochemical oxidation of ammonia to produce clean electrical power when needed. The ammonia combines electrochemically with hydroxyl ions to generate an electrical potential that is supported by the corresponding cathodic interactions of oxygen and water molecules to form hydroxyl ions.

When MEAFC operation is required, the alkaline molten salt becomes the electrolyte that allows the ionic current of OH^- ions. The developed solar and wind-based energy system uses a new integrated electrochemical ammonia synthesis and the fuel cell system has a molten alkaline salt-based thermal energy storage subsystem.

3.3 System 3

The third energy system developed in the present study is shown in Fig. 3.3. Primary input sources to the system comprise of solar and wind-based energy resources. The solar thermal subsystem entails a solar tower and heliostat field that enable the utilization of incoming solar thermal energy for production of useful commodities. A thermal energy storage system comprising of both hot and cold storage tanks is employed to store excess energy available.

The hydrogen and ammonia synthesis subsystems are powered by the wind farm. The PEM electrolyser stack entails water input through stream 1 that is dissociated into hydrogen gas through a portion of the electricity produced by the wind farm. Hydrogen leaves the subsystem at state 2 and is utilized as both a useful commodity and an input to the ammonia synthesis subsystem (ASR). The nitrogen required for synthesizing ammonia is produced by the PSA subsystem that entails an air input through stream 4 while the produced nitrogen exits at state 5. The reaction pressure needed by the ASR subsystem is achieved by the compression subsystem (CPR) that intakes a mixed stream of hydrogen and nitrogen with a respective mole ratio of 3:1 and raises the mixture pressure to the required ASR pressure at state 7.

The product stream of the ASR at state 8 is delivered to the separation subsystem that separates ammonia from unreacted gases. The ammonia synthesized is considered as a useful output as well as an energy storage medium. When a deficit of wind energy occurs, the stored ammonia is utilized for clean power generation. In the present system, an ammonia dissociation subsystem (ADR) is employed that utilizes excess solar thermal energy stored in the HT to generate a pure stream of hydrogen. The exit stream of ADR at state 12 is passed through a membrane separator and the pure hydrogen stream at state 15 enters the fuel cell subsystem (FC) that generates clean electrical power when required.

The oxygen stream exiting the PSA subsystem is utilized as an oxidant for fuel cell operation. At state 35, the products formed during electrochemical FC operation exit the subsystem and comprise of water molecules, hence providing clean electrical power when required. The present system utilizes the heat released from the ASR to provide thermal energy to the CT. The exothermic nature of ammonia synthesis leads to a release of thermal

energy with every mole of ammonia produced. This waste heat can be utilized for system performance enhancement.

Thus, in the present system, the waste heat is utilized to increase the output power obtained from the reheat Rankine cycle. Molten salt is utilized to absorb incoming solar thermal energy, which enters the solar tower at state 20 from the CT and leaves at state 16 after thermal energy absorption. Next, when excess solar energy is available, a portion of the molten salt leaving the solar tower is delivered to the HT for later usage while the remaining is delivered to HX1.

The hot molten salt enters HX1 at state 19 where it delivers thermal energy to the reheat Rankine cycle to generate electrical power. At state 23, high-pressure water is delivered to HX1 where it is converted into superheated vapor at state 24 prior to entering the high-pressure turbine T1 that entails the exit stream at state 25. The first reheat stage in the power generation cycle occurs between streams 25 and 26, where state 25 is sent to HX1 for reheating to state 26 before entering the medium-pressure turbine T2.

State 27 exits T2 and is reheated to state 28 prior to entering the low-pressure turbine T3. The exit stream of T3 at state 29 enters the condenser where it rejects heat to attain the initial cycle state at stream 22. Next, the condensed water stream entailing the low condenser pressure is pressurized by pump P1 to the highest cycle pressure at state 23 before being delivered to HX1 for thermal energy absorption. The waste heat rejected from the condenser is also utilized as a useful heating output. The HT stores excess available solar energy and provides the heat input requirement of the ADR. When a deficit in available wind energy exists, the stored ammonia is dissociated in the ADR through an endothermic reaction. This provides the FC subsystem with a pure stream of hydrogen to generate clean electricity when needed.

To provide solutions for decreasing fossil fuel dependency in the production of these commodities, it is essential to develop renewable energy-based integrated systems that can produce multiple useful outputs through the usage of clean energy resources. The waste heat entailed in the ammonia synthesis process is also utilized to attain higher system outputs. The present system also utilizes a new integrated thermal energy storage system that provides the required input energy for ammonia dissociation while storing the waste heat released during ammonia synthesis..

CHAPTER 4 : EXPERIMENTAL APPARATUS AND PROCEDURE

In this chapter, the experimental apparatus and procedure is presented. Different devices utilized and their specifications are firstly discussed. The experimental setups developed and utilized are presented with their associated system components.

4.1 System components and measurement devices

In this section, the different measurement devices and their corresponding specifications are presented. The components constituting the experimental setups of the ammonia fuel cell and ammonia synthesis subsystems are described providing specific details about each system component.

4.1.1 Potentiostat

The potentiostat (shown in Fig. 4.1) is a device that controls or measures the difference in voltage between a given working electrode and a reference electrode. It can also make galvanostatic measurements as well as impedance spectroscopy. The device utilizes the input of current to the cell via a counter electrode. In most applications, the current or voltage between the working and counter electrodes is measured. The cell potential can be measured or controlled while the current is set at a specific value or is varied across a given range. To investigate the performance of the developed ammonia fuel cell, several electrochemical tests such as open circuit voltage and current-voltage (I-V) polarization tests are performed.

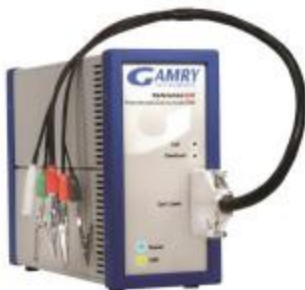


Fig. 4.1 Gamry Reference 3000 potentiostat used in the present system

The no-load or open circuit voltage test includes the measurement of the voltage across the working and reference electrodes under no output load or current. This type of test allows

the assessment of cell performance in the absence of activation as well as Ohmic polarization.

The extent of electrochemical oxidation of ammonia molecules in an ammonia fuel cell can also be assessed via no-load voltages. The I-V polarization curves are generated by the potentiostat by varying the output loads and measuring the corresponding voltages. Starting from minimal loads and thus minimum output currents that provide higher cell voltages, the output currents are increased by increasing the loads and the corresponding output voltages decrease due to increased polarization losses. The Gamry Reference 3000 Galvanostat/Potentiostat is used in this study. The maximum voltage and current of the device are ± 32 V and ± 3 A, respectively [74].

4.1.2 Flow meters

The flow inputs and outputs are measured via FMA mass flow meters shown in Fig. 4.2. The FMA-1600A type meters are utilized that operate through built-in functions derived from the theory of differential pressures to measure the mass or volume flow rate of a specific gas. The FMA flow meters have internal components that generate a laminar stream of flow prior to measuring the pressure drop and thus determining flow rates via Poiseuille theory. The drop in pressure for different inputs is measured via internal pressure sensors within the laminar region. Other temperature as well as pressure sensors are also included to implement appropriate correction factors according to real working conditions. Further details and specifications about these devices are provided in Table 4.1.



Fig. 4.2 FMA-1600A mass flow meter utilized in the present system

Table 4.1 Specifications of FMA mass flow meters

Typical supply current	35 mA
Flow rate measureable	125% FS
Accuracy	$\pm(0.8\% \text{ of reading} + 0.2\% \text{ FS})$
Supply voltage	7-30 V
Zero shift	0.02%
Operating temperature	263 K-323 K
Turndown ratio	200:1
Humidity range	0-100%
Span shift	0.02% FS/oC/atm
Repeatability	$\pm 0.2\%$
Response time	0.01 seconds

Source: Ref. [75]

4.1.3 Temperature measurement

In this study, the K-type thermocouples connected to either Omega or National Instruments (NI) data acquisition hardware are used. These data acquisition platforms provide real time monitoring and recording of different parameters including temperatures. These hardware have multiple ports that allow the temperature to be measured simultaneously at different locations. The range of the thermocouples utilized comprises of -250°C to 1200°C with an accuracy of $\pm 0.5\%$. Further specifications of these devices are provided in Table 4.2.

Table 4.2 Specifications of the temperature measurement systems

Thermocouple type	K type
Temperature range	$-250^{\circ}\text{C}-1200^{\circ}\text{C}$
Accuracy	$\pm 0.5\%$
Resolution	0.1°C
Cold junction compensation	$\pm 0.3^{\circ}\text{C}$
Data acquisition	NI DAQ and Omega DAQPRO

4.1.4 Ammonia synthesis catalysts

In this study, a multi-layer catalyst bed reactor is built. A combination of low and high cost catalysts are utilized. A conventional magnetite-based iron oxide catalyst is used. This type of catalyst is composed of nearly 90% by mass iron oxide (Fe_3O_4) as the primary catalyst component prior to catalyst reduction. Catalyst promoters including aluminum, potassium,

and calcium oxides are also present. Magnetite is generally utilized as the starting material input in the manufacturing process that utilizes the fusion method of catalyst preparation.

These type of catalysts have been employed in various ammonia synthesis plants for several years owing to their cost effectiveness and ease of manufacturing. The magnetite-based raw materials needed for catalyst preparation, for instance, are available at low costs in various countries. The fused iron-based catalysts also entail high thermal stability, poison resistance and mechanical strength. Nevertheless, the activities of the iron-based catalysts have been reported to entail higher values with the presence of cobalt oxide. Changing the type of precursor from magnetite to wustite (Fe_{1-x}O) was also found to provide higher catalyst activities and thus higher yields of ammonia.

A volcanic type relation exists between the catalyst activity and the presence of different types of iron oxides as well as mixtures. However, previous studies reported in the literature found that fused wustite-based iron oxide catalysts provide higher performances as well as rapid rates of reduction as compared to magnetite-based catalysts [104]. The wustite phase structure Fe_{1-x}O was found to entail optimum performances for the range $0.04 < x < 0.10$.

Hence, in this study, the second type of catalyst considered in the multi-bed reactor includes the wustite based fused iron oxide catalyst. The third type of catalyst included in the reactor comprises of the wustite-based catalyst with cobalt oxide support. Both the wustite catalysts included promoters in the form of oxides of aluminum, calcium and potassium. The catalyst used in the multi-bed reactor is ruthenium on activated carbon (Ru/C). This type of catalyst provides the advantage of having higher ammonia production rates owing to its high surface area. It is known to provide satisfactory ammonia yields even at low operating pressures. Finally, Ru/C catalyst are compatible with iron-based catalysts.

4.1.5 Ammonia synthesis reactor

The ammonia synthesis reactor (ASR) designed for this work is shown in Fig. 4.3. The reactor consists of a stainless steel tube 2.54 cm in diameter and 30.5 cm long. A pressure gauge is attached to monitor and record the pressure during reactions. The reactor pressure

is maintained through a high-pressure control valve. The K-type thermocouple integrated with the data acquisition system records the reactor temperature.

A stainless reactor is utilized owing to the high corrosion resistance that is required in experiments entailing ammonia. Ammonia is corrosive in nature towards metallic components and the components involved need to comprise of corrosion-resistant materials. The catalyst required for ammonia synthesis is placed in the tubular reactor as a fixed bed between two layers of quartz wool. The mass of the catalyst loading for each run is recorded before it is placed in the reactor. To ensure no gas leakages exist in the reactor, high-pressure Swagelok fittings are used. Prevention of gas leakage is essential in ammonia synthesis reactors due to the presence of highly flammable hydrogen gas. As the reactor is enclosed in a high-temperature furnace, it is of crucial importance to ensure no gas leakage occurs from the reactor.

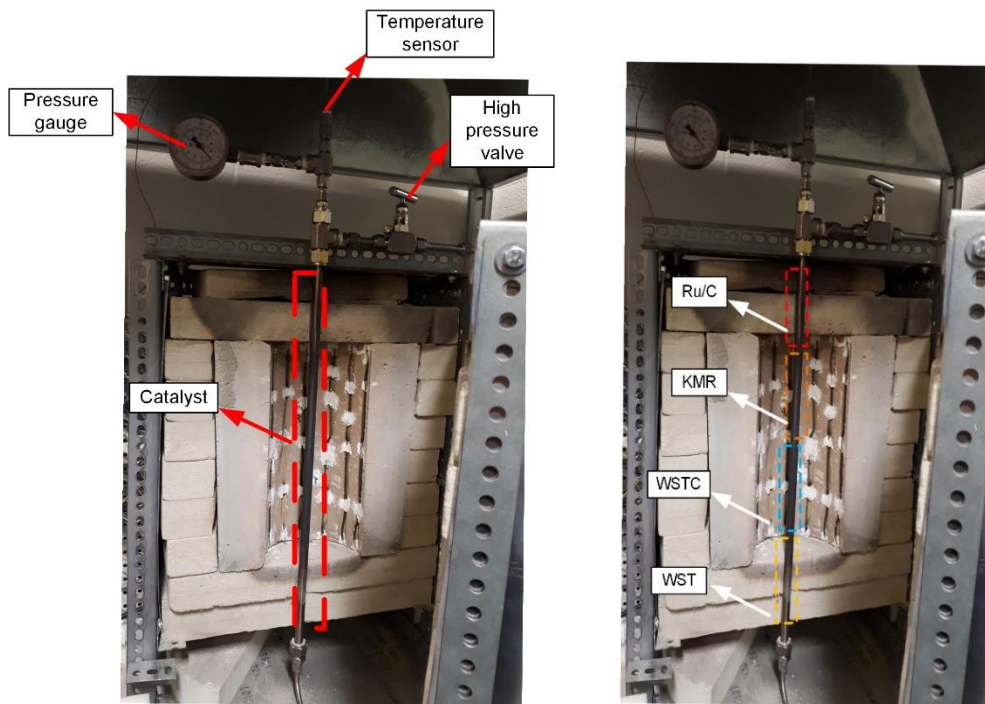


Fig. 4.3 Ammonia synthesis reactor developed in the present study utilizing single-bed conventional iron oxide catalyst and multi-layer catalyst bed

4.1.6 Alkaline membranes

In the present study, an ammonia fuel cell with an alkaline electrolyte is developed and investigated. The quaternary ammonium membrane in the alkaline electrolyte allows the passage of anions. During cathodic operation, water and oxygen molecules combine to form hydroxyl or OH⁻ ions that generates an ionic current of OH⁻ ions from the cathode to the anode. The hydroxyl ions reaching the interface of the anode and membrane combine with ammonia molecules to perform electrochemical oxidization and release electrons. The membrane functionality comprises a strong base exchange of anions while quaternary ammonium can be identified as the functional group. This type of functional group has the chemical structure that includes nitrogen atoms connected with alkyl or aryl group of atoms. The cations depicted entail a permanent charge, which are also independent of the surrounding pH.

The specifications of the quaternary ammonium membrane utilized in the present study are provided in Table 4.3.

Table 4.3 Specifications of the quaternary ammonium membrane

Functional group	Quaternary ammonium
Polymer structure	Cross link between gel polystyrene and divinylbenzene
Color	Light yellow
Maximum stable temperature (°C)	90
Functionality	Strong base anion exchange membrane
Mullen burst test strength (kPa)	>551.6
Max. current density (A/m ²)	<500
Thickness (m)	0.0005 ± 0.000025
Ionic form	Chloride

The membrane thickness is 0.5 ± 0.025 mm while the limit of maximum applicable current per unit area of membrane is 500 A/m². The membrane Mullen strength exceeds 551.6 kPa. The maximum operating temperature is 90°C above which the membrane deteriorates. Cross-linking of gel polystyrene as well as divinylbenzene is used for the development of the polymer structure, and membrane activation is attained via immersion in a 1 M KOH solution.

4.1.7 Gas diffusion layers

Gas diffusion layers (GDL) play an important role in providing effective and efficient diffusion of reactants towards the catalyst layers. The reactants are passed along the flow channels embedded on the bipolar plates. However, to allow suitable diffusion of reactant molecules towards the membrane-catalyst interface, gas diffusion layers are essential. These layers are comprised of embedded diffusion pathways through micro-porous structures. The GDL aids in minimizing the resistance with the surface contact of the catalyst layer. The GDL prevents the particles of the catalyst from transferring onto the micro-porous layers when the stack is sealed and pressurized. When management of water is important in some fuel cell stacks, GDL plays an important role in effectively managing the distribution of water molecules.

The mechanical properties of GDL are set according to the compression strength requirements needed for usage in fuel cell stacks. To prevent any leakage of gases, the fuel cell stacks are compressed at high pressures. Thus, the GDL are designed to have high compression strengths to withstand these compressive pressures. Any cracking or breakage of GDL would lead to a deterioration of fuel cell performance due to reactant leakage, ineffective gas diffusion, etc.

The GDL is a hydrophobic and prevents the flooding or absorption of water. Water is one of the reaction products during fuel cell operation and can cause flooding within the cell components if not appropriately handled. Flooding of water molecules in cell components prevent the reactants from reaching the active sites and the products from diffusing away from reaction sites. Hence, the GDL is treated with Teflon or PTFE to make the surface layer hydrophobic and prevent water droplets from being absorbed or flooded within the cell.

In this study, a catalyst coated GDL with coating of platinum black material acts as the electrocatalyst. Carbon fiber paper-based GDL are used in this study. In the presence of platinum black catalyst, ammonia molecules can be oxidized electrochemically. As ammonia is input to the anodic compartment through the flow channel plates, it diffuses through the GDL and reaches the interface of the membrane and catalyst where it oxidizes

electrochemically in the presence of platinum catalyst. Similarly, the cathodic reactions of the ammonia fuel cell where oxygen molecules combine with water molecules to form hydroxyl ions also require the presence of electrochemical catalysts. This is achieved with the usage of platinum black coatings.

The loading of the catalyst layer is 0.45 mg/cm^2 while the layer of catalyst is composed of 40% platinum on Vulcan carbon support. Having a low electrical resistance is also essential to minimize Ohmic losses in voltage that arise due the electrical resistances of different component within the cell. Sufficient tensile strength as well as high modulus are desired properties for the carbon fibers. Table 4.3 provides the specifications and properties of the GDL.

Table 4.3 Specifications of the gas diffusion layer

Air permeability ($\text{cm}^3/\text{s}/\text{cm}^2$)	1 ± 0.6
PTFE treatment (wt%)	5
Porosity (%)	80
Electrical resistivity through plane ($\text{m}\Omega\text{cm}^2$)	<12
Thickness (mm)	0.24 ± 0.025
Catalyst Type (%)	40% Platinum on Vulcan
Platinum black loading (mg/cm^2)	0.45

Air permeability of the GDL is $1 \pm 0.6 \text{ cm}^3/\text{s}/\text{cm}^2$ while the measured thickness is $0.24 \pm 0.025 \text{ mm}$. The measured resistivity is lower than $12 \text{ m}\Omega\text{cm}^2$ considered in a planar configuration. An 80% porosity is entailed in the GDL that depicts the effectiveness of micro-porous layers. The hydrophobic treatment applied constitutes a PTFE weight consumption of 5%.

4.1.8 Bipolar flow channel plates

Reactants are input to the fuel cell stack from specific inlet ports and the products, as well as unreacted gases, exit the stack from specific exit ports. However, once the reactants enter the stack, they are guided to flow over corresponding anodic or cathodic sides of the membrane via bipolar flow channel plates. For instance, when ammonia enters into the ammonia fuel cell stack, the flow channel plates guide ammonia molecules to flow over the anodic side of the membrane for each cell. Similarly, when humid air enters the stack,

it is guided to flow over the cathodic side of each membrane to complete the overall electrochemical reaction.

The fuel cell stack developed comprises of a series of different cells, which are composed of a membrane and catalyst coated diffusion layers on either sides. The components that sandwich this assembly of the membrane and catalyst coated diffusion layers are the bipolar flow channel plates. They are known as bipolar plates because they have dual charges on either side, which are produced because of the anodic and cathodic electrochemical reactions, respectively. This creates a series connection between each adjacent cell of the ammonia fuel cell stack.

The bipolar plate acts as the anode of one cell and the cathode of the adjacent cell. The bipolar plates have embedded flow channels that ease the flow of reactants and products across each cell. The flow channel plates used in this study are fabricated from stainless steel material to withstand corrosive ammonia. Stainless steel also provides the high strength needed for bipolar plates. The fuel cell stacks are subjected to high compression pressures to avoid any gas leakage, making high strengths necessary. The bipolar plates were required to be electrically conductive. It might be noted that other materials such as graphite as well as carbon-intensive composites can also be utilized owing to their high electrical conductivity, but these were not used in this study.

4.1.9 Gaskets

To prevent reactant or product leakage from the fuel cell stack as it is operated at high pressures, gaskets are employed that seal each component. For instance, either side of the bipolar plate is embedded with grooves where gaskets are placed. These ensure that reactant gases only travel through the flow channels available on the plates. Then reactants are input to the stack, leakages can occur from the interface of the end plate and the first bipolar plate. Thus, gaskets are also placed in these locations to avoid any gaseous leakage.

Similarly, gaskets are placed near each exit port of the stack to prevent leakage at the interface of the end plate and the end bipolar plate. In this study, rubber gaskets are utilized as they are associated with high strengths needed to withstand the compressive pressure.

Being an electrical insulator, rubber is utilized as the gasket material to prevent any short circuits within the cell components. The gasket thickness is measured to be 0.9 mm.

4.1.10 End plates

The components of the fuel cell stack described earlier are arranged in series to form adjacently connected cells. Multiple cells connected in series are enclosed at either ends through the end plates. The end plates serve several other functions besides enclosing the stack components. The compression of stack assembly is performed by applying pressure on the end plates placed at either side of the stack. Thus, the end plates also act as the medium where high pressures can be applied on the stack assembly. The end plates also have input and output ports where the reactants are allowed to enter the stack while the products along with unreacted gases are allowed to exit. The end plates are coated with insulating materials to prevent short circuits.

4.1.11 Fuel cell oxidant humidifier

The cathodic side of each cell in the ammonia fuel cell stack includes the half-cell electrochemical reaction that combines oxygen and water molecules to produce hydroxyl ions, which travel to the anodic fuel cell side via alkaline membranes. The cathodic inlet port of the stack is fed with humidified air to generate a continuous flow of oxygen and water molecules. The stream of humidified air is produced for the ammonia fuel cell stack by a bubbler humidifier. In this type of humidification setup, an air compressor generates an air current that is allowed to pass through a water reservoir before entering the fuel cell stack. As the air stream passes through the water reservoir, the humidity ratio increases and provides the water molecules needed for initial cathodic reactions.

4.1.12 Assembling the ammonia fuel cell stack

The first step is having alkaline membrane electrolytes prepared according to the sizes of the flow channel plates as well as the locations of inlet and outlet ports. The membrane electrode assemblies are constructed for the stack by placing the GDL on either side of the membrane, which are also coated with the required electrochemical catalysts. In the present study, a five cell stack is built.

The flow channel plates were fashioned by attaching rubber gaskets that seal the flow channels and prevent any gas leakages. The membrane electrode assemblies are placed between two such sealed flow channel plates. The five adjacent cells, connected in series, are placed on the bottom plate while the top plate along with attached inlet and outlet ports are positioned on the top of the assembly. The stack assembly is then compressed through insulated screws and nuts that connect the bottom and top plates. Fig. 4.4 (a) depicts the exploded view of the ammonia fuel cell showing different components and their respective arrangements. The five-cell stack developed includes a series arrangement of five such cells shown in the Fig. 4.4 (b). As can be seen, flow channel holes on different components including the membrane, bipolar plates, rubber gaskets *etc.* are aligned to ensure effective flow of reactants and products. This alignment is important to prevent accumulation of gases between different cell components. For instance, if the stream of input ammonia does not pass through concentric flow channels, partial amounts will be accumulated in the blocked sections. The accumulated molecules can travel into different cell components leading to performance deterioration.

As can be observed in Fig. 4.4, the screws utilized for stack compression are equidistant and symmetrical. This is essential to ensure that the stack components are pressurized uniformly throughout the cell. Non-uniform compression can lead to performance deterioration due to two reasons: (i) Non-uniform compression can result in gas leakages that deteriorate the fuel cell performances and present safety hazards; (ii) Non-uniform compression can also damage stack components, for instance, high concentration of pressure on the GDL at a particular location can fracture the layers.

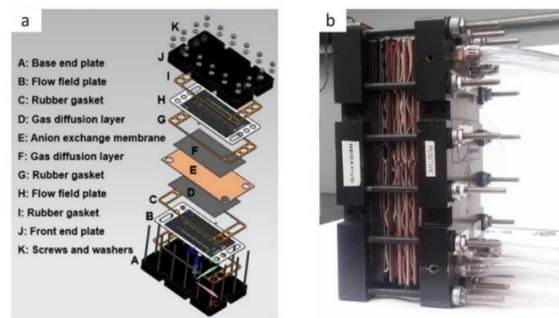


Fig. 4.4 Ammonia fuel cell stack showing (a) components in exploded view and (b) assembled five cell stack

4.2 Experimental setup for the integrated ammonia synthesis and fuel cell system

The experimental setup of the ammonia synthesis and fuel cell system developed at the Clean Energy Research Lab (CERL) is depicted in Fig. 4.5. During the system phase of ammonia synthesis, hydrogen and nitrogen gases are allowed to enter with a mole ratio of 3:1. The input flow rate is controlled via FMA flow controllers described earlier. The flow controllers are connected to hydrogen and nitrogen cylinders equipped with pressure regulators.

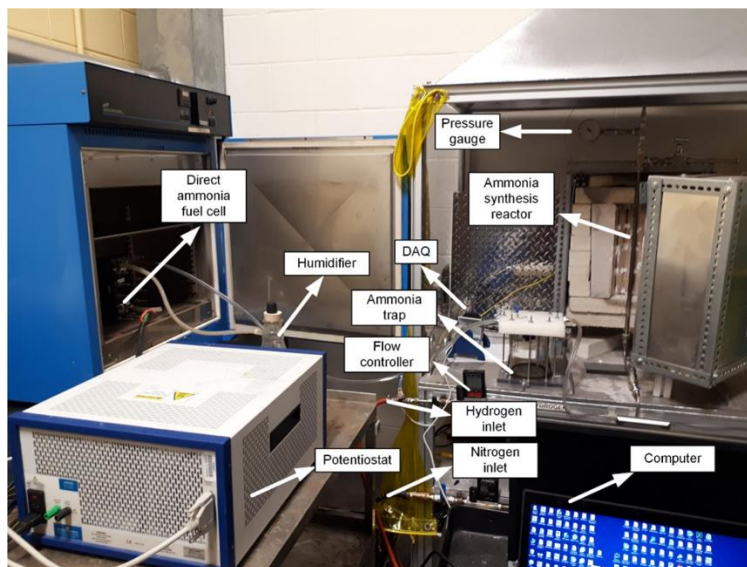


Fig. 4.5 Experimental setup of the ammonia synthesis and fuel cell system

The ammonia synthesis reactor is placed within a temperature controlled high-temperature furnace. This allows the regulation of synthesis temperatures that are varied between 250°C and 350°C. The reactant mixture is allowed to react within the reactor for specific timeframes for each test. The volumetric flow rate of each reactant is set according to the reactor volume and the molar ratio required. The output of the reactor is connected to an ammonia trap to determine the yield of ammonia. The conversion ratio of reactants to products is also determined after evaluating the output yield of ammonia. The ammonia trap used in the present study comprises a boric acid solution that changes pH with ammonia input. The pH change is measured and used to determine the amount of ammonia synthesized.

During ammonia fuel cell operation, the stored ammonia is released and allowed to enter the fuel cell stack for power generation. However, to test the performance of the ammonia fuel cell stack under varying operating conditions, ammonia is entered at an input pressure of 1 bar.

Humid air is entered at the cathodic side at a flow rate of 6 L/min to ensure that an excess oxidant supply to the stack exists during operation. The performance of the stack is investigated at varying humidifier temperatures. Different performance parameters of the fuel cell stack are investigated. These include electrochemical performance tests including the no-load voltage as well as polarization tests. The energetic and exergetic efficiencies of the fuel cell stack are also determined. The Gamry potentiostat is connected to the stack that records the electrochemical measurements and transmits it to the connected computer or workstation.

4.2.1 Ammonia fuel cell utilizing molten electrolyte

Using alkaline molten salts as electrolytes provide a range of opportunities to obtain clean energy through electrochemical ammonia oxidation through the existing energy storage systems such as thermal energy storage systems. In this study, experimental investigation of the molten electrolyte-based ammonia fuel cell is also performed to study their electrochemical, energetic as well as exergetic performances. The alkaline molten salt mixture of sodium and potassium hydroxide in a 1:1 mole ratio is used in this study.

The salt mixture is firstly placed in an alumina crucible reactor that is heated in an enclosed furnace. The temperature-controlled furnace is regulated according to the salt temperature. The operating reactor temperatures are varied between 220°C and 280°C. Nickel coils are employed as fuel cell electrodes for the ammonia fuel cell. The total area of the electrode coils used is $2.4 \pm 0.5 \text{ cm}^2$ for both electrodes. A similar bubbler humidifier, described earlier, is used for the molten electrolyte ammonia fuel cell to provide the oxygen and water molecules needed to produce the hydroxyl ions required for electrochemical oxidation of ammonia.

The electrodes of the ammonia fuel cell are connected to the potentiostat for electrochemical measurements. The hydroxyl ions formed at the cathode as well as the

hydroxyl ions contained in the molten electrolyte react electrochemically with ammonia at the anode to generate a flow of electrons that is detected by the connected potentiostat. The electrochemical performance tests of no-load open circuit voltage as well as polarization behavior are performed. The open circuit voltage test is conducted to determine the cell performance under no output load. This depicts the extent of electrochemical oxidation of ammonia in the molten electrolyte at the anode.

The polarization tests provide an idea about the cell performance under varying output loads. As output loads are raised, the cell voltage drops owing to different types of polarization losses. Once the no-load voltage attains a stable value, the polarization test is initiated that sets different output loads and records the corresponding cell voltages. The polarization behavior tests are also used to determine the peak power outputs of the molten electrolyte ammonia fuel cells. The power densities are determined for the developed fuel cells that are important for assessing the performance, which denote the power output from the cell per unit area of electrode. Specifically, the peak power densities are determined to investigate the maximum power output per unit electrode area. Next, utilizing cell outputs at different load values, the energetic as well as exergetic efficiencies of the cell are determined at varying operating conditions.

CHAPTER 5 : ANALYSIS AND MODELING

This chapter describes the detailed analysis and modelling of the developed systems and associated subsystems. The methodology utilized for the analysis of each subsystem is discussed along with considered simulation parameters. The electrochemical modelling of electrochemical conversion processes and thermodynamic modelling of all system components is described. The scale-up analysis performed is discussed along with the exergoeconomic and multi-objective optimization studies.

5.1 System 1

This section is focused on the analysis and modelling of system 1. The thermodynamic analysis of each system component and corresponding modelling parameters are described in detail. The electrochemical modelling of different electrochemical conversion subsystems is also discussed. The assessment of overall system performance as well as associated subsystems is described.

5.1.1 Solar-based power generation

The developed solar and wind energy-based systems are modelled and analysed considering the hourly dynamic variations in solar intensities and wind speeds. The hourly solar intensities are determined for the city of Toronto considering the average monthly days. Firstly, the normal solar radiation per unit area is determined according to [76]

$$\dot{I}_{nl} = E_{ec} 0.9715 \dot{I}_{st} \tau_{on} \tau_{wt} \tau_{ga} \tau_{rh} \tau_{ar} \quad (5.1)$$

where the factor of eccentricity is denoted by E_{ec} , the solar constant is written as \dot{I}_{st} , and τ denotes transmittance corresponding to aerosols (ar), Rayleigh (rh), ozone (on), gas (ga) and water (wt). Factor of eccentricity is evaluated according to

$$E_{ec} = 1.00011 + 0.00128 \sin(D) + 0.034221 \cos(D) + 0.000077 \sin(2D) + 0.000719 \cos(2D) \quad (5.2)$$

The incoming solar beam radiation intensity is evaluated as

$$\dot{I}_{bm} = \cos \theta_{zh} \dot{I}_{nl} \quad (5.3)$$

where \dot{I}_{bm} is the beam radiation intensity and θ_{zh} denotes angle of zenith that is expressed as

$$\cos\theta_{zh} = (\cos\phi_{dl})(\cos\phi_{la})(\cos\delta_{dc}) + (\sin\phi_{la})(\sin\delta_{dc}) \quad (5.4)$$

where ϕ_{dl} is the day angle, ϕ_{la} denotes geographical latitude and δ_{dc} represents declination angle. The day angle is expressed in terms of the solar time (S_T) as

$$\phi_{dl} = (12 - S_T) \quad (15) \quad (5.5)$$

Next, the total incident solar radiation on the solar collectors is evaluated for a given hour as

$$\dot{Q}_{sr,in} = \dot{I}_{bm}A_{sr,tot} \quad (5.6)$$

where the total collector area is denoted as $A_{sr,tot}$. The total incoming solar energy on monthly average days is evaluated as follows:

$$E_{sr,in} = \int_{t_0}^{t_{sol}} \dot{Q}_{sr,in} dt \quad (5.7)$$

where the integral limits a and b denote the sunrise and sunset times respectively. The total exergy input via solar energy for a given day is evaluated as

$$Ex_{sr,in} = \int_{t_0}^{t_{sol}} \dot{Q}_{sr,in} \left(1 - \frac{T_0}{T_{sn}}\right) dt \quad (5.8)$$

where the temperatures of the ambient are written as T_0 and the sun temperature is T_{sn} (5777 K). For the solar photovoltaic (PV)-based energy system, the total power output from the solar farm is evaluated as

$$\dot{W}_{PV} = \dot{I}_{bm}A_{sr,tot}\eta_{PV}\eta_c \quad (5.9)$$

where η_{PV} and η_c represent the efficiencies of the PV cells and converter respectively. The total energy output from the PV farm on the average day is then evaluated as

$$E_{PV,o} = \int_{t_0}^{t_{sol}} \dot{W}_{PV} dt \quad (5.10)$$

5.1.2 Wind-based power generation

For the analysis of developed systems, the hourly variations in wind speeds for the city of Toronto are also considered for the average monthly days [77]. Considering these variations, the total input wind energy per unit time to the system is evaluated for a given day according to

$$\dot{W}_{wn,in} = \frac{1}{2} \dot{m}_{wn,in} V_h^2 N_{wn} \quad (5.11)$$

where V_h denotes the wind speed and the total rate of inflow of air through the wind turbine is denoted as $\dot{m}_{wn,in}$, and N_{wn} represents the total number of wind turbines. The total air inflow rate to a turbine is evaluated from

$$\dot{m}_{wn,in} = \rho_a V_h A_{wn} \quad (5.12)$$

where ρ_a denotes air density, V_h represents wind speed and A_{wn} is the swept area of the turbine. Next, the total power output from the wind turbine farm is evaluated at a given wind speed value as

$$\dot{W}_{wn,out} = C_p \frac{1}{2} \rho_a A_{wn} V_h^3 \eta_{wn} \eta_c N_{wn} \quad (5.13)$$

where power coefficient is represented by C_p , the efficiency of the turbine is written as η_{wn} and the efficiency of the converter is denoted by η_c . The total input wind energy to the system and the total output electrical energy from the wind farm on the average days are determined respectively as

$$E_{wn,in,tot} = \int_{t_0}^{t_{wn}} \frac{1}{2} \dot{m}_{wn,in} V_h^2 N_{wn} dt \quad (5.14)$$

$$E_{wn,out,tot} = \int_{t_0}^{t_{wn}} C_p \frac{1}{2} \rho_a A_{wn} V_h^3 \eta_{wn} \eta_c N_{wn} dt \quad (5.15)$$

The mass and energy balances are applied on the wind turbines for a given day as

$$\int_{t_0}^{t_{wn}} \dot{m}_{wn,in} dt = \int_{t_0}^{t_{wn}} \dot{m}_{wn,out} dt \quad (5.16)$$

$$\int_{t_0}^{t_{wn}} \dot{m}_{wn,in} \left(h_{in} + \frac{V_{in}^2}{2} \right) dt = \int_{t_0}^{t_{wn}} \dot{m}_{wn,out} \left(h_{out} + \frac{V_{ot}^2}{2} \right) dt + \int_{t_0}^{t_{wn}} \dot{W}_{wn,m,out} dt + \int_{t_0}^{t_{wn}} \dot{Q}_{l,wn} dt \quad (5.17)$$

Next, the entropy as well as exergy balances are applied as follows:

$$\int_{t_0}^{t_{wn}} \dot{m}_{wn,in} s_{in} dt + \int_{t_0}^{t_{wn}} \dot{S}_{gen,wn} dt = \int_{t_0}^{t_{wn}} \dot{m}_{wn,out} s_{out} dt + \int_{t_0}^{t_{wn}} \frac{\dot{Q}_{l,wn}}{T_b} dt \quad (5.18)$$

$$\int_{t_0}^{t_{wn}} \dot{m}_{wn,in} ex_{in} dt = \int_{t_0}^{t_{wn}} \dot{m}_{wn,out} ex_{out} dt + \int_{t_0}^{t_{wn}} \dot{W}_{wn,m,out} dt + \int_{t_0}^{t_{wn}} \dot{Q}_{l,wn} \left(1 - \frac{T_0}{T_b}\right) dt + \int_{t_0}^{t_{wn}} \dot{E}x_{dest,wn} dt \quad (5.19)$$

5.1.3 Hydrogen production via water splitting

The proton exchange membrane (PEM)-based water splitting method is utilized in the present study. In this type of hydrogen production process, water molecules are dissociated through the utilization of electrical power to produce hydrogen and oxygen. The splitting or dissociation of water molecules can be expressed according to the following chemical equation:



The Gibbs energy change for the above reaction is evaluated from

$$\Delta G_{PEM} = \Delta H_{PEM} - T_{PEM} \Delta S_{PEM} \quad (5.21)$$

where ΔG denotes the Gibbs energy change, ΔH represents the enthalpy change that is evaluated from the number of product ($N_{i,p}$) and reactant ($N_{i,r}$) moles, molar specific enthalpies of product ($\bar{h}_{i,p}$) and reactants ($\bar{h}_{i,r}$) as follows:

$$\Delta H = \sum_p N_{i,p} \bar{h}_{i,p} - \sum_r N_{i,r} \bar{h}_{i,r} \quad (5.22)$$

The entropy change ΔS is determined from $N_{i,p}$, $N_{i,r}$ and the specific molar entropy ($\bar{s}_{i,p}$) as

$$\Delta S = \sum_p N_{i,p} \bar{s}_{i,p} - \sum_r N_{i,r} \bar{s}_{i,r} \quad (5.23)$$

The electrochemical conversion process includes water splitting via both anodic as well as cathodic half-cell electrochemical interactions. The cathodic interaction for the PEM electrolysis subsystem occurs according to [78]



where the positively charged H^+ ions are generated at the anode through the electrochemical interaction of water molecules as



Hence, as electrical input is supplied to the electrolyser, a potential difference is generated between the two electrodes of electrolysis cells that results in the half-cell electrochemical reactions described. At a given current density value (J_{PEM}), the molar rate of hydrogen production ($\dot{N}_{H_2,PEM}$) is evaluated from the columbic efficiency ($\eta_{c,PEM}$), number of electron moles (n), electrode area (A_{PEM}) and Faraday's constant (F) as

$$\dot{N}_{H_2,PEM} = \frac{J_{H_2} A_{PEM}}{nF} \eta_{c,PEM} \quad (5.26)$$

However, the current input varies according to the available solar and wind energy. As the input current varies, the voltage across the electrolyser stack also changes that constitutes several electrochemical losses that need to be accounted. The actual operating cell voltage can be written in terms of these losses as follows:

$$V_{PEM,H_2} = V_{PEM,H_2,OC} + V_{PEM,H_2,conc} + V_{PEM,H_2,act} + V_{PEM,H_2,ohm} \quad (5.27)$$

where the no-load voltage under open circuit conditions is written as $V_{PEM,H_2,OC}$ that is evaluated according to

$$V_{PEM,H_2,OC} = \frac{\Delta G_{PEM}}{nF} \quad (5.28)$$

However, as the current input rises, electrochemical polarization losses occur in the electrolysis cells that result in an increase in the input voltage and thus input power requirement. The first type of polarization loss includes the voltage loss due to limitations in charge transfer, which is referred to as the activation loss that is evaluated as

$$V_{PEM,H_2,act} = \sinh^{-1}\left(\frac{J_{H_2}}{2J_{ex,i,PEM}}\right) \quad (5.29)$$

where the exchange current density is represented as $J_{ex,i,PEM}$ and the subscript i refers to the type of electrode comprising of cathode (c) or anode (a). The exchange current density

at a given electrode is dependent on the activation energy ($E_{PEM,act,i}$), operating temperature (T_{PEM}) and electrode pre-exponential parameter (J_i^f) as

$$J_{ex,i,PEM} = J_i^f \exp\left(-\frac{E_{PEM,act,i}}{RT_{PEM}}\right) \quad (5.30)$$

Next, the polarization loss occurring due to the Ohmic resistances in the electrolyser stack is determined as

$$V_{PEM,H_2,Ohm} = J_{PEM,H_2} \Omega_{PEM} \quad (5.31)$$

where the Ohmic resistance denoted by Ω_{PEM} is evaluated from the amount of moisture in the membrane denoted by $\phi_{PEM,ic}$, the ionic conductivity represented as $\sigma_{PEM,ic}$ and the thickness of the membrane written as u :

$$\Omega_{PEM} = \int_0^u \frac{1}{\sigma_{PEM,ic}(\phi_{PEM,ic}(z))} dz \quad (5.32)$$

where the amount of moisture is evaluated considering the content of moisture at the interfaces of the membrane-anode ($\phi_{PEM,a}$) and membrane-cathode ($\phi_{PEM,c}$) as

$$\phi_{PEM,ic}(z) = \frac{\phi_{PEM,a} - \phi_{PEM,c}}{u} z + \phi_{PEM,c} \quad (5.33)$$

The conductivity of ionic current is determined from

$$\sigma_{PEM}(\phi_{PEM,ic}(z)) = (0.5139\phi_{PEM,ic}(z) - 0.326) \left(\exp\left(1268 \left(\frac{1}{303} - \frac{1}{T_{PEM}} \right) \right) \right) \quad (5.34)$$

The relation between the electrolyser power input, current density, total electrode area and operating voltage can be denoted as

$$\dot{W}_{PEM,H_2,in} = V_{PEM,H_2} J_{PEM,H_2} A_{PEM} \quad (5.35)$$

The power input to the PEM subsystem is dependent on the available wind and solar energy, and is utilized according to the system operational algorithm that will be discussed in the proceeding chapters. For a given day, the total PEM energy input is evaluated as

$$E_{PEM,H_2,in} = \int_{t_0}^{t_{PEM}} \dot{W}_{PEM,H_2,in} dt \quad (5.36)$$

The mass and energetic balances are applied on the PEM subsystem according to

$$\int_{t_0}^{t_{PEM}} \dot{m}_1 dt = \int_{t_0}^{t_{PEM}} \dot{m}_2 dt + \int_{t_0}^{t_{PEM}} \dot{m}_3 dt \quad (5.37)$$

$$\int_{t_0}^{t_{PEM}} \dot{m}_1 h_1 dt + \int_{t_0}^{t_{PEM}} \dot{W}_{PEM,H_2,in} dt = \int_{t_0}^{t_{PEM}} \dot{m}_2 h_2 dt + \int_{t_0}^{t_{PEM}} \dot{m}_3 h_3 dt \quad (5.38)$$

The PEM subsystem is analysed through entropy and exergy analyses according to

$$\int_{t_0}^{t_{PEM}} \dot{m}_1 s_1 dt + \int_{t_0}^{t_{PEM}} \dot{S}_{gen,PEM} dt = \int_{t_0}^{t_{PEM}} \dot{m}_2 s_2 dt + \int_{t_0}^{t_{PEM}} \dot{m}_3 s_3 dt \quad (5.39)$$

$$\int_{t_0}^{t_{PEM}} \dot{m}_1 ex_1 dt + \int_{t_0}^{t_{PEM}} \dot{W}_{PEM,H_2,in} dt = \int_{t_0}^{t_{PEM}} \dot{m}_2 ex_2 dt + \int_{t_0}^{t_{PEM}} \dot{m}_3 ex_3 dt + \int_{t_0}^{t_{PEM}} \dot{E}x_{dest,PEM} dt \quad (5.40)$$

5.1.4 Nitrogen production via air separation

As air enters the PSA subsystem at state 4, the selective adsorption process separates the nitrogen molecules from other gas constituents. Nitrogen at state 5 exits the subsystem and is utilized for ammonia production while the remaining oxygen concentrated stream at state 6 is used to operate the direct ammonia fuel cell. The Skarstrom PSA cycle for air separation is considered [79]. In this PSA system, there exist two beds of adsorbent filled containers. These two packed beds are utilized simultaneously in a series of processes to separate oxygen or nitrogen from air. The cycle comprises of four processes. The first process comprises of pressurization of one of the beds. In this process, one of beds is pressurized to the suitable pressure required according to the adsorbents utilized, while the second bed is allowed to release the stored gases.

The second process is the adsorption step where owing to the presence of high pressure in the packed bed, nitrogen molecules are preferentially adsorbed and the remaining molecules of oxygen as well as other gases are left unadsorbed. The third step comprises of depressurizing packed bed 1, consequentially obtaining the required nitrogen output and pressurizing packed bed 2. The fourth step involves pressurizing packed bed 2 and the cycle is repeated with sequential processes from steps 1 to 4. The drop in pressure across the packed adsorbent beds can be evaluated through the Ergun equation:

$$-(1.5 \times 10^{-3} \frac{\mu(1-e_i)^2}{(2r_p\psi)^2} v_g + 1.75 \times 10^{-3} \frac{\rho_g MW(1-e_i)}{2r_p\psi e_i^3} v_g^2) = \frac{\partial P}{\partial z} \quad (5.41)$$

where ψ represents the shape factor of the particles, r_p is the radius of the particles, μ denotes the viscosity, P represents the drop in pressure, z is the distance in the axial direction across the packed bed and e represents the voidage of the packed bed, q_i denotes the specie i concentration. The PSA based air separation unit is modelled in ASPEN Plus simulation software [80]. The PSA power input is related to the temperature of inlet air (T_4), ratio of specific heats of air (k), inlet air mass flow rate (\dot{m}_4), isentropic efficiency of the air compressor (η_{is}) and mechanical efficiency of the compressor (η_m) as

$$\dot{W}_{PSA,in} = \frac{\dot{m}_4}{\eta_{is}\eta_m} RT_4 \left[\left[\frac{P_o}{P_i} \right]^{\frac{k-1}{k}} - 1 \right] \left(\frac{k}{k-1} \right) \quad (5.42)$$

The power input supplied to the PSA subsystem is also a function of the excess available wind power. The total energy input provided to the subsystem on a given day is calculated for the considered average day according to

$$E_{PSA,in} = \int_{t_0}^t \dot{W}_{PSA,in} dt \quad (5.43)$$

The mass and energetic analyses is performed according to

$$\int_{t_0}^{t_{PSA}} \dot{m}_4 dt = \int_{t_0}^{t_{PSA}} \dot{m}_5 dt + \int_{t_0}^{t_{PSA}} \dot{m}_6 dt \quad (5.44)$$

$$\int_{t_0}^{t_{PSA}} \dot{m}_4 h_4 dt + \int_{t_0}^{t_{PSA}} \dot{W}_{PSA,in} dt = \int_{t_0}^{t_{PSA}} \dot{m}_5 h_5 dt + \int_{t_0}^{t_{PSA}} \dot{m}_6 h_6 dt \quad (5.45)$$

Next, the entropy and exergy analyses of the PSA subsystem are summarized according to

$$\int_{t_0}^{t_{PSA}} \dot{m}_4 s_4 dt + \int_{t_0}^{t_{PSA}} \dot{S}_{gen,PSA} dt = \int_{t_0}^{t_{PSA}} \dot{m}_5 s_5 dt + \int_{t_0}^{t_{PSA}} \dot{m}_6 s_6 dt \quad (5.46)$$

$$\int_{t_0}^{t_{PSA}} \dot{m}_4 ex_4 dt + \int_{t_0}^{t_{PSA}} \dot{W}_{PSA,in} dt = \int_{t_0}^{t_{PSA}} \dot{m}_5 ex_5 dt + \int_{t_0}^{t_{PSA}} \dot{m}_6 ex_6 dt + \int_{t_0}^{t_{PSA}} \dot{E}x_{dest,PSA} dt \quad (5.47)$$

5.1.5 Clean ammonia synthesis

The clean hydrogen and nitrogen produced are utilized for synthesizing ammonia. Firstly, a reactant mixture entailing a mole ratio of 3 mol H₂:1 mol N₂ is sent to C-1 at state 7 to attain the synthesis pressure prior to entering the ASR at state 8. The power input to C-1 is

also set as a function of the input power requirements of the PEM and PSA subsystems. For a given average day, the mass and energetic balances are applied on C-1 according to

$$\int_{t_0}^{t_{C-1}} \dot{m}_7 dt = \int_{t_0}^{t_{C-1}} \dot{m}_8 dt \quad (5.48)$$

$$\int_{t_0}^{t_{C-1}} \dot{m}_7 h_7 dt + \int_{t_0}^{t_{C-1}} \dot{W}_{C-1} dt = \int_{t_0}^{t_{C-1}} \dot{m}_8 h_8 dt \quad (5.49)$$

The entropy and exergy analyses of C-1 for an average day is summarized as

$$\int_{t_0}^{t_{C-1}} \dot{m}_7 s_7 dt + \int_{t_0}^{t_{C-1}} \dot{S}_{gen,C-1} dt = \int_{t_0}^{t_{C-1}} \dot{m}_8 s_8 dt \quad (5.50)$$

$$\int_{t_0}^{t_{C-1}} \dot{m}_7 ex_7 dt + \int_{t_0}^{t_{C-1}} \dot{W}_{C-1} dt = \int_{t_0}^{t_{C-1}} \dot{m}_8 ex_8 dt + \int_{t_0}^{t_{C-1}} \dot{E}x_{dest,C-1} dt \quad (5.51)$$

The synthesis of ammonia from hydrogen and nitrogen constitutes a reversible reaction that can be represented as



In this chemical reaction, the conversion of nitrogen can be denoted as

$$X_{N_2} = \frac{n_{NH_3,i} - n_{NH_3,e}}{n_{NH_3,i}} \quad (5.53)$$

In this study, the yield of ammonia under varying operating conditions comprising of different reaction pressures and temperatures is analysed. These variations in operating conditions result in different ammonia production rates as well as conversion ratios. The synthesis reaction, owing to its reversible nature, occurs in both directions. The synthesis of ammonia corresponds to the forward reaction while the backward direction is associated with dissociation of ammonia. For system modelling, the Gibbs energy minimization technique is utilized for evaluating the rates of ammonia production at different operating parameters. The derivative of Gibbs free energy (dg) can be denoted according to

$$dg = du + Pdv - Tds \quad (5.54)$$

The first and second law of thermodynamics can be implemented to obtain:

$$dg \leq 0 \quad (5.55)$$

where the relation denotes the occurrence of a spontaneous reaction under the same pressure and temperature takes place until the minimum value of the Gibbs free energy is attained. This point in the reaction corresponds to the equilibrium. Denoting the dependency of Gibbs free energy on the number of moles of different species involved in the chemical reaction (N), pressure (P) and temperature (T) as

$$g = g(P, T, N_1, N_2, N_N) \quad (5.56)$$

The general derivative of this relation is written as

$$dg = \left(\frac{\partial g}{\partial T}\right)_{P,N} dT + \left(\frac{\partial g}{\partial P}\right)_{T,N} dP + \sum_i^N \left(\frac{\partial g}{\partial N_i}\right)_{T,P,N_i} dN_i \quad (5.57)$$

Considering constant reaction pressure and temperature, the general derivative can be denoted according to

$$dg = \sum_i^N \mu_i dN_i = 0 \quad (5.58)$$

where μ_i represents the chemical potential that is represented as

$$\mu_i = \left(\frac{\partial g}{\partial N_j}\right)_{P,T,N_i} \quad (5.59)$$

The ASPEN Plus simulation software is utilized to model the ammonia synthesis subsystem via the Gibbs energy minimization technique. The ASR mass and energy analyses can be summarized as

$$\int_{t_0}^{t_{ASR}} \dot{m}_8 dt + \int_{t_0}^{t_{ASR}} \dot{m}_{20} dt = \int_{t_0}^{t_{ASR}} \dot{m}_9 dt \quad (5.60)$$

$$\int_{t_0}^{t_{ASR}} \dot{m}_8 h_8 dt + \int_{t_0}^{t_{ASR}} \dot{m}_{20} h_{20} dt = \int_{t_0}^{t_{ASR}} \dot{m}_9 h_9 dt + \int_{t_0}^{t_{ASR}} \dot{Q}_{ASR} dt \quad (5.61)$$

The ASR entropy and exergy balances are summarized as

$$\int_{t_0}^{t_{ASR}} \dot{m}_8 s_8 dt + \int_{t_0}^{t_{ASR}} \dot{m}_{20} s_{20} dt + \int_{t_0}^{t_{ASR}} \dot{S}_{gen,ASR} dt = \int_{t_0}^{t_{ASR}} \dot{m}_9 s_9 dt + \int_{t_0}^{t_{ASR}} \frac{\dot{Q}_{ASR}}{T_{ASR}} dt \quad (5.62)$$

$$\int_{t_0}^{t_{ASR}} \dot{m}_8 ex_8 dt + \int_{t_0}^{t_{ASR}} \dot{m}_{20} ex_{20} dt = \int_{t_0}^{t_{ASR}} \dot{m}_9 ex_9 dt + \int_{t_0}^{t_{ASR}} \dot{Q}_{ASR} \left(1 - \frac{T_0}{T_{ASR}}\right) dt + \int_{t_0}^{t_{ASR}} \dot{E}x_{dest,ASR} dt \quad (5.63)$$

As stream 9 exits the ASR, it constitutes the synthesized ammonia as well as unreacted hydrogen and nitrogen that need to be separated. Firstly, HX-1 is utilized to drop the mixture temperature that is essential to condense and thus separate ammonia. The mass and energetic analyses of HX-1 is represented for a given average day as

$$\int_{t_0}^{t_{HX1}} \dot{m}_9 dt + \int_{t_0}^{t_{HX1}} \dot{m}_{18} dt = \int_{t_0}^{t_{HX1}} \dot{m}_{10} dt + \int_{t_0}^{t_{HX1}} \dot{m}_{15} dt \quad (5.64)$$

$$\int_{t_0}^{t_{HX1}} \dot{m}_9 h_9 dt + \int_{t_0}^{t_{HX1}} \dot{m}_{18} h_{18} dt = \int_{t_0}^{t_{HX1}} \dot{m}_{10} h_{10} dt + \int_{t_0}^{t_{HX1}} \dot{m}_{15} h_{15} dt + \int_{t_0}^{t_{HX1}} \dot{Q}_{L,HX1} dt \quad (5.65)$$

The entropy and exergy balances are summarized for HX-1 as

$$\int_{t_0}^{t_{HX1}} \dot{m}_9 s_9 dt + \int_{t_0}^{t_{HX1}} \dot{m}_{18} s_{18} dt + \int_{t_0}^{t_{HX1}} \dot{S}_{gen,HX1} dt = \int_{t_0}^{t_{HX1}} \dot{m}_{10} s_{10} dt + \int_{t_0}^{t_{HX1}} \dot{m}_{15} s_{15} dt + \int_{t_0}^{t_{HX1}} \frac{\dot{Q}_{L,HX1}}{T_b} dt \quad (5.66)$$

$$\int_{t_0}^{t_{HX1}} \dot{m}_9 ex_9 dt + \int_{t_0}^{t_{HX1}} \dot{m}_{18} ex_{18} dt = \int_{t_0}^{t_{HX1}} \dot{m}_{10} ex_{10} dt + \int_{t_0}^{t_{HX1}} \dot{m}_{15} ex_{15} dt + \int_{t_0}^{t_{HX1}} \dot{Q}_l \left(1 - \frac{T_0}{T_b}\right) dt + \int_{t_0}^{t_{HX1}} \dot{E}x_{dest,HX1} dt \quad (5.67)$$

The refrigerant leaves HX-1 at state 15 and is delivered to C-2 for compression. The thermodynamic analysis of C-2 is performed similar to C-1 as described earlier. At state 16, the refrigerant is sent to CON for heat rejection that is analysed through mass and energy balances according to

$$\int_{t_0}^{t_{con}} \dot{m}_{16} dt = \int_{t_0}^{t_{con}} \dot{m}_{17} dt \quad (5.68)$$

$$\int_{t_0}^{t_{con}} \dot{m}_{16} h_{16} dt = \int_{t_0}^{t_{con}} \dot{m}_{17} h_{17} dt + \int_{t_0}^{t_{con}} \dot{Q}_{con} dt \quad (5.69)$$

The CON is analysed through the following entropy and exergy balances:

$$\int_{t_0}^{t_{con}} \dot{m}_{16} s_{16} dt + \int_{t_0}^{t_{con}} \dot{S}_{gen} dt = \int_{t_0}^{t_{con}} \dot{m}_{17} s_{17} dt + \int_{t_0}^{t_{con}} \frac{\dot{Q}_{con}}{T_b} dt \quad (5.70)$$

$$\int_{t_0}^{t_{con}} \dot{m}_{16} ex_{16} dt = \int_{t_0}^{t_{con}} \dot{m}_{17} ex_{17} dt + \int_{t_0}^{t_{con}} \dot{Q}_{con} \left(1 - \frac{T_0}{T_b}\right) dt + \int_{t_0}^{t_{con}} \dot{E}x_{dest,con} dt \quad (5.71)$$

Next, the refrigerant undergoes the throttling process between states 17 and 18. The mass and energetic balances for the TV are expressed according to

$$\int_{t_0}^{t_{TV}} \dot{m}_{17} dt = \int_{t_0}^{t_{TV}} \dot{m}_{18} dt \quad (5.72)$$

$$\int_{t_0}^{t_{TV}} \dot{m}_{17} h_{17} dt = \int_{t_0}^{t_{TV}} \dot{m}_{18} h_{18} dt \quad (5.73)$$

The entropy and exergy analyses of the TV is summarized as

$$\int_{t_0}^{t_{TV}} \dot{m}_{17} s_{17} dt + \int_{t_0}^{t_{TV}} \dot{S}_{gen} dt = \int_{t_0}^{t_{TV}} \dot{m}_{18} s_{18} dt \quad (5.74)$$

$$\int_{t_0}^{t_{TV}} \dot{m}_{17} ex_{17} dt = \int_{t_0}^{t_{TV}} \dot{m}_{18} ex_{18} dt + \int_{t_0}^{t_{TV}} \dot{E}x_{dest,TV} dt \quad (5.75)$$

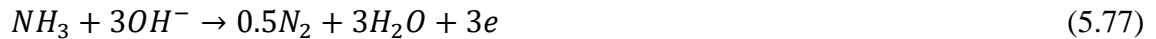
The ammonia produced is utilized as both a useful system output as well as an energy storage medium, which is used via a direct ammonia fuel cell stack to generate clean electricity when required.

5.1.6 Anion exchange membrane-based ammonia fuel cell

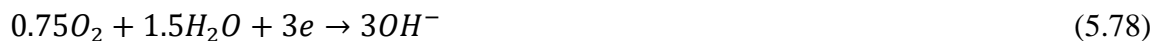
The ammonia synthesized is also utilized to generate clean electrical power through electrochemical conversion in the direct ammonia fuel cell subsystem (AFC). Ammonia at state 12 is sent to the AFC while the concentrated oxygen stream generated by the PSA is utilized as the fuel cell oxidant that enters the AFC subsystem at state 13. Series of electrochemical interactions occur in the alkaline membrane-based ammonia fuel cell stack that electrochemically oxidize ammonia molecules to generate clean electrical power. The overall reaction that corresponds to the combined half-cell interactions occurring in the AFC can be written as



However, electrochemical oxidation reaction that denotes the conversion of ammonia molecules through an oxidation process that releases electrons can be denoted for the anodic AFC reaction as



where the hydroxyl ions (OH^-) are generated through the following half-cell cathodic reaction:



The overall reaction described above is utilized to determine the fuel cell voltage under no-load condition that signifies the open circuit voltage:

$$V_{AFC,oc} = \frac{\Delta G_{AFC}}{nF} \quad (5.79)$$

The Gibbs energy change for the ammonia fuel cell denoted by ΔG_{AFC} is determined through a similar procedure described in Section 5.1.2. As current output from the AFC subsystem is increased, different polarization losses take place within the electrochemical cells that result in voltage drops at different values of current outputs. The voltage loss that occurs due to limitations in charge transfer at initial values of current densities is referred to as the activation loss, which can be evaluated as

$$V_{AFC,act} = \ln\left(\frac{J_{AFC}}{J_{0,AFC}}\right) \frac{T_{AFC}R}{\alpha nF} \quad (5.80)$$

where α represents the charge transference coefficient, J_{AFC} is the operational ammonia fuel cell current density, $J_{0,AFC}$ denotes the ammonia fuel cell exchange current density and T_{AFC} represents the operation fuel cell temperature. Next, after the initial low values of current densities are exceeded, the voltage loss because of Ohmic resistance in the cell attains more significance that can be evaluated according to

$$V_{AFC,Ohm} = \Omega_{AFC} J_{AFC} \quad (5.81)$$

Significant voltage losses occur in the ammonia fuel cell at high current outputs that are referred to as concentration polarization losses, which are determined according to

$$V_{AFC,conc} = \ln\left(\frac{J_{L,AFC}}{J_{L,AFC} - J_{AFC}}\right) \frac{RT_{AFC}}{\alpha nF} \quad (5.82)$$

where the limiting current per unit area is denoted as $J_{L,AFC}$. Ammonia fuel cells entail an irreversible drop in voltage that lowers the no-load voltage from the theoretical value ($V_{AFC,ir}$). Considering these losses in voltage, the operational voltage of the ammonia fuel cell is evaluated for a given current output according to

$$V_{AFC} = V_{AFC,oc} - V_{AFC,ir} - V_{AFC,Ohm} - V_{AFC,act} - V_{AFC,conc} \quad (5.83)$$

The rate of energy output from the fuel cell stack is then evaluated from the operational voltage and current density according to

$$\dot{W}_{AFC} = N_{AFC} J_{AFC} V_{AFC} A_{AFC} \quad (5.84)$$

where the total number of cells utilized in the fuel cell stack is written as N_{AFC} and the electrode area is represented as A_{AFC} . Next, the total energy output obtained from the ammonia fuel cell stack is evaluated as

$$E_{out,AFC} = \int_{t_0}^{t_{AFC}} \dot{W}_{AFC} dt \quad (5.85)$$

The mass and energy balances are applied on the ammonia fuel cell subsystem as follows:

$$\int_{t_0}^{t_{AFC}} \dot{m}_{12} dt + \int_{t_0}^{t_{AFC}} \dot{m}_{13} dt = \int_{t_0}^{t_{AFC}} \dot{m}_{19} dt \quad (5.86)$$

$$\int_{t_0}^{t_{AFC}} \dot{m}_{12} h_{12} dt + \int_{t_0}^{t_{AFC}} \dot{m}_{13} h_{13} dt = \int_{t_0}^{t_{AFC}} \dot{m}_{19} h_{19} dt + \int_{t_0}^{t_{AFC}} \dot{W}_{AFC} dt \quad (5.87)$$

The ammonia fuel cell is also analysed via entropy and exergy analyses according to

$$\int_{t_0}^{t_{AFC}} \dot{m}_{12} s_{12} dt + \int_{t_0}^{t_{AFC}} \dot{m}_{13} s_{13} dt + \int_{t_0}^{t_{AFC}} \dot{S}_{gen,AFC} dt = \int_{t_0}^{t_{AFC}} \dot{m}_{19} s_{19} dt \quad (5.88)$$

$$\int_{t_0}^{t_{AFC}} \dot{m}_{12} ex_{12} dt + \int_{t_0}^{t_{AFC}} \dot{m}_{13} ex_{13} dt = \int_{t_0}^{t_{AFC}} \dot{m}_{19} ex_{19} dt + \int_{t_0}^{t_{AFC}} \dot{W}_{AFC} dt + \int_{t_0}^{t_{AFC}} \dot{E}x_{dest,AFC} dt \quad (5.89)$$

5.1.7 Algorithm for system 1 modelling and analysis

The algorithm implemented for analysis of system 1 is depicted in Fig. 5.1. Firstly, the wind speed as well as the solar insolation at a given hour are compared to the average value for the day. When the wind speed exceeds the daily average, the excess available power is evaluated and delivered to the hydrogen as well as ammonia synthesis subsystems. The power output from the wind farm that corresponds to the daily average is utilized as useful electrical power output from the system. However, when the wind speed is lower than the daily average, the available wind energy is utilized to produce only electrical energy output. The incident solar radiation intensity is also compared to the mean daily value.

When the intensity exceeds the mean value, the excess available electrical power produced by the PV farm is utilized for hydrogen and ammonia synthesis. During this time, the daily average electrical output from the PV farm is utilized as useful system output. However, when the solar intensity is comparatively lower than the daily average value, the available solar radiation is utilized to produce only electrical power output.

Considering hourly operation of the system throughout the day, the daily energy, hydrogen and ammonia outputs are determined. The ammonia fuel cell stack is analysed in conjunction with the amount of ammonia stored to determine the energy output capacities.

To assess the performance of the developed system during different times of the year, transient analysis is performed for the monthly average day. The system algorithm developed for daily operation entails the utilization of available solar and wind energy to produce useful commodities of electricity, hydrogen and ammonia. Since the daily average is chosen as the threshold to determine the operational points corresponding to the production of hydrogen as well as ammonia, wastage of excess solar or wind energy is eliminated.

During the presence of excess energy, clean hydrogen and ammonia are produced. As a partial amount of ammonia synthesized is also utilized for energy storage, the ammonia fuel cell provides clean electricity when required. The stored ammonia can be electrochemically oxidized in the ammonia fuel cell during low availability of solar or wind energy. Hence, providing flexibility in energy production when needed. As the ammonia fuel cell power output is dependent on the amount of fuel input to the subsystem, power generation flexibility is provided.

The fuel input rate can be varied to increase or decrease the required output from the subsystem. The operational algorithm utilized also provides stable energy production during excess available solar or wind energy. During periods of excess energy, a stable output of power is attained through the utilized algorithm that is essential for intermittent and fluctuant energy sources. The modelling parameters, component capacities and simulation conditions considered for system 1 are provided in Table 5.1.

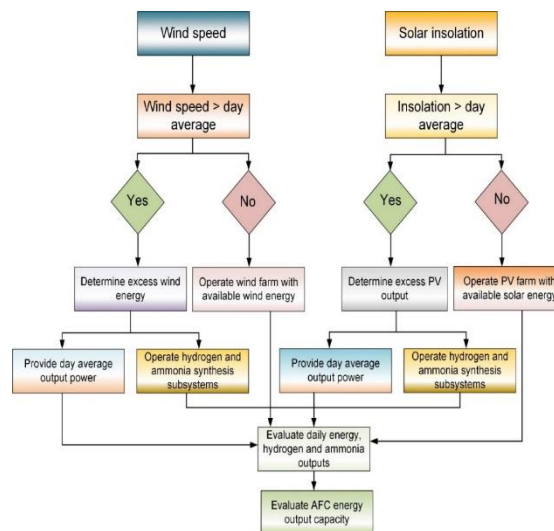


Fig. 5.1 Schematic representing the algorithm for system 1 modelling and analysis

Table 5.1 Input parameters utilized for modelling and analysis of system 1

Parameter	Value
Geographical latitude	43.6532 (Toronto)
PV Cell type	Poly-Si-CSX-310 (Canadian Solar)
PV unit capacity	0.31 kW
Frame area	1.918 m ²
Total PV cell area	1500000 m ²
Number of PV cells	782065
PV Capital cost	3200 \dot{W}_{PV}
Wind turbine type	Vestas V82
Diameter	82 m
Swept area	5281 m ²
Number of wind turbines	170
Wind turbine capital cost	2500 \dot{W}_{WT}
Type of water splitting	Proton conducting electrolyte based
Membrane thickness	100 μm
PEM temperature	30°C
PEM pre-exponential factors	Anodic: $1.7 \times 10^5 \text{ A/m}^2$ Cathodic: $4.6 \times 10^3 \text{ A/m}^2$
Faraday's constant	96485 C/mol
PEM operating pressure	101 kPa
PEM capital cost	1000 \dot{W}_{PEM}
Electrode area	6.4 m ²
Gas constant	8.314 kJ/kmol K
PEM capital cost	1000 \dot{W}_{PEM}
ASR reactor type	Gibbs reactor
ASR operating pressure	15000 kPa
ASR operating temperature	250°C
ASR capital cost	304054 \dot{N}_{NH_3}
Minimum refrigerant temperature	-4.89 °C
Minimum refrigerant pressure	244 kPa
Compressor isentropic efficiency	85%
Reactant inlet molar ratio	3 H ₂ :1 N ₂
Ammonia fuel cell type	Anion exchange membrane electrolyte based
Operating temperature	25°C
Operating pressure	101 kPa
Limiting current density	73 A/m ²
Exchange current density	0.0028 A/m ²

Sources: Refs. [81-85]

5.2 System 2

This chapter describes the analysis of system 2 and associated subsystems included. The solar tower-based concentrated solar thermal system is utilized that comprises of heliostat mirrors reflecting incoming solar radiation unto a central tower that receives and transmits the incoming thermal energy to the circulating molten salt. The analysis of this subsystem as well as the reheat Rankine cycle is described in this chapter. The analysis of the integrated electrochemical ammonia synthesis and fuel cell system is discussed. The operational algorithm implemented for the developed system is also elucidated.

5.2.1 Solar and wind-based power generation

In case of the solar tower-based power generation technique utilized in systems 2 and 3, different types of heat losses are considered. Firstly, as the incoming solar radiation is reflected by the heliostat field to reach the receiver, it is accompanied with energy losses. The ratio of the total reflected and incident solar radiation is denoted by the heliostat efficiency (η_{hf}). The total solar energy reaching the receiver per unit time is thus evaluated as

$$\dot{Q}_{sr,rec} = \dot{I}_{bm} A_{sr,tot} \eta_{hf} \quad (5.90)$$

The central receiver also entails several energy losses that need to be accounted. The convective rate of heat loss associated with the receiver is evaluated from the coefficient of convective heat transfer ($h_{con,rec}$), area of the receiver (A_{rec}), receiver temperature T_{rec} and ambient temperature (T_0) as

$$\dot{Q}_{l,con,rec} = h_{con,rec} A_{rec} (T_{rec} - T_0) \quad (5.91)$$

Radiation heat losses associated with the central receiver are evaluated from the Stefan-Boltzmann constant (σ_{sb}), emissivity of the receiver (ϵ_{rec}), receiver area (A_{rec}), receiver temperature (T_{rec}) and ambient temperature (T_0) as

$$\dot{Q}_{l,rad,rec} = \sigma_{sb} \epsilon_{rec} A_{rec} (T_{rec}^4 - T_0^4) \quad (5.92)$$

The thermal energy absorbed by the molten salt is utilized for power generation via a reheat Rankine cycle. The rate of thermal energy absorption entailed by the molten salt in the central receiver is evaluated as

$$\dot{Q}_{abs,ms} = \dot{Q}_{sr,rec} - \dot{Q}_{l,con,rec} - \dot{Q}_{l,rad,rec} \quad (5.93)$$

The thermal energy absorption rate associated with the molten salt in system 2 is expressed as

$$\dot{Q}_{abs,ms} = \dot{m}_{18}h_{18} - \dot{m}_{17}h_{17} \quad (5.94)$$

Next, the central receiver is analysed through entropy and exergy analyses according to

$$\int_{t_0}^{t_{ST}} \dot{m}_{17}s_{17}dt + \int_{t_0}^{t_{ST}} \frac{\dot{Q}_{sr,rec}}{T_{rec}} dt + \int_{t_0}^{t_{ST}} \dot{S}_{gen,ST} dt = \int_{t_0}^{t_{ST}} \dot{m}_{18}s_{18}dt + \int_{t_0}^{t_{ST}} \frac{\dot{Q}_{l,con,rec}}{T_{rec}} dt + \int_{t_0}^{t_{ST}} \frac{\dot{Q}_{l,rad,rec}}{T_{rec}} dt \quad (5.95)$$

$$\int_{t_0}^{t_{ST}} \dot{m}_{17}ex_{17}dt + \int_{t_0}^{t_{ST}} \dot{E}x\dot{Q}_{sr,rec} dt = \int_{t_0}^{t_{ST}} \dot{E}x\dot{Q}_{l,con,rec} dt + \int_{t_0}^{t_{ST}} \dot{E}x\dot{Q}_{l,rad,rec} dt + \int_{t_0}^{t_{ST}} \dot{m}_{18}ex_{18}dt + \int_{t_0}^{t_{ST}} \dot{E}x_{dest,ST} dt \quad (5.96)$$

where the rate of exergy associated with a heat transfer process is written as $\dot{E}x\dot{Q}$ and the rate of exergy destruction is denoted by $\dot{E}x_{dest}$. After leaving the central tower, the hot molten salt is delivered to the HT where depending on the available solar energy the salt is passed through HX1 to transfer thermal energy to the reheat Rankine cycle. The mass and energy balances are applied on HX1 on a particular day as

$$\int_{t_0}^{t_{HX1}} \dot{m}_{19} dt + \int_{t_0}^{t_{HX1}} \dot{m}_{22} dt + \int_{t_0}^{t_{HX1}} \dot{m}_{24} dt + \int_{t_0}^{t_{HX1}} \dot{m}_{26} dt = \int_{t_0}^{t_{HX1}} \dot{m}_{20} dt + \int_{t_0}^{t_{HX1}} \dot{m}_{23} dt + \int_{t_0}^{t_{HX1}} \dot{m}_{25} dt + \int_{t_0}^{t_{HX1}} \dot{m}_{27} dt \quad (5.97)$$

$$\int_{t_0}^{t_{HX1}} \dot{m}_{19}h_{19} dt + \int_{t_0}^{t_{HX1}} \dot{m}_{22}h_{22} dt + \int_{t_0}^{t_{HX1}} \dot{m}_{24}h_{24} dt + \int_{t_0}^{t_{HX1}} \dot{m}_{26}h_{26} dt = \int_{t_0}^{t_{HX1}} \dot{m}_{20}h_{20} dt + \int_{t_0}^{t_{HX1}} \dot{m}_{23}h_{23} dt + \int_{t_0}^{t_{HX1}} \dot{m}_{25}h_{25} dt + \int_{t_0}^{t_{HX1}} \dot{m}_{27}h_{27} dt + \int_{t_0}^{t_{HX1}} \dot{Q}_l dt \quad (5.98)$$

Next, HX1 is analysed via entropy and exergy balances according to

$$\begin{aligned}
& \int_{t_0}^{t_{HX1}} \dot{m}_{19} s_{19} dt + \int_{t_0}^{t_{HX1}} \dot{m}_{22} s_{22} dt + \int_{t_0}^{t_{HX1}} \dot{m}_{24} s_{24} dt + \int_{t_0}^{t_{HX1}} \dot{m}_{26} s_{26} dt + \\
& \int_{t_0}^{t_{HX1}} \dot{S}_{gen,HX1} dt = \int_{t_0}^{t_{HX1}} \dot{m}_{20} s_{20} dt + \int_{t_0}^{t_{HX1}} \dot{m}_{23} s_{23} dt + \int_{t_0}^{t_{HX1}} \dot{m}_{25} s_{25} dt + \\
& \int_{t_0}^{t_{HX1}} \dot{m}_{27} s_{27} dt + \int_{t_0}^{t_{HX1}} \frac{\dot{Q}_l}{T_b} dt
\end{aligned} \tag{5.99}$$

$$\begin{aligned}
& \int_{t_0}^{t_{HX1}} \dot{m}_{19} ex_{19} dt + \int_{t_0}^{t_{HX1}} \dot{m}_{22} ex_{22} dt + \int_{t_0}^{t_{HX1}} \dot{m}_{24} ex_{24} dt + \int_{t_0}^{t_{HX1}} \dot{m}_{26} ex_{26} dt = \\
& \int_{t_0}^{t_{HX1}} \dot{m}_{20} ex_{20} dt + \int_{t_0}^{t_{HX1}} \dot{m}_{23} ex_{23} dt + \int_{t_0}^{t_{HX1}} \dot{m}_{25} ex_{25} dt + \int_{t_0}^{t_{HX1}} \dot{m}_{27} ex_{27} dt + \\
& \int_{t_0}^{t_{HX1}} \dot{Q}_l \left(1 - \frac{T_0}{T_b}\right) dt + \int_{t_0}^{t_{HX1}} \dot{E}x_{dest,HX1} dt
\end{aligned} \tag{5.100}$$

Before entering HX1, water is pressurized to the high-pressure level of the cycle by P2 that raises the water pressure from the condenser pressure at state 21 to the high pressure at state 22. The mass and energetic balance for P2 is written as

$$\int_{t_0}^{t_{P2}} \dot{m}_{21} dt = \int_{t_0}^{t_{P2}} \dot{m}_{22} dt \tag{5.101}$$

$$\int_{t_0}^{t_{P2}} \dot{m}_{21} h_{21} dt + \int_{t_0}^{t_{P2}} \dot{W}_{P2} dt = \int_{t_0}^{t_{P2}} \dot{m}_{22} h_{22} dt \tag{5.102}$$

P2 is analysed via entropy and exergy balances as

$$\int_{t_0}^{t_{P2}} \dot{m}_{21} s_{21} dt + \int_{t_0}^{t_{P2}} \dot{S}_{gen,P2} dt = \int_{t_0}^{t_{P2}} \dot{m}_{22} s_{22} dt \tag{5.103}$$

$$\int_{t_0}^{t_{P2}} \dot{m}_{21} ex_{21} dt + \int_{t_0}^{t_{P2}} \dot{W}_{P2} dt = \int_{t_0}^{t_{P2}} \dot{m}_{22} ex_{22} dt + \int_{t_0}^{t_{P2}} \dot{E}x_{dest,P2} dt \tag{5.104}$$

The exit stream of HX1 is delivered to T1 for power generation, which analysed energetically as

$$\int_{t_0}^{t_{T1}} \dot{m}_{23} dt = \int_{t_0}^{t_{T1}} \dot{m}_{24} dt \tag{5.105}$$

$$\int_{t_0}^{t_{T1}} \dot{m}_{23} h_{23} dt = \int_{t_0}^{t_{T1}} \dot{m}_{24} h_{24} dt + \int_{t_0}^{t_{T1}} \dot{W}_{T1} dt \tag{5.106}$$

T1 is analysed through entropy and exergy analyses as follows:

$$\int_{t_0}^{t_{T1}} \dot{m}_{23} s_{23} dt + \int_{t_0}^{t_{T1}} \dot{S}_{gen,T1} dt = \int_{t_0}^{t_{T1}} \dot{m}_{24} s_{24} dt \tag{5.107}$$

$$\int_{t_0}^{t_{T1}} \dot{m}_{23} ex_{23} dt = \int_{t_0}^{t_{T1}} \dot{m}_{24} ex_{24} dt + \int_{t_0}^{t_{T1}} \dot{W}_{T1} dt + \int_{t_0}^{t_{T1}} \dot{E}x_{dest,T1} dt \tag{5.108}$$

After leaving T1, stream 24 is reheated prior to entering T2 at state 25. The exit stream of T2 at state 26 is reheated to state 27 before it delivered to T3. The thermodynamic analysis of T2 and T3 are performed similar to T1 as described earlier. After leaving T3 under saturated conditions, stream 28 is passed through the condenser for heat rejection. The waste heat rejected in the condenser is also utilized in the present system for space heating. The mass and energy balances applied on the condenser of system 2 are expressed as

$$\int_{t_0}^{t_{con}} \dot{m}_{28} dt = \int_{t_0}^{t_{con}} \dot{m}_{21} dt \quad (5.109)$$

$$\int_{t_0}^{t_{con}} \dot{m}_{28} h_{28} dt = \int_{t_0}^{t_{con}} \dot{m}_{21} h_{21} dt + \int_{t_0}^{t_{con}} \dot{Q}_l dt + \int_{t_0}^{t_{con}} \dot{Q}_{con} dt \quad (5.110)$$

System 2 condenser is analysed through the following entropy and exergy balances:

$$\int_{t_0}^{t_{con}} \dot{m}_{28} s_{28} dt + \int_{t_0}^{t_{con}} \dot{S}_{gen} dt = \int_{t_0}^{t_{con}} \dot{m}_{21} s_{21} dt + \int_{t_0}^{t_{con}} \frac{\dot{Q}_l}{T_b} dt + \int_{t_0}^{t_{con}} \frac{\dot{Q}_{con}}{T_b} dt \quad (5.111)$$

$$\int_{t_0}^{t_{con}} \dot{m}_{28} ex_{28} dt = \int_{t_0}^{t_{con}} \dot{m}_{21} ex_{21} dt + \int_{t_0}^{t_{con}} \dot{Q}_l \left(1 - \frac{T_0}{T_b}\right) dt + \int_{t_0}^{t_{con}} \dot{Q}_{con} \left(1 - \frac{T_0}{T_b}\right) dt + \int_{t_0}^{t_{con}} \dot{E}x_{dest,con} dt \quad (5.112)$$

The wind-based power generation subsystem is analysed similar to the procedure described in Section 5.1.1. The analysis details of the PEM water electrolysis and PSA air separation subsystems are discussed in Section 5.1.2 and 5.1.3.

5.2.2 Electrochemical synthesis of ammonia

The developed system utilizes an electrochemical ammonia synthesis (EAS) method that uses the alkaline molten salt from CT as the electrolyte. In the EAS subsystem, series of electrochemical reactions result in the production of ammonia via hydrogen and nitrogen. The nitrogen molecules are reduced at the cathode through the half-cell cathodic reaction expressed as



where nitrogen molecules are firstly dissociated into nitrogen atoms followed by electron acceptance and ion formation. The anions formed at the cathode reach the anode through

the molten salt electrolyte to react electrochemically with hydrogen molecules and form ammonia molecules according to the following anodic reaction:



The difference in electrical potential that is required to initiate and proceed the electrochemical reaction is obtained through an electrical power input. The overall ammonia synthesis reaction in the EAS can be denoted as



Next, the theoretical voltage input required for electrochemical synthesis of ammonia under no-load conditions is determined from

$$V_{EAS,oc} = \frac{-\Delta G^0}{nF} + \frac{T_{EAS}R}{nF} \ln\left(\frac{P_{NH_3}}{P_{N_2}^{\frac{1}{2}} P_{H_2}^{\frac{3}{2}}}\right) \quad (5.116)$$

where the Gibbs energy change under standard conditions is written as ΔG^0 , the pressure of produced ammonia is written as P_{NH_3} , the pressure of input nitrogen is denoted by P_{N_2} , the inlet pressure of hydrogen is denoted as P_{H_2} and the operating EAS temperature is represented as T_{EAS} . Several energy losses occur in the EAS during accompanying electrochemical processes. These are reflected through various voltage losses that occur in the electrochemical cells. The actual voltage of the EAS cell considering these losses can be written as

$$V_{EAS} = V_{EAS,oc} + V_{EAS,act} + V_{EAS,Ohm} + V_{EAS,conc} \quad (5.117)$$

where voltage losses during electrochemical ammonia synthesis under low operating currents due to charge transfer hindrances are denoted by $V_{EAS,act}$, which are evaluated as

$$V_{EAS,act} = \ln\left(\frac{J_{EAS}}{2J_{0,i}}\right) \frac{RT_{EAS}}{nF} \quad (5.118)$$

where the exchange current per unit area at either electrode is denoted as $J_{0,i}$ and the subscript i represents either the cathode ($i = c$) or anode ($i = a$).

Next, the losses in cell voltage owing to Ohmic resistances in the EAS are determined as described earlier. When the EAS current input is raised to considerably higher values, the

voltage losses occurring in the electrochemical cell due to mass transfer limitations become significant that are associated to the concentration polarization phenomenon. This type of electrochemical voltage loss in the EAS considering the cathodic reaction can be determined according to

$$V_{EAS,conc,c} = \ln\left[\left(1 + \frac{T_{EAS}\delta_c J_{EAS} R}{nF P_{N_2}^0 D_{N_2}^e}\right)^{\frac{1}{2}}\right] \frac{RT_{EAS}}{nF} \quad (5.119)$$

where the thickness of the cathode is denoted as δ_c , the effective diffusion coefficient of nitrogen is written as $D_{N_2}^e$ and the partial pressure of nitrogen is denoted as $P_{N_2}^0$. Similarly, the concentration polarization loss at the anode can be determined from

$$V_{EAS,conc,a} = \ln\left[\frac{1 + \frac{J_{EAS} RT_{EAS} \delta_a}{nF D_{NH_3}^e P_{H_2}^0}}{1 - \frac{J_{EAS} RT_{EAS} \delta_a}{nF D_{NH_3}^e P_{NH_3}^0}}\right] \frac{RT_{EAS}}{nF} \quad (5.120)$$

The molar rate of ammonia synthesis in the EAS subsystem is evaluated according to

$$\dot{N}_{NH_3,EAS} = \frac{J_{EAS} A_{EAS}}{nF} \eta_{c,EAS} \quad (5.121)$$

where the total electrode area in the EAS subsystem is denoted as A_{EAS} and the columbic efficiency is represented as $\eta_{c,EAS}$. The total power input supplied to the EAS is related to the actual voltage, current density as well as electrode area according to

$$\dot{W}_{i,EAS} = A_{EAS} V_{EAS} J_{EAS} \quad (5.122)$$

Considering system operation on a given day, the total energy input to the EAS is evaluated as

$$E_{i,EAS} = \int_{t_0}^{t_{EAS}} \dot{W}_{i,EAS} dt \quad (5.123)$$

The mass and energy analyses of the EAS subsystem are summarized as

$$\int_{t_0}^{t_{EAS}} \dot{m}_{13} dt = \int_{t_0}^{t_{EAS}} \dot{m}_{14} dt ; \int_{t_0}^{t_{EAS}} \dot{m}_7 dt + \int_{t_0}^{t_{EAS}} \dot{m}_{11} dt = \int_{t_0}^{t_{EAS}} \dot{m}_8 dt \quad (5.124)$$

$$\int_{t_0}^{t_{EAS}} \dot{m}_7 h_7 dt + \int_{t_0}^{t_{EAS}} \dot{m}_{11} h_{11} dt + \int_{t_0}^{t_{EAS}} \dot{m}_{13} h_{13} dt + \int_{t_0}^{t_{EAS}} \dot{W}_{i,EAS} dt = \int_{t_0}^{t_{EAS}} \dot{m}_8 h_8 dt + \int_{t_0}^{t_{EAS}} \dot{m}_{14} h_{14} dt \quad (5.125)$$

The entropy and exergy analyses of the EAS are summarized according to

$$\int_{t_0}^{t_{EAS}} \dot{m}_7 s_7 dt + \int_{t_0}^{t_{EAS}} \dot{m}_{11} s_{11} dt + \int_{t_0}^{t_{EAS}} \dot{m}_{13} s_{13} dt + \int_{t_0}^{t_{EAS}} \dot{S}_{gen,EAS} dt = \int_{t_0}^{t_{EAS}} \dot{m}_8 s_8 dt + \int_{t_0}^{t_{EAS}} \dot{m}_{14} s_{14} dt \quad (5.126)$$

$$\int_{t_0}^{t_{EAS}} \dot{m}_7 ex_7 dt + \int_{t_0}^{t_{EAS}} \dot{m}_{11} ex_{11} dt + \int_{t_0}^{t_{EAS}} \dot{m}_{13} ex_{13} dt + \int_{t_0}^{t_{EAS}} \dot{W}_{i,EAS} dt = \int_{t_0}^{t_{EAS}} \dot{m}_8 ex_8 dt + \int_{t_0}^{t_{EAS}} \dot{m}_{14} ex_{14} dt + \int_{t_0}^{t_{EAS}} \dot{E}x_{dest,EAS} dt \quad (5.127)$$

5.2.3 Molten alkaline electrolyte-based ammonia fuel cell subsystem

Once ammonia is synthesized, it is partially stored for electricity production to be pursued when solar intensities or wind speeds are not sufficient. The integrated ammonia synthesis and fuel cell system utilized in system 2 entails the usage of a molten salt electrolyte. The electrochemical reactions at separate electrodes as well as the overall ammonia oxidation reaction occurring in the molten alkaline electrolyte-based ammonia fuel cell (MEAFC) system are similar to the electrochemical reactions described earlier.

The rate of molar consumption of ammonia in the MEAFC is evaluated from the output current per unit area (J_{MEAFC}) as well as the total area of electrodes (A_{MEAFC}) according to

$$\dot{N}_{NH_3,MEAFC} = \frac{A_{MEAFC} J_{MEAFC}}{nF} \quad (5.128)$$

The output voltage from the MEAFC is dependent on the output current extracted per unit area and can be evaluated as

$$V_{MEAFC} = V_{MEAFC,oc} - V_{MEAFC,act} - V_{MEAFC,ohm} - V_{MEAFC,conc} \quad (5.129)$$

where $V_{MEAFC,oc}$ represents the open circuit voltage that can be evaluated for the MEAFC utilizing the Gibbs energy change as discussed earlier. The MEAFC also entails voltage losses due to concentration polarization that are evaluated from the limiting current per unit electrode area ($J_{L,MEAFC}$) according to

$$V_{MEAFC,conc} = \ln \left(\frac{J_{L,MEAFC}}{J_{L,MEAFC} - J_{MEAFC}} \right) \frac{T_{MEAFC} R}{\alpha n F} \quad (5.130)$$

The power output from the MEAFC subsystem is calculated from

$$\dot{W}_{MEAFC} = J_{MEAFC} V_{MEAFC} A_{MEAFC} \quad (5.131)$$

where the total area of electrodes is represented as $A_{ME AFC}$, power output is denoted as \dot{W}_{AFC} , the output voltage and current per unit area are expressed as V_{AFC} and J_{AFC} respectively. The amount of energy output capacity entailed with the ME AFC subsystem on a considered day is determined from

$$E_{tot,ME AFC} = \int_{t_0}^{t_{ME AFC}} \dot{W}_{ME AFC} dt \quad (5.132)$$

The mass and energy balances are applied on the ME AFC subsystem according to the following equations:

$$\int_{t_0}^{t_{ME AFC}} \dot{m}_{14} dt = \int_{t_0}^{t_{ME AFC}} \dot{m}_{15} dt ; \int_{t_0}^{t_{ME AFC}} \dot{m}_{30} dt + \int_{t_0}^{t_{ME AFC}} \dot{m}_{10} dt = \int_{t_0}^{t_{ME AFC}} \dot{m}_{31} dt \quad (5.133)$$

$$\int_{t_0}^{t_{ME AFC}} \dot{m}_{14} h_{14} dt + \int_{t_0}^{t_{ME AFC}} \dot{m}_{10} h_{10} dt + \int_{t_0}^{t_{ME AFC}} \dot{m}_{30} h_{30} dt = \int_{t_0}^{t_{ME AFC}} \dot{W}_{o,ME AFC} dt + \int_{t_0}^{t_{ME AFC}} \dot{Q}_{ME AFC} dt + \int_{t_0}^{t_{ME AFC}} \dot{m}_{15} h_{15} dt + \int_{t_0}^{t_{ME AFC}} \dot{m}_{31} h_{31} dt \quad (5.134)$$

The ME AFC subsystem is also analysed via entropy and exergy analyses according to

$$\int_{t_0}^{t_{ME AFC}} \dot{m}_{14} s_{14} dt + \int_{t_0}^{t_{ME AFC}} \dot{m}_{10} s_{10} dt + \int_{t_0}^{t_{ME AFC}} \dot{m}_{30} s_{30} dt + \int_{t_0}^{t_{ME AFC}} \dot{S}_{gen} dt = \int_{t_0}^{t_{ME AFC}} \dot{m}_{15} s_{15} dt + \int_{t_0}^{t_{ME AFC}} \dot{m}_{31} s_{31} dt + \int_{t_0}^{t_{ME AFC}} \dot{Q}_{AFC} \left(1 - \frac{T_0}{T_b}\right) dt \quad (5.135)$$

$$\int_{t_0}^{t_{ME AFC}} \dot{m}_{14} ex_{14} dt + \int_{t_0}^{t_{ME AFC}} \dot{m}_{10} ex_{10} dt + \int_{t_0}^{t_{ME AFC}} \dot{m}_{30} ex_{30} dt = \int_{t_0}^{t_{ME AFC}} \dot{m}_{15} ex_{15} dt + \int_{t_0}^{t_{ME AFC}} \dot{m}_{31} ex_{31} dt + \int_{t_0}^{t_{ME AFC}} \dot{Q}_{AFC} \left(1 - \frac{T_0}{T_{AFC}}\right) dt + \int_{t_0}^{t_{ME AFC}} \dot{W}_{AFC} dt + \int_{t_0}^{t_{ME AFC}} \dot{E}x_{dest,AFC} dt \quad (5.136)$$

The parameters utilized for the analysis and modelling of system 2 and associated subsystems are listed in Table 5.2.

5.2.4 Algorithm for system 2 modelling and analysis

The algorithm implemented for system 2 analysis is depicted in Fig. 5.2. The available wind speeds as well as solar insolation are firstly compared to the daily average values. When the wind speed exceeds the daily average, the excess wind electricity produced is utilized to operate the electrochemical hydrogen and ammonia synthesis systems. The power input provided to each subsystem from the excess wind electricity is a function of their respective unit power inputs.

When the wind speed entails a lower value than the average value for the day, the wind farm is operated only for generation of electrical power. When the solar insolation exceeds the average value of the day, the excess thermal energy absorbed by the molten salt is stored for later usage. The amount of molten salt delivered to provide thermal energy to the reheat Rankine results in the power generation corresponding to the daily average value.

When the solar intensity is lower than the daily average value, the solar-based power generation cycle is operated with the available solar energy. Next, for the considered monthly average days, the total amounts of electricity, hydrogen, ammonia and heating outputs are evaluated. The energy discharge capacities of the TES as well as the MEAFC subsystems are also evaluated to assess the overall system performance. The total production of these useful commodities on the considered days is utilized along with the total inputs of solar and wind energy to determine the overall energetic as well as exergetic efficiency of the developed system. The operational algorithm provides an effective way of producing sufficient quantities of different useful commodities and thus attaining higher overall efficiencies.

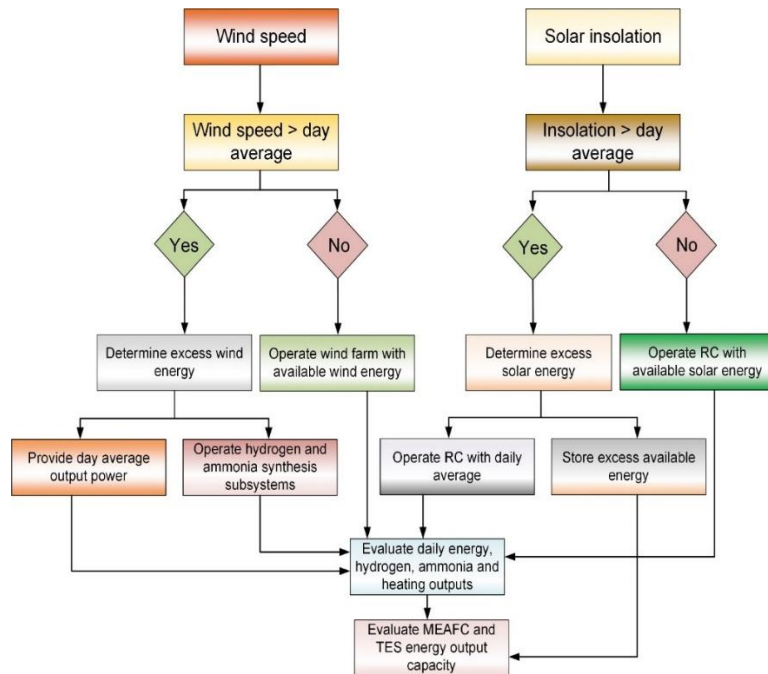


Fig. 5.2 Schematic representing the algorithm for system 2 modelling and analysis

Table 5.2 Input parameters utilized for modelling and analysis of system 2

Parameter	Value
Geographical latitude	43.6532 (Toronto)
Dimensions of heliostat	11 m x 11 m
Number of heliostats	4959
Capital cost of heliostat field	150 A_{hf}
First stage steam turbine inlet pressure	15000 kPa
Second stage steam turbine inlet pressure	5000 kPa
Third stage steam turbine inlet pressure	1000 kPa
Capital cost of steam turbine	6000 $(\dot{W}_T)^{0.7}$
Condenser pressure	10 kPa
Receiver temperature	1000°C
Receiver emissivity	0.88
Capital cost of receiver	$A_{rec} (79 T_{rec} - 42000)$
TES efficiency	95%
TES capital cost	40.7 Q_{TES}
Isentropic efficiency of pump and turbines	85%
Wind turbine type	Vestas V82
Diameter	82 m
Swept area	5281 m ²
Number of wind turbines	110
Wind turbine power coefficient	0.49
Wind turbine capital cost	2500 \dot{W}_{WT}
Molten salt for EAS and MEAFC	NaOH+KOH
Salt mole ratio	1:1
EAS limiting current density	21000 A/m ²
EAS capital cost	8400000 \dot{N}_{NH_3}
EAS exchange current density	0.37 A/m ²
MEAFC limiting current density	22 A/m ²
Type of water splitting	Proton exchange membrane
Gas constant	8.314 kJ/kmol K
Operating pressure	101 kPa
Faraday's constant	96485 C/mol
PEM pre-exponential factors	1.7 × 10 ⁵ A/m ² for anode 4.6 × 10 ³ A/m ² for cathode
PEM temperature	50°C
Membrane thickness	100×10 ⁻⁶ m
PEM capital cost	1000 \dot{W}_{PEM}

Source: Refs. [91-95]

5.3 System 3

This section describes the analysis of system 3 and associated subsystems. The ammonia synthesis as well as dissociation subsystems analysed in conjunction with waste heat recovery methods are described. The thermodynamic analysis of different system components performed is also discussed. System 3 operational algorithm utilized for modelling and analysis is also discussed.

5.3.1 Solar and wind-based power generation

The solar tower-based concentrating solar technique is utilized in system 3 that comprises of heliostat mirrors reflecting incident solar radiation unto a central tower receiver. The analysis of the solar tower is performed similar to the procedure described in Section 5.1.1. Depending on the available solar energy, the molten salt absorbing the incoming solar radiation is delivered to HX1 where thermal energy is delivered to the three-stage reheat Rankine cycle. The mass and energy analyses of HX1 utilized in system 3 is summarized as follows:

$$\int_{t_0}^{t_{HX1}} \dot{m}_{19} dt + \int_{t_0}^{t_{HX1}} \dot{m}_{23} dt + \int_{t_0}^{t_{HX1}} \dot{m}_{25} dt + \int_{t_0}^{t_{HX1}} \dot{m}_{27} dt = \int_{t_0}^{t_{HX1}} \dot{m}_{30} dt + \int_{t_0}^{t_{HX1}} \dot{m}_{24} dt + \int_{t_0}^{t_{HX1}} \dot{m}_{26} dt + \int_{t_0}^{t_{HX1}} \dot{m}_{28} dt \quad (5.137)$$

$$\int_{t_0}^{t_{HX1}} \dot{m}_{19} h_{19} dt + \int_{t_0}^{t_{HX1}} \dot{m}_{23} h_{23} dt + \int_{t_0}^{t_{HX1}} \dot{m}_{25} h_{25} dt + \int_{t_0}^{t_{HX1}} \dot{m}_{27} h_{27} dt = \int_{t_0}^{t_{HX1}} \dot{m}_{30} h_{30} dt + \int_{t_0}^{t_{HX1}} \dot{m}_{24} h_{24} dt + \int_{t_0}^{t_{HX1}} \dot{m}_{26} h_{26} dt + \int_{t_0}^{t_{HX1}} \dot{m}_{28} h_{28} dt + \int_{t_0}^{t_{HX1}} \dot{Q}_l dt \quad (5.138)$$

The entropy and exergy analyses of HX1 is summarized as

$$\int_{t_0}^{t_{HX1}} \dot{m}_{19} s_{19} dt + \int_{t_0}^{t_{HX1}} \dot{m}_{23} s_{23} dt + \int_{t_0}^{t_{HX1}} \dot{m}_{25} s_{25} dt + \int_{t_0}^{t_{HX1}} \dot{m}_{27} s_{27} dt + \int_{t_0}^{t_{HX1}} \dot{S}_{gen,HX1} dt = \int_{t_0}^{t_{HX1}} \dot{m}_{30} s_{30} dt + \int_{t_0}^{t_{HX1}} \dot{m}_{24} s_{24} dt + \int_{t_0}^{t_{HX1}} \dot{m}_{26} s_{26} dt + \int_{t_0}^{t_{HX1}} \dot{m}_{28} s_{28} dt + \int_{t_0}^{t_{HX1}} \frac{\dot{Q}_l}{T_b} dt \quad (5.139)$$

$$\begin{aligned}
& \int_{t_0}^{t_{HX1}} \dot{m}_{19} ex_{19} dt + \int_{t_0}^{t_{HX1}} \dot{m}_{23} ex_{23} dt + \int_{t_0}^{t_{HX1}} \dot{m}_{25} ex_{25} dt + \int_{t_0}^{t_{HX1}} \dot{m}_{27} ex_{27} dt = \\
& \int_{t_0}^{t_{HX1}} \dot{m}_{30} ex_{30} dt + \int_{t_0}^{t_{HX1}} \dot{m}_{24} ex_{24} dt + \int_{t_0}^{t_{HX1}} \dot{m}_{26} ex_{26} dt + \int_{t_0}^{t_{HX1}} \dot{m}_{28} ex_{28} dt + \\
& \int_{t_0}^{t_{HX1}} \dot{Q}_l \left(1 - \frac{T_0}{T_b}\right) dt + \int_{t_0}^{t_{HX1}} \dot{E}x_{dest,HX1} dt
\end{aligned} \tag{5.140}$$

The superheated vapor generated at state 24 is delivered to T1, which constitutes the high-pressure turbine. The mass and energy balances applied on T1 can be summarized as

$$\int_{t_0}^{t_{T1}} \dot{m}_{24} dt = \int_{t_0}^{t_{T1}} \dot{m}_{25} dt \tag{5.141}$$

$$\int_{t_0}^{t_{T1}} \dot{m}_{24} h_{24} dt = \int_{t_0}^{t_{T1}} \dot{m}_{25} h_{25} dt + \int_{t_0}^{t_{T1}} \dot{W}_{T1} dt \tag{5.142}$$

The entropy as well as exergy analyses applied on T1 are summarized as

$$\int_{t_0}^{t_{T1}} \dot{m}_{24} s_{24} dt + \int_{t_0}^{t_{T1}} \dot{S}_{gen,T1} dt = \int_{t_0}^{t_{T1}} \dot{m}_{25} s_{25} dt \tag{5.143}$$

$$\int_{t_0}^{t_{T1}} \dot{m}_{24} ex_{24} dt = \int_{t_0}^{t_{T1}} \dot{m}_{25} ex_{25} dt + \int_{t_0}^{t_{T1}} \dot{W}_{T1} dt + \int_{t_0}^{t_{T1}} \dot{E}x_{dest,T1} dt \tag{5.144}$$

The thermodynamic analysis of the medium-pressure and low-pressure turbines are also performed similar to T1. At state 29, the saturated steam passes through the condenser that is analysed via mass and energy balances according to

$$\int_{t_0}^{t_{con}} \dot{m}_{29} dt = \int_{t_0}^{t_{con}} \dot{m}_{22} dt \tag{5.145}$$

$$\int_{t_0}^{t_{con}} \dot{m}_{29} h_{29} dt = \int_{t_0}^{t_{con}} \dot{m}_{22} h_{22} dt + \int_{t_0}^{t_{con}} \dot{Q}_l dt + \int_{t_0}^{t_{con}} \dot{Q}_{con} dt \tag{5.146}$$

System 2 condenser is analysed through the following entropy and exergy balances:

$$\int_{t_0}^{t_{con}} \dot{m}_{29} s_{29} dt + \int_{t_0}^{t_{con}} \dot{S}_{gen} dt = \int_{t_0}^{t_{con}} \dot{m}_{22} s_{22} dt + \int_{t_0}^{t_{con}} \frac{\dot{Q}_l}{T_b} dt + \int_{t_0}^{t_{con}} \frac{\dot{Q}_{con}}{T_b} dt \tag{5.147}$$

$$\begin{aligned}
& \int_{t_0}^{t_{con}} \dot{m}_{29} ex_{29} dt = \int_{t_0}^{t_{con}} \dot{m}_{22} ex_{22} dt + \int_{t_0}^{t_{con}} \dot{Q}_l \left(1 - \frac{T_0}{T_b}\right) dt + \int_{t_0}^{t_{con}} \dot{Q}_{con} \left(1 - \frac{T_0}{T_b}\right) dt + \\
& \int_{t_0}^{t_{con}} \dot{E}x_{dest,con} dt
\end{aligned} \tag{5.148}$$

Next, the analysis of the wind-based power generation is performed similar to the procedure described in Section 5.1.1.

5.3.2 Ammonia synthesis and dissociation subsystems

The analysis of hydrogen and nitrogen production subsystems were discussed earlier where electrochemical water splitting is utilized to produce hydrogen and selective adsorption of air is used for nitrogen generation. At state 7, the reactant mixture is delivered to the ASR for ammonia synthesis. The synthesis process is modelled in ASPEN Plus simulation software as described in Section 5.1.4. However, the thermal energy released by the ASR is recovered and delivered to the CT. The mass and energy balances of the ASR in system 3 are summarized as

$$\int_{t_0}^{t_{ASR}} \dot{m}_7 dt + \int_{t_0}^{t_{ASR}} \dot{m}_{10} dt + \int_{t_0}^{t_{ASR}} \dot{m}_{32} dt = \int_{t_0}^{t_{ASR}} \dot{m}_8 dt + \int_{t_0}^{t_{ASR}} \dot{m}_{31} dt \quad (5.149)$$

$$\int_{t_0}^{t_{ASR}} \dot{m}_7 h_7 dt + \int_{t_0}^{t_{ASR}} \dot{m}_{10} h_{10} dt + \int_{t_0}^{t_{ASR}} \dot{m}_{32} h_{32} dt = \int_{t_0}^{t_{ASR}} \dot{m}_8 h_8 dt + \int_{t_0}^{t_{ASR}} \dot{m}_{31} h_{31} dt \quad (5.150)$$

The ASR entropy and exergy balances are summarized as

$$\int_{t_0}^{t_{ASR}} \dot{m}_7 s_7 dt + \int_{t_0}^{t_{ASR}} \dot{m}_{10} s_{10} dt + \int_{t_0}^{t_{ASR}} \dot{m}_{32} s_{32} dt + \int_{t_0}^{t_{ASR}} \dot{S}_{gen,ASR} dt = \int_{t_0}^{t_{ASR}} \dot{m}_8 s_8 dt + \int_{t_0}^{t_{ASR}} \dot{m}_{31} s_{31} dt \quad (5.151)$$

$$\int_{t_0}^{t_{ASR}} \dot{m}_7 ex_7 dt + \int_{t_0}^{t_{ASR}} \dot{m}_{10} ex_{10} dt + \int_{t_0}^{t_{ASR}} \dot{m}_{32} ex_{32} dt = \int_{t_0}^{t_{ASR}} \dot{m}_8 ex_8 dt + \int_{t_0}^{t_{ASR}} \dot{m}_{31} ex_{31} dt + \int_{t_0}^{t_{ASR}} \dot{E}x_{dest,ASR} dt \quad (5.152)$$

System 3 utilizes the excess solar energy stored in HT to dissociate ammonia when required for power generation. The mass and energy balances on the ADR are applied according to

$$\int_{t_0}^{t_{ADR}} \dot{m}_{11} dt + \int_{t_0}^{t_{ADR}} \dot{m}_{33} dt = \int_{t_0}^{t_{ADR}} \dot{m}_{12} dt + \int_{t_0}^{t_{ADR}} \dot{m}_{34} dt \quad (5.153)$$

$$\int_{t_0}^{t_{ADR}} \dot{m}_{11} h_{11} dt + \int_{t_0}^{t_{ADR}} \dot{m}_{33} h_{33} dt = \int_{t_0}^{t_{ADR}} \dot{m}_{12} h_{12} dt + \int_{t_0}^{t_{ADR}} \dot{m}_{34} h_{34} dt \quad (5.154)$$

The entropy as well as exergy balances are applied on the ADR according to

$$\int_{t_0}^{t_{ADR}} \dot{m}_{11} s_{11} dt + \int_{t_0}^{t_{ADR}} \dot{m}_{33} s_{33} dt + \int_{t_0}^{t_{ADR}} \dot{S}_{gen} dt = \int_{t_0}^{t_{ADR}} \dot{m}_{12} dt + \int_{t_0}^{t_{ADR}} \dot{m}_{34} dt \quad (5.155)$$

$$\int_{t_0}^{t_{ADR}} \dot{m}_{11} ex_{11} dt + \int_{t_0}^{t_{ADR}} \dot{m}_{33} ex_{33} dt = \int_{t_0}^{t_{ADR}} \dot{m}_{12} ex_{12} dt + \int_{t_0}^{t_{ADR}} \dot{m}_{34} ex_{34} dt + \int_{t_0}^{t_{ADR}} \dot{E} x_{dest,ADR} dt \quad (5.156)$$

Next, the electrochemical as well as thermodynamic analyses of the fuel cell subsystem is performed as described in Section 5.1.

5.3.3 Algorithm for system 3 modelling and analysis

The algorithm implemented for system 3 analysis is depicted in Fig. 5.3. The incoming wind speeds as well as solar intensities are firstly compared with the daily average values. In case of excess availability of wind energy, the electrical power output obtained from the wind farm that is utilized as a useful output attains the daily average value. The excess electricity available is utilized to operate the hydrogen as well as ammonia synthesis subsystems. The thermal energy released during the exothermic ammonia synthesis reaction is delivered to the cold molten salt tank (CT).

This raises the temperature of CT and thus allows the usage of waste heat generated in the ASR to increase the amount of energy production entailed with the reheat Rankine cycle. However, when the wind speeds are lower than the daily average, the wind farm is utilized for electricity production. When the solar intensities are lower than daily average, power generation through available solar energy is considered. However, when solar intensities are higher than daily average, the excess available thermal energy is stored in the thermal energy storage system.

The hot tank (HT) of the energy storage system entails a high temperature and is thus suitable to be utilized for ammonia dissociation in the ADR. A portion of the produced ammonia is stored as an energy storage medium. During low solar or wind energy availability, the stored ammonia is utilized for clean electricity.

The ADR is employed to firstly dissociate ammonia molecules through the usage of excess solar energy stored in the HT followed by electrochemical energy production via the fuel cell (FC) subsystem.

Hence, for system analysis, the energy production capacity of the FC subsystem is evaluated considering the daily amount of ammonia stored. The corresponding energy input requirement of the ADR is determined based on the amount of ammonia to be dissociated. Considering the variations in the solar intensities as well as wind speeds on the monthly average days, the developed system is modelled and analysed through the algorithm discussed.

The developed system thus provides clean electricity, hydrogen, ammonia and heating via solar and wind energy resources. The waste heat recovery techniques utilized allow the usage of available waste heat from the ASR, which further results in higher amounts of power generation potentials from the energy storage system. The usage of excess solar thermal energy to dissociate ammonia when required for power generation allows effective usage of available high-temperature excess energy.

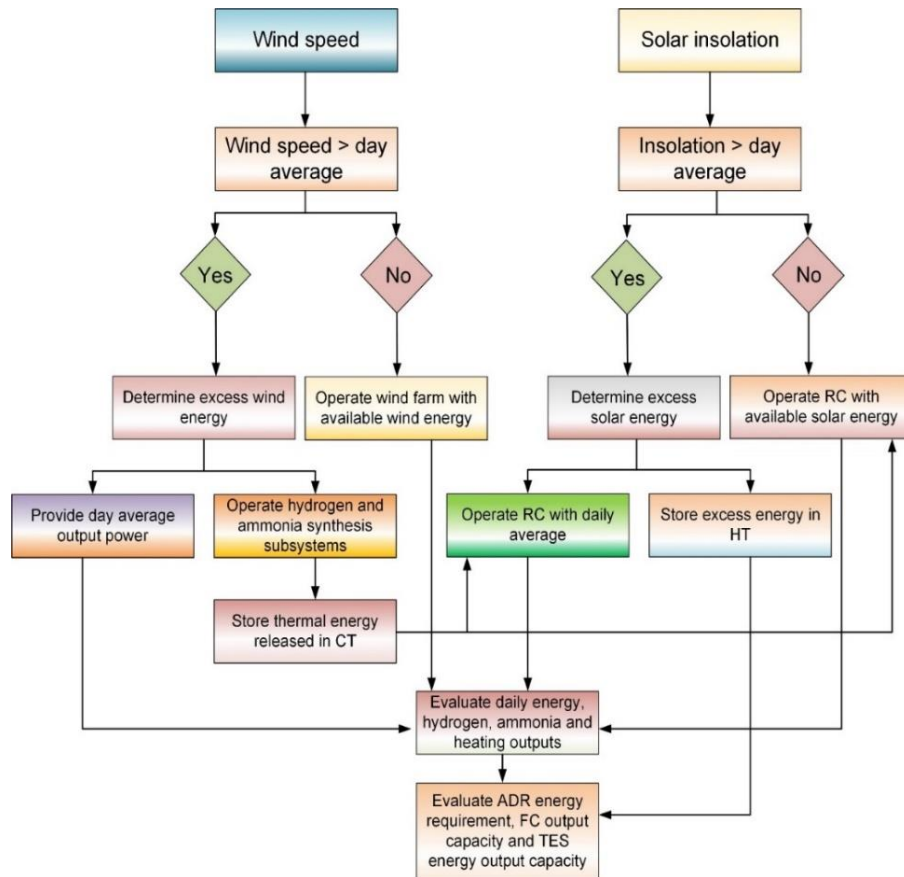


Fig. 5.3 Schematic representing the algorithm for system 3 modelling and analysis

Table 5.3 Input parameters utilized for modelling and analysis of system 3

Parameter	Value
Geographical latitude	43.6532 (Toronto)
Dimensions of heliostat	11 m × 11 m
Number of heliostats	4959
RC turbine inlet pressures	T1: 15000 kPa T2: 5000 kPa T3: 1000 kPa
Condenser pressure	10 kPa
Isentropic efficiency of pump and turbines	85%
Wind turbines used	Vestas V82
Swept area of single turbine	5281 m ²
Number of wind turbines	170
Diameter	82 m
Wind turbine power coefficient	0.49
Type of ADR	Gibbs Reactor
ADR operating pressure	1000 kPa
ADR operating temperature	500 °C
Membrane type for water splitting	Proton exchange membrane
Total PEM active area	6.43 m ²
PEM temperature	30°C
PEM operating pressure	101.3 kPa
Electrolysis electrode pre-exponential factors	1.7 × 10 ⁵ A/m ² for anode 4.6 × 10 ³ A/m ² for cathode
Type of ASR	Gibbs Reactor
ASR operating conditions	Temperature: 250°C Pressure: 10000 kPa
FC membrane type	Proton exchange membrane
Operating temperature	25°C

Source: Refs. [96-101]

5.4 System efficiencies

This chapter discusses the performance assessment of the developed systems. Firstly, the thermodynamic performance is assessed via both energy as well as exergy efficiencies. The efficiencies of the overall systems as well as major subsystems are evaluated. The energy efficiency of the hydrogen production subsystem is evaluated from

$$\eta_{en,PEM,H_2} = \frac{\int_{t_0}^{t_{PEM}} \dot{N}_{H_2,PEM} \overline{LHV}_{H_2} dt}{\int_{t_0}^{t_{PEM}} \dot{W}_{PEM,H_2,in} dt} \quad (5.157)$$

The exergy efficiency for the hydrogen production subsystem is denoted as

$$\eta_{ex,PEM,H_2} = \frac{\int_{t_0}^{t_{PEM}} \dot{N}_{H_2,PEM} \overline{ex}_{H_2} dt}{\int_{t_0}^{t_{PEM}} \dot{W}_{PEM,H_2,in} dt} \quad (5.158)$$

where $\dot{N}_{H_2,PEM}$ denotes the molar hydrogen production rate at a given input power value, \overline{LHV}_{H_2} represents the molar lower heating value of hydrogen, $\dot{W}_{PEM,H_2,in}$ represents the power input to the subsystem and \overline{ex}_{H_2} denotes the specific molar exergy of hydrogen.

The energy efficiency of the ammonia synthesis subsystem is denoted as

$$\eta_{en,ASR} = \frac{\int_{t_0}^{t_{ASR}} \dot{N}_{NH_3,ASR} \overline{LHV}_{NH_3} dt}{\int_{t_0}^{t_{ASR}} \dot{N}_{H_2} \overline{LHV}_{H_2} dt} \quad (5.159)$$

The ASR exergy efficiency is evaluated according to

$$\eta_{ex,ASR} = \frac{\int_{t_0}^{t_{ASR}} \dot{N}_{NH_3,ASR} \overline{ex}_{NH_3} dt}{\int_{t_0}^{t_{ASR}} \dot{N}_{H_2} \overline{ex}_{H_2} dt} \quad (5.160)$$

where $\dot{N}_{NH_3,ASR}$ represents the molar ammonia production rate in the ASR, \overline{LHV}_{NH_3} is the molar lower heating value of ammonia and \overline{ex}_{NH_3} denotes the molar specific exergy of ammonia.

The energy efficiency of electrochemical ammonia synthesis subsystem is determined according to

$$\eta_{en,EAS} = \frac{\int_{t_0}^{t_{EAS}} \dot{N}_{NH_3,EAS} \overline{LHV}_{NH_3} dt}{\int_{t_0}^{t_{EAS}} \dot{W}_{i,EAS} dt} \quad (5.161)$$

The EAS exergy efficiency is determined as

$$\eta_{ex,EAS} = \frac{\int_{t_0}^{t_{EAS}} \dot{N}_{NH_3,EAS} \overline{ex}_{NH_3} dt}{\int_{t_0}^{t_{EAS}} \dot{W}_{i,EAS} dt} \quad (5.162)$$

where the power input to the EAS at a specific operational point is written as $\dot{W}_{i,EAS}$ and the corresponding ammonia synthesis rate in the EAS is denoted as $\dot{N}_{NH_3,EAS}$. Next, the energetic performance of the ammonia fuel cell subsystem is determined according to

$$\eta_{en,AFC} = \frac{\int_{t_0}^{t_{AFC}} \dot{W}_{AFC} dt}{\int_{t_0}^{t_{AFC}} \dot{N}_{NH_3,AFC} \overline{LHV}_{NH_3} dt} \quad (5.163)$$

The exergetic performance of the ammonia fuel cell subsystem is evaluated as

$$\eta_{ex,AFC} = \frac{\int_{t_0}^{t_{AFC}} \dot{W}_{AFC} dt}{\int_{t_0}^{t_{AFC}} \dot{N}_{NH_3,AFC} \overline{ex}_{NH_3} dt} \quad (5.164)$$

where the power output from the subsystem is written as \dot{W}_{AFC} and the input ammonia flow rate is denoted as $\dot{N}_{NH_3,AFC}$.

The energetic as well as exergetic performance of the reheat power generation Rankine cycle in system 2 is denoted respectively as

$$\eta_{en,RC,S2} = \frac{\int_{t_0}^{t_{RC}} \eta_{gen} \dot{W}_{T1} dt + \int_{t_0}^{t_{RC}} \eta_{gen} \dot{W}_{T2} dt + \int_{t_0}^{t_{RC}} \eta_{gen} \dot{W}_{T3} dt + \int_{t_0}^{t_{RC}} \dot{Q}_h dt}{\int_{t_0}^{t_{RC}} \dot{m}_{23} (h_{23} - h_{22}) dt + \int_{t_0}^{t_{RC}} \dot{m}_{24} (h_{25} - h_{24}) dt + \int_{t_0}^{t_{RC}} \dot{m}_{26} (h_{27} - h_{26}) dt} \quad (5.165)$$

$$\eta_{ex,RC,S2} = \frac{\int_{t_0}^{t_{RC}} \eta_{gen} \dot{W}_{T1} dt + \int_{t_0}^{t_{RC}} \eta_{gen} \dot{W}_{T2} dt + \int_{t_0}^{t_{RC}} \eta_{gen} \dot{W}_{T3} dt + \int_{t_0}^{t_{RC}} \dot{Q}_h (1 - \frac{T_0}{T_b}) dt}{\int_{t_0}^{t_{RC}} \dot{m}_{23} (ex_{23} - ex_{22}) dt + \int_{t_0}^{t_{RC}} \dot{m}_{24} (ex_{25} - ex_{24}) dt + \int_{t_0}^{t_{RC}} \dot{m}_{26} (ex_{27} - ex_{26}) dt} \quad (5.166)$$

where the turbine power outputs are denoted as \dot{W}_T , the generator efficiencies are represented a η_{gen} , the heating output obtained from the system is written as \dot{Q}_h , \dot{m} represents the mass flow rates, h denotes specific enthalpies and ex represents specific exergies at the state points depicted in the schematic of the system described earlier.

Similarly, the energetic and exergetic performances of the reheat Rankine cycle entailed in system 3 are evaluated respectively as

$$\eta_{en,RC,S3} = \frac{\int_{t_0}^{t_{RC}} \eta_{gen} \dot{W}_{T1} dt + \int_{t_0}^{t_{RC}} \eta_{gen} \dot{W}_{T2} dt + \int_{t_0}^{t_{RC}} \eta_{gen} \dot{W}_{T3} dt + \int_{t_0}^{t_{RC}} \dot{Q}_h dt}{\int_{t_0}^{t_{RC}} \dot{m}_{23} (h_{24} - h_{23}) dt + \int_{t_0}^{t_{RC}} \dot{m}_{25} (h_{26} - h_{25}) dt + \int_{t_0}^{t_{RC}} \dot{m}_{27} (h_{28} - h_{27}) dt} \quad (5.167)$$

$$\eta_{ex,RC,S3} = \frac{\int_{t_0}^{t_{RC}} \eta_{gen} \dot{W}_{T1} dt + \int_{t_0}^{t_{RC}} \eta_{gen} \dot{W}_{T2} dt + \int_{t_0}^{t_{RC}} \eta_{gen} \dot{W}_{T3} dt + \int_{t_0}^{t_{RC}} \dot{Q}_h (1 - \frac{T_0}{T_b}) dt}{\int_{t_0}^{t_{RC}} \dot{m}_{23} (ex_{24} - ex_{23}) dt + \int_{t_0}^{t_{RC}} \dot{m}_{25} (ex_{26} - ex_{25}) dt + \int_{t_0}^{t_{RC}} \dot{m}_{27} (ex_{28} - ex_{27}) dt} \quad (5.168)$$

Next, the energetic and exergetic performance of the ammonia dissociation subsystem is determined according to

$$\eta_{en,ADR} = \frac{\int_{t_0}^{t_{ADR}} \dot{N}_{H_2,ADR} \overline{LHV}_{H_2} dt}{\int_{t_0}^{t_{ADR}} \dot{N}_{NH_3} \overline{LHV}_{NH_3} dt + \int_{t_0}^{t_{ADR}} \dot{Q}_{ADR} dt} \quad (5.169)$$

$$\eta_{ex,ADR} = \frac{\int_{t_0}^{t_{ADR}} \dot{N}_{H_2,ADR} \overline{ex}_{H_2} dt}{\int_{t_0}^{t_{ADR}} \dot{N}_{NH_3} \overline{ex}_{NH_3} dt + \int_{t_0}^{t_{ADR}} \dot{Q}_{ADR} \left(1 - \frac{T_0}{T_b}\right) dt} \quad (5.170)$$

The overall energy efficiency of system 1 is evaluated according to the following relation:

$$\eta_{en,ov,S1} = \frac{\text{Net electricity output} + (\text{H}_2 \text{ produced})(\text{Lower heating value of H}_2) + (\text{NH}_3 \text{ produced})(\text{Lower heating value of NH}_3)}{\text{Solar energy input} + \text{Wind energy input}} \quad (5.171)$$

$$\eta_{en,ov,S1} = \frac{\int_{t_0}^{t_{PV}} \dot{W}_{PV,o} dt + \int_{t_0}^{t_{wn}} \dot{W}_{wn,o} dt + \int_{t_0}^{t_{AFC}} \dot{W}_{AFC} dt + \int_{t_0}^{t_{PEM}} \dot{N}_{H_2,o} \overline{LHV}_{H_2} dt + \int_{t_0}^{t_{ASR}} \dot{N}_{NH_3,o} \overline{LHV}_{NH_3} dt}{\int_{t_0}^{t_{sol}} \dot{Q}_{sr,in} dt + \int_{t_0}^{t_{wn}} \dot{W}_{wn,in} dt} \quad (5.172)$$

The overall exergy efficiency of system 1 is expressed as

$$\eta_{ex,ov,S1} = \frac{\text{Net electricity output} + (\text{H}_2 \text{ produced})(\text{Specific exergy of H}_2) + (\text{NH}_3 \text{ produced})(\text{Specific exergy of NH}_3)}{\text{Solar exergy input} + \text{Wind exergy input}} \quad (5.173)$$

$$\eta_{ex,ov,S1} = \frac{\int_{t_0}^{t_{PV}} \dot{W}_{PV,o} dt + \int_{t_0}^{t_{wn}} \dot{W}_{wn,o} dt + \int_{t_0}^{t_{AFC}} \dot{W}_{AFC} dt + \int_{t_0}^{t_{PEM}} \dot{N}_{H_2,o} \overline{ex}_{H_2} dt + \int_{t_0}^{t_{ASR}} \dot{N}_{NH_3,o} \overline{ex}_{NH_3} dt}{\int_{t_0}^{t_{sol}} \dot{Q}_{sr,in} \left(1 - \frac{T_0}{T_s}\right) dt + \int_{t_0}^{t_{wn}} \dot{E}x_{wn,in} dt} \quad (5.174)$$

where $\dot{W}_{PV,o}$ denotes the electrical power output from the PV farm that is utilized as useful electrical output, $\dot{W}_{wn,o}$ represents the power output from the wind farm considered as useful electrical output, $\dot{N}_{H_2,o}$ denotes the molar output hydrogen rate from the system, $\dot{N}_{NH_3,o}$ represents the molar useful ammonia output rate, \dot{W}_{AFC} is the ammonia fuel cell power output, $\dot{Q}_{sr,in}$ is the solar energy input rate, $\dot{W}_{wn,in}$ denotes the wind energy input to the system per unit time, $\dot{E}x_{wn,in}$ represents the rate of exergy input to the system associated with incoming wind energy, T_0 represents the ambient temperature and T_s denotes the sun temperature.

The overall energy and exergy efficiencies of system 2 are evaluated respectively as follows:

$$\eta_{en,ov,S2} = \frac{\text{Net electricity output} + (\text{H}_2 \text{ produced})(\text{Lower heating value of H}_2) + (\text{NH}_3 \text{ produced})(\text{Lower heating value of NH}_3) + \text{Thermal energy output}}{\text{Solar energy input} + \text{Wind energy input}} \quad (5.175)$$

$$\eta_{en,ov,S2} = \frac{\int_{t_0}^{t_{RC}} \eta_{gen} \dot{W}_{T,tot} dt + \int_{t_0}^{t_{st}} \dot{Q}_{st} \eta_{RC} dt + \int_{t_0}^{t_{MEAFc}} \dot{W}_{MEAFc} dt + \int_{t_0}^{t_{wn}} \dot{W}_{wn,o} dt + \int_{t_0}^{t_{EAS}} \dot{N}_{NH_3,o} dt (\overline{LHV}_{NH_3}) + \int_{t_0}^{t_{PEM}} \dot{N}_{H_2,o} \overline{LHV}_{H_2} dt + \int_{t_0}^{t_{RC}} \dot{Q}_h dt}{\int_{t_0}^{t_{sol}} \dot{Q}_{sr,in} dt + \int_{t_0}^{t_{wn}} \dot{W}_{wn,in} dt} \quad (5.176)$$

$$\eta_{ex,ov,S2} = \frac{\text{Net electricity output} + (\text{NH}_3 \text{ produced})(\text{Specific exergy of NH}_3) + (\text{H}_2 \text{ produced})(\text{Specific exergy of H}_2) + \text{Thermal exergy output}}{\text{Solar exergy input} + \text{Wind exergy input}} \quad (5.177)$$

$$\eta_{ex,ov,S2} = \frac{\int_{t_0}^{t_{RC}} \eta_{gen} \dot{W}_{T,tot} dt + \int_{t_0}^{t_{st}} \dot{Q}_{st} \eta_{RC} dt + \int_{t_0}^{t_{MEAFc}} \dot{W}_{MEAFc} dt + \int_{t_0}^{t_{wn}} \dot{W}_{wn,o} dt + \int_{t_0}^{t_{EAS}} \dot{N}_{NH_3,o} dt (\overline{ex}_{NH_3}) + \int_{t_0}^{t_{PEM}} \dot{N}_{H_2,o} \overline{ex}_{H_2} dt + \int_{t_0}^{t_{RC}} \dot{Q}_h (1 - \frac{T_0}{T_b}) dt}{\int_{t_0}^{t_{sol}} \dot{Q}_{sr,in} (1 - \frac{T_0}{T_s}) dt + \int_{t_0}^{t_{wn}} \dot{E}x_{wn,in} dt} \quad (5.178)$$

where the total turbine power output ($\dot{W}_{T,tot}$) is denoted as

$$\dot{W}_{T,tot} = \dot{W}_{T1} + \dot{W}_{T2} + \dot{W}_{T3} \quad (5.179)$$

where \dot{Q}_{st} denotes the rate of thermal energy stored during excess solar intensities, \dot{W}_{MEAFc} represents the power output of the molten alkaline electrolyte-based ammonia fuel cell, $\dot{W}_{wn,o}$ is the useful electricity output obtained from the wind farm, $\dot{N}_{NH_3,o}$ denotes the molar rate of output ammonia from the system, $\dot{N}_{H_2,o}$ is the molar rate of hydrogen output obtained from the system, \dot{Q}_h represents the rate of waste heat recovered and utilized as a useful heating output during Rankine cycle operation, \overline{LHV}_{NH_3} is the molar lower heating value of ammonia, \overline{LHV}_{H_2} denotes the molar lower heating value of hydrogen and \overline{ex}_{NH_3} is the molar specific exergy of ammonia.

Next, the overall energy and exergy efficiencies of system 3 are evaluated respectively as

$$\eta_{en,ov,S3} = \frac{\text{Net electricity output} + (\text{NH}_3 \text{ produced})(\text{Lower heating value of NH}_3) + (\text{H}_2 \text{ produced})(\text{Lower heating value of H}_2) + \text{Thermal energy output}}{\text{Solar energy input} + \text{Wind energy input}}$$

(5.180)

$$\eta_{en,ov,S3} = \frac{\int_{t_0}^{t_{RC}} \eta_{gen} \dot{W}_{T,tot} dt + \int_{t_0}^{t_{wn}} \dot{W}_{wn,o} dt + \int_{t_0}^{t_{FC}} \dot{W}_{FC} dt + \int_{t_0}^{t_{st}} \dot{Q}_{st} \eta_{RC} dt + \int_{t_0}^{t_{ASR}} \dot{N}_{NH_3,o} (\overline{LHV}_{NH_3}) dt + \int_{t_0}^{t_{RC}} \dot{Q}_h dt + \int_{t_0}^{t_{PEM}} \dot{N}_{H_2,o} (\overline{LHV}_{H_2}) dt}{\int_{t_0}^{t_{sol}} \dot{Q}_{sr,in} dt + \int_{t_0}^{t_{wn}} \dot{W}_{wn,in} dt} \quad (5.181)$$

$$\eta_{ex,ov,S3} = \frac{\text{Net electricity output} + (\text{NH}_3 \text{ produced})(\text{Specific exergy of NH}_3) + (\text{H}_2 \text{ produced})(\text{Specific exergy of H}_2) + \text{Thermal exergy output}}{\text{Solar exergy input} + \text{Wind exergy input}} \quad (5.182)$$

$$\eta_{ex,ov,S3} = \frac{\int_{t_0}^{t_{RC}} \eta_{gen} \dot{W}_{T,tot} dt + \int_{t_0}^{t_{wn}} \dot{W}_{wn,o} dt + \int_{t_0}^{t_{FC}} \dot{W}_{FC} dt + \int_{t_0}^{t_{st}} \dot{Q}_{st} \eta_{RC} dt + \int_{t_0}^{t_{ASR}} \dot{N}_{NH_3,o} (\overline{ex}_{NH_3}) dt + \int_{t_0}^{t_{RC}} \dot{Q}_h (1 - \frac{T_0}{T_b}) dt + \int_{t_0}^{t_{PEM}} \dot{N}_{H_2,o} (\overline{ex}_{H_2}) dt}{\int_{t_0}^{t_{sol}} \dot{Q}_{sr,in} (1 - \frac{T_0}{T_s}) dt + \int_{t_0}^{t_{wn}} \dot{Ex}_{wn,in} dt} \quad (5.183)$$

where the excess solar power stored is denoted as \dot{Q}_{st} , the efficiency of the Rankine cycle is represented as η_{RC} , the lower heating value is represented as \overline{LHV} , the specific exergy is written as \overline{ex} , the total power output from the steam turbines is written as $\dot{W}_{T,tot}$, the electrical power output obtained from the wind farm is denoted as $\dot{W}_{wn,o}$, the solar energy input per unit time is written as $\dot{Q}_{sr,in}$, the fuel cell power output is denoted as \dot{W}_{FC} , the amount of ammonia used as useful output per unit time is denoted as $\dot{N}_{NH_3,o}$ and the amount of hydrogen used as useful output per unit time is written as $\dot{N}_{H_2,o}$.

5.5 Exergoeconomic analysis

The economic performance of the system is studied through exergoeconomic analysis, which integrates both exergetic and economic performance. The cost balance equation that is applied on each subsystem can be generalized as

$$\sum_i \dot{C}_j + \dot{C}_{Q,j} + \dot{Z}_j = \dot{C}_{w,j} + \sum_o \dot{C}_j \quad (5.178)$$

where the sum of the costs of exergy in all input streams is written as $\sum_i \dot{C}_j$, the sum of the exergy costs of outlet streams is $\sum_o \dot{C}_j$, the sum of the investment and operational as well as maintenance costs is written as \dot{Z}_j and the cost rates of exergy associated with heat and

work interactions are denoted as $\dot{C}_{Q,j}$ and $\dot{C}_{w,j}$ respectively. The cost rate of exergy associated with a given stream is determined as

$$\dot{C}_j = \dot{m}_j ex_j c_j \quad (5.179)$$

where \dot{m}_j is the rate of mass flow, ex_j is the specific exergy and c_j is the specific cost. \dot{Z}_j is determined from the total component cost (TCC) and number of operational hours (t_{oph}) as

$$\dot{Z}_j = \frac{TCC}{t_{oph}} \quad (5.180)$$

The capital investment cost (CC), operation and maintenance cost (ORM) and the factor of capital recovery (CR) can be used to determine TCC as

$$TCC = CR(CC + ORM) \quad (5.181)$$

CR can be found from the interest rate (ir) and the number of lifetime years (y) considered:

$$CR = \frac{(1+ir)^y i}{(1+ir)^y - 1} \quad (5.182)$$

The ORM is evaluated from the ratio of CC and ORM considered (R_{ORM}):

$$ORM = CCR_{ORM} \quad (5.183)$$

The exergy destruction cost rates ($\dot{C}_{Ex_d,j}$) are determined from the exergy destruction rate of each subsystem ($\dot{E}x_{dst,j}$) and the average specific exergy cost of fuel ($c_{F,j}$) for the subsystem as

$$\dot{C}_{Ex_d,j} = c_{F,j} \dot{E}x_{dst,j} \quad (5.184)$$

where $c_{F,j}$ is evaluated for each component according to

$$c_{F,j} = \frac{\dot{C}_{F,j}}{\dot{E}x_{F,j}} \quad (5.185)$$

The exergoeconomic performance of a given system component is analysed through the exergoeconomic factor ($f_{ex,j}$) as

$$f_{ex,j} = \frac{z_j}{z_j + \dot{c}_{Exd,j}} \quad (5.186)$$

5.6 Multi-objective optimization

As the system performance is dependent on several operating parameters as well as design conditions, it is important to perform a multi-objective optimization that allows the determination of operating conditions that would provide optimal system performance. The genetic algorithm-based multi-objective optimization is performed through the Matlab optimization toolbox. A stochastic technique is implemented in the optimization method that determines optimal points by imitating the evolutionary biological process. Populations of individuals constituting decision variables is utilized by the evolutionary algorithm to obtain optimal solutions. This type of optimization technique comprises of four different steps as depicted in Fig. 5.4.

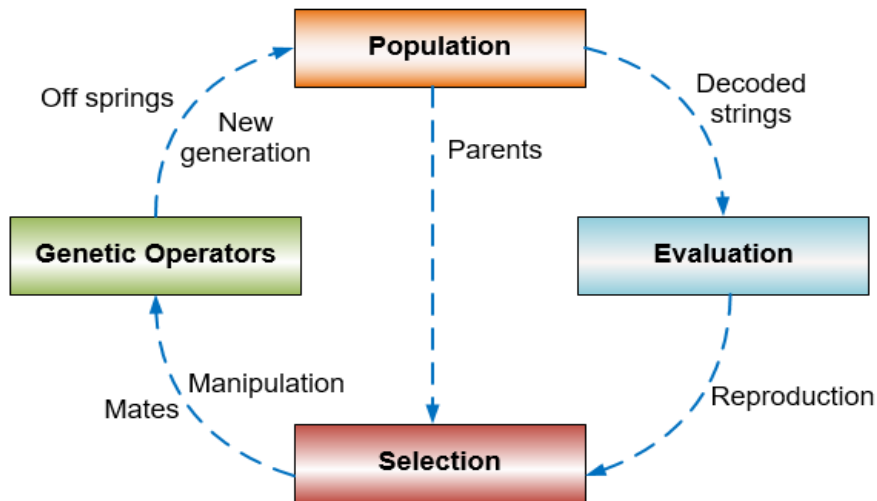


Fig. 5.4 Steps associated with a genetic algorithm cycle (Reproduced from [86])

A population string is generated. This is followed by individual string performance evaluation. Next, the string that entails the best performance is survived and taken to the next process step. New strings are generated through repetitive iterations. Further information about this type of evolutionary optimization technique is available elsewhere [86]. The optimal solutions are obtained in this study to maximize overall exergy efficiency and minimize total rate of system costs at different levels of high and low solar radiations and wind speeds.

The objective functions chosen for the optimization study are the overall exergetic efficiency and the total rate of cost of the system. The overall exergetic efficiencies for the developed systems were described in earlier sections. The exergy efficiency is chosen over the energy efficiency for the optimization study as exergy provides information about both the quality as well as the quantity of energy. On the other hand, the energy efficiency provides a ratio of the quantity of energy output and the required quantity of energy input. The total rate of costs for the overall systems are determined as

$$\dot{C}_{sys,tot} = \sum \dot{C}_{Exd,j} + \sum \dot{Z}_j \quad (5.187)$$

where $\dot{C}_{Exd,j}$ is the cost rate of exergy destruction of each system component and \dot{Z}_j is the summation of the investment, operation and maintenance costs. The decision variables considered in the optimization study of each system are provided in Tables 5.4-5.6. The upper and lower bounds of constraints considered for each decision variable are also listed. System optimization of each system is performed under different scenarios of solar intensity and wind speed combinations to better comprehend the optimal performances under different levels of energy inputs. The lower bound for the interest rate is chosen to be 5% while the upper bound is 20%. This range is chosen considering the variations in the interest rate across different economies, where the rate of interest is dependent on the economic situation as well as local legislations.

Table 5.4 Decision variables and associated constraints utilized for multi-objective optimization of system 1

	Lower bound	Upper bound
Total area of solar collectors (m ²)	1000000	2000000
Isentropic efficiency	0.65	0.85
PV panel efficiency	0.1	0.2
Wind turbine cross sectional area (m ²)	2000	10000
Interest rate (%)	5	20
AFC current density (A/m ²)	20	70
Ambient temperature (°C)	-20	30
AFC operating temperature (°C)	10	80
PEM operating temperature (°C)	10	80
Operational lifetime (years)	10	30

Table 5.5 Decision variables and associated constraints utilized for multi-objective optimization of system 2

	Lower bound	Upper bound
Heliostat area (m ²)	200000	1000000
Isentropic efficiency	0.65	0.85
Heliostat efficiency	0.65	0.8
Wind turbine cross sectional area (m ²)	2000	10000
Interest rate (%)	5	20
Ambient temperature (°C)	-20	30
MEAFC operating temperature (°C)	200	280
EAS operating temperature (°C)	200	280
PEM operating temperature (°C)	10	80
Operational lifetime (years)	10	30

Table 5.6 Decision variables and associated constraints utilized for multi-objective optimization of system 3

	Lower bound	Upper bound
Heliostat area (m ²)	200000	1000000
Isentropic efficiency	0.65	0.85
Heliostat efficiency	0.65	0.8
Wind turbine cross sectional area (m ²)	2000	10000
Interest rate (%)	5	20
Ambient temperature (°C)	-20	30
Turbine inlet pressure (kPa)	10000	20000
FC operating temperature (°C)	10	80
PEM operating temperature (°C)	10	80
Operational lifetime (years)	10	20

5.7 Scale-up analysis

The scaling factor (Y) for a given system parameter or variable (X) for chemical systems can be denoted in a general form as

$$Y_X = \frac{X_{FS}}{X_{PS}} \quad (5.188)$$

where the design variable or parameter under pilot or laboratory scale is written as X_{PS} and the variable at full scale is represented as X_{FS} . In the present study, a tubular reactor is utilized for the lab-scale experimental investigation. For such reactors, the combination of length and radius can be utilized to obtain the volumetric scaling factor according to:

$$Y_V = \frac{V_2}{V_1} = \left(\frac{R_2}{R_1}\right)^2 \left(\frac{L_2}{L_1}\right) = Y_R^2 Y_L \quad (5.189)$$

The scaling factor for the volumetric flow rate as well as the reactor radius can be utilized to express the ratio of linear velocities as

$$Y_u = \frac{u_2}{u_1} = \frac{\left(\frac{Q_1}{\pi R_1^2}\right)}{\left(\frac{Q_2}{\pi R_2^2}\right)} = Y_Q Y_R^{-2} \quad (5.190)$$

Next, the ratios of the capital costs of pilot scale and full-scale equipment can be expressed as follows [102]:

$$\frac{CC_2}{CC_1} = \left(\frac{A_2}{A_1}\right)^N \quad (5.191)$$

where the cost attribute of the required equipment size is denoted as A_2 , the cost attribute of the base size is represented as A_1 and CC denotes the capital cost. The superscript N represents the cost exponent that is dependent on the type of equipment considered. The equation can also be rewritten as

$$CC_2 = K A_2^N \quad (5.192)$$

where the parameter K is set as CC_1/A_1^N and the above equation is generally referred to as the six-tenths rule. In the present study, the experimental ammonia synthesis reactor as well as the direct ammonia fuel cell system developed are scaled up according to the required capacities corresponding to the designed solar and wind based multigeneration systems.

5.8 Experimental uncertainty analysis

Different devices utilized during the experimental investigation have associated accuracies that need to be accounted for to determine the uncertainties in the overall output results. The general correlation that can be utilized to obtain the uncertainty corresponding to a given evaluated variable can be written in terms of the specific uncorrelated and random measurement as:

$$U_y = \sqrt{\sum_i \left(\frac{\partial y}{\partial x}\right)^2 U_x^2} \quad (5.193)$$

The range of measurement as well as the accuracy of each experimental device utilized are provided in Table 5.7. The total uncertainty associated with an experimental investigation is a function of both the random error (R_e) and systematic error (S_e), which can be expressed according to

$$U_{ex} = \sqrt{R_{ex}^2 + S_{ex}^2} \quad (5.194)$$

Two important uncertainties that occur during experimentation and need to be accounted for include the systematic uncertainty and random uncertainty. Systematic uncertainty is denoted via relative and absolute bias error.

Next, the random uncertainty is expressed as relative precision error. Systematic uncertainties arise due to inaccuracies associated with experimental techniques or measurement instruments utilized in the system. The random uncertainties are linked to the variations in the conditions of experimentation.

Table 5.7 Measurement devices and corresponding ranges and accuracies

Device	Parameter	Measuring Range	Accuracy
Gamry Refeence 3000	Voltage	±32 Volts	±0.2%
Omega PPH103A pH Meter	pH	0-14 pH	0.02 pH
Omega FMA1700 Flowmeter (for ammonia)	Volume flow rate	0-500 SCCM	±1.5% of full scale, ±3% of full scale
Omega FMA-1600A Flowmeter (for nitrogen)	Volume flow rate	0-100 SCCM	±(0.8% of reading + 0.2% FS)
OM-DAQPRO-5300 Thermocouple K (for ammonia reactor)	Temperature	-250 to 1200°C	±0.5%
Omega FMA-1600A Flowmeter (for hydrogen)	Volume flow rate	0-100 SCCM	±(0.8% of reading + 0.2% FS)

Multiple reasons are attributed to errors or uncertainties in experimental investigation. These include resolution and accuracy of instruments, calibration, physical conditions and zero offset. To quantify the random errors arising during experimental measurements, the standard deviation is utilized that compares the uncertainties associated with multiple measurements of a parameter.

Table 5.8 List of the bias and precision errors of experimental equipment used

Device	Measurement Parameter	Ref. Value	Absolute Bias Error	Relative Bias Error (%)	Relative Precision Error (%)	U (%)
Gamry Reference 3000	Voltage	2 V	0.006 V	0.3	2.190	2.21
Omega PPH103A PH Meter	pH	7 pH	0.02 pH	0.2000	1.479	1.49
Omega FMA1700/1800 Flowmeter (for ammonia)	Volume flow rate	60 SCCM	0.9 SCCM	1.5000	1.321	2.00
Omega FMA-1600A Flowmeter (for nitrogen)	Volume flow rate	90 SCCM	0.72 SCCM	0.8000	1.145	1.40
OM-DAQPRO-5300 Thermocouple K (for ammonia reactor)	Temperature	400°C	2°C	0.5000	0.481	0.69
Omega FMA-1600A Flowmeter (for hydrogen)	Volume flow rate	30 SCCM	0.24 SCCM	0.8000	2.59	2.71

The standard deviation can be evaluated via each measurement in the set (y), statistical mean of each set (\bar{y}) and number of measurements (n):

$$\text{Standard Deviation} = \sqrt{\frac{\sum(y-\bar{y})^2}{(n-1)}} \quad (5.195)$$

Next, the relative standard deviation is evaluated from the standard deviation (s) and statistical mean (\bar{x}) as follows:

$$\text{Relative standard deviation} = \frac{s}{\bar{x}} \quad (5.196)$$

CHAPTER 6 : RESULTS AND DISCUSSION

This chapter presents the results of the experimental investigations as well modeling and simulation. The performances of each system developed are presented along with the corresponding subsystem assessments. The comparative assessments performed are also presented.

6.1 Experimental results

This section presents the experimental results obtained for both the ammonia synthesis as well as ammonia fuel cell systems. The experimental performance of both the iron oxide-catalyst based ammonia synthesis as well the multi-bed catalyst layer-based ammonia synthesis is presented. The performance of both anion exchange membrane and alkaline molten salt electrolyte-based direct ammonia fuel cell is discussed. The performances of a single ammonia fuel cell as well as a five cell stack under varying operating conditions are described.

6.1.1. Ammonia synthesis results

The results obtained for the ammonia synthesis subsystem investigated via the boric acid ammonia trap are given in Tables 6.1 and 6.2. Two different operating pressures of 800 kPa and 700 kPa are considered at a reaction temperature of 350°C. The amount of ammonia synthesized is evaluated via the titrimetric method from the total titrant volume needed to stabilize the final pH value to the initial reading.

The average titrant volume and the corresponding ammonia production at 800 kPa are found to be 11.2 ml and 0.224 mmol respectively. The results obtained for an operating pressure of 700 kPa are provided in Table 6.2. The average titrant volume and corresponding ammonia synthesis amounts evaluated at this pressure are 8.4 ml and 0.168 mmol respectively. The lower synthesis amount is attributed to the nature of the reversible exothermic ammonia synthesis process that favors the forward reaction under high pressures and the backward reaction under low reaction pressures.

Table 6.1 Ammonia synthesis results obtained via boric acid trap with single-bed iron-oxide based catalyst

Pressure (kPa)	Average initial pH	Average final pH	Average titrant volume (ml)	Average ammonia synthesis (mmol)
800	3.6±0.06	6.8±0.11	11.2±0.17	0.224±0.003
700	3.7±0.06	5.5±0.08	8.4±0.13	0.168±0.002

The results of nitrogen conversion obtained for these reaction pressures are depicted in Fig. 6.1. The nitrogen conversion percentage obtained at a reaction pressure of 800 kPa entails a value of 7.3% that is observed to be 4.7% lower than the nitrogen conversion percentage obtained via simulation results. The nitrogen conversion percentage evaluated at 800 kPa via simulation results considering the same reaction pressure and temperature in the Gibbs energy minimization technique is found to be 12%.

The difference observed can be attributed to the non-attainment of equilibrium in the experimental ammonia synthesis system. At a reaction pressure of 700 kPa, the nitrogen conversion percentage is observed to be 5.6% in experimental synthesis. This entails a difference of 5.1% as compared to the simulation value of 10.7%. The lower nitrogen conversion at a lower synthesis pressure is attributed to the backward reaction favored at lower synthesis pressures. The nitrogen conversion can be increased by raising the residence time of reactants in the reactor or utilizing higher activity synthesis catalysts. The energetic and exergetic performance of the ammonia synthesis process is investigated through thermodynamic energy and exergy efficiencies.

The comparison of energy and exergy efficiencies for the reaction pressure of 800 kPa are depicted in Fig. 6.2 and compared with the corresponding efficiencies evaluated for simulation results. The experimental energy efficiency evaluated at 800 kPa entails a value of 6.5%. As simulation results correspond to the equilibrium efficiencies, they are found to be higher than the experimental values.

The experimental exergy efficiency found for the reaction pressure of 800 kPa entails a value of 7.1%. The corresponding exergy efficiency obtained via simulation results is 11.7%. The higher exergetic efficiency value obtained for the ammonia synthesis

subsystem as compared to the energetic efficiency can be attributed to the differences in the specific chemical exergies and lower heating values of ammonia and hydrogen.

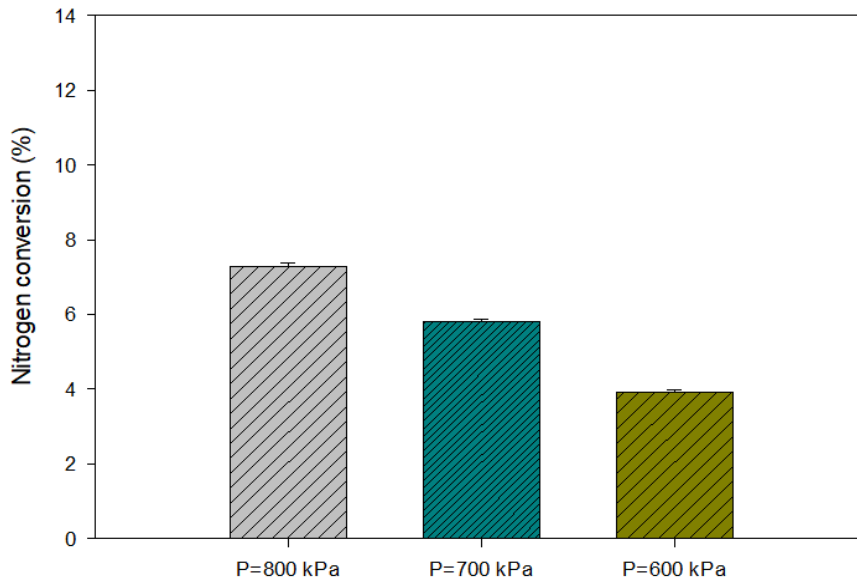


Fig. 6.1 Comparison of nitrogen conversion in the ammonia synthesis reactor at an operating pressure of 800 kPa and 700 kPa

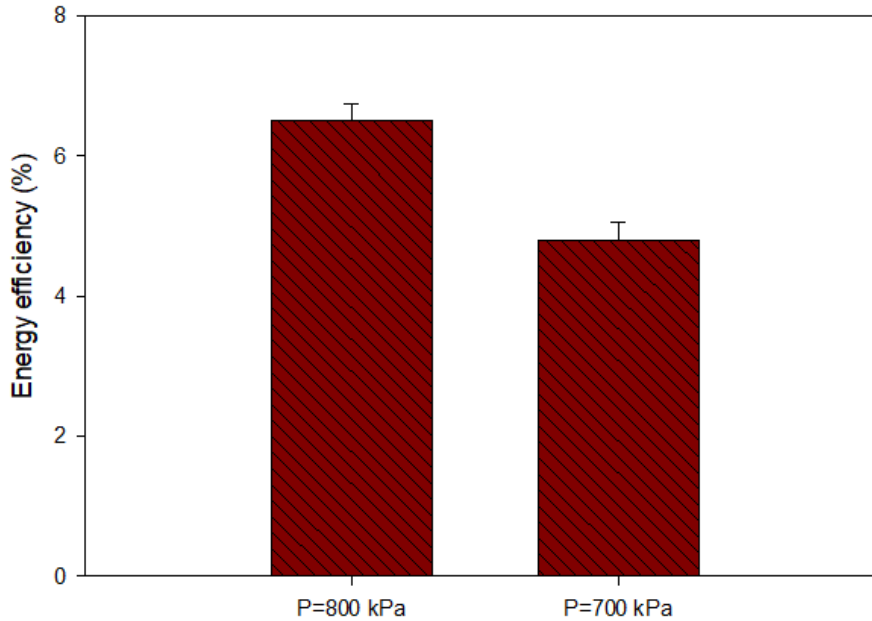


Fig. 6.2 Comparison of energy efficiencies at operating pressures of 800 kPa and 700 kPa
The specific chemical exergy of ammonia, for instance, entails a higher value than the lower heating value. However, hydrogen entails a lower specific exergy than the lower

heating value. The efficiency results obtained for a synthesis pressure of 700 kPa are depicted in Fig. 6.3.

The energy and exergy efficiencies obtained experimentally for the ammonia synthesis subsystem at this pressure are 4.8% and 5.3% respectively. The comparatively lower efficiencies obtained at a pressure of 700 kPa can be attributed to the lower nitrogen conversion at this pressure as compared to 800 kPa. However, these efficiencies correspond to the absence of the recycling. Nevertheless, the unreacted gases can be recycled by separating the ammonia synthesized.

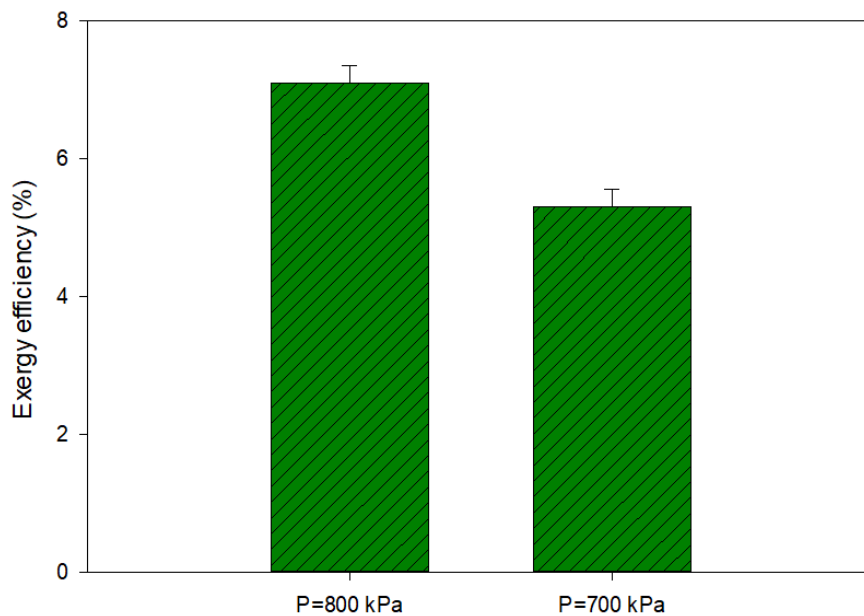


Fig. 6.3 Comparison of exergy efficiencies at operating pressures of 800 kPa and 700 kPa

The performance of the ammonia synthesis subsystem in terms of the energy and exergy efficiencies considering the reaction efficiencies is depicted in Fig. 6.4. The energy efficiency is found to be 86.8% and the exergy efficiency entails a value of 95.4%. These efficiencies correspond to the ratios of the energy and exergy outputs and the corresponding energy and exergy inputs consumed. As can be observed, there exists a considerable difference between the efficiencies obtained without considering recycling of unreacted gases and with complete usage of reactants.

In the solar and wind based multigeneration systems that are developed in the present study, the recycling of unreacted gases is considered. This is attained through ammonia

condensation followed by separation from unreacted hydrogen and nitrogen gases. In the present study, a new multi-bed catalyst reactor is developed to attain higher conversion ratios and thus higher energetic as well as exergetic efficiencies.

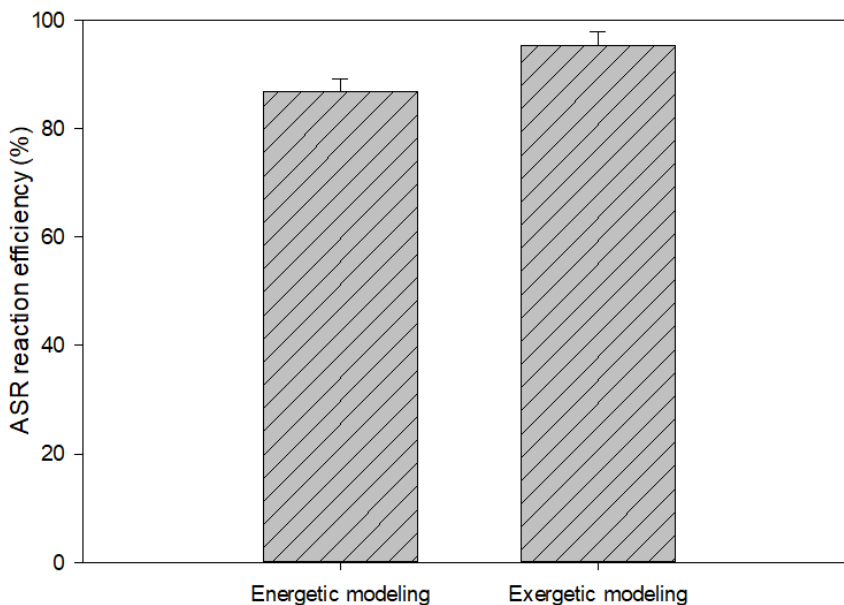


Fig. 6.4 Ammonia synthesis reaction energy and exergy efficiencies

The ammonia synthesis results obtained for the multi-bed catalyst reactor through the titrimetric method are summarized in Table 6.3. At a pressure of 700 kPa, the required titrant volume to attain the initial pH entails a value of 11.1 ml, which corresponds to an ammonia synthesis amount of 0.222 mmol.

This corresponds to an increase of 32.1% as compared to the single conventional catalyst reactor. At 800 kPa, the required titrant volume entails a value of 15.7 ml corresponding to an ammonia synthesis amount of 0.314 mmol. This corresponds to a rise of 40.2% as compared to the results obtained for conventional single catalyst reactor described earlier.

Table 6.2 Ammonia synthesis results obtained via boric acid trap at operating pressures of 700 kPa and 800 kPa with the multi-bed catalyst reactor

Pressure (kPa)	Initial pH	Final pH	Titrant volume (ml)	Ammonia synthesis (mmol)
700	3.7±0.06	7.7±0.12	11.1±0.17	0.222±0.003
800	3.7±0.06	8.9±0.13	15.7±0.24	0.314±0.005

The results of nitrogen conversion obtained for the multi-bed catalyst reactor at 800 kPa are depicted in Fig. 6.5. A nitrogen conversion of 10.2% is obtained that is higher than the conventional single catalyst reactor, which entails a nitrogen conversion of 7.3%. The multi-bed catalyst reactor is also found to entail a lower difference as compared to the conversion ratio obtained from the Gibbs energy minimization method.

The nitrogen conversion obtained at 700 kPa is 7.8% that also entails an increase in the conversion as compared to the single conventional catalyst reactor. Hence, the developed multi-bed catalyst reactor provides an effective method to attain higher yields of ammonia through the usage of a combination of both low and high cost catalysts. The catalysts utilized in the present study comprising of iron oxide magnetite as well as wustite, and ruthenium on activated carbon entail compatibility in terms of operational methods utilized during ammonia synthesis.

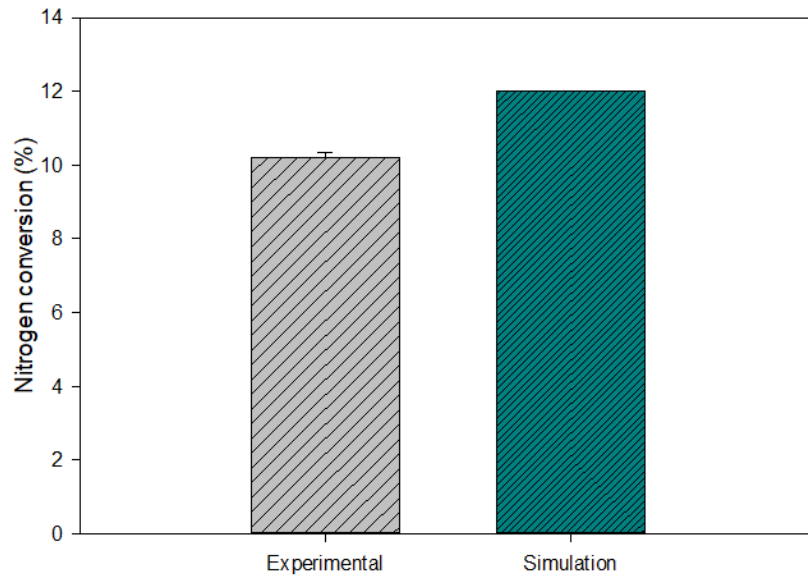


Fig. 6.5 Comparison of nitrogen conversion in the ammonia synthesis reactor at an operating pressure of 800 kPa

The energy and exergy efficiencies of the multi-bed reactor obtained at 800 kPa are depicted in Fig. 6.6. As can be observed, the efficiencies entail higher proximity to the efficiencies obtained via Gibbs energy minimization as compared to the single catalyst bed reactor. The experimental energy efficiency, for instance, is found to be 9.1% and the exergy efficiency entails a value of 9.9% that are in closer proximity to the simulation

values of 10.7% and 11.7% respectively. These efficiency values correspond to the absence of recycling of unreacted hydrogen and nitrogen.

The reaction efficiency considering the amount of ammonia formed and the corresponding amount of hydrogen consumed, an energetic performance of 86.8% and an exergetic performance of 95.4% is attained. Hence, as discussed earlier, recycling of unreacted gases entails significance in ammonia synthesis systems.

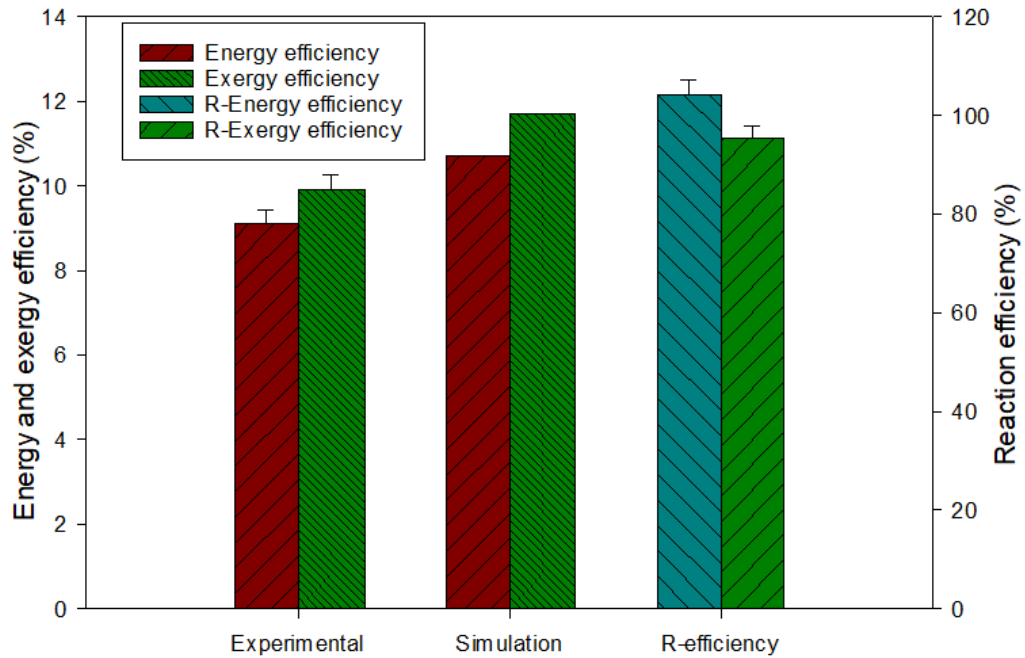


Fig. 6.6 Comparison of energy and exergy efficiencies at an operating pressure of 800 kPa

The energetic efficiency obtained at a pressure of 700 kPa entails a value of 6.7% as shown in Fig. 6.7. This entails a difference of 2.5% as compared to the energy efficiency evaluated for simulation results, which is associated with an energy efficiency of 9.2%. The lower energy efficiency value obtained at 700 kPa as compared to a higher pressure of 800 kPa is attributed to a comparatively higher rate of backward reaction at a lower pressure.

When the backward reaction is more favored at a lower pressure, lower ammonia synthesis amounts are obtained that lead to lower subsystem efficiencies. The exergy efficiency at 700 kPa is found to be 7.4%, which entails a difference of 2.8% as compared to the exergy efficiency evaluated for the simulation-based ammonia synthesis result.

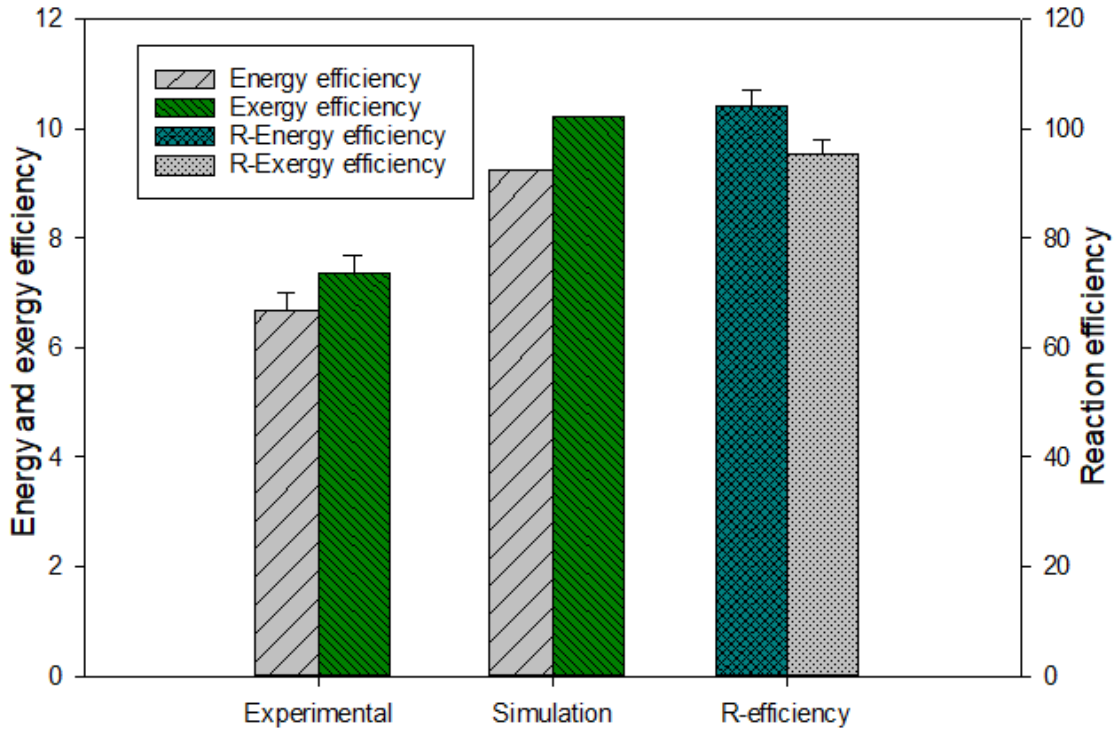


Fig. 6.7 Comparison of energy and exergy efficiencies at an operating pressure of 700 kPa

To further compare the single catalyst reactor with the multi-bed reactor, the characterization of the different types of catalyst utilized is performed. Firstly, the BET surface area is determined for the conventional iron oxide catalyst, ruthenium on activated carbon catalyst as well as the iron oxide wustite catalysts. Fig. 6.8 depicts the relation between the relative pressure and the volume adsorbed by the catalyst. As the relative pressure is raised, after a relative value of 0.8, the volume adsorbed entails a considerable rise. When the relative pressure entails a value of 0.995, the maximum volume adsorbed entails a value of 43.8 cm³/g. Similarly, as the desorption process is initiated from this adsorbed volume, a considerable drop in the adsorbed volume is observed until a relative pressure of 0.8.

As the pressure is reduced further, the desorption process follows a similar trend to the adsorption process. The BET surface area plot is depicted in Fig. 6.9. In this plot, the ratio $1/Q(p^0/p-1)$ entails a highest value of 0.14 at a corresponding relative pressure of 0.3. These plots are utilized to determine the BET surface area that is found to be 9.194 m²/g for the conventional iron oxide catalyst.

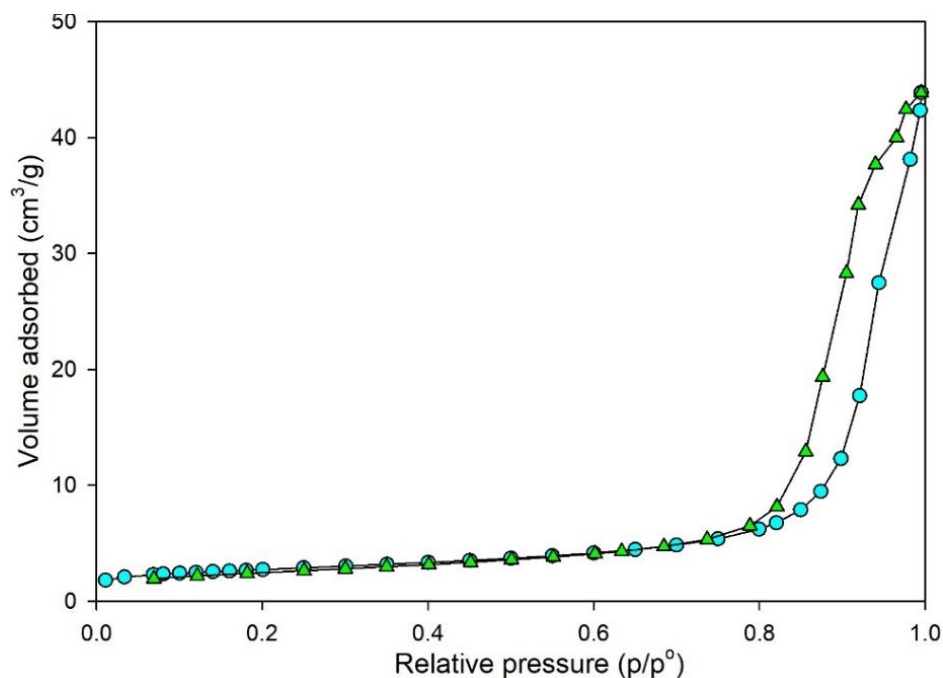


Fig. 6.8 Adsorption-desorption plot for conventional iron oxide catalyst depicting volume adsorbed vs relative pressure

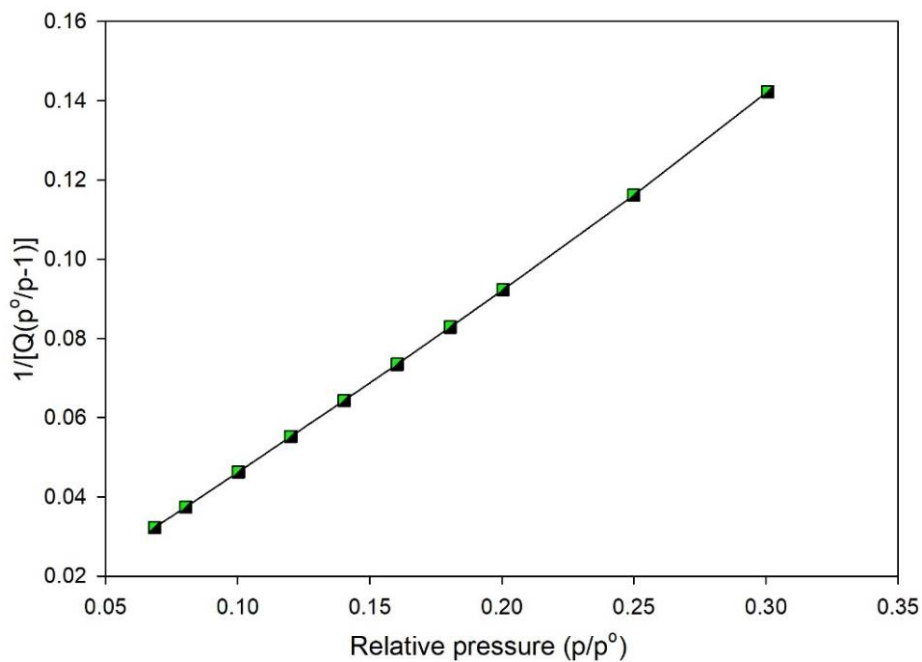


Fig. 6.9 BET surface area plot for conventional iron oxide catalyst

The relation obtained between the relative pressure and the volumes adsorbed as well as desorbed during the surface analysis test is depicted in Fig. 6.10. The considerable rise in volume adsorbed as well as desorbed is observed to occur for the ruthenium-based catalyst

at a relative pressure of 0.8. However, the maximum volume adsorbed at the highest relative pressure of 0.99 entails a value of 479.9 cm³/g. This value is higher than the maximum adsorbed volume obtained for the conventional iron oxide catalyst. The BET surface area plot for the ruthenium based catalyst is depicted in Fig. 6.11.

The ratio depicted on the y-axis entails a maximum value 0.0019 at a relative pressure of 0.3. The BET surface area of the ruthenium-based catalyst is found to be 693.6 m²/g. This is considerably higher as compared to the BET surface area obtained for the conventional iron oxide catalyst that entails a value of 9.194 m²/g. Hence, the higher amount of ammonia synthesized can also be attributed to the usage of the ruthenium-based catalyst that entails a considerably higher surface area than the conventional iron oxide catalyst.

Higher surface area allows higher adsorption of reactant molecules and thus aids in increasing the reaction rates. As the volume of reactants adsorbed increases, the rate of conversion of reactants into products also rises. Specifically, in the case of ammonia synthesis, nitrogen and hydrogen molecules form adsorbed species of nitrogen and hydrogen atoms, which combine together to form ammonia molecules. The adsorption-desorption graph depicting the volume adsorbed in relation to the relative pressure for the wustite-based catalyst is shown in Fig. 6.12.

The specific volume adsorbed reaches a maximum value of 184.1 cm³/g at the peak relative pressure of 0.99. The abrupt rise in the volume adsorbed is observed to occur after a relative pressure of nearly 0.5. Similarly, during the desorption process, the abrupt drop in the volume desorbed occurs until a relative pressure of nearly 0.5 is attained. After this value, the rate of desorption decreases and the rate of adsorption rises considerably.

The BET surface area plot for the wustite-based catalyst is depicted in Fig. 6.13. The peak value of the parameter $1/Q(p^0/p-1)$ is observed to be 0.0026 at a relative pressure of 0.3. The peak value of volume adsorbed by the wustite based catalyst entails a higher value than the conventional iron oxide catalyst. The conventional catalyst entailed a peak-adsorbed volume of 43.9 cm³/g and the wustite-based catalyst is found to have a peak volume adsorbed of 184.1 cm³/g. The BET surface area of the wustite-based catalyst is found to be 484.8 m²/g. This is found to be considerably higher than the conventional catalyst that entails a BET surface area of 9.2 m²/g. Thus, the higher surface areas of the

catalyst beds employed after conventional bed of catalyst can be attributed as one of primary reasons of attaining higher yields of ammonia.

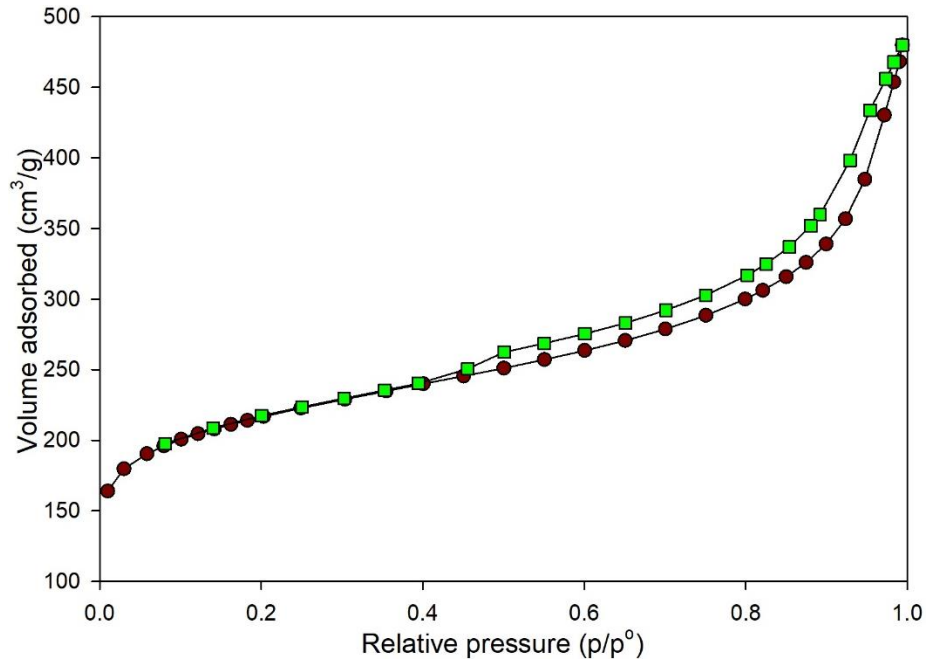


Fig. 6.10 Adsorption-desorption plot for ruthenium-based catalyst depicting volume adsorbed vs relative pressure

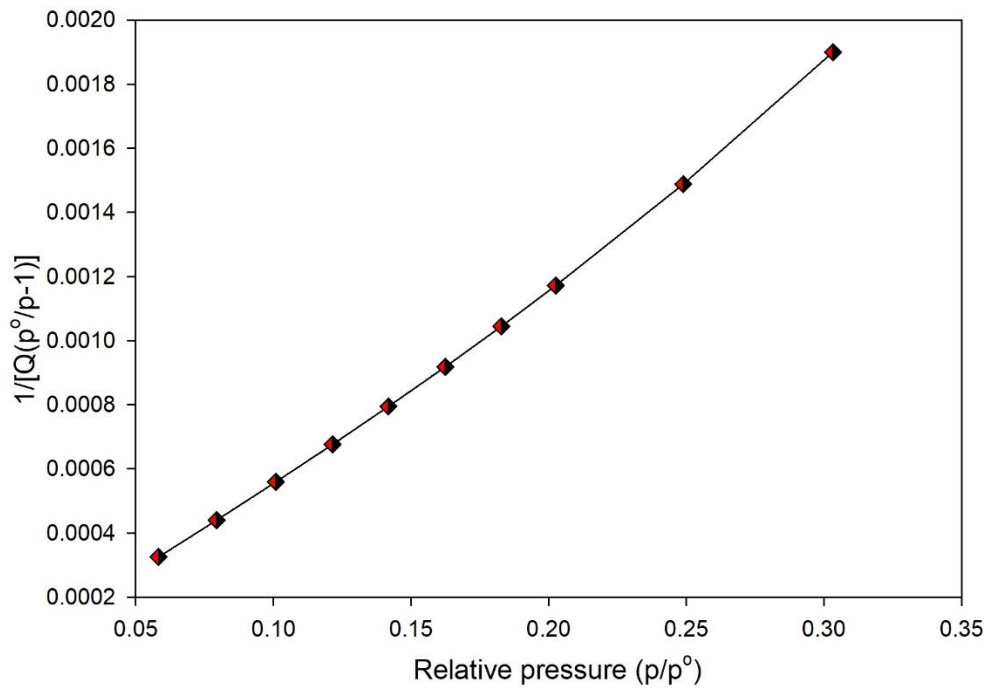


Fig. 6.11 BET surface area plot for ruthenium-based catalyst

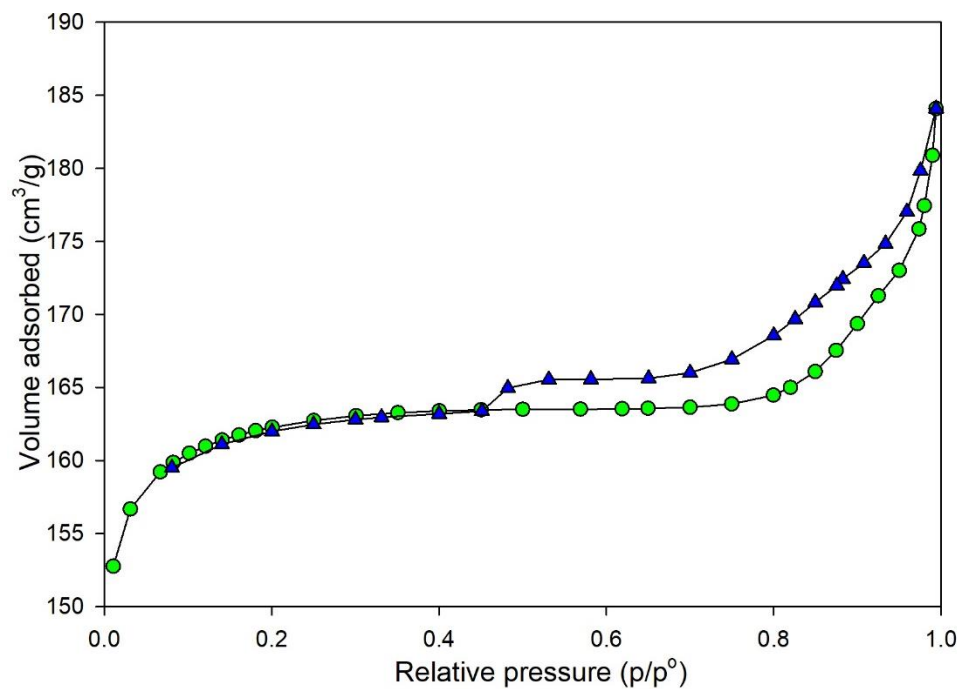


Fig. 6.12 Adsorption-desorption plot for wustite-based catalyst depicting volume adsorbed vs relative pressure

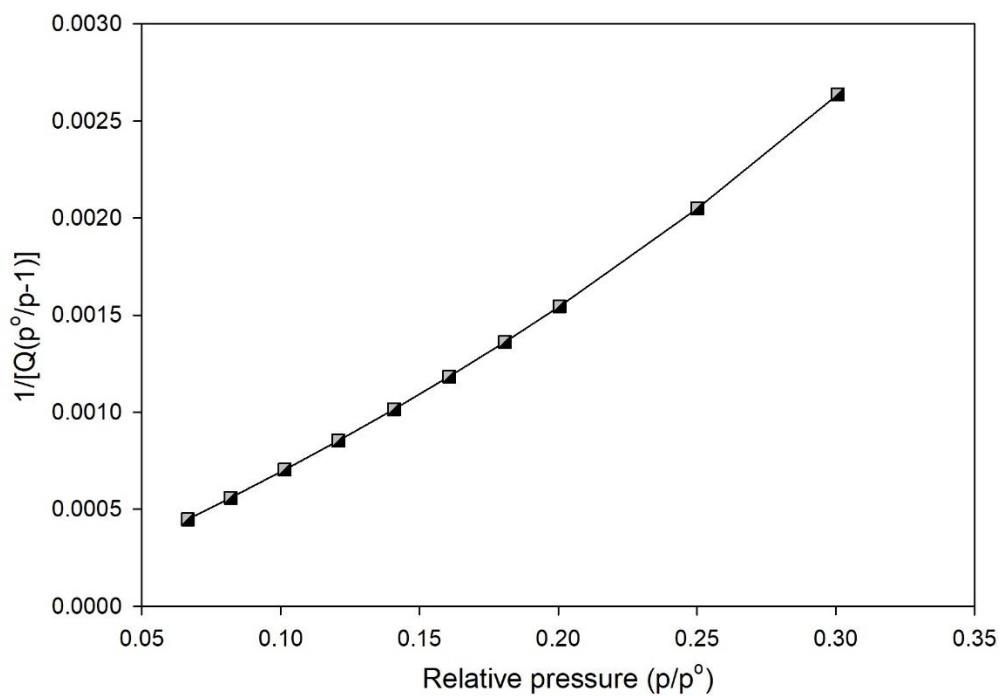


Fig. 6.13 BET surface area plot for wustite-based catalyst

The SEM characterization and EDS results of the conventional iron oxide catalyst is depicted in Fig. 6.14. The elemental analysis is performed on two different locations as shown. Firstly, the base is analysed that is found to entail an elemental weight composition of 9.1% carbon, 6.6% oxygen, 1.8% aluminum and 82.5% iron. However, the deposit on the base layer is also analysed elementally and is found to entail a weight composition of 13.9% carbon, 13.5% oxygen, 1.8% aluminum, 0.6% potassium, 1.6% calcium and 68.5% iron.

Hence, firstly the compositions of the catalyst promoters that have been utilized is confirmed via EDS spectroscopy. Aluminum oxide and calcium oxide can be identified as major catalyst promoters that are employed in the iron oxide-based catalyst. Potassium oxide is also used in comparatively lower quantities. Promoters are essential to enhance the activity of catalysts and increase the catalyst efficiencies.

Molybdenum can also be employed in the ammonia synthesis catalyst that is known to increase the catalyst activity. Other types of catalyst promoters are being investigated for iron oxide-based catalysts that can also be added to conventional catalysts to enhance their activities. The SEM and EDS results of the ruthenium-based catalyst are depicted in Fig. 6.15. The elemental composition results reveal that ruthenium entails a weight percentage of nearly 2%. However, activated carbon entails the catalyst support, which comprises of an elemental weight percentage of nearly 87%.

The ruthenium-based catalyst also includes the usage of molybdenum as well silicon atoms indicating the presence catalyst promoters in the form of silicon dioxide and molybdenum. The catalyst promoters have been proved to enhance the catalyst activities as well as the efficiencies. The ruthenium-based catalyst entails a considerably higher surface area as revealed from the BET surface area analysis described earlier.

The comparatively higher surface area can also be attributed to the usage of activated carbon as support, which constitutes more than 85% in elemental analysis. This type of catalyst support entails considerably higher surface area where ruthenium is affixed, leading to higher overall catalyst efficiencies. Although the catalyst utilized in the present study entails a low concentration of noble ruthenium, higher yields of ammonia are obtained.

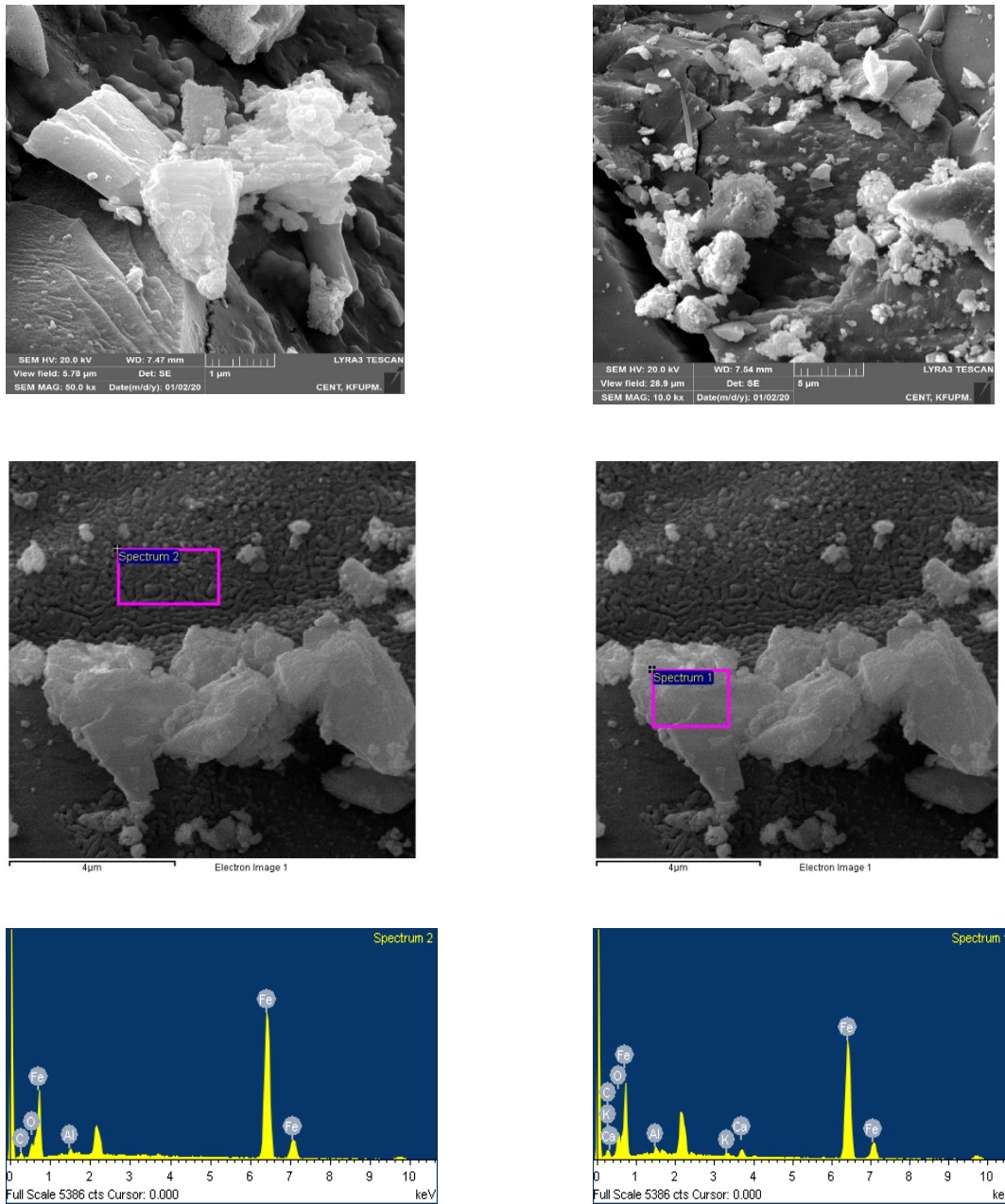


Fig. 6.14 SEM characterization and EDS results of conventional iron oxide-based catalyst. This can be attributed to the usage of both high surface area activated carbon catalyst support as well as catalyst supports such as molybdenum and silicon. The results of SEM and EDS characterization results for the wustite-based catalyst employed are depicted in Fig. 6.16. The catalyst supports layer the base layer as can be observed from the figure.

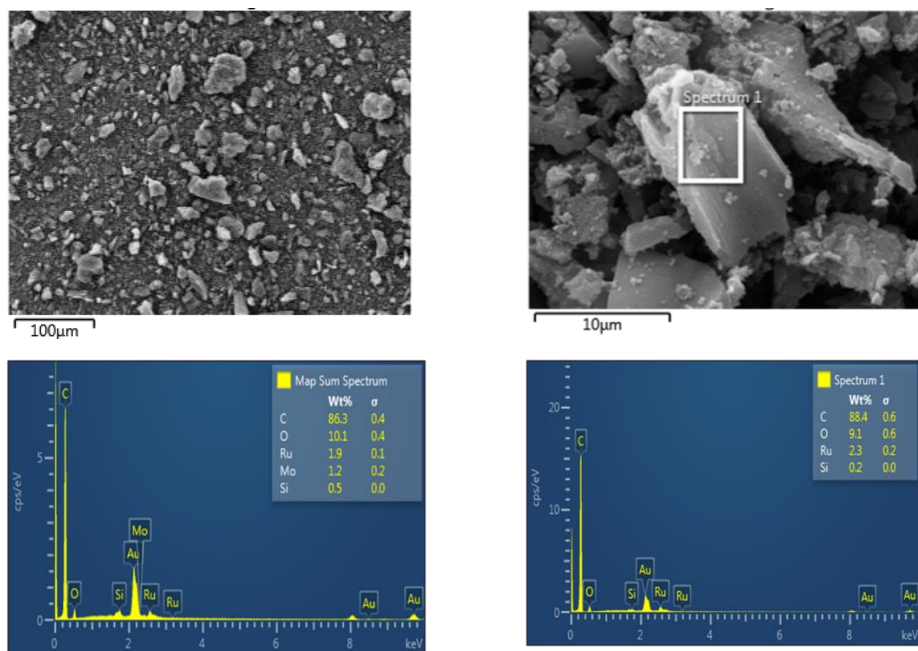


Fig. 6.15 SEM characterization and EDS results of ruthenium-based catalyst

The elemental composition analysis reveals that the catalyst entails an iron weight percentage of 37.1% while the oxygen element entails a composition of 41.2%. Hence, as compared to the conventional iron oxide catalyst, the wustite-based catalyst entails a lower iron to oxygen ratio in the iron oxide molecules. The catalyst supports are revealed to entail aluminum, potassium and calcium oxides. Aluminum entails an elemental weight percentage of 4.4% whereas the total calcium composition is found to be 0.34%. The weight percentage of potassium is found to be 3.75%.

Hence, as compared to the conventional iron oxide catalyst, the wustite-based catalyst is incorporated with a higher percentage of aluminum as well as potassium-based catalyst supports. However, comparatively lower usage of calcium is associated with wustite-based catalyst. The SEM and EDS results of the wustite-based catalyst with cobalt are depicted in Fig. 6.17. The adherence of catalyst supports to the base layer is revealed, which aids in enhancing the performance of the catalyst.

The elemental composition analysis reveals an iron weight percentage of 61.5%. A considerable cobalt content of 20.4% is associated with the cobalt-based catalyst. A lower aluminum composition of 0.72% is obtained and a lower potassium composition of 1.7% is found to be entailed with the catalyst. The total oxygen element composition is 10.6%

while the carbon weight percentage is found to be 3.9% and calcium has a composition of 1% by weight.

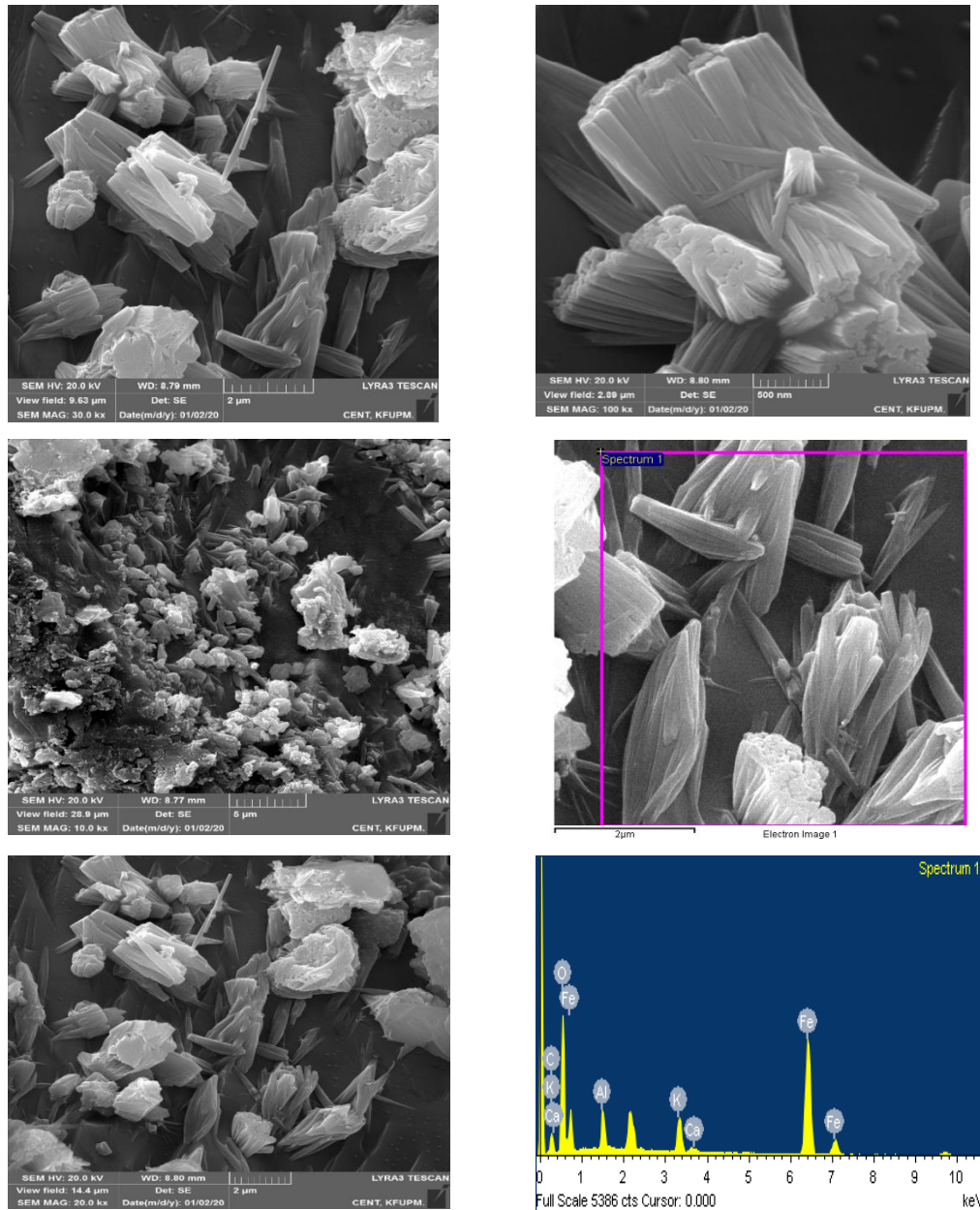


Fig. 6.16 SEM characterization and EDS results of wustite-based catalyst

Thus, the higher yields of ammonia that have been reported with the usage of cobalt-based wustite catalysts can be attributed to the enhancement in the catalyst performance that the presence of cobalt-based supports can provide. Cobalt entails other advantageous characteristics such as lower catalyst reduction temperatures. Hence, the multi-bed catalyst

reactor developed in the present study entails the advantages associated with different types of catalysts, which provide higher energetic as well as exergetic performances.

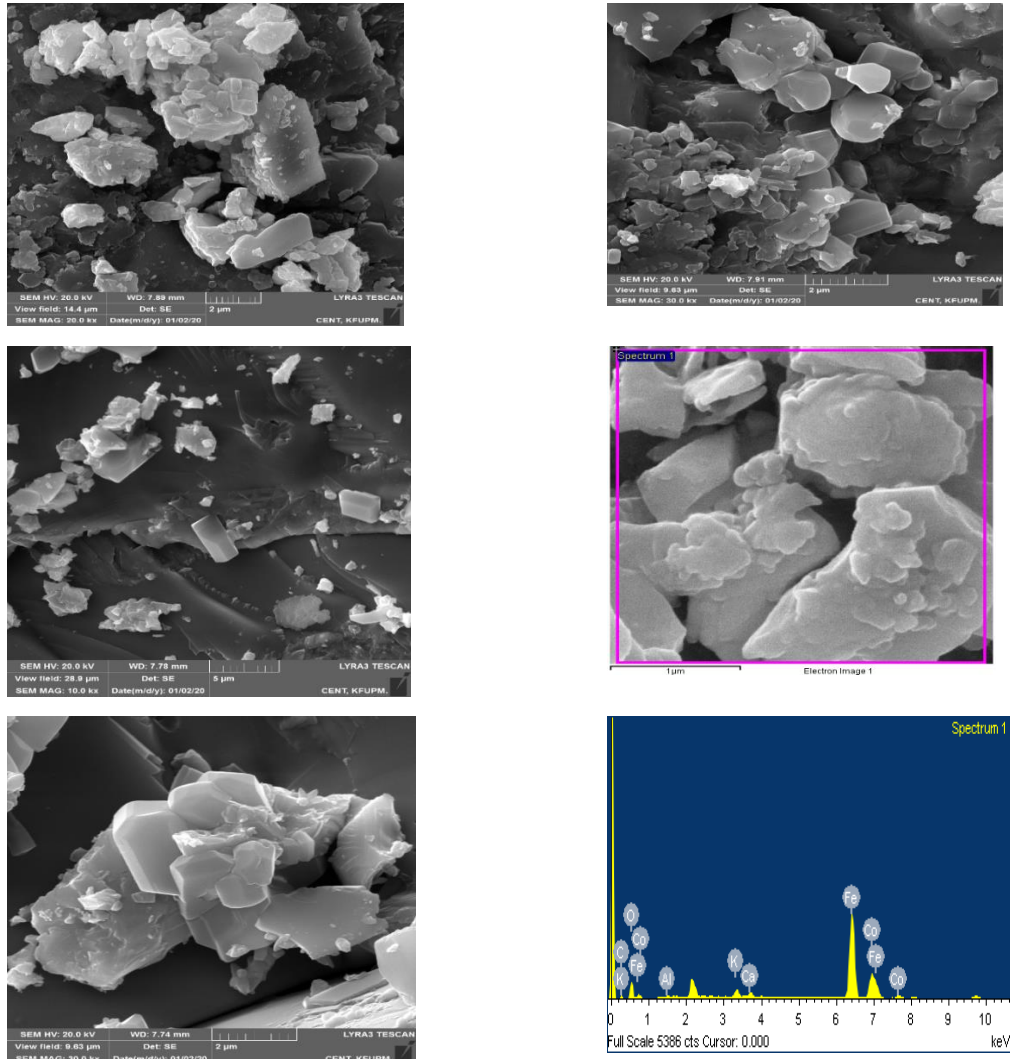


Fig. 6.17 SEM characterization and EDS results of wustite-based catalyst with cobalt

6.1.2 Ammonia fuel cell results

The open circuit voltage obtained for single cell arrangement is 280 mV at ambient atmospheric temperature and a bubbler humidifier temperature of 25°C as can be observed from Fig. 6.18. The obtained voltage is lower than the Nernst value for ammonia fuel cells of 1.17 V. The low open circuit voltage can be attributed to various reasons. The catalyst layers can be deteriorated by ammonia molecules. Hence, reducing their catalytic activity. This results in low voltages as well as overall performance. The reason for deterioration has been proposed to be the high rate of nitrogen adsorption (N_{ads}) on the layer of catalyst

attributed to their high adsorption energy on platinum. Alternative catalysts have been suggested to be investigated for the electro-oxidation of ammonia. Thus, other substances including iridium as well as ruthenium have been investigated in the literature. Iridium was reported to entail comparatively lower catalyst poisoning owing to a limited coverage for saturation of 20%. This is comparatively lower than the normal transitional metals that entail around 50% saturation coverage. The phenomenon of fuel cross over is also suggested to be an important factor that results in low open circuit voltages. Particularly, in fuel cells consisting of anion exchange membrane electrolytes, the fuel crossover phenomenon was found to be considerable. In case of ammonia molecules crossing over to the cathodic side, their oxidation at the cathodic platinum black catalyst can affect the voltages significantly. Studies investigating these phenomena should be conducted to determine their actual effects on fuel cell performances. The membrane thickness also plays an important role in determining the performance of ammonia fuel cells. Developing and utilizing membranes with lower thicknesses is expected to aid in achieving higher fuel cell performances. This can be primarily attributed to the reduction in the Ohmic losses. However, the fuel cross over phenomenon can be increased due to a decrease in membrane thickness. For a single-cell arrangement, the power density at the peak value is found to be 6.4 W/m^2 at a 25°C of humidifying temperature as can be depicted from Fig. 6.19. The peak power densities are also observed to increase marginally with increasing humidifier temperatures.

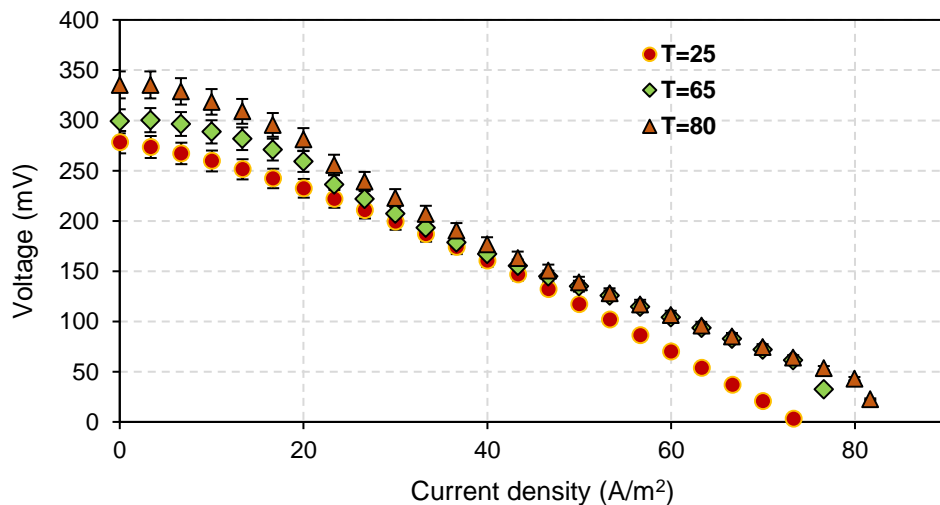


Fig. 6.18 Voltage vs current density results obtained for the single cell ammonia fuel cell

The peak power density is observed to increase from 6.4 W/m² at 25 °C to 7.1 W/m² at a humidifier temperature of 80°C. A current density of 39.9 A/m² and voltage of 176.7 mV are observed at this peak power density value at 80°C. The enhancement in fuel cell performance with increasing humidifier temperatures can be attributed to increased reaction rates. Increasing the humidifier temperature helps in increasing the rates of reactions within the fuel cell. Specifically, as the cathode side of fuel cell comprises of humidified air input, higher humidifier temperatures aid in accelerating the oxygen reduction reaction at the cathode.

Although marginal, humidifier temperatures are found to enhance fuel cell performances. Higher electrochemical conversion rates of reactants are obtained under higher temperatures leading to higher fuel cell performances. However, as the membrane as well as catalyst layers entail a specific maximum stable temperature, the humidifier temperatures cannot exceed certain values depending on the type of membrane and catalysts utilized. For the anion exchange membrane-based electrolyte utilized in the present study, the maximum stable temperature is 80°C. Thus, a maximum humidifier temperature of 80°C is utilized in this study.

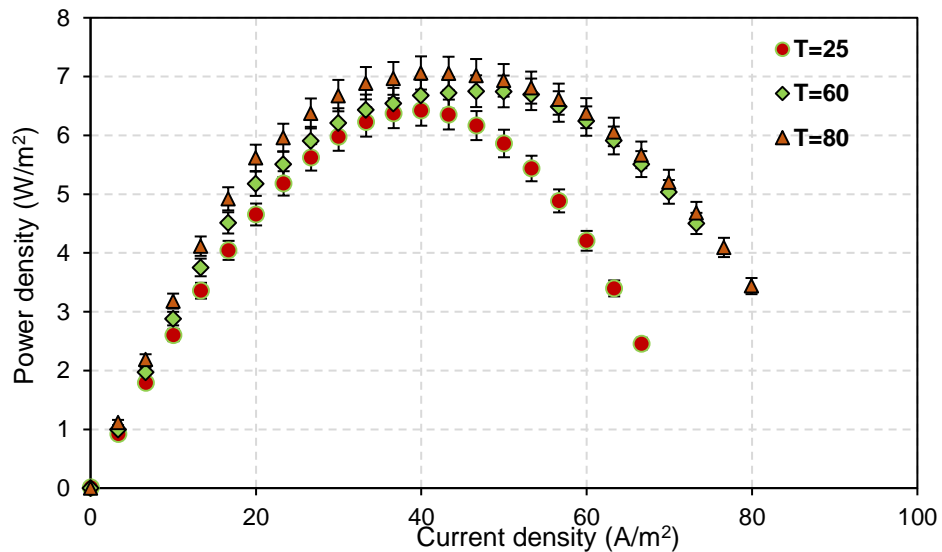


Fig. 6.19 Power density vs current density results obtained for the single cell ammonia fuel cell

The developed single-cell ammonia fuel cell is also investigated with aqueous ammonia as the fuel at varying temperatures. The fuel cell performance is observed to increase considerably with increasing ammonia reservoir temperatures. The performance is firstly assessed at ambient condition of 25°C. In the subsequent experiments, the reservoir temperature is increased to 45°C and 65°C. The open circuit voltage is observed to increase from 110 mV at ambient conditions to 147 mV at a reservoir temperature of 65°C.

A maximum reservoir temperature of 65°C was chosen due to significantly high evaporation rates of ammonia at temperatures higher than the utilized value. The polarization curves obtained are depicted in Fig. 6.20 and the peak power density vs current density curves are depicted in 6.20. As can be observed from the figure, the current densities increase considerably with increasing solution temperatures.

The peak power densities occur at 10 A/m², 20 A/m² and 23.3 A/m² for ammonia storage reservoir temperatures of 25°C, 45°C and 65°C respectively. The peak power density with aqueous ammonia as fuel is found to entail a value of 0.72 W/m² at a reservoir temperature of 25°C. However, an increase of 0.58 W/m² is obtained when the reservoir temperature is raised to 45°C, where a peak power density of 1.3 W/m² is obtained. When the temperature is raised further to 65°C, the power density at the peak value increases further to 2.0 W/m². This signifies an increase of 35% as compared to a reservoir temperature of 45°C and an increase of 71% as compared to the reservoir temperature of 25°C.

In order to obtain higher fuel cell performances with aqueous ammonia fuel, higher reservoir temperatures can be employed. The increase in performance can be attributed to higher anodic reaction rates. As the ammonia solution temperature is increased, the molecular activity of the solution increases. Hence, more ammonia molecules are allowed to interact at the catalyst sites.

As can be observed from Fig. 6.21, higher reservoir temperatures would result in higher short circuit current densities. The increase in short circuit current densities can be attributed to the decrease in polarization losses. The rate of ammonia evaporation as well as the diffusion coefficient also increase with increasing temperatures. The rise in current densities with increasing temperatures can also be attributed to the aggravated activity of ammonia molecules in the solution. At higher temperatures, the molecular activity of

dissolved ammonia molecules is enhanced that results in lower mass transfer limitations during electrochemical reactions. Lower mass transfer limitations result in lower concentration polarization losses in voltage at higher current densities, thus leading to higher fuel cell performances.

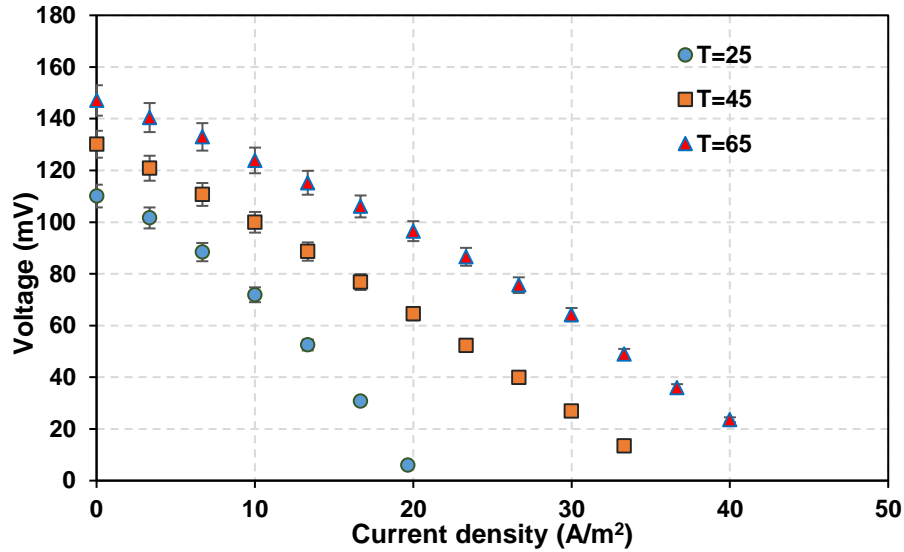


Fig. 6.20 Voltage vs current density results obtained for the single cell ammonia fuel cell with aqueous ammonia

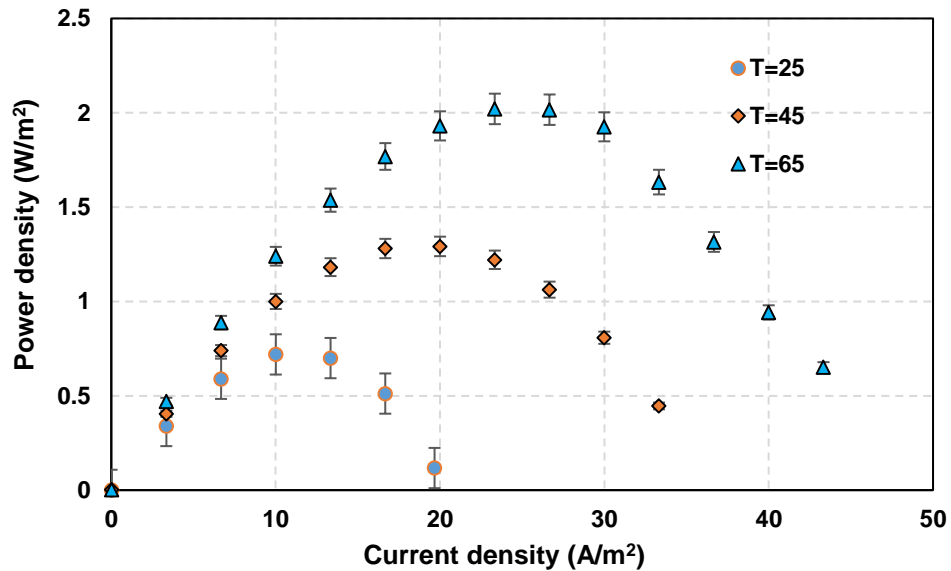


Fig. 6.21 Power density vs current density results obtained for the single cell ammonia fuel cell

The performance of the developed 5-cell ammonia fuel cell stack is also investigated as depicted in Figs. 6.22 and 6.23. For a 5-cell stack arrangement, the open circuit voltage is obtained as 1249 mV at a humidification temperature of 25°C. The power density at the maximum point value is found as 13.4 W/m². The voltage and current density at this power density value are 23.4 A/m² and 574.2 mV respectively as can be observed from the results.

Effects of varying humidifier temperatures are also investigated for the 5-cell ammonia fuel cell stack. The open circuit voltage rises from 1249 mV at a 25°C humidifier temperature to 1399 mV at a 60°C humidifier temperature. At a higher humidifier temperature of 80°C, 1582 mV is found to be the voltage under open circuit conditions. The peak power density of 13.4 W/m² at 25°C is found to increase to 17 W/m² at an 80°C humidifier temperature. A voltage of 730 mV and a current density of 23.3 A/m² are found at the maximum power density.

In case of a 5-cell stack, the Ohmic resistance can be a significant contributor to the lower performance. In fuel cells, membranes are the cell components with the highest Ohmic resistances. Hence, anion exchange membranes with lower resistances should be developed. Lower membrane thickness can be utilized to reduce the membrane Ohmic resistance. New types of electrochemical catalysts need to be developed that can aid in enhancing the initial electrochemical oxidation of ammonia molecules. As there exists a considerable difference between the theoretical voltage expected for ammonia fuel cells and the actual experimental voltage obtained, new electrochemical catalysts that can aid in increasing the open circuit potentials need to be developed.

Through an increase in the open circuit potentials, the overall performance of ammonia fuel cells can be enhanced significantly. For instance, if the open circuit voltage for a single cell ammonia fuel cell is enhanced from the actual experimental value of 280 mV to a value approaching 1 V, this would signify an improvement of nearly 2.5 times that would also be reflected in the power outputs that can be obtained from the ammonia fuel cell at peak power density points. The adsorption of nitrogen atoms and high adsorption energies associated with their interactions with the electrochemical catalyst surface can lead to the inhibition of active catalyst sites. The inhibition of catalyst sites can lead to considerable deterioration in cell performance and can be a primary reason for the attainment of low

open circuit voltages associated with the ammonia fuel cell. In ammonia fuel cell stacks, the crossover of fuel can lead to higher voltage losses as compared to a single cell arrangement. This can be attributed to the transfer of ammonia molecules to the cathodic compartments of other cells.

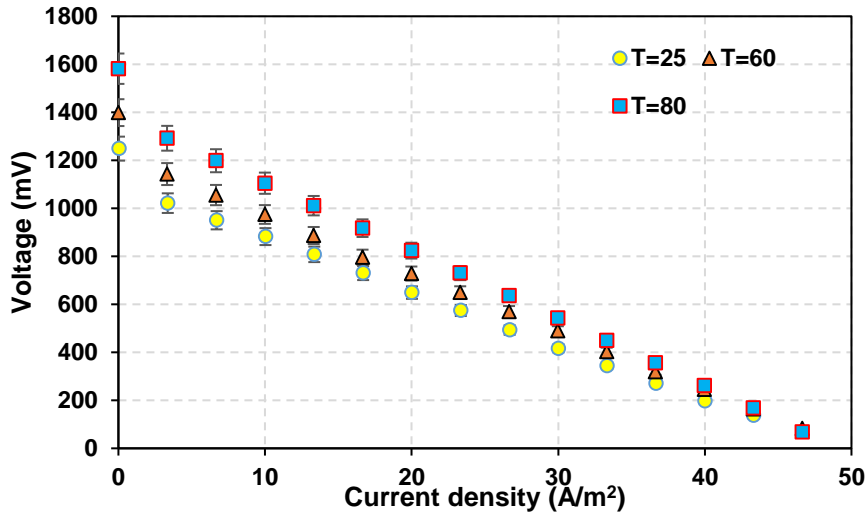


Fig. 6.22 Voltage vs current density results obtained for the 5-cell ammonia fuel cell stack

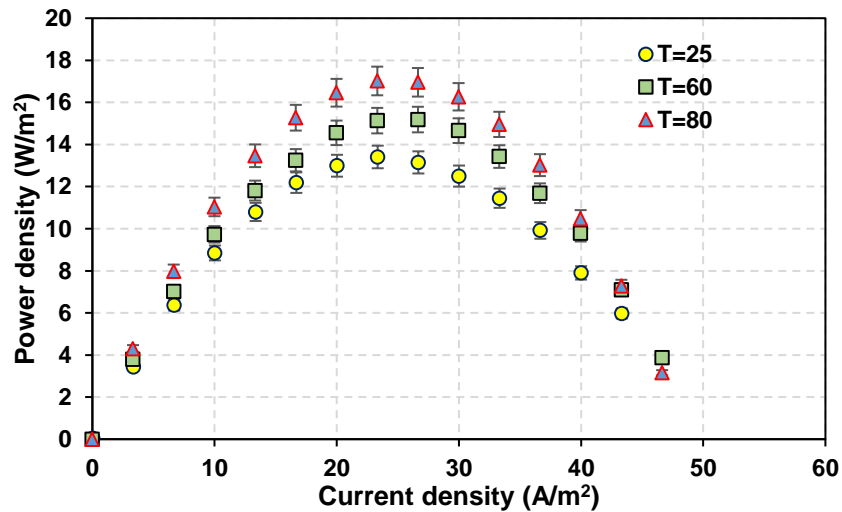


Fig. 6.23 Power density vs current density results obtained for the 5-cell ammonia fuel cell stack

The performance of the developed molten alkaline electrolyte salt-based ammonia fuel cell is also investigated at varying operating temperatures. The open circuit voltage of the developed molten electrolyte ammonia fuel cell is obtained as 520 mV at an electrolyte

temperature of 220°C as depicted in Fig. 6.24. The short circuit current density is observed to be 14.5 A/m² at the same electrolyte temperature. The open circuit voltage is found to decrease with rising electrolyte temperatures. For instance, as the temperature of the electrolyte is raised to a value of 280°C, the open circuit voltage decreases to 388 mV at an electrolyte temperature of 280°C from 520 mV at an electrolyte temperature of 220°C. At an electrolyte temperature of 250°C, an open circuit voltage of 484 mV is obtained.

Hence, the open circuit voltages are observed to decrease with increasing electrolyte temperatures. This can be attributed to changes in the reaction kinetics with temperature. The optimum temperature range for the electrochemical reaction of ammonia in molten alkaline electrolyte needs to be further investigated. A decrease in open circuit voltage with increasing electrolyte temperatures suggests that the optimum temperature range for this electrochemical reaction can be situated in the vicinity of 200°C. The peak power density is observed to be 2.1 W/m² at an electrolyte temperature of 220°C and 2.3 W/m² at an electrolyte temperature of 280°C. The short circuit current densities are observed to increase with increasing electrolyte temperatures resulting in marginally higher peak power densities at higher operating temperatures.

The short circuit current density is observed to increase from 14.5 A/m² at an electrolyte temperature of 220°C to 22 A/m² at an electrolyte temperature of 280°C. This increase in short circuit current density is attributed to a rise in the diffusion coefficients with increasing molten electrolyte temperatures. As the temperature of the electrolyte is raised, both the reactant as well as product molecules entail higher rates of diffusion in the electrolyte. This leads to lower concentration polarization losses at higher current densities. Under this type of polarization voltage loss, the cell voltage is decreased owing to limitations in the mass transfer mechanisms. As reactant molecules are adsorbed at the electrode surface to further proceed the electrochemical reaction and form respective products, at higher current densities, excessive number of reactant as well as product molecules hinder the movement of the formed products as well as incoming reactants. This leads to abrupt voltage drops at high current densities. Hence, at higher molten alkaline electrolyte temperatures, as the activity as well as diffusion coefficients of products and

reactants rises, the hindrances towards mass transfer limitations are limited. Thus, leading to lower concentration polarization voltage losses.

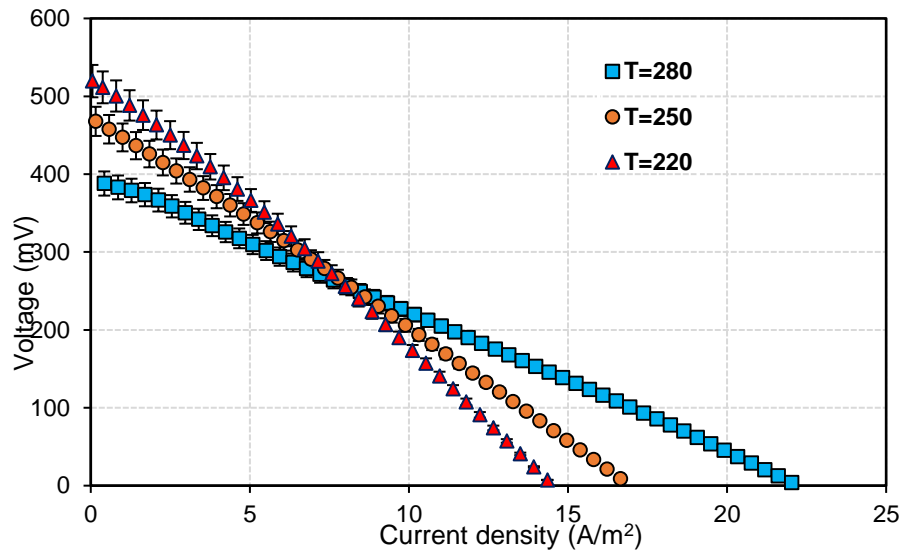


Fig. 6.24 Voltage vs current density results obtained for the molten alkaline electrolyte fuel cell

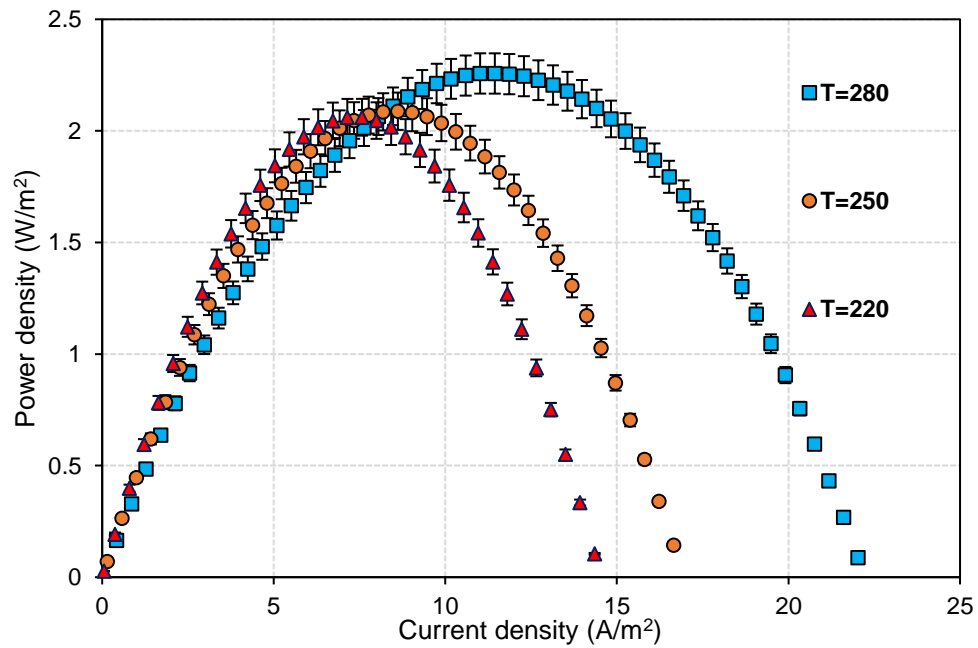


Fig. 6.25 Power density vs current density results obtained for the molten alkaline electrolyte fuel cell

The energy and exergy efficiencies evaluated at the peak power densities for the five-cell ammonia fuel stack are depicted in Fig. 6.26. The effect of utilizing different temperatures of the humidifier are also shown. At a humidifier temperature of 25°C, the energy efficiency of the developed fuel cell stack is determined to be 52.5% at the peak power density. When a higher temperature of 60°C is used, the energy efficiency is found to increase to 59.4%.

The energy efficiency is found to rise to 66.8% when the humidifier temperature is raised to 80°C. This can be attributed to a drop in polarization losses as the humidifier temperature is increased. Similar trends are observed in exergy efficiencies. At the maximum power density, the exergy efficiency is evaluated to be 49.2% at a humidifier temperature of 25°C. This is observed to increase to 55.6% and 62.6% at temperatures of 60°C and 80°C respectively.

This can also be attributed to lower polarization losses at higher humidifier temperatures that result in lower exergy destruction rates leading to higher exergy efficiencies. Hence, it is recommended to utilize higher humidifier temperatures during ammonia fuel cell operation. Nevertheless, further studies should be conducted to develop anion exchange membranes as well as electrochemical catalysts that entail higher stabilities at higher operating temperatures.

As discussed earlier, higher operating temperatures when implemented in ammonia fuel cells provide higher fuel cell outputs as well as efficiencies. Hence, there is a need to develop ammonia fuel cells that can operate in the medium temperature range via cost-effective anion exchange membranes. It is recommended to perform electrochemical impedance spectroscopy on ammonia fuel cell stacks to determine the different impedances present in the stack, which deteriorate the overall system performances. Also, durability tests should be performed to investigate the deterioration rate of platinum catalyst under ammonia exposure.

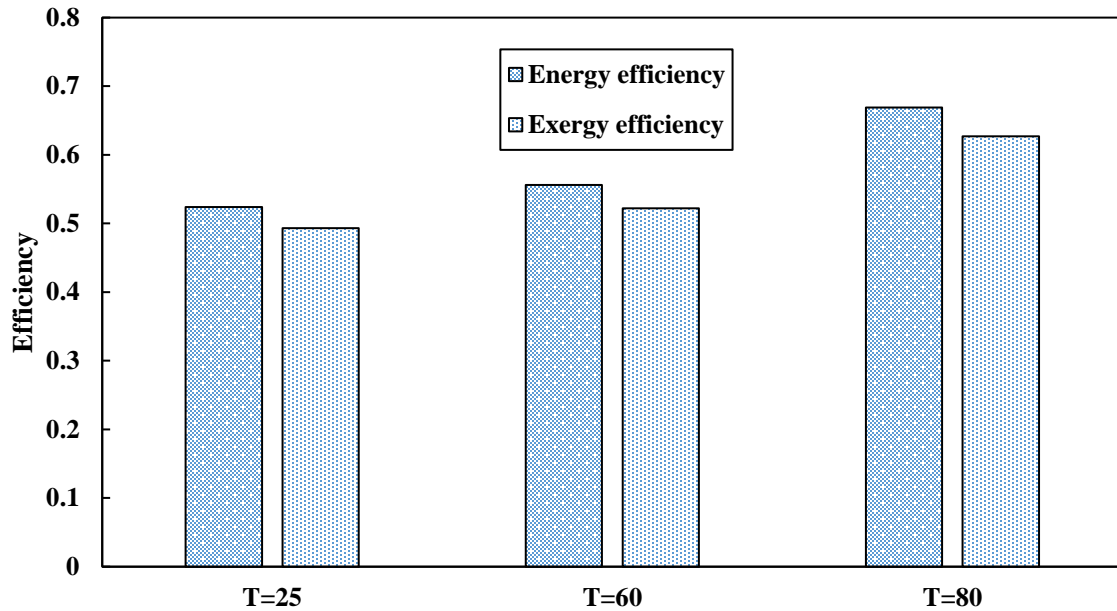


Fig. 6.26 Energy and exergy efficiency results obtained for the five-cell ammonia fuel cell stack utilizing anion exchange membrane electrolyte

6.2 System 1 analysis and modelling results

System 1 is analysed considering both integrated solar and wind energy inputs as well as only solar energy as the primary system input. The results of the dynamic simulation considering the usage of only solar PV as the primary energy input source of the system are depicted in Fig. 6.27. The hourly and monthly variation in the power generation via solar PV farm are presented. The maximum power outputs across the year are found to be 346.2 MW and 340.4 MW that occur in June and July respectively.

The peak power during the low solar potential months of January and December are found to be 168.9 MW and 155.3 MW respectively. The daylight hours also entail large variations between the summer and winter months. In winter months for instance, 8 daylight hours are observed. On the other hand, 16 daylight hours are obtained for the summer month of June. As discussed earlier, in the present study, the daily average solar intensity is utilized to determine the power input point to the hydrogen and ammonia synthesis systems, where the daily average value of the electrical power generated by the PV farm is utilized as the useful electricity output.

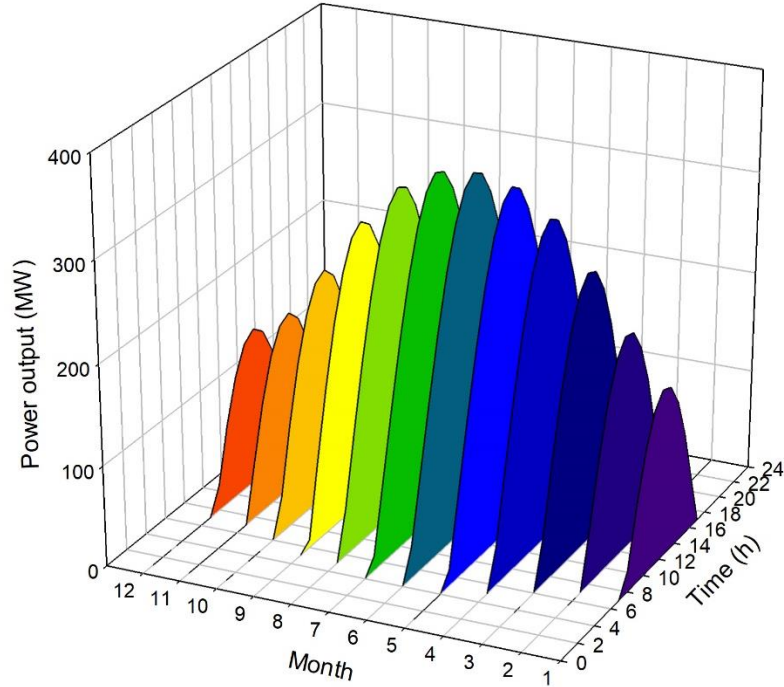


Fig. 6.27 Solar PV power generation results on monthly average days

The results of hydrogen and nitrogen production rates on the monthly average days are depicted in Figs. 6.28 and 6.29. The peak hydrogen production rate occurring in the month of June, as shown in Fig. 6.28 reaches 378.2 mol/s. The peak production rates for hydrogen during the months with low solar radiation intensities (January and December) are found to be 159.6 and 157.1 mol/s respectively.

The maximum nitrogen production rate across the year is found to reach 126.1 mol/s as depicted in Fig. 6.29. The maximum production rates for the months of January and December are found to be 53.2 and 52.4 mol/s respectively. The production occurs during the hours 10 to 14. This is in accordance with the hours of excess power availability. The large variations in the production rates can be attributed to the considerable variations in the solar power outputs. As discussed earlier, the solar power outputs entail a large range owing to significant changes in the solar intensities throughout the year. Integration with other renewable energy sources such as wind turbines would aid in obtaining higher system performances. The low rates of hydrogen and nitrogen production can be mitigated according to the availability of both wind and solar based-energy resources. The results of

system 1 considering the utilization of both solar PV as well as wind turbines is discussed in the proceeding sections.

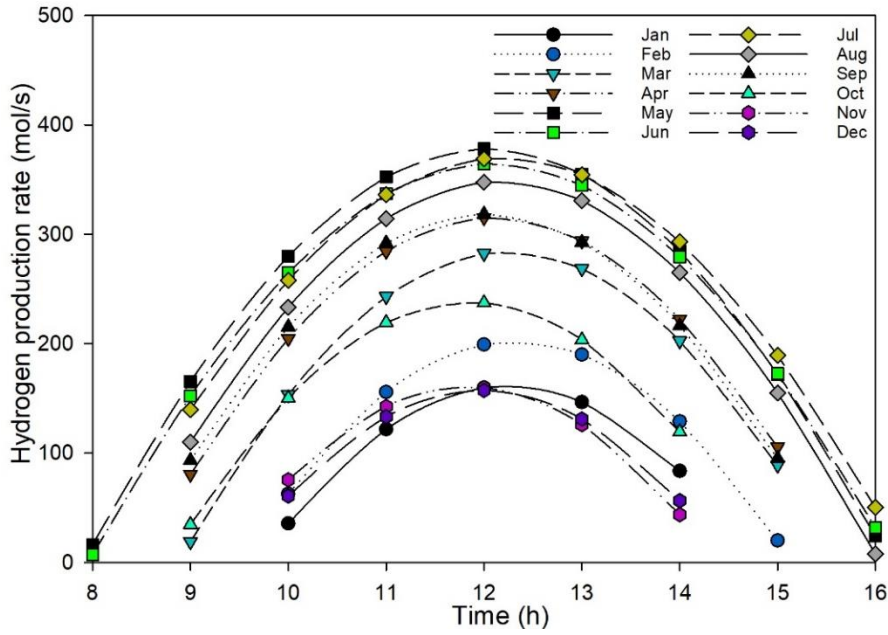


Fig. 6.28 Hydrogen production rate results for the monthly average days

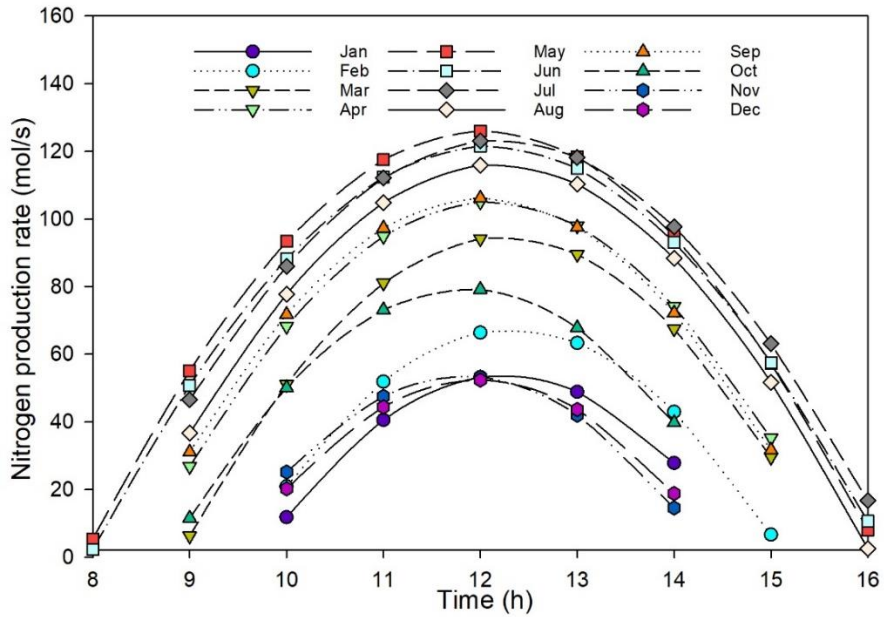


Fig. 6.29 Nitrogen production rate results for the monthly average days

The results of ammonia production rates are depicted in Fig. 6.30. The peak ammonia synthesis rate is found to reach 219.4 mol/s during the month of June. The peak production rates during January, which entails a low solar intensity is found to reach 92.6 mol/s. The total ammonia production for a given day is dependent on both the ammonia production rates and the number of synthesis hours. During months of high solar radiation intensities (May-August), higher ammonia production occurs.

The ammonia synthesis during these months occurs for 9 hours whereas during the months with low radiation intensities, the synthesis takes place for 5 hours. Ammonia, which constitutes a major component of various types of applications and industries can be produced through the utilization of environmentally benign energy resources. During periods of excess power, the ammonia synthesis subsystem is operated and a portion of the produced ammonia is used for other useful purposes. The average day of July entails comparatively higher peak ammonia synthesis after June and entails rates that reach up to 219.4 mol/s. This is followed by August that is associated with a peak production rate of 214.2 mol/s.

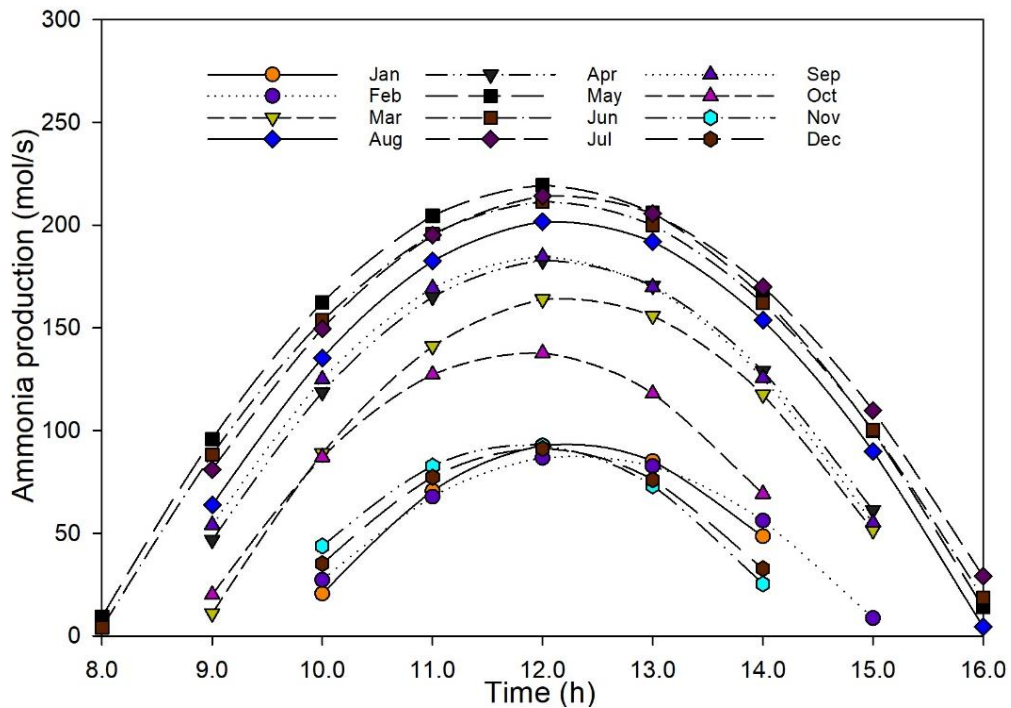


Fig. 6.30 Ammonia production rate results for the monthly average days

The daily amounts of useful hydrogen and ammonia produced by the system are depicted in Fig. 6.31. The peak daily ammonia production reaches a value of 2117.2 kmol that is associated with average day of May. The peak daily production of hydrogen attained from the system entails a value of 3650.3 kmol. This is followed by the average day of July, which is associated with a daily ammonia production of 2077.8 kmol and a daily hydrogen production of 3582.4 kmol. The hydrogen production amounts obtained for the average days of low solar intensity months such as January and December are 984.1 kmol and 969.2 kmol respectively.

The daily ammonia production amounts obtained for the average days of these months are 570.7 kmol and 562.1 kmol respectively. The daily production amounts entail dependency on both the peak solar intensities reached as well as the total duration of daylight hours available during the day. Nevertheless, the present system entails daily ammonia output amount in the range of 562.1 kmol and 2117.2 kmol. The daily hydrogen output amount is found to vary between 969.2 kmol and 3650 kmol across the year.

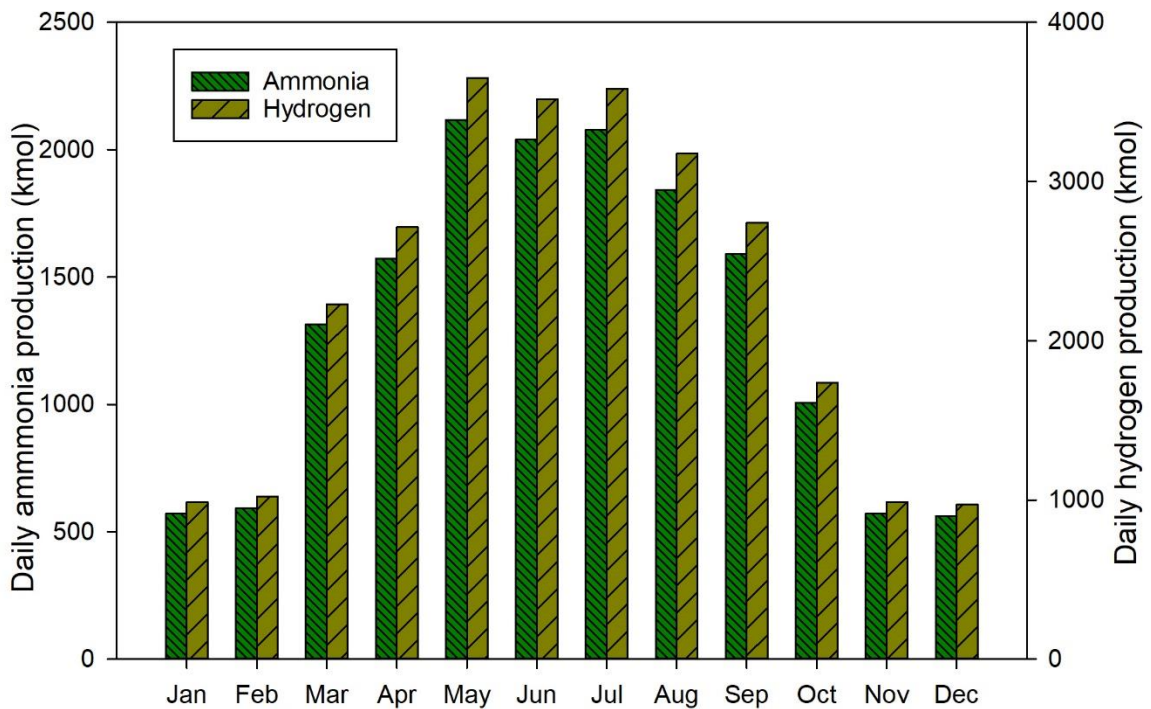


Fig. 6.31 Daily hydrogen and ammonia production rate results for the monthly average days

The AFC energy output capacity results obtained for the monthly average days are depicted in Fig. 6.32. These are evaluated considering fuel cell operation at the peak power point obtained via experimental studies described earlier. The procedure to evaluate the ammonia consumption at this power density was described earlier in Section 5. The present system entails an energy storage method that allows flexible fuel cell power output. System parameters such as ammonia input rate and total electrode area can be varied, which will allow the variation of power outputs as well as discharge times.

The AFC energy output capacities are in accordance with the respective daily ammonia production amounts. The maximum AFC energy capacity is found to reach 18153.7 kWh that is associated with the average day of May. The average day of July entails an AFC energy output capacity of 17816.1 kWh. A minimum output energy capacity of 4819.9 kWh is observed to be associated with the average day of December. The average day of January entails an AFC energy output capacity of 4893.9 kWh. However, during the winter months when solar intensities are lower, wind velocities may be higher that can aid in attaining higher hydrogen and ammonia outputs. These will lead to higher energy output capacities entailed with the AFC.

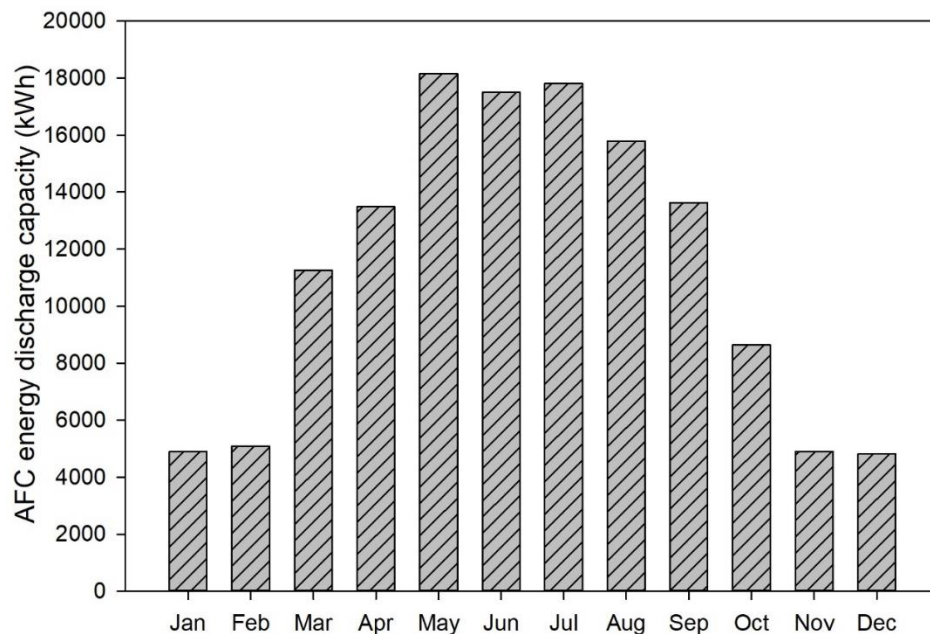


Fig. 6.32 Daily AFC energy output capacity results for the monthly average days

The results obtained for the total exergy destructions for the PEM and ASR subsystems are shown in Fig. 6.33. Exergy destruction depicts the amount of useful work potential lost due to irreversibilities. The maximum exergy destruction in the ASR is found to reach 83.5 MWh. The average day of May entails an ASR exergy destruction of 81.7 MWh. The minimum ASR exergy destruction is 19.6 MWh entailed with average day of January.

The high amounts of exergy destructions during the months of May-August can be attributed to higher ammonia synthesis that occurred for longer periods of time in these months. However, although there exists a direct relation between the ASR exergy destruction and ammonia production, it is recommended to develop new ASR subsystems that entail lower irreversibilities.

The temperature differences between the inlet and exit streams can also be minimized to achieve lower exergy destructions. The daily exergy destruction in the PEM water electrolysis subsystem reaches a maximum value of 85.3 MWh in May. This is followed by the average day of July, entailing an exergy destruction amount of 83.7 MWh. The exergy destructions during the monthly average days with low amounts of hydrogen production are 22.7 MWh and 23.0 MWh for December and January respectively. These are attributed primarily to the irreversibilities that occur during the electrochemical interactions that take place for water splitting.

It is thus recommended to develop electro-catalysts that entail lower activation polarization losses, which will aid in reducing the overall exergy destructions. Reducing the irreversibilities during PEM water electrolysis will also aid in decreasing the required power inputs to the subsystem, which will result in higher overall efficiencies. The ASR and PEM subsystems comprise major system components that entail comparatively higher exergy destruction amounts than other operational components.

Different efforts are being directed towards developing PEM and ASR subsystems that are associated with lower irreversibilities. The ASR subsystem needs to be entailed with lower temperature gradients that can aid in reducing exergy losses as well as exergy destruction amounts. The usage of higher activity catalysts can also aid in overcoming exergy losses entailed in the ammonia synthesis process. The high-energy intensity required for the production of hydrogen via water electrolysis needs to be addressed to attain lower exergy

destruction rates as well as higher efficiencies. Both the energetic as well as the exergetic performances of the water electrolysis subsystem can be enhanced by reducing the energy input requirements.

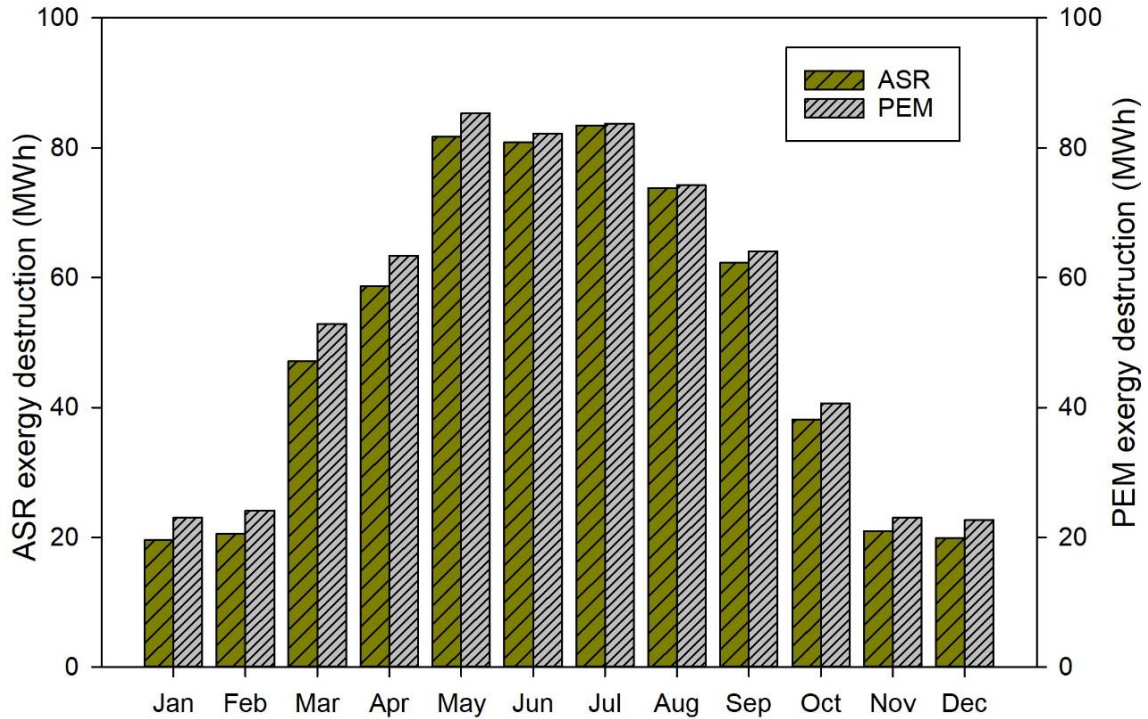


Fig. 6.33 Daily ASR and PEM exergy destruction results for the monthly average days of each month

The results for exergy destruction in the compression subsystem (COMP) are depicted in Fig. 6.34. The maximum exergy destruction in COMP is found to reach 4.61 MWh that corresponds to the average day of May. This is followed by an exergy destruction amount of 4.53 MWh associated with the average day of July. However, the winter months entailing lower operation of the ammonia synthesis subsystem are associated with lower exergy destruction amounts in the compression subsystem.

An exergy destruction amount of 1.22 MWh corresponds to the daily COMP subsystem operation in December. January is associated with an exergy destruction amount of 1.24 MWh. Hence, it is recommended to develop compressors that entail high isentropic efficiencies, which will decrease the entropy generated and thus the exergy destroyed during operation.

Lowering the exergy destructions will also aid in lowering the power input requirements. Thus, allowing the system to achieve higher overall energy and exergy efficiencies. The power input requirements as well as the corresponding exergy destruction rates associated with the COMP subsystem can be reduced by decreasing the operating pressures of the ASR subsystem. Hence, catalysts that can provide satisfactory ammonia yields at low operating pressures need to be developed and utilized.

The results for the overall energy and exergy efficiencies of system 1 considering only solar PV-based operation are depicted in Fig. 6.35. The peak energy efficiency across the year reaches 14.9% and the exergy efficiency attains a value of 15.7%.

The comparatively higher efficiencies obtained for the month of May can be attributed to several reasons. The overall output on the monthly average day is higher than other months that aid in attaining higher overall efficiencies.

The exergy efficiencies are evaluated considering ambient temperatures at the chosen location (Toronto) on the monthly average days. Thus, larger variation is observed in the overall exergy efficiencies as compared to energy efficiencies. Hence, it is recommended to employ exergy analysis during the assessment of any given energy system to obtain a better overall understanding of the performance under varying ambient conditions.

The system presented in this study provides an effective method to produce environmentally benign hydrogen, ammonia as well as electricity. Several large-scale PV power plants are currently under construction and currently the major PV plants in Ontario include the Sarnia PV plant that entails a capacity of 97 MW and can provide electrical power to nearly 12000 homes. Thus, through the implementation of the present system, this plant can produce considerable amounts of hydrogen as well as ammonia during excess solar availability.

The produced ammonia is also used as an energy storage medium that can be utilized in the ammonia fuel cell system to generate clean electricity during low solar availability. Concerned authorities that monitor and control the amount of power input to the grid from different power plants regulate electrical power supply in Ontario. Hence, higher stability

as well as energy storage capacities can be attained by the Sarnia power plant through the production and storage of a clean fuel that is synthesized during peak solar availability.

Although the current power plant is equipped with batteries for storing energy, the capacity factors of solar power plants entail low values. This is attributed to the requirement of a steady power input to the grid from a given power plant.

For instance, the grid operators provide a solar PV plant with a set amount of power input that it needs to provide to the grid, thus, to ensure the plant does not entail lower energy availability at any time, this power input value is kept lower than the actual capacity of the plant.

The presented system can also be utilized to increase the capacity factors of solar PV plants by allowing the synthesis of ammonia fuel during excess solar availability and utilizing it for power generation later when required without having any energy degradation with time as in the case of batteries.

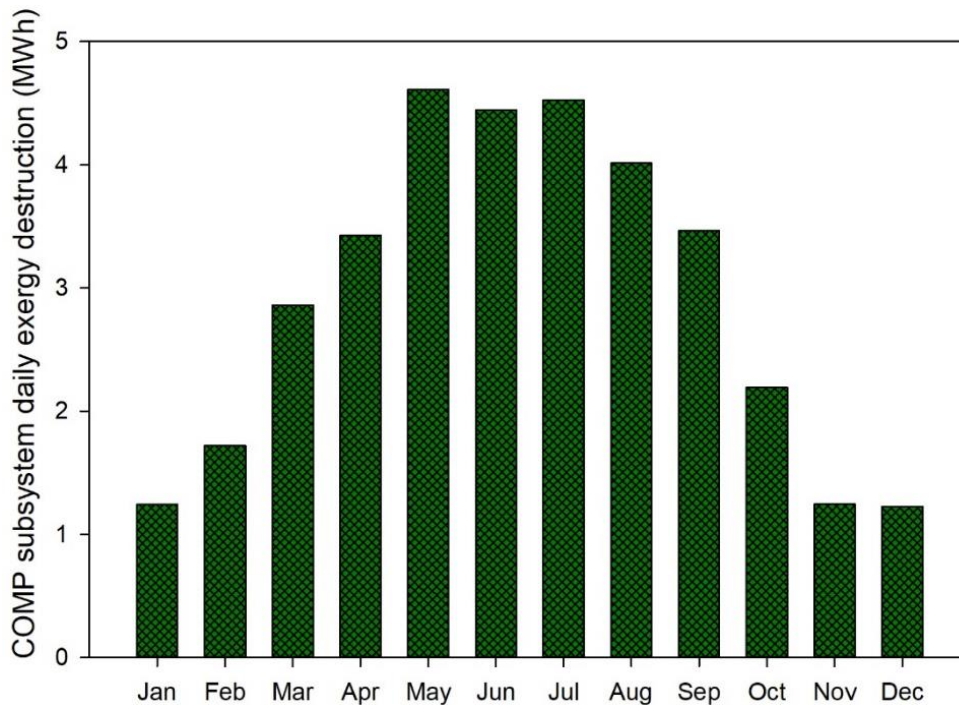


Fig. 6.34 Daily exergy destruction results for the monthly average days for the compression subsystem

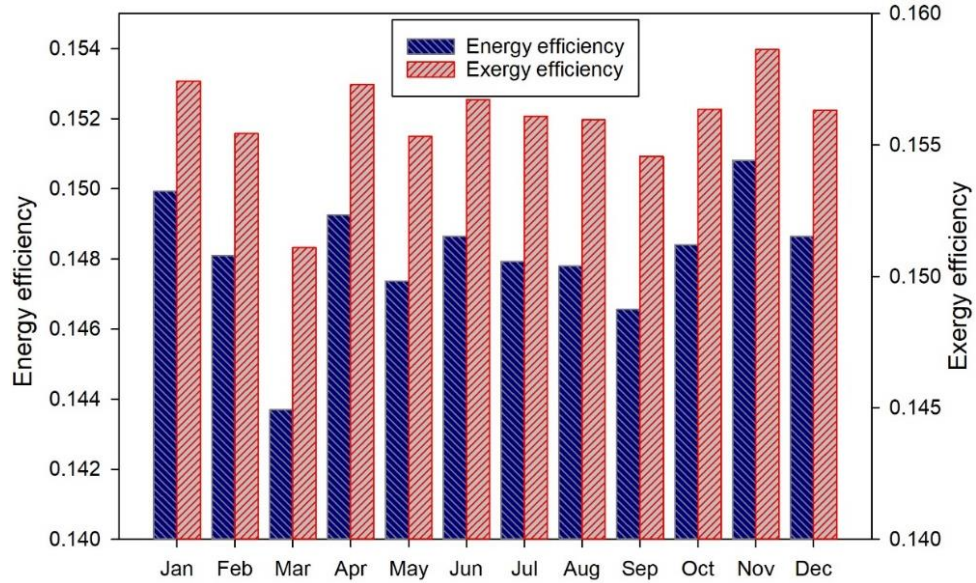


Fig. 6.35 Daily energy and exergy efficiency results for the monthly average days for system 1 considering only solar PV-based operation

The electrical power output results of the solar PV farm are depicted in Figs. 6.36-6.37. The constant power output that can be observed on the monthly average days is the power generation at the average solar intensity on that corresponding day. The electricity produced by the solar farm exceeding the average value is utilized for both hydrogen and ammonia production. The highest power output is observed to be in the month of June where the maximum power output of 108.2 MW is attained.

The monthly average days of July and August are observed to have maximum daily power outputs of 104.4 MW and 98.2 MW respectively. The least maximum stable power output of 49.7 MW is obtained on the monthly average day of December at the average solar intensity, followed by January that entails a power output of 56.0 MW.

The results show that stable output power obtained from the solar-based system entails varying time ranges. During the summer months of June to August, stable power output can be provided for 7-9 hours. However, during the winter months, this decreases based upon the number of daylight hours. The maximum stable power output obtained for the months April to June entails values between 101.1 MW and 108.2 MW.

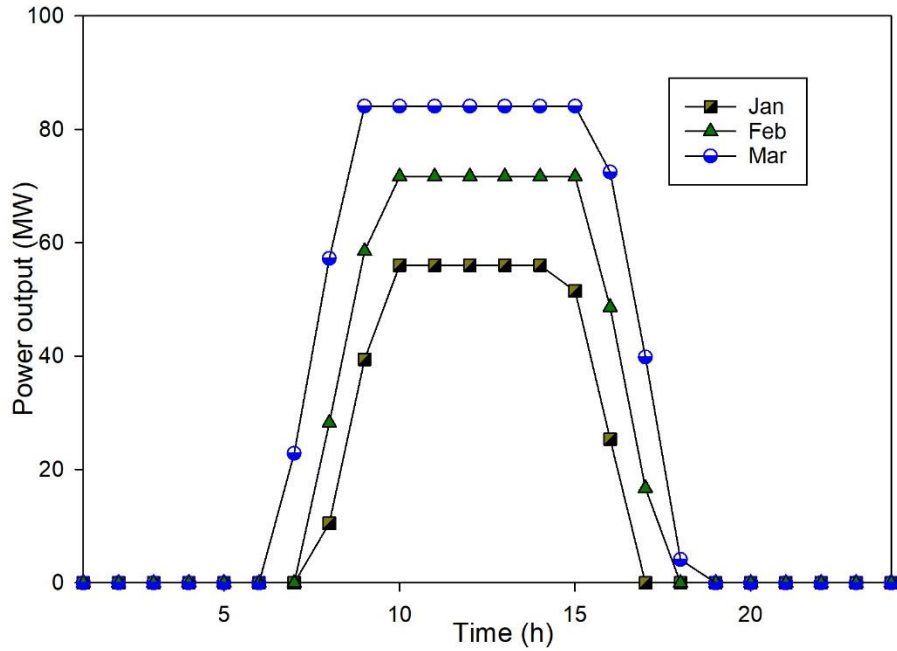


Fig. 6.36 Results of PV output electricity for the monthly average days of January to March for system 1 considering both solar PV and wind farm operation

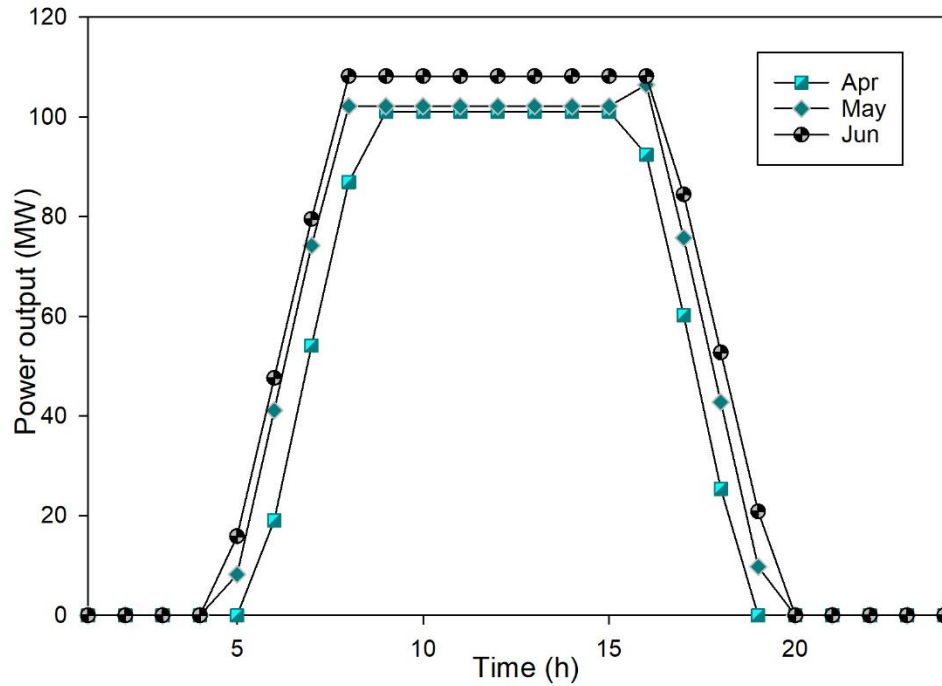


Fig. 6.37 Results of PV output electricity for the monthly average days of April to June for system 1 considering both solar PV and wind farm operation

The stable power outputs for average days of July to September are found to entail values between 104.4 MW and 83.9 MW respectively. For average days of October to December,

the respective maximum stable power output values range between 71.5 MW and 49.7 MW. As the electrical power produced by the PV farm exceeds the average daily value, it is utilized to synthesize hydrogen as well as ammonia. Hence, the developed system allows the production of clean electricity with available solar as well as wind energy, and produces sufficient amounts of hydrogen and ammonia as will be discussed further.

System 1 is analysed considering operation of both configurations, which comprise only the solar PV farm operation as well as the operation of integrated solar PV and wind farms. The results obtained for the first configuration were discussed earlier and results obtained for the solar PV-based electrical output associated with the second configuration have been presented. The useful electrical outputs obtained from the wind farm on the monthly average days are presented in Figs. 6.40-6.42. The results presented are based on the system operation algorithm considered for the analysis of system 1 that was described in Section 5.

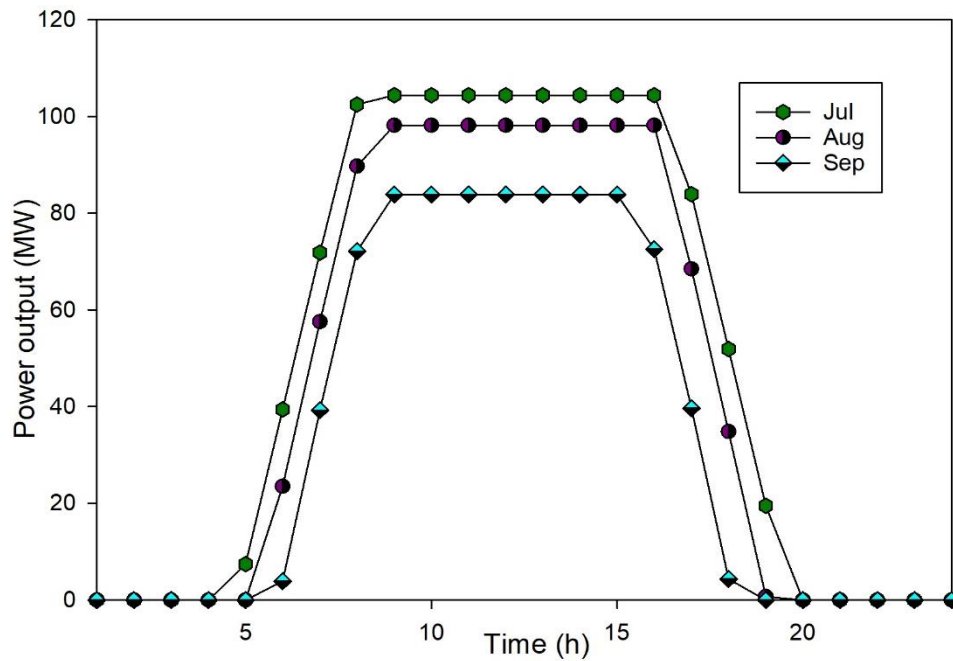


Fig. 6.38 Results of PV output electricity for the monthly average days of April to June for system 1 considering both solar PV and wind farm operation

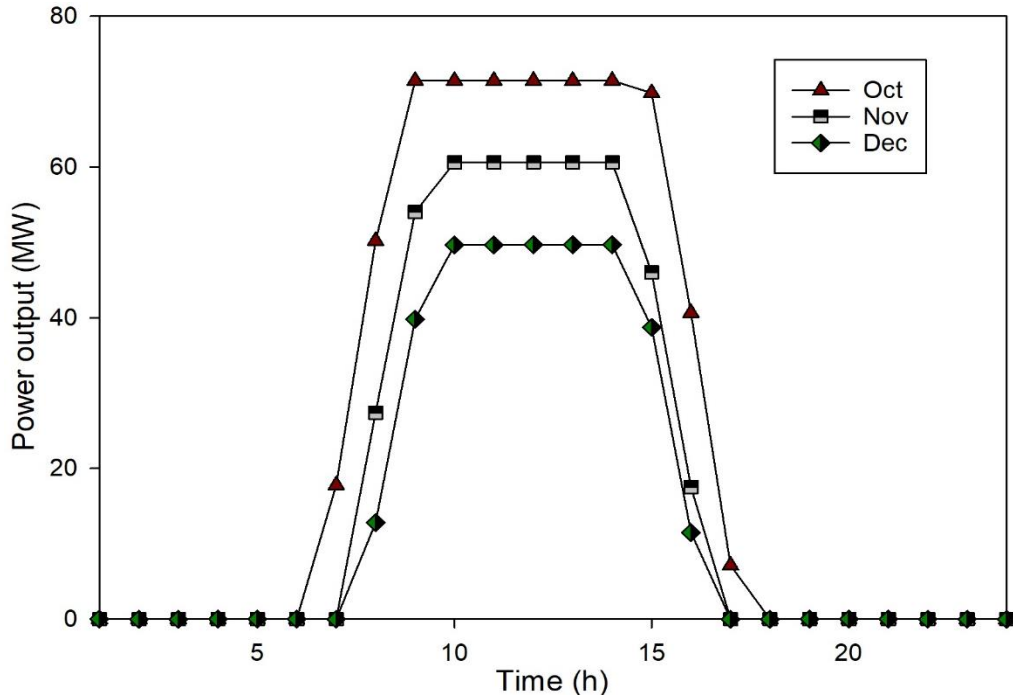


Fig. 6.39 Results of PV output electricity for the monthly average days of April to June for system 1 considering both solar PV and wind farm operation

The maximum stable power output obtained during the average days of January to March entails a value of 134.2 MW that is associated with the average day of March. The stable output power entails a duration of 8 hours on the monthly average day. The stable outputs on the average days of January and February entail values of 14.3 MW and 51.1 MW respectively. The respective durations for these outputs were 6 and 9 hours respectively.

The results for the average days of April to June are depicted in Fig. 6.41. The average day of April entails high variability in the electrical power outputs, which are attributed to high variations in the wind speeds in conjunction with the average value of the day. However, May and June are found to entail stable power outputs of 23.4 MW and 47.8 MW for 7 hours and 8 hours respectively. Next, in the July to September period, the average day of August is associated with the highest stable power output of 158.2 MW that is entailed for 6 hours. However, the average days of July and September are associated with lower maximum stable power outputs of 18.0 MW and 6.7 MW respectively. In the month of December, the availability of high wind speeds allows the production of a stable power output of 44.7 MW for 6 hours. Thus, the integration of solar and wind energy resources allows the mitigation of low resource availability during a given month. As depicted in Fig.

6.43, availability of sufficient wind energy can be utilized to mitigate the low availability of solar energy in this month.

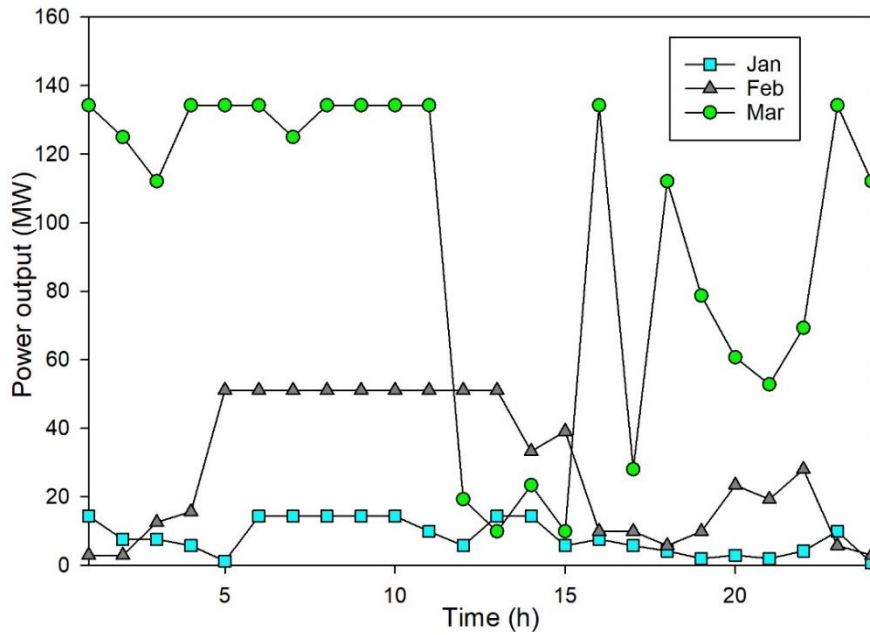


Fig. 6.40 Results of wind-based output electricity for the monthly average days of January to March for system 1 considering both solar PV and wind farm operation

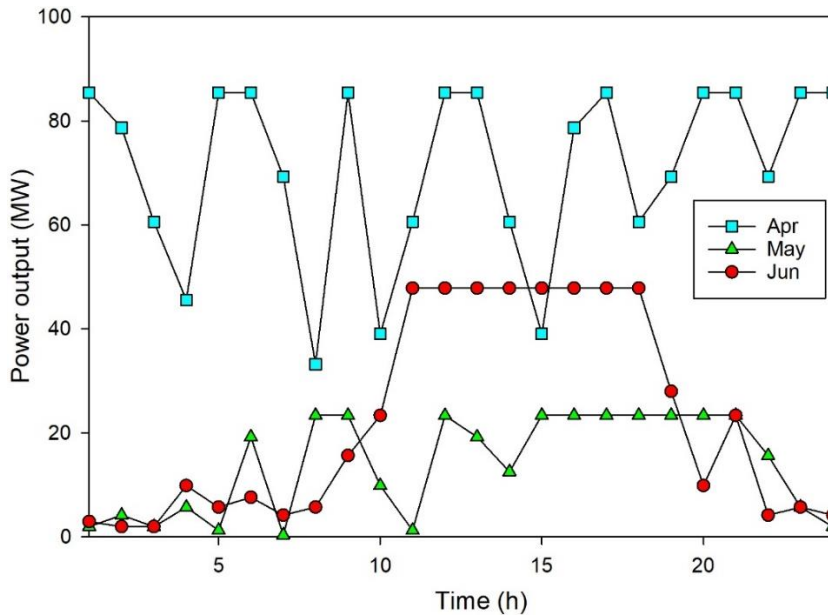


Fig. 6.41 Results of wind-based output electricity for the monthly average days of April to June for system 1 considering both solar PV and wind farm operation

As described earlier, the month of December entails lower outputs considering only solar PV-based operation. The wind power output results obtained correspond to the wind speed values on the monthly average days. However, wind speeds entail high amounts of variabilities in magnitudes and directions that can effect the power output results. Hence, models need to be developed that can predict the wind speeds with sufficient accuracies that can aid in designing and operating wind-based power plants with higher performances.

The daily ammonia production amounts on the monthly average days are depicted in Fig. 6.44. A can be observed, the months entailing combinations of excess wind and solar energy are associated with ammonia production amounts. System operation considering both solar and wind based operation entails higher ammonia production amounts as compared to solar-based configuration. The solar-based configuration entails a peak daily ammonia production of nearly 2000 kmol, however, the integrated solar and wind-based configuration is found to have a peak daily production amount of 5067.9 kmol. This is attributed to the mitigation of low solar energy availability with wind energy.

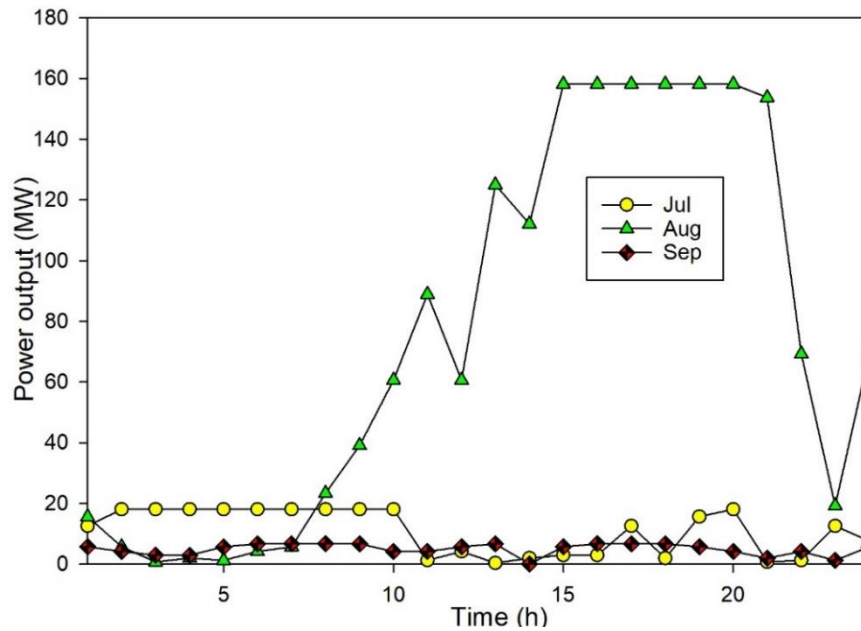


Fig. 6.42 Results of wind-based output electricity for the monthly average days of July to September for system 1 considering both solar PV and wind farm operation

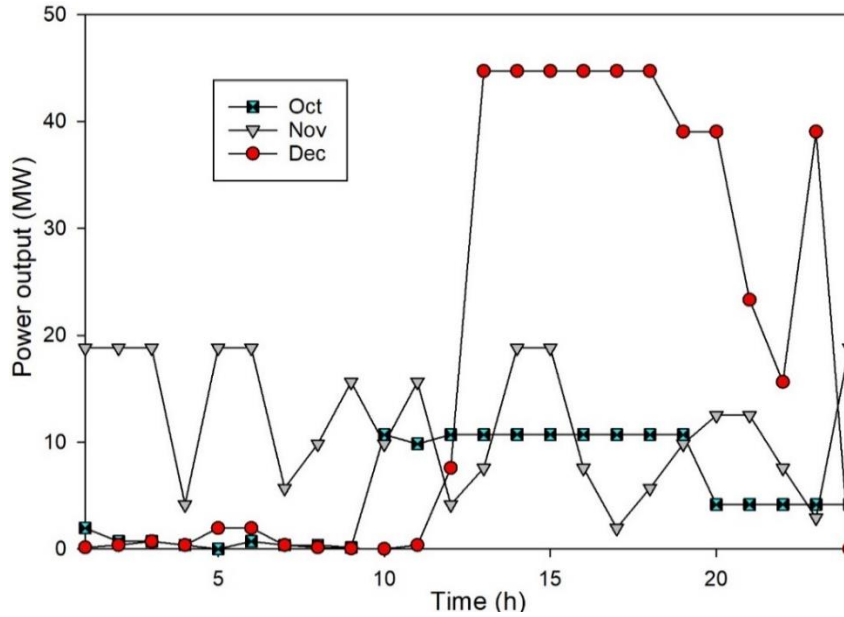


Fig. 6.43 Results of wind-based output electricity for the monthly average days of October to December for system 1 considering both solar PV and wind farm operation

The highest daily ammonia production of 5067.9 kmol is associated with the month of August owing to the availability of both high solar as well as wind energy. Next, the average day of March entails an ammonia production of 2561.9 kmol that can be attributed to the higher availability of wind energy. The average day of December is found to be associated with a daily ammonia production of 1606.5 kmol that is considerably higher than the ammonia production obtained considering only solar-based system operation.

Although low solar intensities are available in December, the availability of high amounts of wind energy result in higher ammonia production amounts. The average days of May and July, which entail comparatively higher ammonia production amounts considering only solar-based system operation, are associated with comparatively lower ammonia production amounts in the integrated solar and wind-based configuration.

The average day of May, for instance, entails an ammonia production of 1282.2 kmol. The average day of July is associated with a daily ammonia production of 1162.0 kmol. Next, the daily hydrogen production amounts as well as the corresponding daily exergy destructions are presented in Fig. 6.45. Both daily production as well as the exergy destruction are in conjunction with the trend observed in the ammonia synthesis subsystem

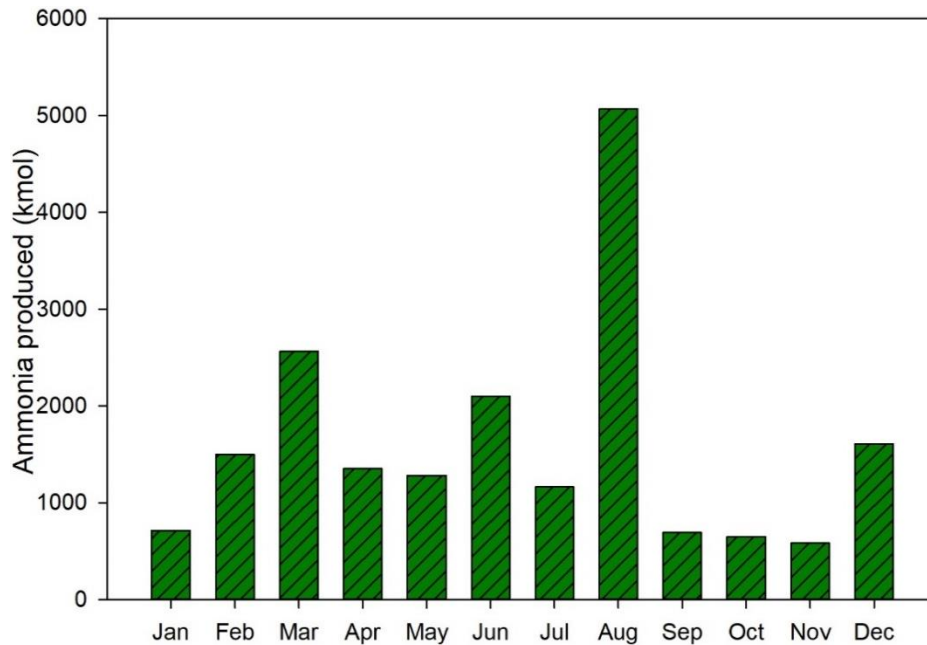


Fig. 6.44 Results of daily ammonia production for the monthly average days for system 1 considering both solar PV and wind farm operation

Comparatively higher hydrogen production is observed on the average day of August that entails a value of 11650.4 kmol. The corresponding exergy destruction in the PEM subsystem is found to be 272.4 MWh. The development of water electrolysis systems entailing low exergy destructions is recommended. This includes the development of new catalyst materials as well as electrode compositions that aid in lowering the power input requirements. The primary losses in energy as well as exergy in the electrolysis cell include the occurrence of different types of polarization losses such as activation, Ohmic and concentration polarization losses.

Efforts should be directed towards investigating the exergy losses associated with these different types of polarization losses. The average day of March entails a high hydrogen production amount of 5889.4 kmol and the corresponding daily exergy destruction is found to be 137.7 MWh. During solar-based system operation, the average day of December was found to be associated with a low daily hydrogen production of nearly 1000 kmol. This rises to 3693 kmol under the integrated solar and wind-based operation. Nevertheless, the daily exergy destruction amounts also rise correspondingly in the PEM subsystem.

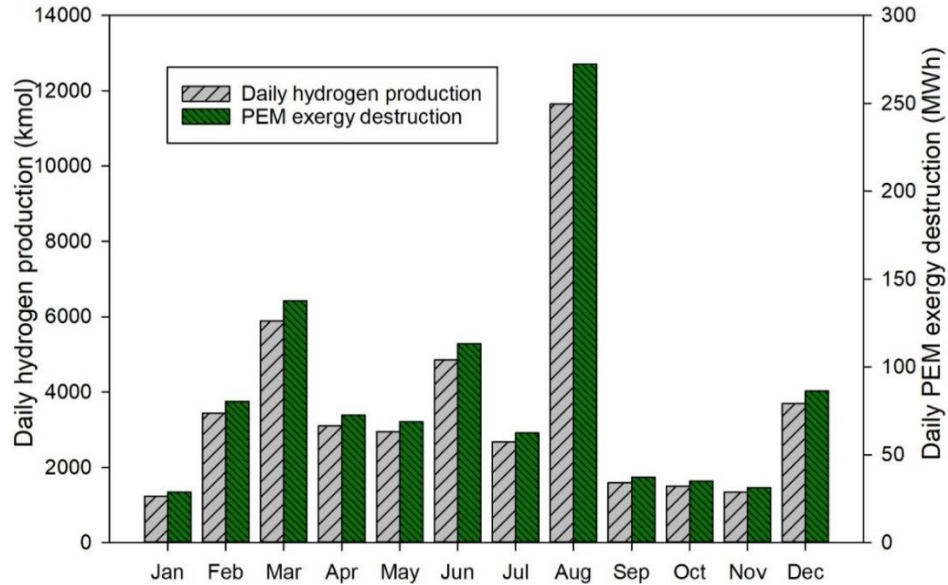


Fig. 6.45 Results of daily hydrogen production and PEM exergy destruction for the monthly average days for system 1 considering both solar PV and wind farm operation

The results of daily exergy destruction amounts entailed in the ASR and COMP subsystems are depicted in Fig. 6.46. The average day of August entails highest daily exergy destructions of 175.6 MWh and 14.7 MWh for the ASR and COMP subsystems respectively. The comparatively higher exergy destructions on this average day are attributed to the higher ammonia production amounts. The ASR is operated for higher ammonia synthesis rates under the availability of higher amounts of excess wind energy. Hence, it is recommended to develop and implement ammonia synthesis reactors that are associated with lower amounts of irreversibilities and thus entropy generation rates.

These can also be attained through the minimization of temperature gradients in the ammonia synthesis subsystem. The average day of March is found to entail daily ASR and COMP exergy destruction amounts of 88.8 MWh and 7.4 MWh respectively. The average day of December is associated with an ASR exergy destruction amount of 55.7 MWh. The corresponding COMP exergy destruction amount is 4.7 MWh. To attain higher system performances, it is essential to decrease the exergy destruction occurring in the reactant compression process. This can be attained by developing and implementing compressors that have higher isentropic efficiencies. As higher isentropic efficiency compressors will be utilized, the entropy generation rates during the compression process can be reduced, leading to lower exergy destruction amounts.

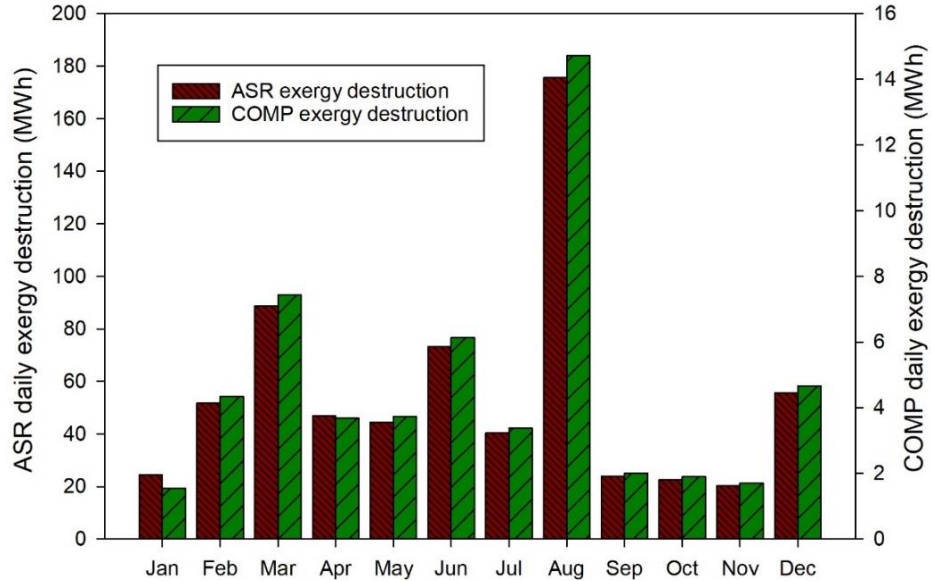


Fig. 6.46 Results of daily hydrogen production and PEM exergy destruction on monthly average days for system 1 considering both solar PV and wind farm operation

The results of AFC energy discharge capacities for the considered average days of the month are depicted in Fig. 6.47. The energy discharge capacity obtained for the average day of August entails a comparatively higher value of 43.5 MWh. This is in conjunction with the total amount of ammonia synthesized during excess solar or wind energy. This is followed by the average day of March, which is associated with an AFC output capacity of 21.9 MWh. Owing to the high ammonia synthesis on the average day of December, an AFC discharge capacity of 13.8 MWh is obtained.

The output capacities are evaluated from the total ammonia stored for energy storage as described in Section 5. The overall thermodynamic performance of System 1 considering the integrated operation of both solar and wind farms is depicted in Fig. 6.48. The energy efficiency of the overall system is found to entail a peak value of 29.3% occurring on the average day March. The corresponding overall exergy efficiency is evaluated to be 30.0%. The exergy efficiencies are evaluated considering the respective average ambient temperatures of each month across the year. The average day of August also entails a comparatively higher energy efficiency of 25.8% and a corresponding exergy efficiency of 26.5%. The higher system efficiencies obtained during these average days can be attributed to the combined effects of available excess solar as well as wind energy.

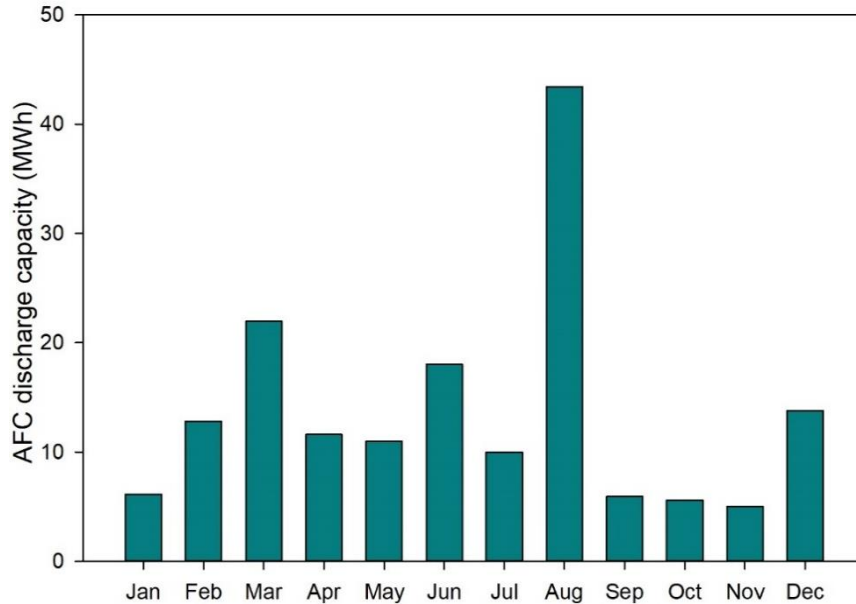


Fig. 6.47 Results of daily AFC energy discharge capacity on the monthly average days for system 1 considering both solar PV and wind farm operation

The average daily value of solar intensity or wind speed is utilized as the threshold criteria for determining the amount of excess available energy. Hence, the months entailing higher ratios of electrical outputs as compared to hydrogen or ammonia outputs are associated with higher overall performances. Nevertheless, the present system provides an effective method to produce clean hydrogen, ammonia and electricity with the usage of clean solar and wind energy. The lowest energy efficiency is observed to be associated with the average day of September, which is observed to have an energy efficiency of 15.7%.

The corresponding exergy efficiency entails a value of 16.5%. This can be attributed to the presence of comparatively lower solar as well as wind energy. The thermodynamic performance of System 1 can be enhanced through the development and utilization of higher-efficiency solar PV panels. The solar panels considered in the analysis of the present system entail a low efficiency of 16.2% that lower the overall performances considerably. However, next generation solar cells such as perovskites or multi-junction solar cells that have attained efficiencies of nearly 47% can aid in enhancing the system performances considerably. The development and utilization of higher efficiency wind turbines is recommended to achieve higher overall energetic as well as exergetic performances.

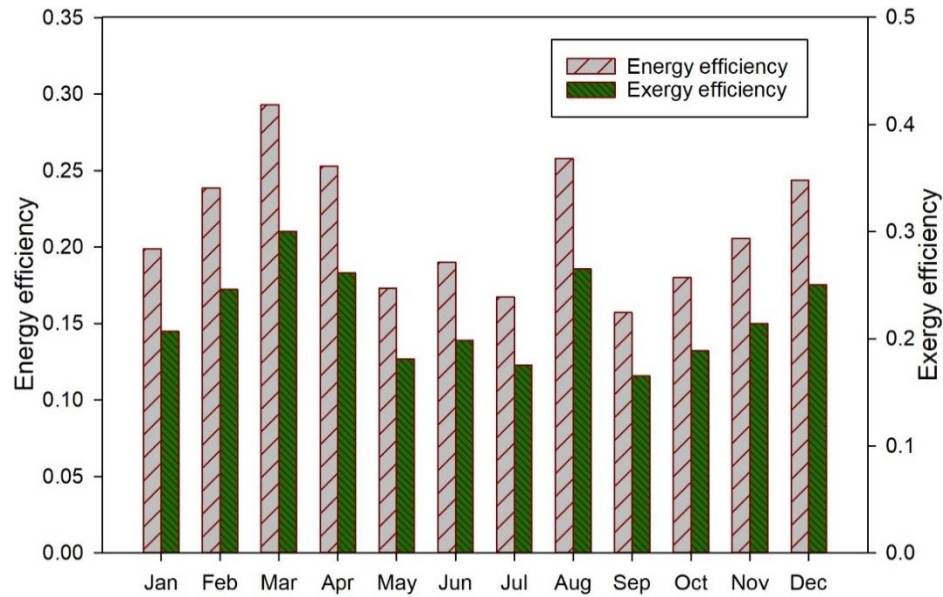


Fig. 6.48 Results of energy and exergy efficiencies of System 1 considering both solar PV and wind farm operation

6.3 System 2 analysis and modelling results

The power output results of the Rankine power generation cycle of system 2 are shown in Figs. 6.49-6.52. Power generation corresponding to the average solar intensities on the monthly average days is denoted by the constant power output lines. During Rankine cycle operation, a portion of the waste heat rejected in the condenser is also utilized as a useful output employed for space heating. When the incoming solar intensities exceed the average value of the day, the excess thermal energy absorbed is stored for later usage. The maximum stable power output is attained for the average day of June that has a stable output of 104.5 MW.

The average days of July and August are found to have peak stable outputs of 100.7 MW and 101.8 MW respectively. However, average day of December entails the least maximum stable output of 43.2 MW. The average day of January is found to have a stable power output of 49.8 MW. As can be observed, the stable outputs entailed with the power generation cycle are associated with varying time ranges. For instance, average days of June to August have stable power outputs entailing durations of 7-9 hours. Nevertheless, this decreases as the daylight hours during a given day reduce.

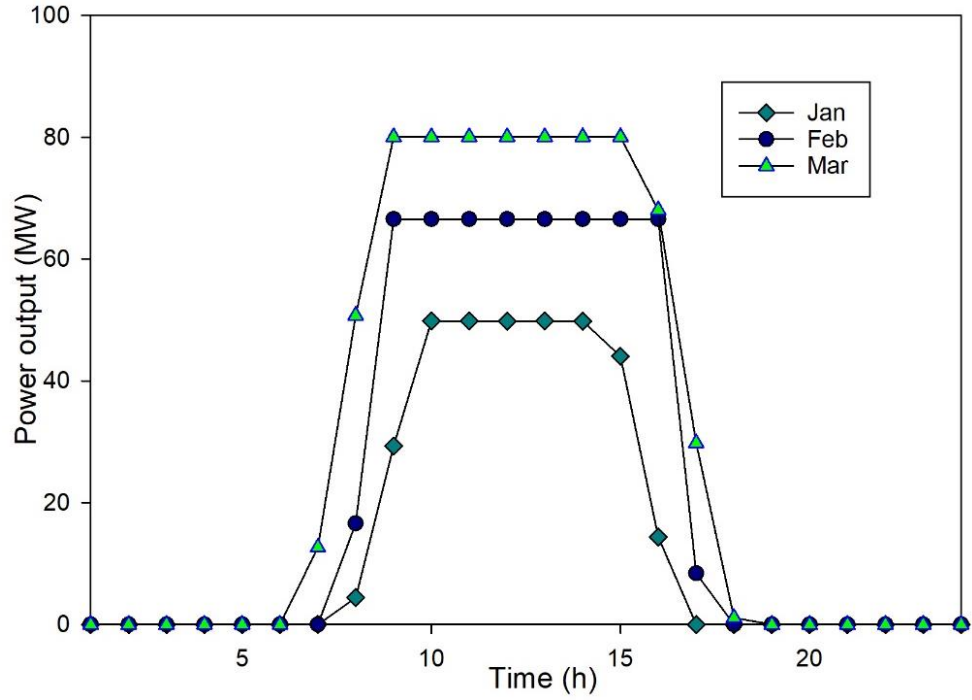


Fig. 6.49 Results of power generation cycle output for the monthly average days of January to March for system 2

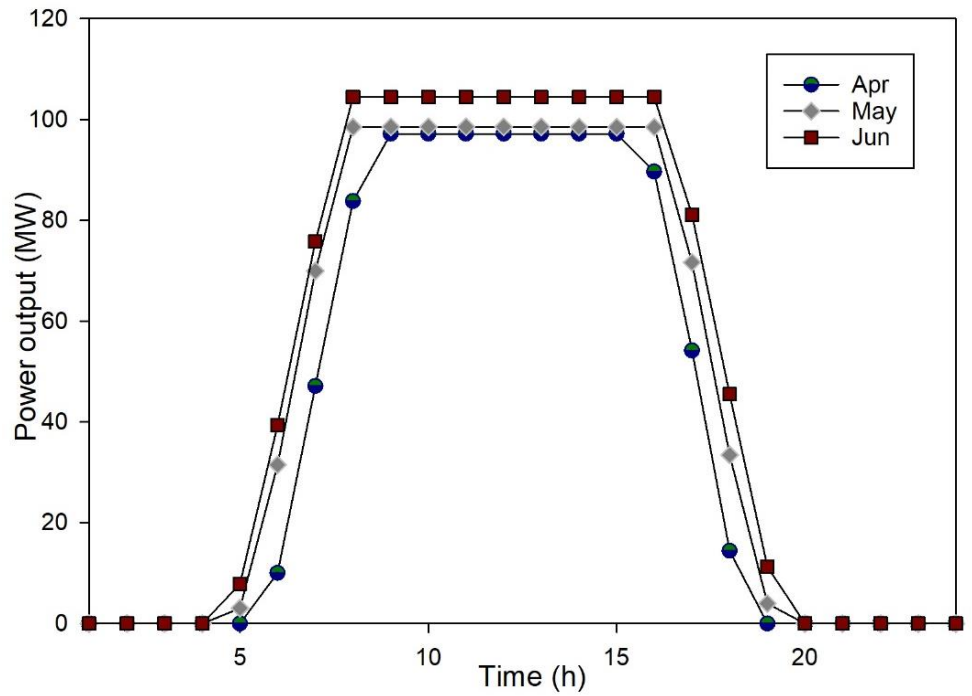


Fig. 6.50 Results of power generation cycle output for the monthly average days of April to June for system 2

The peak stable outputs for the average days of April to June entail values between 97.2 MW and 104.5 MW. Stable outputs between 100.7 MW and 80.2 MW are found to be entailed with the average days of July to September, respectively. Maximum stable power output values ranging between 66.9 MW and 43.2 MW are obtained respectively for the average days of October to December. In the present system, the excess available solar energy is stored to be utilized for power generation when solar intensities are insufficient. Excess wind energy is utilized to synthesize hydrogen as well as ammonia.

The cold tank of the molten salt-based thermal energy storage system provides the electrolyte required for both electrochemical ammonia synthesis as well as the direct ammonia fuel cell. Thus, the developed integrated system firstly produces clean electrical power with available solar as well as wind energy, and synthesizes sufficient amounts of hydrogen as well as ammonia. The electrical output results from the wind farm can be obtained from Figs. 6.38-6.41. Same number of wind turbines are considered in system 2 for comparison. The results obtained correspond to the algorithm utilized for system analysis as described in the previous section.

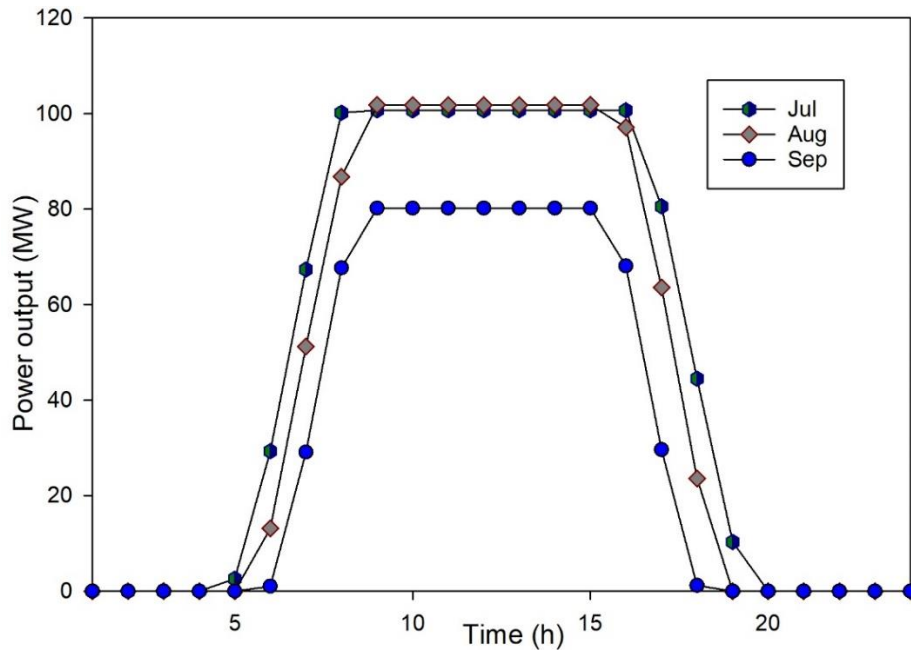


Fig. 6.51 Results of power generation cycle output for the monthly average days of July to September for system 2

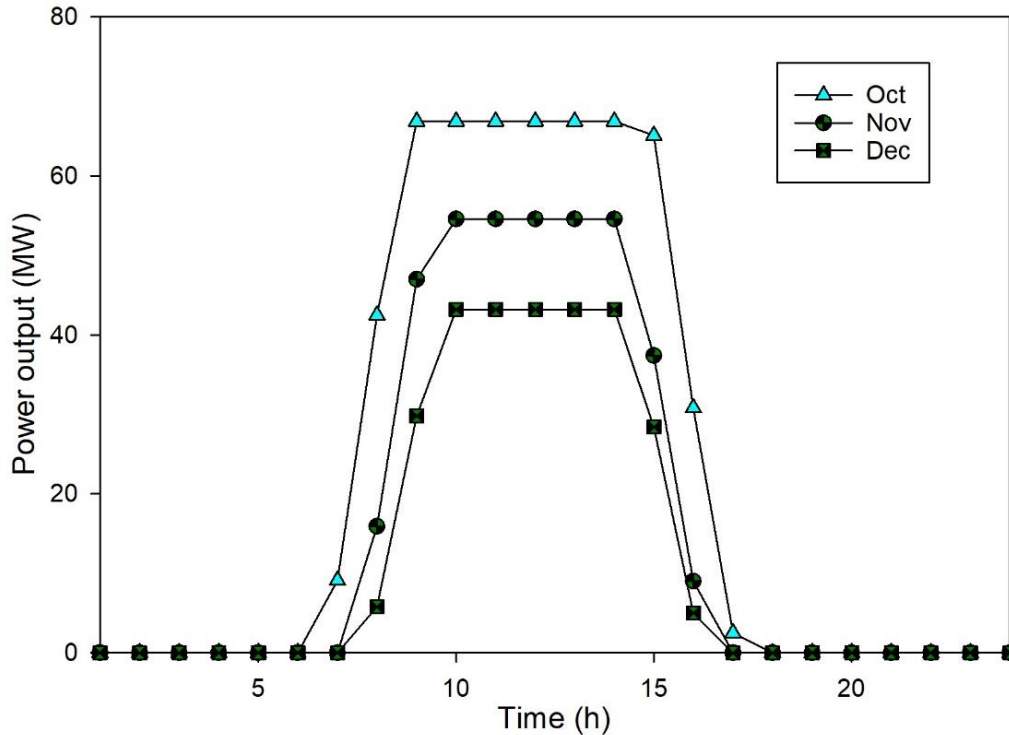


Fig. 6.52 Results of power generation cycle output for the monthly average days of October to December for system 2

Fig. 6.53 depicts a comparison of the amount of ammonia produced on monthly average days. The highest ammonia production is observed to occur in the month of August, where 3204.7 kmol are synthesized. This is followed by the month of March, which entails an ammonia production of 1483.7 kmol. The lowest production occurs on the average day of September, where 69.2 kmol are synthesized. The ammonia synthesis subsystem is integrated with the wind turbine farm, for the utilization of excess available wind energy. As the monthly average day of August entails a higher wind potential, higher amount of ammonia is synthesized. The average day of December, which entailed low availability of solar energy as depicted has a high wind energy potential.

The daily ammonia production, for instance, reaches 1021.8 kmol on this average day. The comparatively lower ammonia synthesis amount obtained for the average day of September can be associated to the lower availability of excess wind energy. The excess amount to be utilized for hydrogen and ammonia production is a function of both the average wind speed of the day as well as the hourly wind speed at a given hour. For the average days entailing higher wind speeds than the average value for longer hours entail comparatively higher

ammonia as well as hydrogen production amounts. A portion of the produced ammonia is also stored for later usage in the direct ammonia fuel cell during periods of low wind energy availability.

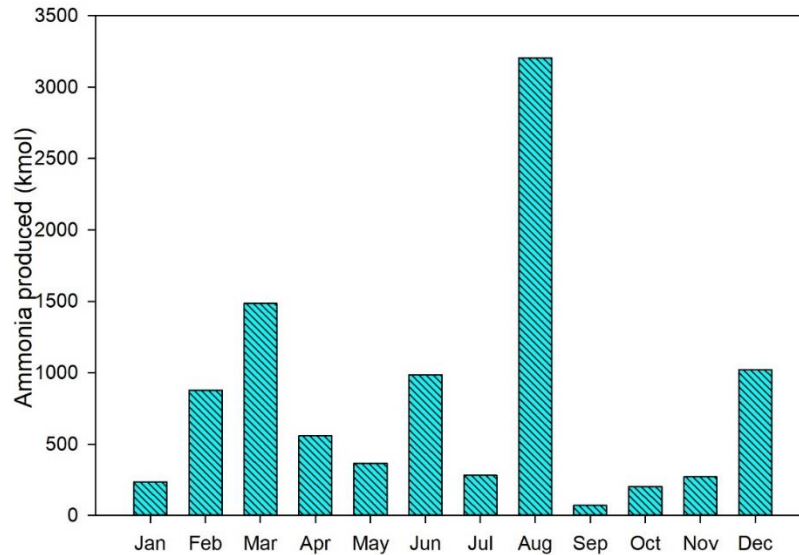


Fig. 6.53 Results of daily ammonia production for the monthly average days for system 2. The results of MEAFC energy discharge capacities after system operation on average days are shown in Fig. 6.54. The highest energy discharge capacity of 47.5 MWh is obtained for the average day of August followed by March, which is associated with 21.9 MWh of energy discharge capacity. The least MEAFC energy discharge capacity is found for the average monthly day of September, which entails 1.03 MWh of discharge capacity after system operation on the monthly average day. The results depict that although the present system can be utilized for clean ammonia synthesis as well as energy production during low solar or wind energy availability, the amount of useful outputs obtained are a function of solar radiation intensities and wind velocities that occur during a given day.

Hence, other auxiliary energy production sources can also be integrated with the developed system to obtain steady outputs. The MEAFC energy output capacity results are in conjunction with the results obtained for daily ammonia synthesis. The average days entailing higher ammonia synthesis amounts are also associated with higher MEAFC energy output capacities. The energy output capacities of the MEAFC subsystem can be further improved with the development of molten alkaline electrolytes that entail higher

ionic conductivities. Electrochemical catalysts that are more compatible with the electrochemical oxidation of ammonia need to be developed that can enhance the peak power densities of these type of direct ammonia fuel cells.

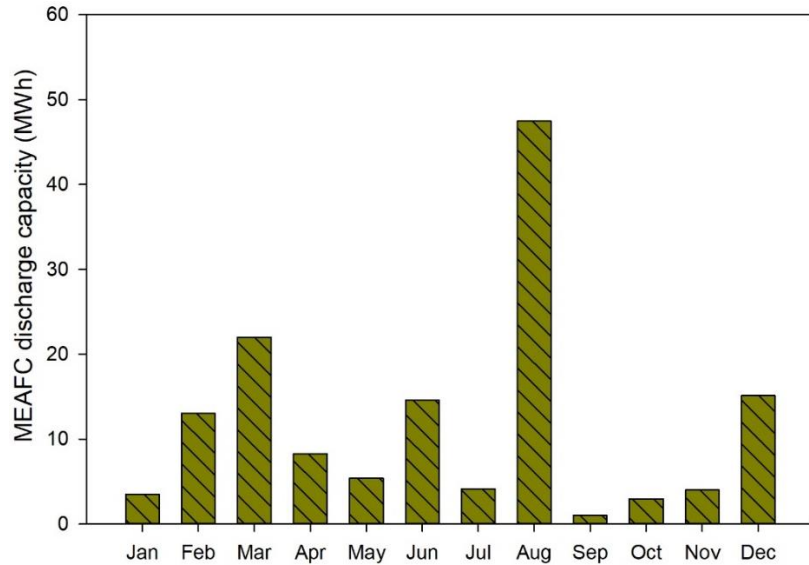


Fig. 6.54 Results of daily MEAFC energy discharge capacities on the monthly average days for system 2

The comparative daily hydrogen production amounts are depicted in Fig. 6.55. The peak daily production of 5634.4 kmol is observed on the average day of August. However, the corresponding exergy destruction associated with the electrolyser is found to be 131.7 MWh. Thus, although high amounts of hydrogen can be produced during the presence of excess wind energy, water electrolyzers having lower irreversibilities need to be developed. The power input requirements need to be specifically reduced to attain higher overall system performances. Electrolysis cells entailing lower exergy losses associated with different types of polarization losses also need to be considered.

In the present system, the average day of March also entails a comparatively high hydrogen production amount of 2608.7 kmol. The daily hydrogen production results are also in conjunction with the amount of excess wind energy available during the average days of each month. For instance, the months of January and February are found to entail daily hydrogen production amounts of 413.3 kmol and 1543 kmol respectively. However, the average day of December is associated with a higher daily production of 1796.5 kmol. The

least daily hydrogen production is found to occur on the monthly average day of September, which entails a hydrogen production of 121.6 kmol.

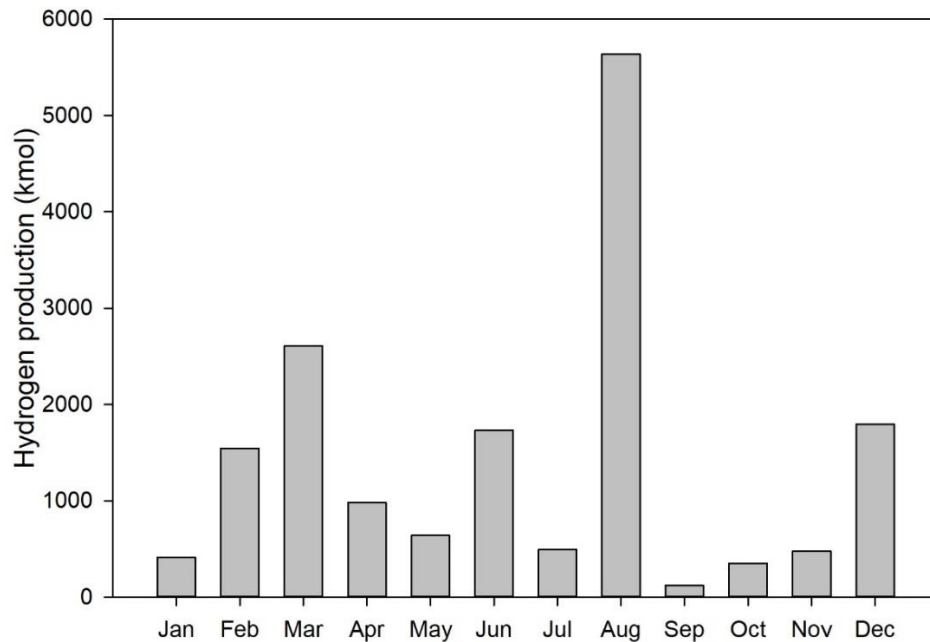


Fig. 6.55 Results of daily hydrogen production amounts on the monthly average days for system 2

The results obtained for the useful heating outputs are presented in Fig. 6.56. The peak daily heating output amount reaches a value of 761.8 MWh on the average day of June. The average days of July and August entail daily heating outputs of 723.7 MWh and 664.9 MWh respectively. However, the monthly average days entailing lower solar energy availability such as January and December, the daily heating outputs are evaluated to be 216.5 MWh and 180.7 MWh respectively. The heating output results correspond to the operation of the solar-based power generation cycle.

The amount of heating that can be obtained from the system is a function of the amount of thermal energy provided to the reheat Rankine cycle and the corresponding amount of thermal energy released in the condenser. The utilization of available waste heat results in the attainment of higher overall performances as will be described in the proceeding discussions. The present system, hence, provides useful outputs of clean electricity, hydrogen, ammonia and heating. The multigeneration of these useful commodities results in higher overall energetic as well as exergetic performances as compared to conventional

plants that rely on the production of a single commodity such as electricity or cogeneration of electricity and heat.

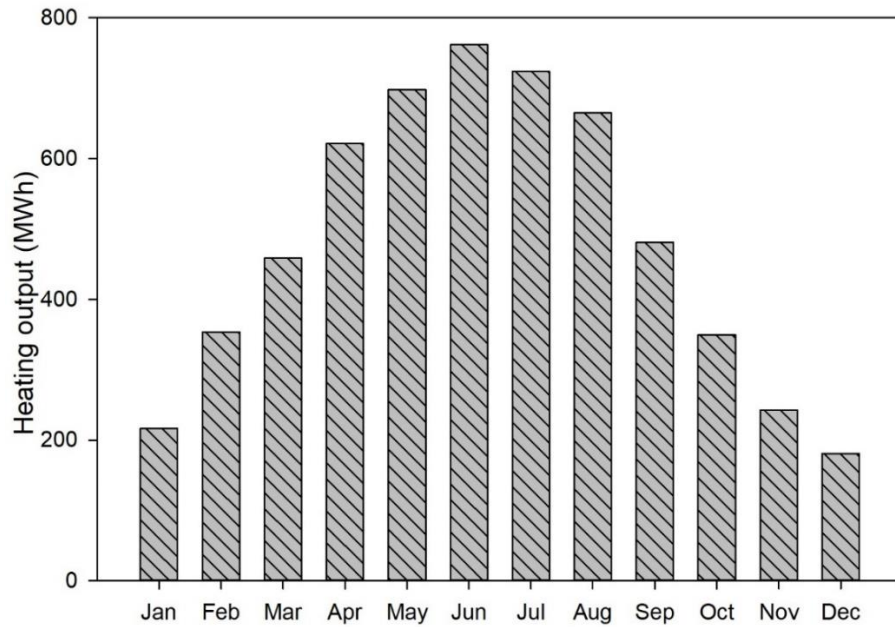


Fig. 6.56 Results of daily heating outputs on the monthly average days for system 2

It is essential to integrate the clean production of hydrogen as well as ammonia in solar and wind energy-based systems to produce the important commodities that are used extensively across the globe, through environmentally benign energy resources. The results of the energy discharge capacities from the power generation cycle considering the amount of excess solar energy stored during a given day are depicted in Fig. 6.57. The peak energy discharge capacity reaches 358.8 MWh that is associated with the average day of May. This is followed by July, which entails an energy discharge capacity of 351.7 MWh.

As low amounts of excess solar energy are available during the average days of January and December, the energy discharge capacity of the power generation cycle entails values of 101.9 MWh and 98.5 MWh respectively. The average days of April, August and September are found to be associated with similar discharge capacities of 269.8 MWh, 261.8 MWh and 270.1 MWh respectively. The energy discharge capacities are evaluated from the excess solar thermal energy stored considering the efficiencies of the reheat Rankine cycle at different energy input values corresponding to the excess solar thermal energy stored during a given day.

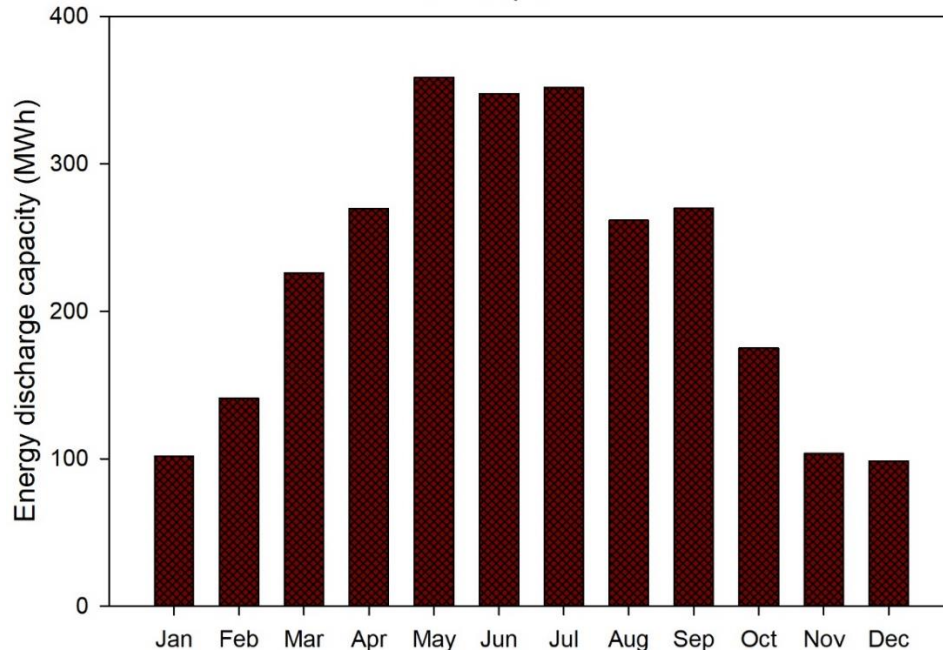


Fig. 6.57 Results of daily energy output capacities from the power generation cycle on the monthly average days

The results of daily exergy destructions associated with steam turbines are depicted in Figs. 6.58-6.60. The peak daily exergy destruction evaluated for T1 entails a value of 10.5 MWh associated with the average day of June. T2 entails an exergy destruction amount of 10.9 MWh at the peak value on the average day of June. However, T3 is observed to be associated with higher daily exergy destructions. For instance, on the average day of June, T3 entails a daily exergy destruction of 45.6 MWh. Similarly, the average day of July entails daily exergy destructions of 9.9 MWh and 10.4 MWh respectively. Nevertheless, T3 is found to be associated with a higher daily exergy destruction of 43.4 MWh. This can be attributed to the higher power generation rates entailed in T3.

As the amount of power generated in T3 increases, the amount of corresponding irreversibilities arising during the process also entail a rising trend. Hence, as the power generation in the turbine rises, the corresponding exergy destruction rate also increases. The monthly average days having low solar availability such as January are found to have daily exergy destructions of 2.97 MWh, 3.1 MWh and 12.9 MWh for T1, T2 and T3 respectively. As the exergy destruction amount signifies the amount of useful work potential lost, it is recommended to direct efforts towards developing steam turbines

entailing higher isentropic efficiencies that can aid in reducing the irreversibilities associated with power generation process.

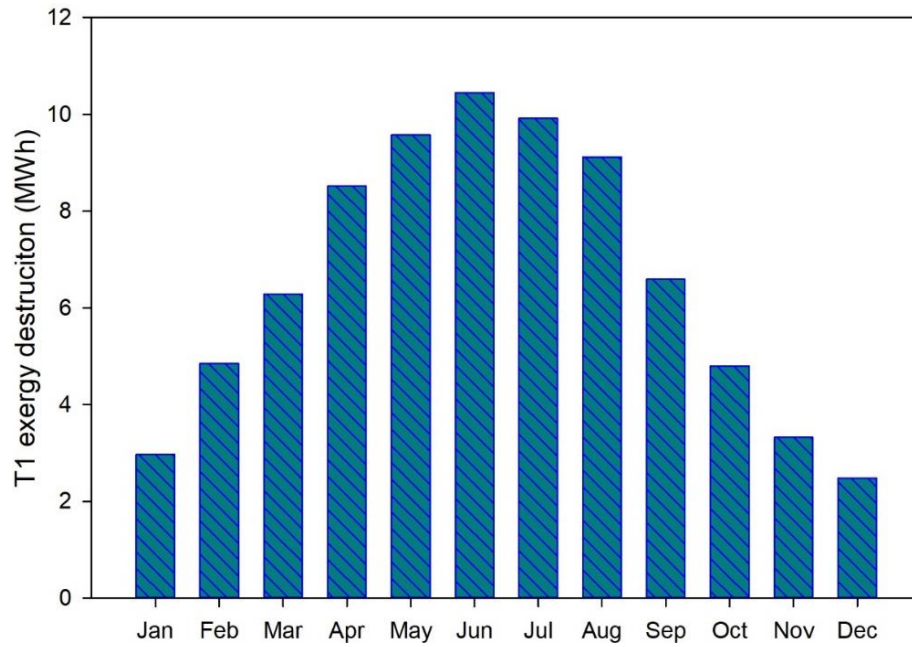


Fig. 6.58 Results of daily T1 exergy destructions on the monthly average days

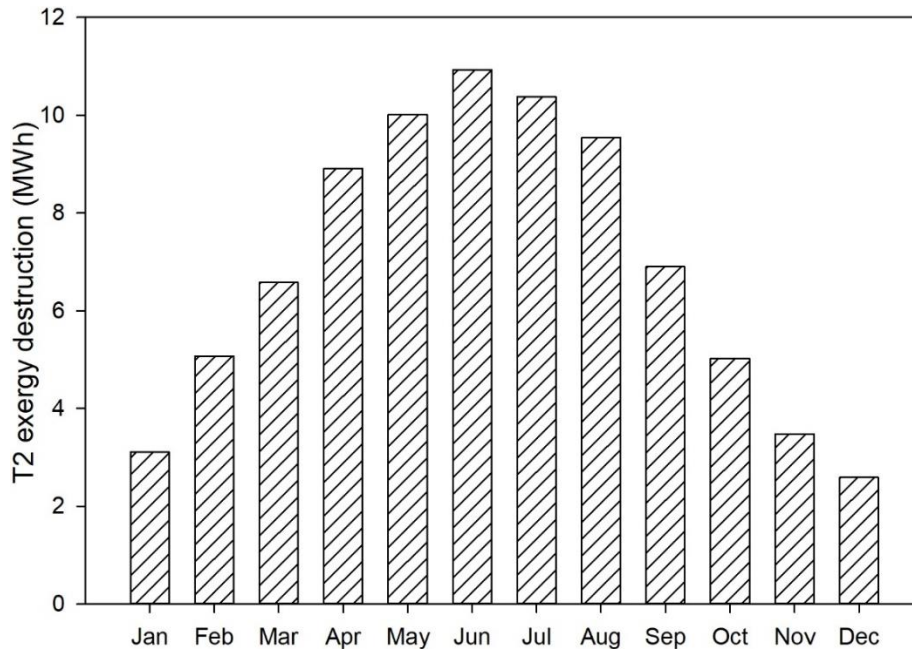


Fig. 6.59 Results of daily T2 exergy destructions on monthly average days

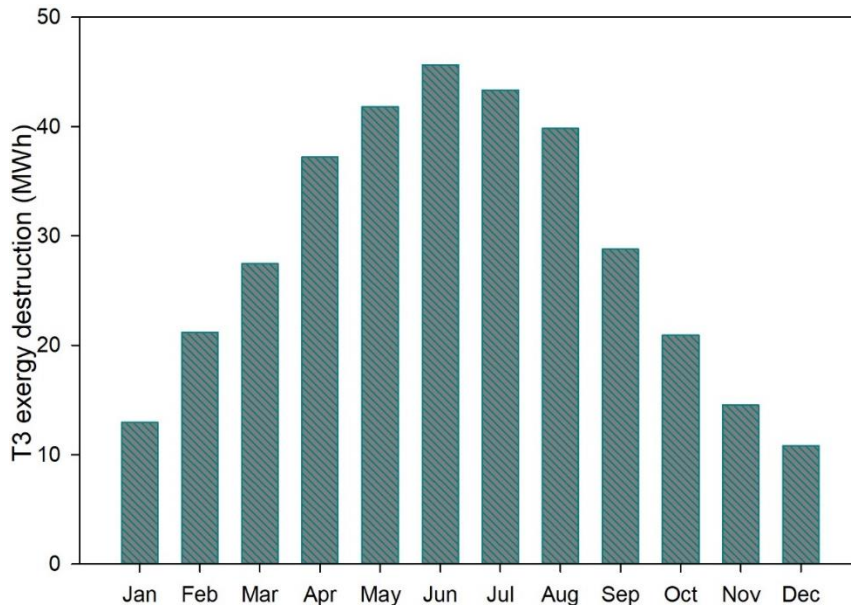


Fig. 6.60 Results of daily T3 exergy destructions on monthly average days

The overall performance results of the system for monthly average days are depicted in Fig. 6.61. The monthly average day of September is found to entail comparatively high efficiencies. For instance, the energy efficiency is found to be 51.1% and the exergy efficiency is determined as 52.7%. However, the months of December and August are observed to entail comparatively lower efficiencies. The energy efficiency for the monthly average day of December, for instance, is evaluated as 35.6% and the corresponding exergy efficiency is determined to be 35.9%. For the monthly average day of August, the energy efficiency is found to be 38.5% and the exergetic efficiency is 38.9%.

It should be noted that although the month of August entails a comparatively lower efficiency, it is associated with higher useful outputs. The amount of electrical energy output, for instance, is higher on the monthly average day of August owing to high wind speeds. The amount of ammonia synthesized is also higher on this average day. Thus, through the operational strategy implemented in the present study that includes storing energy when solar intensities as well as wind speeds exceed the daily average, some months with lower overall efficiencies can entail higher amounts of useful outputs. It is also recommended to investigate the integration of other energy storage methods with the developed system to analyze the change in overall efficiencies.

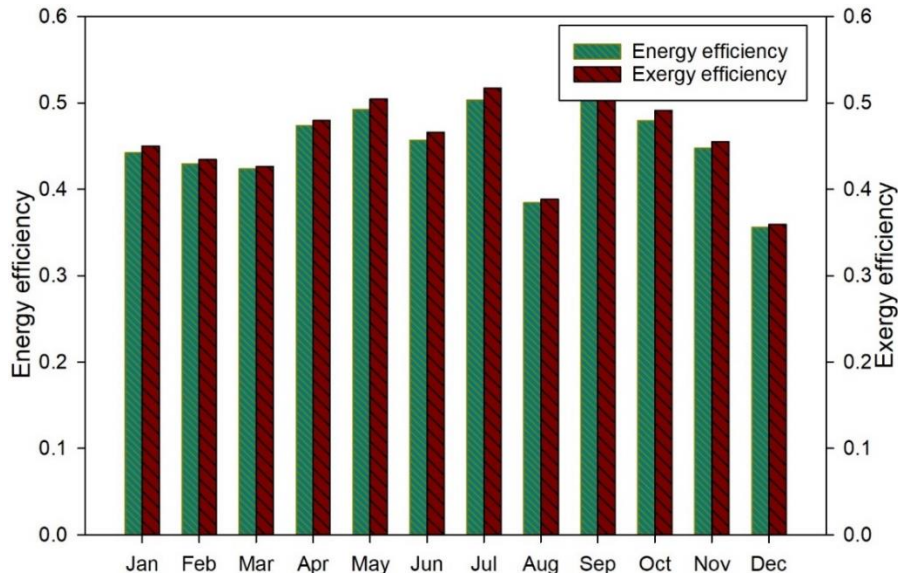


Fig. 6.61 Results of daily energy and exergy efficiencies of system 2 on monthly average days

6.4 System 3 analysis and modelling results

The results of the solar-based electricity production are depicted in Figs. 6.62-63. These are based upon the working methodology described earlier, which includes the daily average solar insolation as the criteria for deciding the excess solar energy. When the incoming solar radiation intensity exceeds the day average, the power generation cycle is operated to produce a power output at the average value and the excess available solar energy is stored in the HT. The flat curves observed denote the power output values with average solar intensities on the respective monthly average days.

The maximum power output value of 104.5 MW occurs for June where the constant power output value is attained for 8 hours. A maximum power output of 100.7 MW is attained in July where the stable value is maintained for 8 hours. On the monthly average day of December, the least peak stable value of 43.2 MW is attained that maintains for 6 hours. A low peak stable value of 49.8 MW is obtained for January that is maintained for 5 hours. The excess solar power is stored in the HT for later usage. In the months with low solar intensities such as January and December, the peak values of excess solar power on the monthly average days are observed to be 70.4 MW and 69.3 MW respectively. The durations of excess power on these days are 7 hours. The developed system with the

proposed working methodology allows the operation of the solar-powered RC with a stable power output for durations between 6 and 8 hours. The amount of maximum stable electrical power output that could be obtained from the power generation cycle is a function of the daily solar radiation intensities and the number of daylight hours. Thus, the working methodology of the present system can also be adapted for different applications. The amounts of hydrogen and ammonia synthesized and used as useful outputs on the monthly average days are depicted in Figs. 6.64-65. The highest amounts of 9943.8 kmol and 5767.4 kmol are obtained for daily hydrogen and ammonia synthesis that are observed to occur in August.

This is attributed to the high amount of excess wind energy potential on this day. The average day of March also entails high synthesis amounts. In March, the daily hydrogen synthesis is evaluated to be 4602.1 kmol and the ammonia synthesis is found as 2669.2 kmol. In months with low wind energy potential such as September and October, 105.2 kmol and 360.3 kmol of ammonia are synthesized respectively. Thus, the present system provides an effective method of synthesizing clean ammonia and hydrogen across the year. However, it is recommended to investigate the developed system with different operational strategies that can be designed for specific applications.

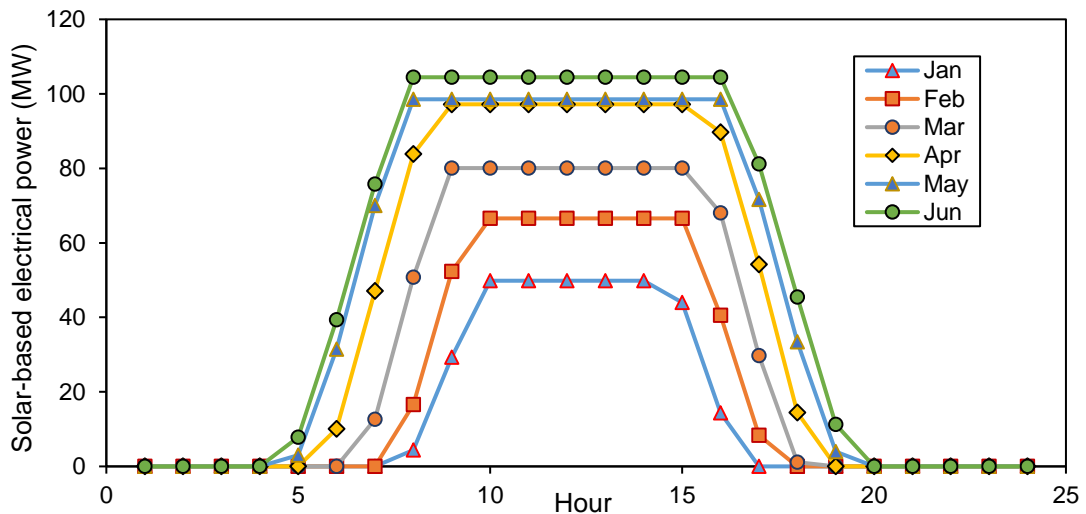


Fig. 6.62 Results of solar-based power output for system 3 on monthly average days of January to June

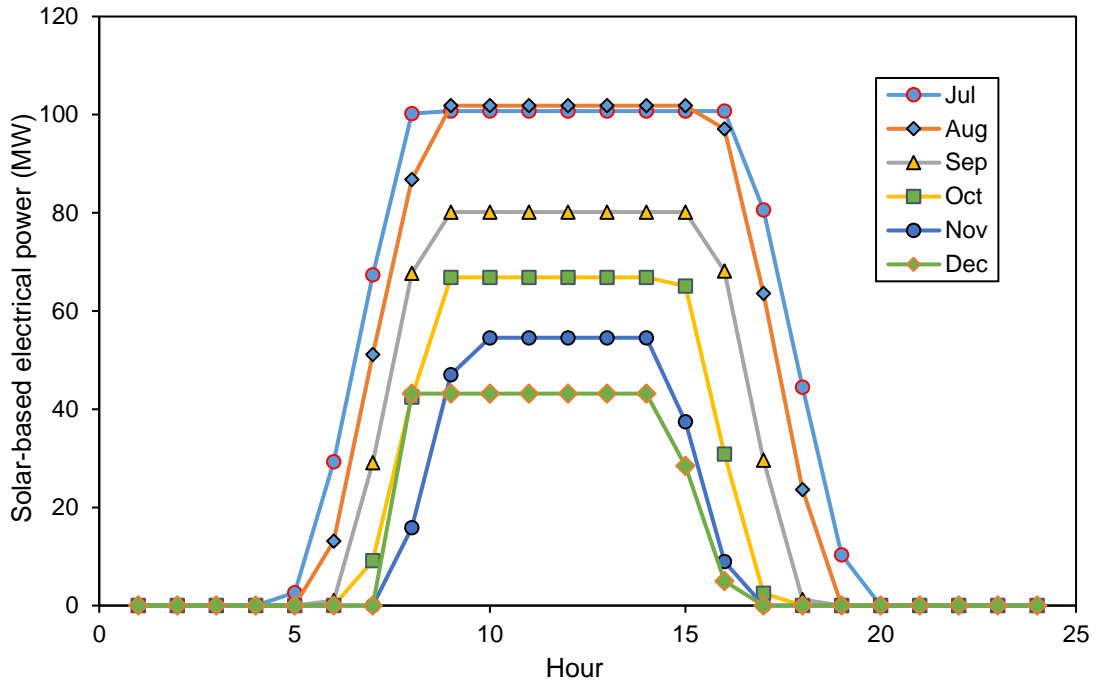


Fig. 6.63 Results of solar-based power output for system 3 on monthly average days for July to December

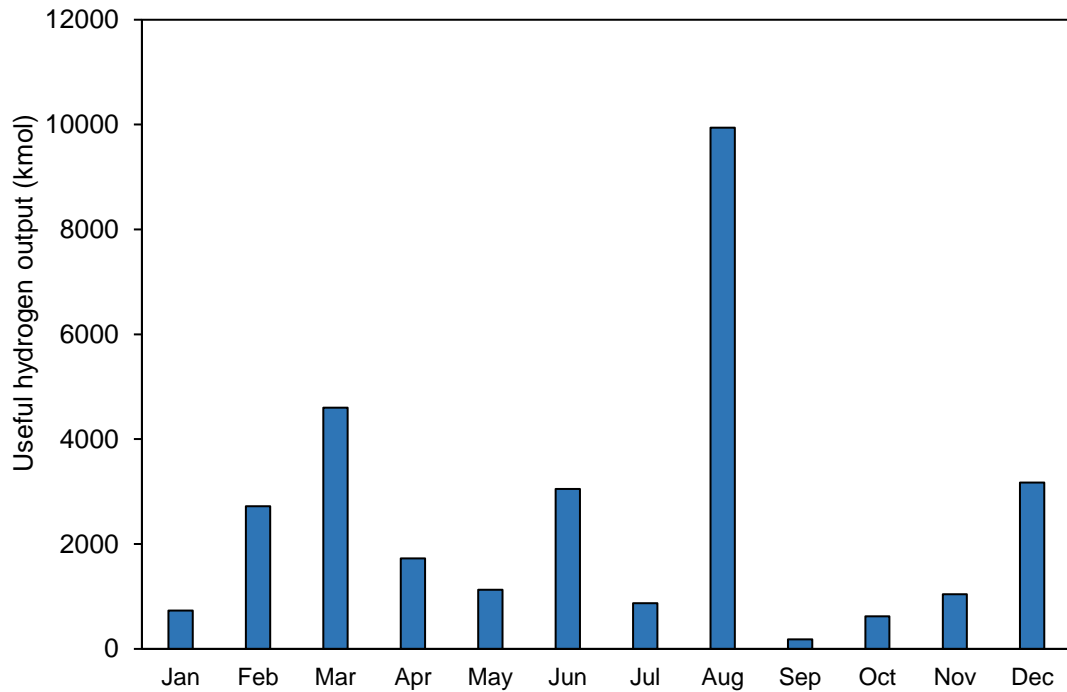


Fig. 6.64 Results of daily hydrogen production on the monthly average days for system 3

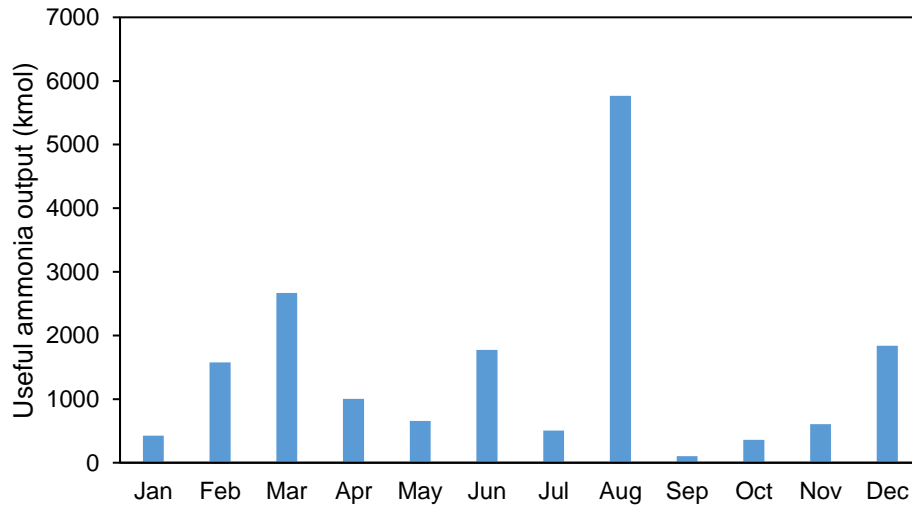


Fig. 6.65 Results of daily ammonia production on the monthly average days for system 3. The amount of heat output provided by the developed system during average days is depicted in Fig. 6.66. The maximum heat output potential is found for June where 754.5 MWh of daily heat output is evaluated. This is followed by July that entails a daily heat output value of 716.8 MWh. The least heat output potential of 178.6 MWh is obtained for February. Hence, the proposed system provides an effective and environmentally benign method to provide heat as a useful commodity.

The thermal energy input provided to the ADR on the monthly average days is depicted in Fig. 6.67. The highest thermal energy input requirement of 96.1 MWh is found in August. This is attributed to the high amount of ammonia synthesized on this day. This is followed by March and December, which entail requirements of 44.5 MWh and 30.7 MWh respectively. The least requirement is entailed with September, which is associated with a requirement of 1.8 MWh. Nevertheless, the amount of thermal energy input required for the ADR is considerably lower than the excess solar energy stored in the HT.

For instance, in January, the excess solar energy stored in the HT is 241 MWh whereas the ADR energy requirement is 7 MWh. Similarly, in August, the excess solar energy stored is 777.7 MWh, however, the ADR energy requirement is 96.5 MWh. Thus, this shows that the developed system would provide an effective integration methodology for multigeneration. Fig. 6.68 depicts the energy discharge capacities from the FC subsystem

for the monthly average days. The highest FC energy capacity of 199.5 MWh is found for August.

This is followed by March in which the capacity is found to be 92.3 MWh. December is found to entail a capacity of 63.6 MWh. The minimum FC energy discharge capacity of 3.6 MWh is found for September, which is followed by October (12.5 MWh) and November (20.9 MWh). As the total ammonia synthesized is utilized as a useful output of the system and as an energy storage medium, the FC energy output capacity is a function of the excess wind energy. The reheat Rankine power generation cycle (RC) discharge time capacity of each day is depicted in Fig. 6.69.

These discharge capacities are a function of the excess solar energy available during the day as well as the daily average RC power outputs. The amount of total solar energy stored is discharged at the average power output of the day to determine the discharge time capacities. A discharge time of 1.4 hours is found for the average days of January and February. This is obtained at the average RC power outputs of 49.8 MW and 66.6 MW respectively, which also denote the stable power outputs for these months. May is found to entail a high discharge time capacity of 2.7 hours, when discharged at the power output value of 98.5 MW. The least discharge time of 1.3 hours is observed to occur in November, which is obtained for a discharge power of 54.6 MW. Thus, the present system provides an effective method to store excess solar as well as wind energy.

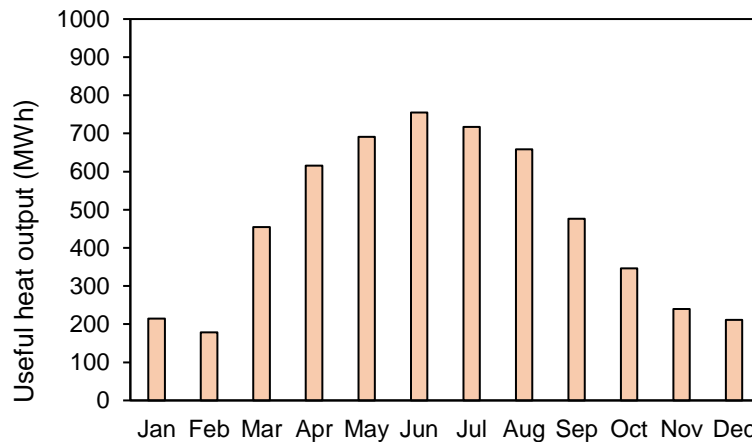


Fig. 6.66 Results of daily useful heating outputs on monthly average days for system 3

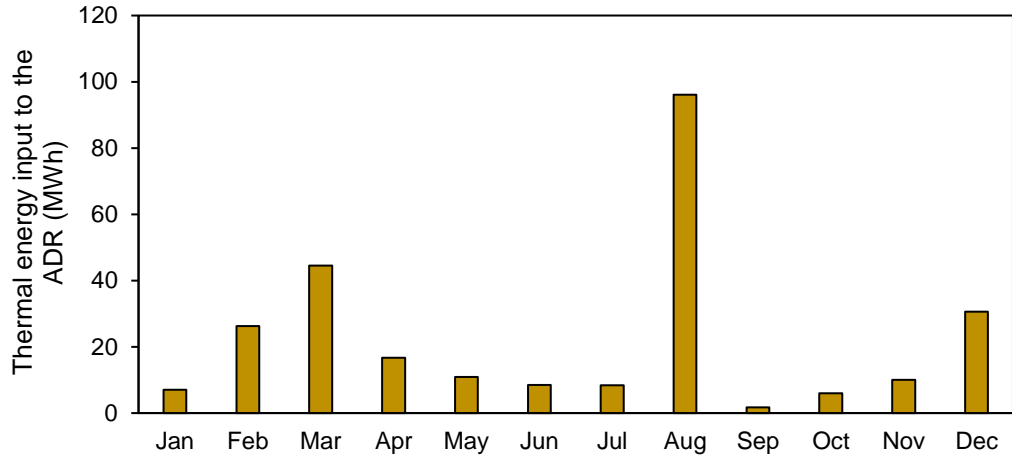


Fig. 6.67 Results of daily ADR thermal energy input requirement on monthly average days

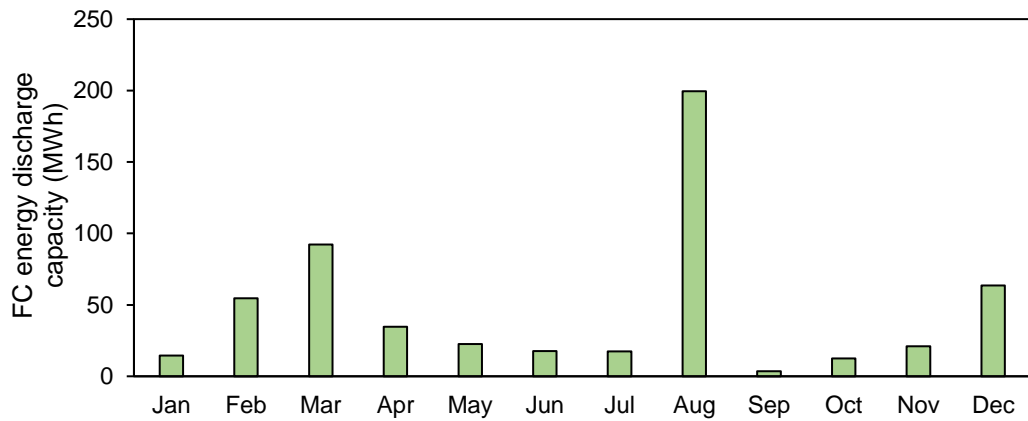


Fig. 6.68 Results of daily FC energy discharge capacities on monthly average days

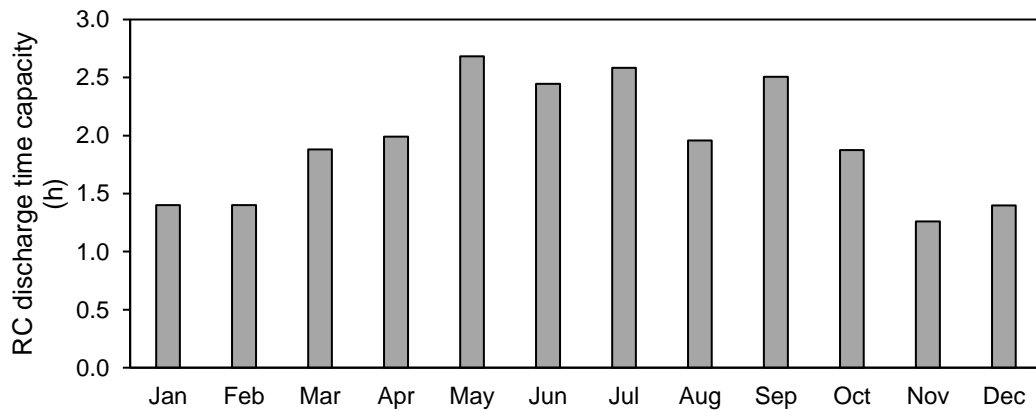


Fig. 6.69 Results of daily RC energy discharge capacities on monthly average days

The overall energetic and exergetic performance of the system 3 is depicted in Fig. 6.70. The highest performance is observed for July, which is found to entail energetic and exergetic performances of 57.8% and 60.5% respectively in terms of efficiencies. September entails high performances with efficiencies of 57.5% energetically and 60.4% exergetically.

The month of May is found to have efficiencies of 56.8% and 59.2% energetically and exergetically respectively. The lowest efficiencies of 49.9% and 51.1% are obtained energetically and exergetically for February.

The developed system entails higher efficiencies across the year than stand-alone solar or wind power plants and thus provides an effective way of producing clean electricity, ammonia, hydrogen and heat.

The challenge of intermittent solar intensities across different months is also addressed and satisfactory system performance is obtained through the proposed operational methodology. It is recommended to expand the developed system with its operational algorithm for producing different useful commodities along with currently produced outputs.

These can include the production of methanol or ethanol incorporating carbon capture and conversion to useful products. The present system can also be investigated with other sources of renewable energy such as geothermal and biomass-based resources.

Nevertheless, solar and wind energy resources are considered in the present study as they comprise the primary renewable energy resources that are being currently implemented at large-scales across the globe.

It is recommended to develop different operational strategies for the proposed systems depending on the solar and wind availability. The portion of solar or wind energy to be used by the systems is dependent on the availability of these sources at a given location.

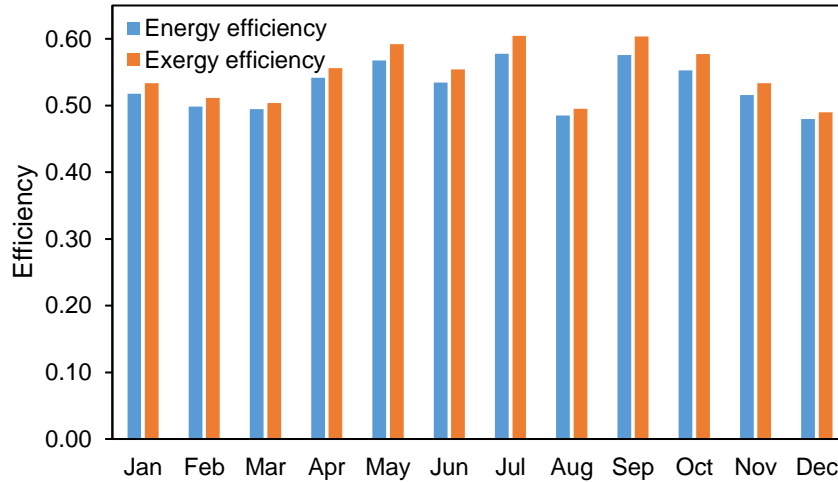


Fig. 6.70 Results of daily overall energy and exergy efficiencies of System 3 on monthly average days

6.5 Exergoeconomic analysis results

In this section, the results of the exergoeconomic analysis performed are described. The results obtained for each system are presented in separate chapters. Different parametric studies have been performed to investigate how the exergoeconomic performance of each system varies with changing operating conditions and system parameters.

6.5.1 System 1 exergoeconomic analysis results

The results of the exergoeconomic analysis performed on system 1 are presented in this chapter. Primary results obtained from the parametric analysis considering changes in the ambient temperature are shown in Fig. 6.71. For an ambient temperature variation from -20°C to 30°C , the exergetic efficiency changes from 28.5% to 28.6% respectively. Although the change in overall exergy efficiency is not significant, the ambient temperature effects the exergy destruction rates as well as the exergy destruction costs in different system components. The ASR exergy destruction rate, for instance, changes from 23105 kW to 29035 kW for the same change in temperature. Similarly, the PV rate of exergy destruction is 177723 kW at -20°C , which decreases to 172530 kW at a higher temperature of 30°C . Thus, although higher temperatures increase exergy destruction rates in the ASR, they provide better exergetic performance of the PV-based power generation subsystem.

This signifies the need for optimizing energy systems to determine optimal operating conditions for system operation. The effect of ambient temperature on the total exergy destruction cost rate as well as exergy destruction cost rates of major system components is also depicted in Fig. 6.71.

The total change in exergy destruction cost rate entails a value of 1084 \$/h for the range of ambient temperature considered. Although the changes in the exergy destruction cost rates are not significant for the PSA and PV subsystems, the ASR exergy destruction cost rate changes by 1158 \$/h for the 50°C change in ambient temperature considered.

During the development of new energy systems, it is suggested to investigate system conditions providing optimal performances depending on the location chosen and associated ambient conditions. The solar intensity varies the system exergoeconomic performances as shown in Figs. 6.72 and 6.73. The effects on major subsystems including the ASR, PEM and PV are shown in Fig. 6.72. The rates of exergy destruction are observed to rise with increasing solar intensities.

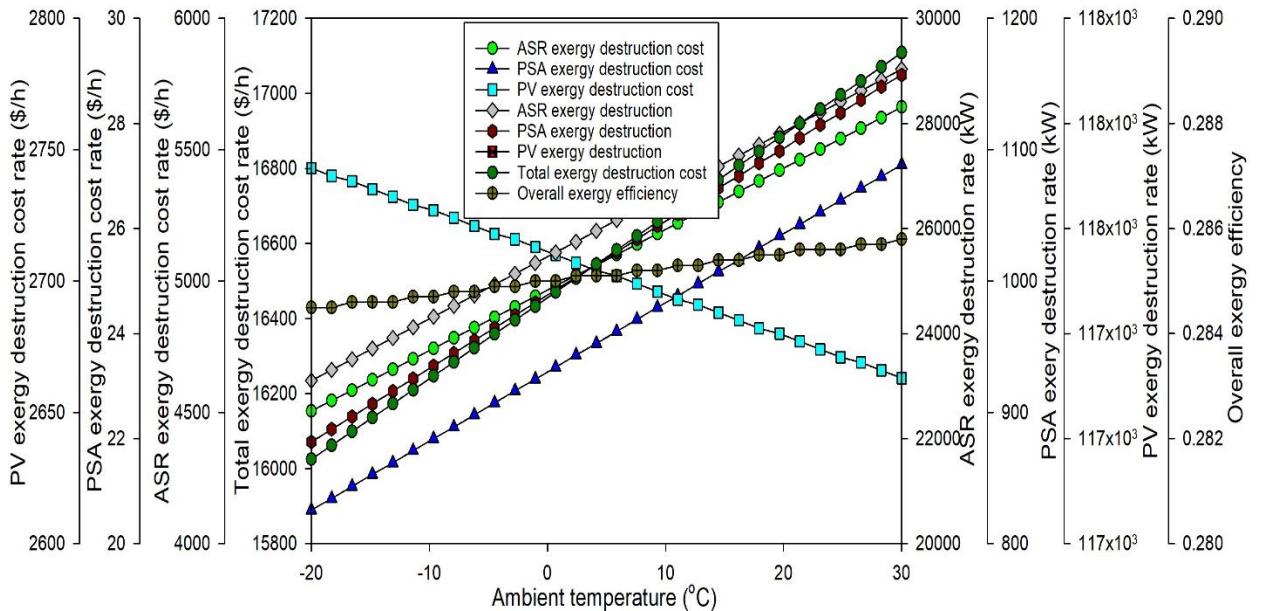


Fig. 6.71 Effects of changes in the ambient temperature on the exergoeconomic performance of System 1

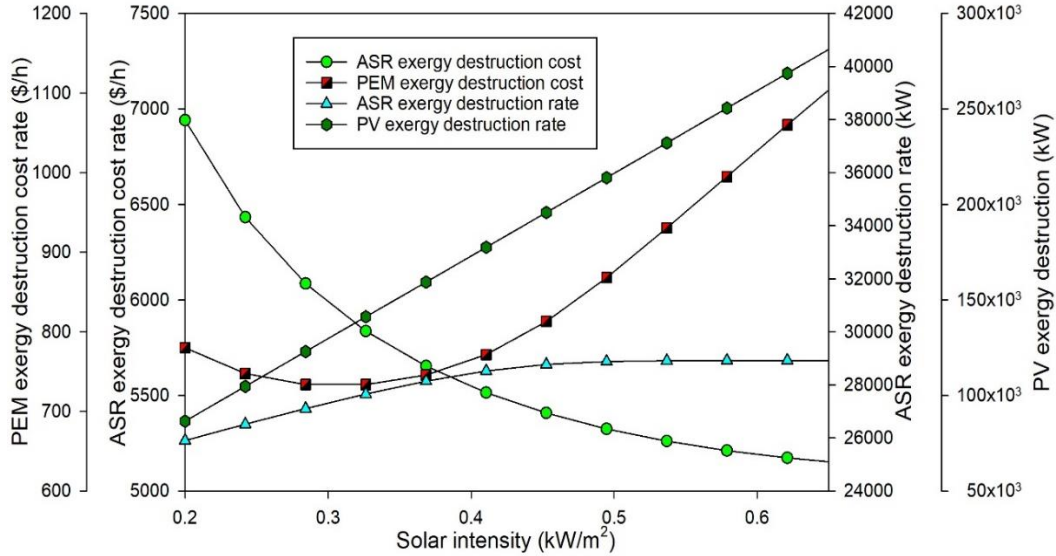


Fig. 6.72 Effects of changes in the solar intensity on the exergoeconomic performance of the ASR and PV subsystems

The highest increase is observed to occur in the PV power generation subsystem, which entails a rise of 346.1 MW in the exergy destruction rate for an increase in the solar intensity from 0.2 kW/m² to 1.0 kW/m². The ASR and PEM subsystems are associated with increases of 14.5 MW and 10.7 MW for the same solar intensity change, respectively. However, the exergy destruction cost rates have a reducing trend with rising intensities for the ASR subsystem. Hence, it is essential to determine conditions, which would provide the lowest exergy destruction costs.

Overall exergoeconomic performance as a function of the solar intensity is shown in Fig. 6.73. The exergy efficiency decreases from 34.2% to 22.4% for the considered change in the solar intensity. This can be attributed to the increased exergy destruction rates in different system components with rising intensities. However, the overall exergoeconomic factor is observed to be higher at elevated solar intensities.

This can be attributed to the decrease in the total exergy destruction cost rate as well as the PV exergy destruction cost rate. The total exergy destruction cost rate of the system, for example, decreases from 18516 \$/h to 16429 \$/h as the intensity varies from 0.2 kW/m² to 1.0 kW/m². However, the total investment cost rate increases as the intensity rises, this can be attributed to the additional operational costs that would be associated with the higher power generation.

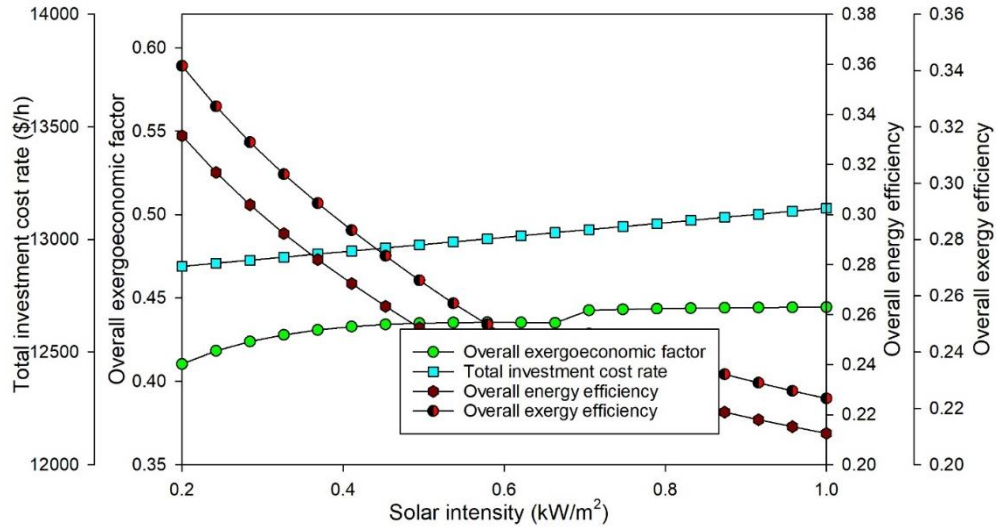


Fig. 6.73 Effects of changes in the solar intensity on the overall exergoeconomic performance of System 1

Depending on the available solar energy resource at a given location, the system parameters should be set such that they provide minimal cost rates and maximum efficiencies. PV energy conversion efficiency affects overall performance as well as the subsystem performances as shown in Figs. 6.74 and 6.75. The effect of PV efficiency on major exergy destruction rates and exergy destruction cost rates is shown in Fig. 6.74.

The exergy destruction cost rate entails a decreasing trend for the ASR and PV subsystems while an increasing trend is found for the PEM subsystem, when the PV efficiency is increased. For instance, the ASR exergy destruction cost rate reduces from 6358 \$/h to 5316 \$/h, while the PV exergy destruction cost decreases from 5163 \$/h to 1840 \$/h. The exergy destruction rates are found to rise with increasing PV efficiencies for the ASR and PEM subsystems.

This can be attributed to higher hydrogen production and ammonia synthesis at higher PV efficiencies. As the rate of hydrogen production rises, the exergy destruction in the PEM electrolyser also increases owing to associated irreversibilities. Similarly, as the rate of ammonia production is increased in the ASR, the exergy destruction amount also rises. The increase in overall exergoeconomic performance of the system is shown in Fig. 6.75.

The overall exergoeconomic factor of the system is found to change from 38.8% to 44.7% as the PV efficiency varies from 10% to 20%. The exergetic efficiency increases from

26.3% to 29.8% for the same variation in PV efficiency. The overall performance improvements can also be attributed to the decrease in total exergy destruction cost rates with rising PV efficiencies. When the PV efficiency rises from 10% to 20%, total exergy destruction cost rate reduces from 20345 \$/h to 16034 \$/h respectively.

Hence, although the total investment cost rate rises, better system exergoeconomic performances can be achieved through the usage of PV panels entailing high energy conversion efficiencies. Interest rate considered in the design parameters can fluctuate depending on the economic situation and other contributing factors. Thus, the effect of interest rate on the exergoeconomic system performance is depicted in Figs. 6.76 and 6.77.

The rise in exergy destruction cost rate of different subsystems with the interest rate is shown in Fig. 6.76. The PV subsystem is found to be associated with a 2.6 times increase in the exergy destruction cost rate when the interest rate is changed from 5% to 20%. The ASR and AFC subsystems also entail similar increases respectively for the same change in interest rate. Interest rate is hence an important factor that should be minimized to obtain better system economic performances.

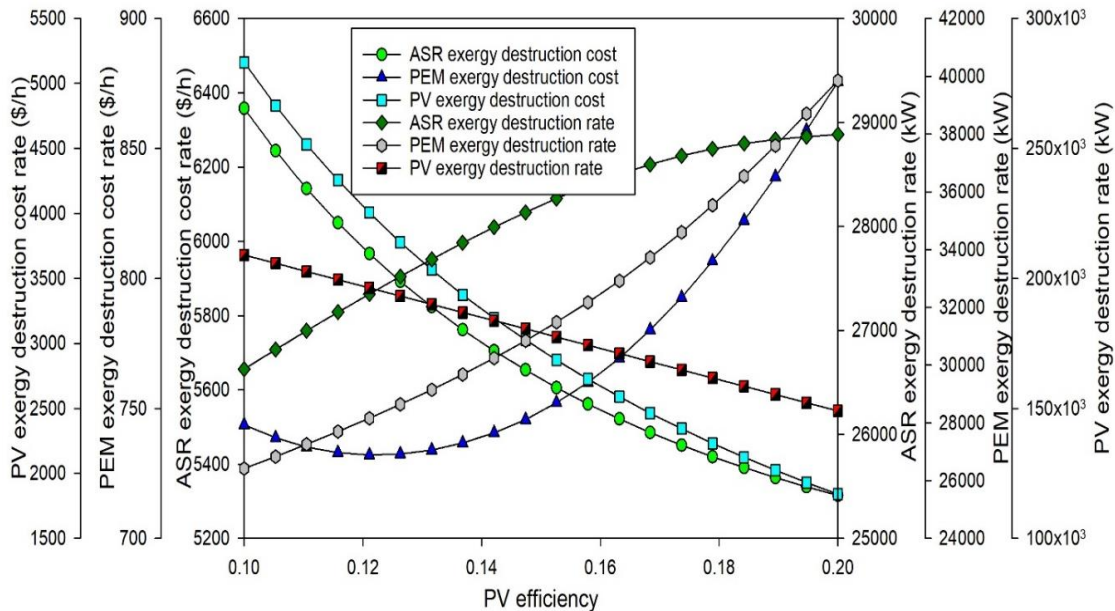


Fig. 6.74 Effects of changes in the PV efficiency on the exergoeconomic performances of the ASR, PEM and PV subsystems

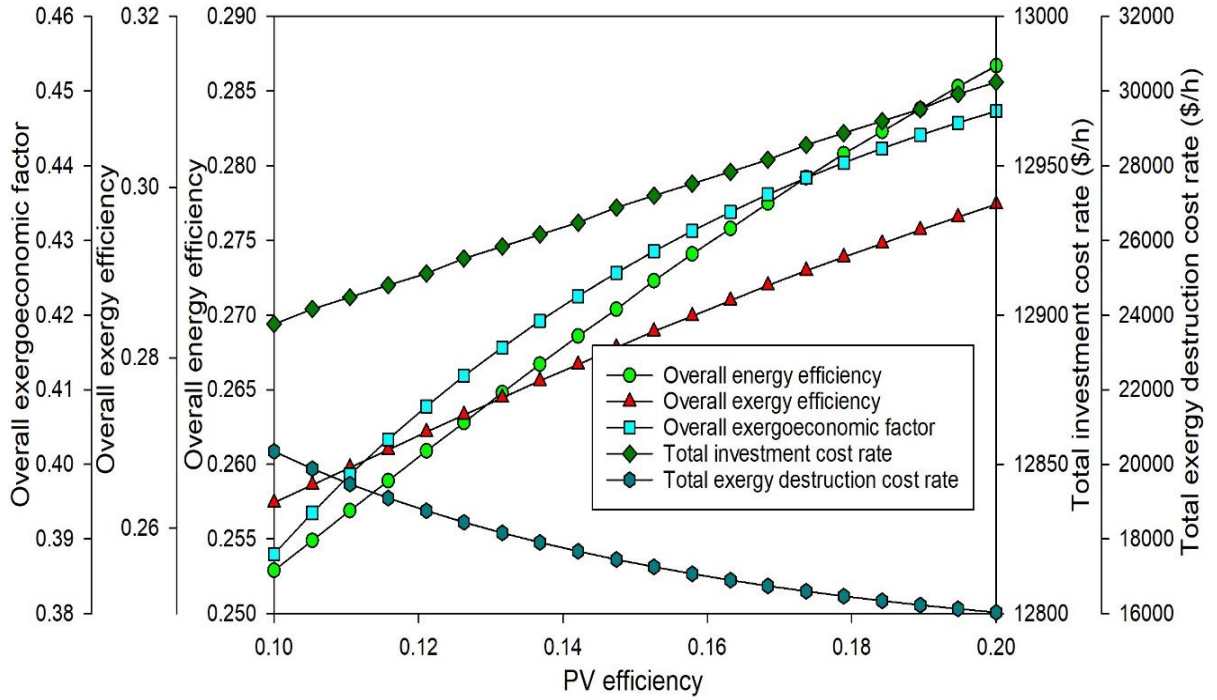


Fig. 6.75 Effects of changes in the PV efficiency on the overall exergoeconomic performance of System 1

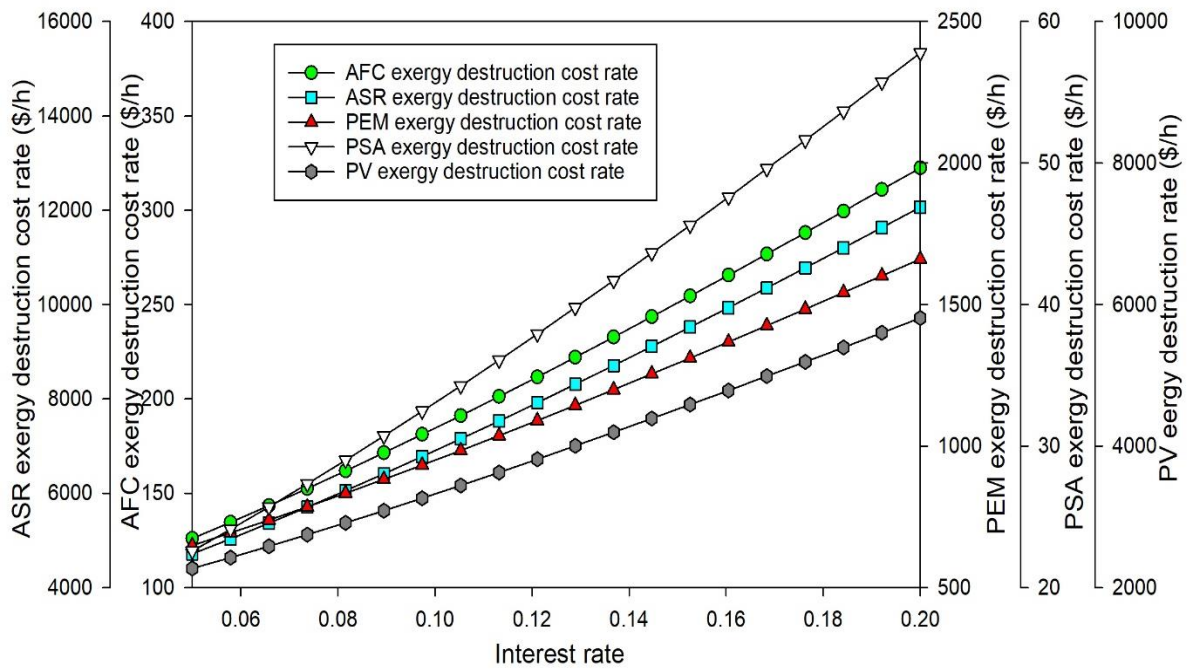


Fig. 6.76 Effects of interest rate on the exergoeconomic performance of major subsystems of System 1

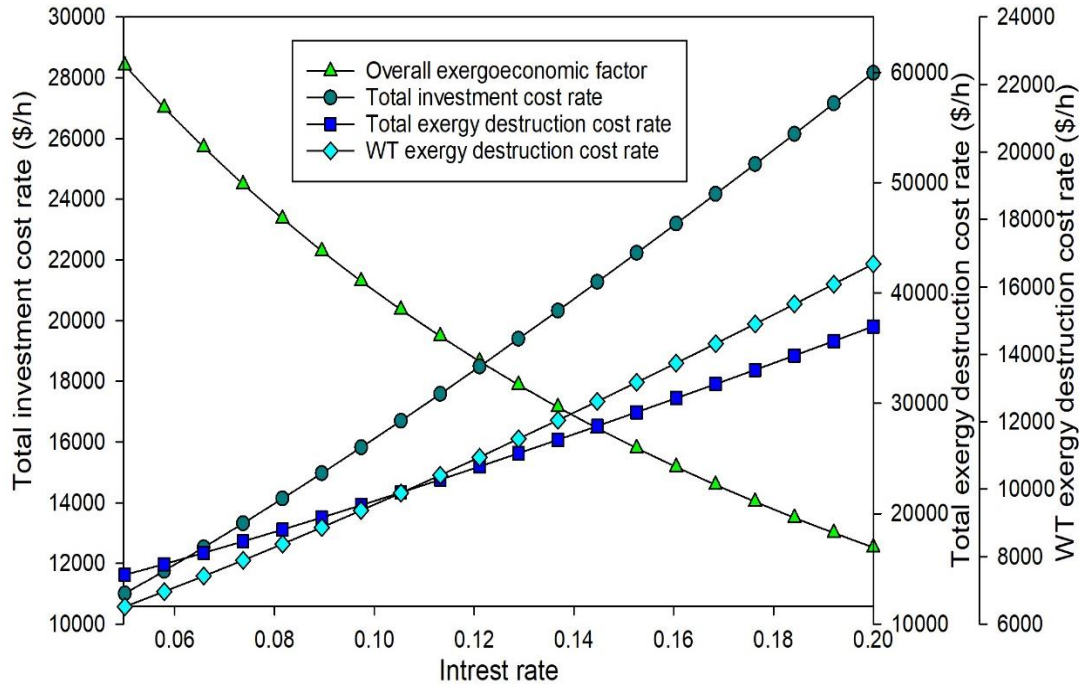


Fig. 6.77 Effects of changes in the interest rate on the overall exergoeconomic performance of System 1

A drop in the overall exergoeconomic factor and the rise in the total investment as well as exergy destruction cost rates is also observed. This is attributed to the significant rise in total investment cost that rises from 11005 \$/h to 28164 \$/h respectively. The total exergy destruction cost rate rises from 14451 \$/h to 36983 \$/h respectively. Thus, this shows the significance of considering the variations in the interest rate during the economic analysis and planning of energy systems.

These results also show the implications of an increase in the interest rate that needs to be considered while economic fluctuations are made. The effects of the system lifetime considered in the exergoeconomic analysis of the system are depicted in Figs. 6.78 and 6.79. The lifetime in the parametric study performed includes the variation from 10 years to 30 years. The cost rates of all major subsystems are found to decrease considerably with increasing system lifetimes.

The ASR subsystem, for instance, entails a decrease in exergy destruction cost rate from 15953 \$/h to 3303 \$/h for an increase in the system lifetime from 10 years to 30 years. The exergy destruction cost rate in the PV subsystem entails a drop from 8058 \$/h to 1520 \$/h for the same change in the system lifetime considered.

The PEM subsystem is observed to entail a decrease in the exergy destruction cost rate from 2190 \$/h to 456 \$/h, which signifies a 4.8 times decrease. The PSA subsystem entails a decrease in the exergy destruction cost rate from 76.2 \$/h at a system lifetime of 10 years to 15.9 \$/h at a 30 years system lifetime. The total investment cost rate is observed to decrease from 36780 \$/h to 7797 \$/h as the system lifetime is raised from 10 years to 30 years.

The total exergy destruction cost rate drops from 48646 \$/h to 10173 \$/h for the same change in the system lifetime. The overall exergoeconomic factor is found to increase from 43.1% to 43.4%. Hence, efforts need to be directed towards developing and utilizing system components that entail higher lifetimes. An average lifetime of 20 years is generally considered for such energy systems, however, as depicted by the results presented, increasing the system lifetimes further can aid in achieving better economic performances. The wind speed plays a significant role in the exergoeconomic performance of the proposed system. The effect of changing wind speeds on the exergy destruction cost rates as well as exergy destruction rates of major subsystems is depicted in Fig. 6.80. Although the costs of exergy destruction are found decrease with increasing wind speeds, the rates of exergy destruction are found to rise.

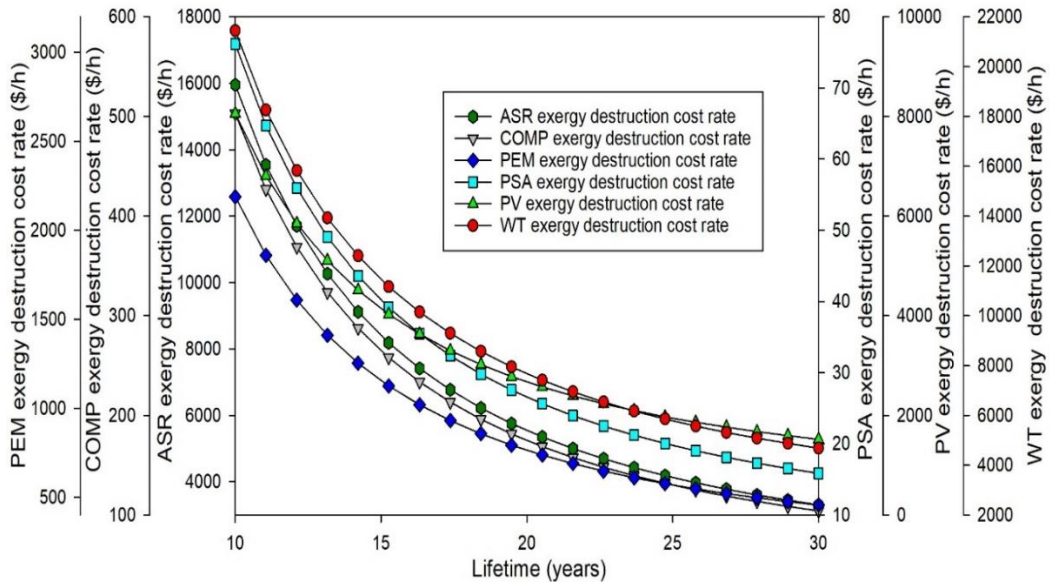


Fig. 6.78 Effects of changes in the system lifetime on the exergoeconomic performances of different subsystems of System 1

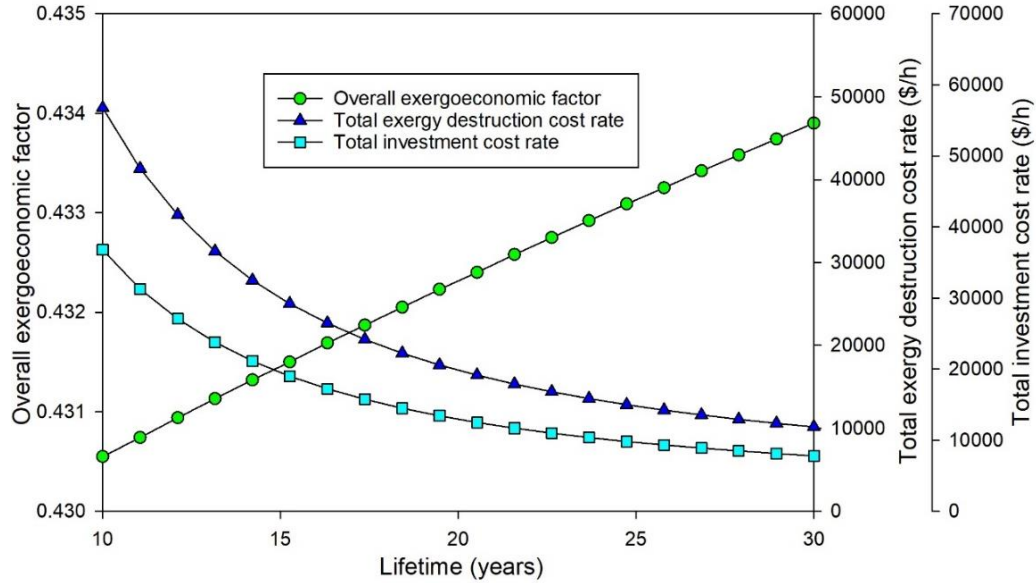


Fig. 6.79 Effects of changes in the system lifetime on the overall exergoeconomic performance of System 1

For instance, when the wind speed rises from 5 m/s to 15 m/s, the WT rate of exergy destruction increases from 30.3 MW and reaches up to 819.1 MW respectively. Therefore, the change in total cost rate of exergy destruction has to be analysed to determine the overall effect of wind speed on the system performance. As the wind speed is raised from 5 m/s to 15 m/s, the cost rate of exergy destruction in the ASR is observed to decrease from 29959 \$/h to 3137 \$/h. The corresponding exergy destruction rate in the ASR increases from 10240 kW to 85158 kW for the same rise in wind speed.

The decrease in the cost rate can be attributed to the decrease in the cost of wind electricity produced. At higher wind speeds, higher electrical power outputs reduce the cost per unit energy produced. Thus, leading to lower cost rates in different subsystems. Fig. 6.81 shows the effect of wind speed on the overall system efficiencies, cost rates and exergoeconomic factor. Increasing wind speeds are found to have advantageous effects on the overall performance in terms of efficiencies and exergoeconomic factor.

The energetic and exergetic performances, for example, rise from 16.3% and 17.3% to 36.9% and 37.8% respectively, when the speed increases from 5 m/s to 15 m/s. The overall exergoeconomic factor increases from 22.5% to 47.2% for the same wind speed variation. Thus, although the total exergy destruction cost rates are higher when wind speeds are high,

the overall exergoeconomic performance of the system is observed to be more favorable at elevated wind speeds.

Hence, at locations where high potential for wind energy exists, the proposed system can provide an effective method for producing clean electrical power, ammonia and hydrogen. The operating temperature of the PEM electrolyser is a design parameter that can be varied and corresponding system performances are effected. The study of PEM temperature effects on the exergoeconomic performances is shown in Figs. 6.82 and 6.83. Rates of exergy destruction as well as the exergy destruction cost rates of major subsystems are presented.

While the exergy destruction rate in ASR rises with elevated PEM temperatures, the PEM and compressor subsystems have a reducing pattern in exergy destruction rates. Exergy destruction cost rate of the ASR subsystem increases while the costs of the PEM and compressor subsystems entail an decreasing behavior with rising PEM temperature. Thus, this depicts the significance of performing exergoeconomic analysis on energy systems considering different system components. Although the overall energetic and exergetic efficiencies increase with rising PEM temperatures, the overall exergoeconomic factor decreases.

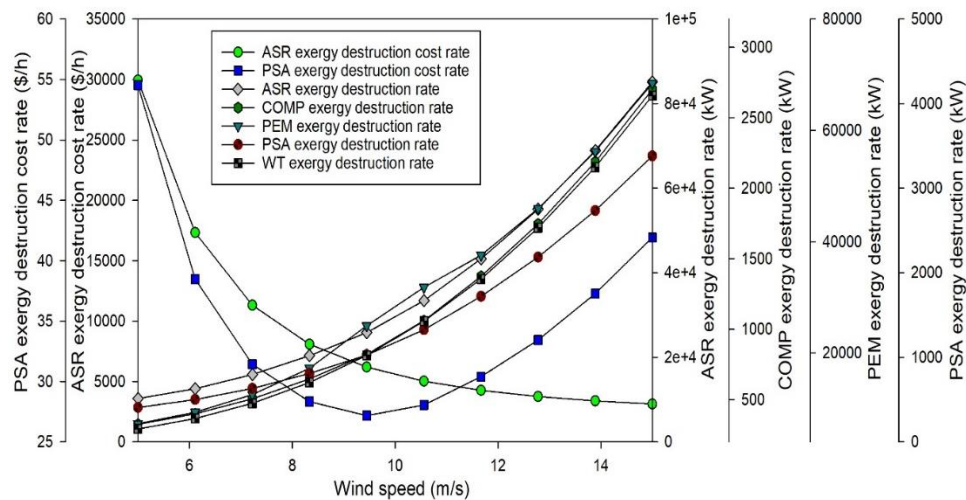


Fig. 6.80 Effects of varying wind speeds on the exergoeconomic performance of different subsystems of System 1

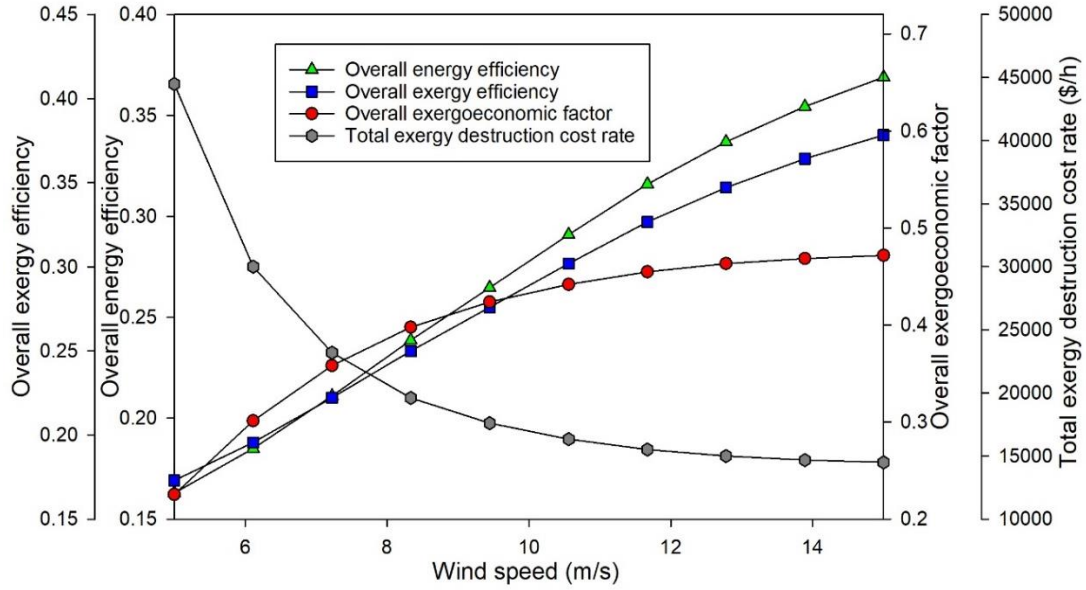


Fig. 6.81 Effects of varying wind speeds on the overall exergoeconomic performance of System 1

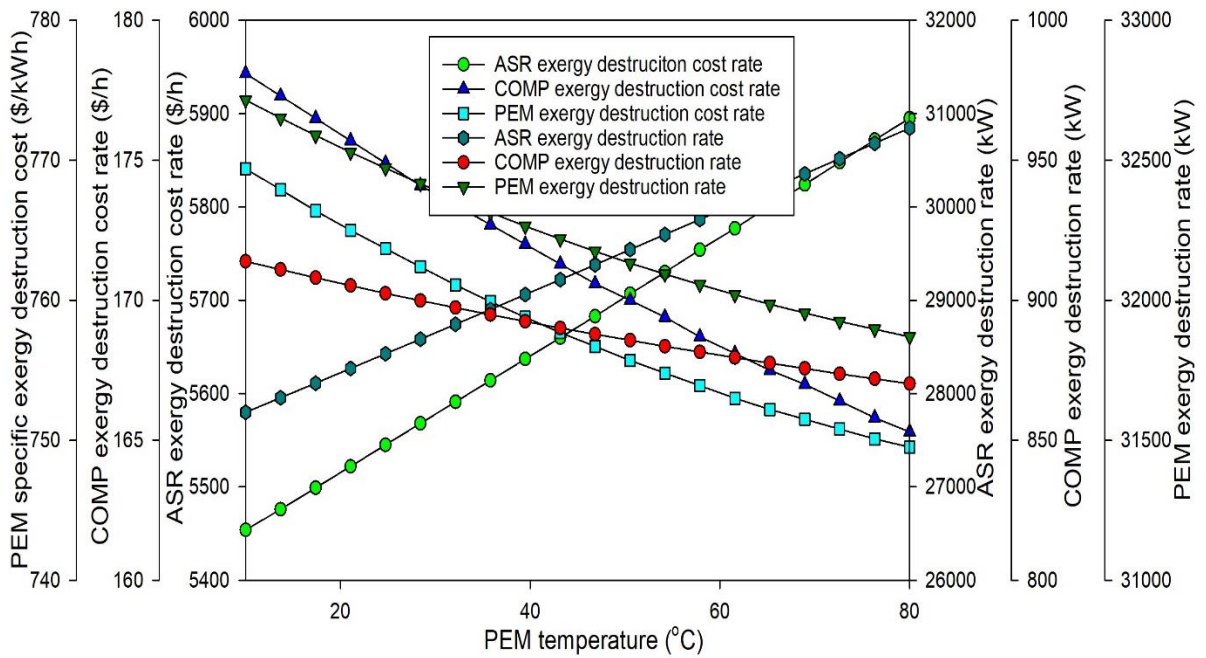


Fig. 6.82 Effects of PEM temperature on the exergoeconomic performances of different subsystems of System 1

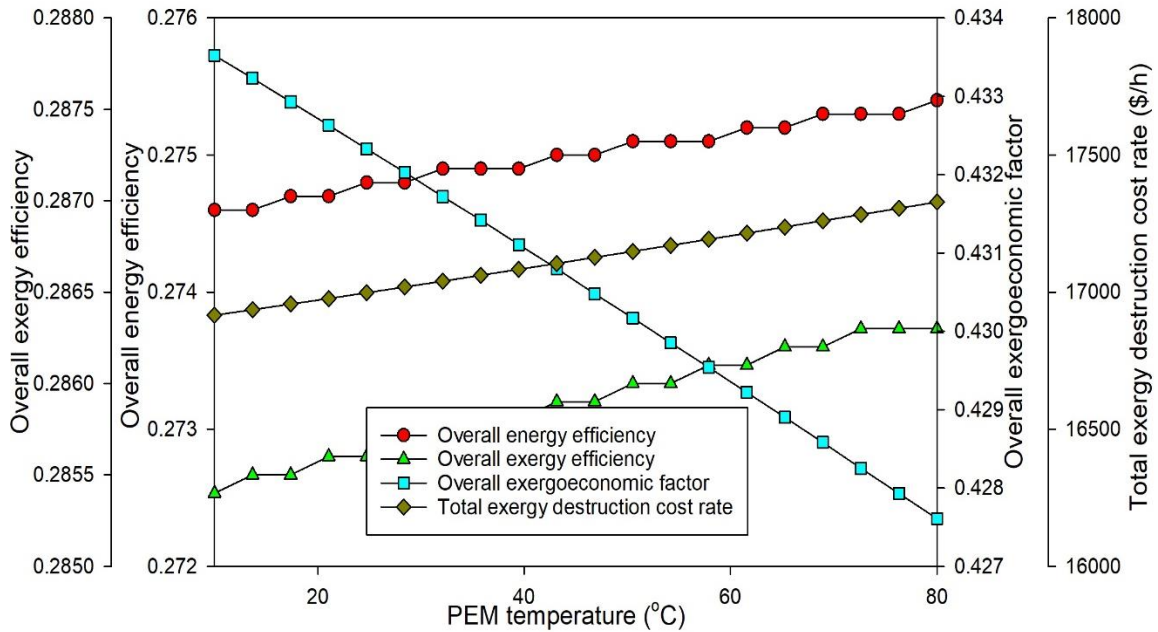


Fig. 6.83 Effects of PEM temperature on the overall exergoeconomic performance of System 1

This can be attributed to rise in total cost of exergy destruction with PEM temperature. Hence, it is recommended to set PEM operating temperatures at values that provide optimal performances. Next, the isentropic efficiency of the compressors utilized for reactant compression entails important significance that effects the exergoeconomic performance of various subsystems as well as the overall system. In the parametric study depicted in Fig. 6.84, the isentropic efficiency of the compressor is varied from 65% to 85%.

The overall exergoeconomic factor of the system is observed to entail an increasing trend with the isentropic efficiency. As the isentropic efficiency is raised from 65% to 85%, the overall exergoeconomic factor rises from 41.9% to 43.2%. The exergoeconomic factor of the compression subsystem entails an increasing trend. Due to the higher isentropic efficiency, the exergy destruction rates in different subsystems are observed to decrease along with their corresponding cost rates of exergy destruction. For instance, the ASR subsystem is found to be associated with a decrease in the exergy destruction cost rate from 6196 \$/h to 5546 \$/h as the isentropic efficiency is raised from 65% to 85%. The exergy destruction rate in the PSA subsystem drops from 1643 kW to 1129 kW for the same change in isentropic efficiency.

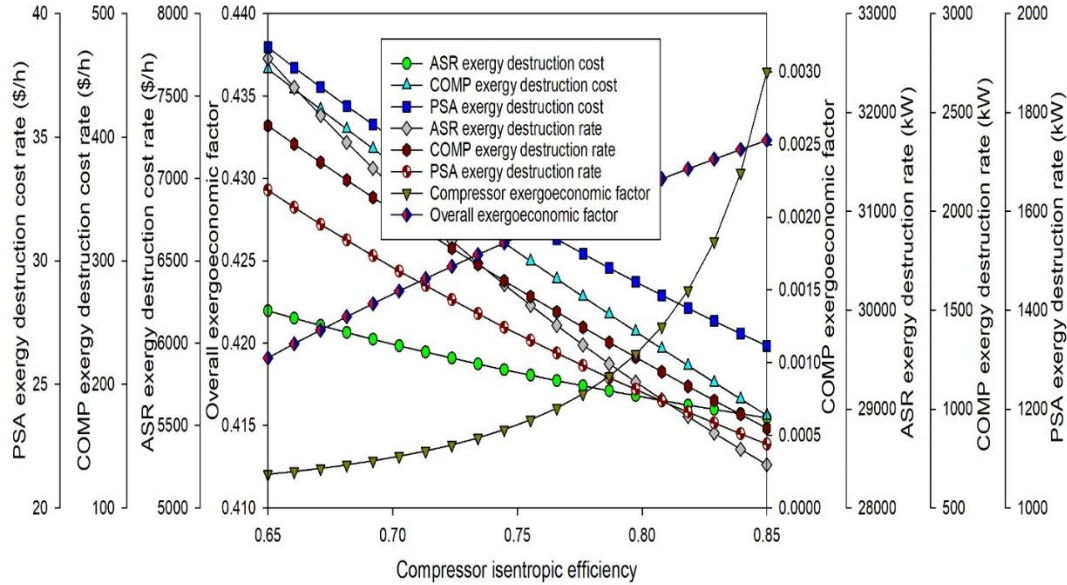


Fig. 6.84 Effects of isentropic efficiency of compressors on the overall exergoeconomic performance of System 1

6.5.2 System 2 exergoeconomic analysis results

The results of exergoeconomic analysis of System 2 are presented in this chapter. The exergoeconomic performance of the overall system as well as associated subsystems are determined at varying operating conditions as well as system parameters. The ambient temperature is a system parameter that is often neglected in the analysis of various energy systems. However, along with variations in the ambient temperature, the exergoeconomic performances are also effected as can be observed from Figs. 6.85-6.87. The effects on MEAFC and PEM subsystems are shown in Fig. 6.85. Exergoeconomic performance of the PEM subsystem is found to marginally decrease as the ambient temperature rises.

The rate of exergy destruction in PEM, for example, rises from 11336 kW to 11337 kW when ambient temperature is raised from -20°C to 30°C . The rate of cost of exergy destruction in PEM increases from 407.4 \$/h to 410.4 \$/h. The effect of ambient temperature on other major subsystems is shown in Fig. 6.86. The rate of exergy destruction in the heliostat field (HF) is found to be 31.8 MW at a low ambient temperature of -20°C , which is found to rise to 38.1 MW at 30°C .

The exergoeconomic performance of the PSA is found reduce with rising ambient temperatures. Both exergy destruction rate as well as the associated cost rate in the PSA subsystem increases with rising ambient temperatures. Other major subsystems are observed to entail higher performances at higher temperatures. For instance, the TES subsystem entails a decreasing trend in the exergy destruction rates as well as the associated costs as the ambient temperature rises.

At an ambient temperature of -20°C , the exergy destruction rate is found to be 76.1 MW. This is observed to decrease to 43.6 MW as the ambient temperature rises to 30°C . Although the exergoeconomic performance is decreased at higher temperatures, the overall exergy efficiency rises. The overall exergy efficiency, for instance, rises from 36.9% at a temperature of -20°C to 37% at a temperature of 30°C .

The overall exergoeconomic factor drops marginally from 54.6% to 54.5% for the same temperature change. Hence, a multi-objective optimization study is required to investigate which operational points comprising of different ranges of parameters provide maximum exergetic efficiencies and minimum cost rates. The results of the multi-objective optimization study performed for System 2 will be described in the proceeding sections.

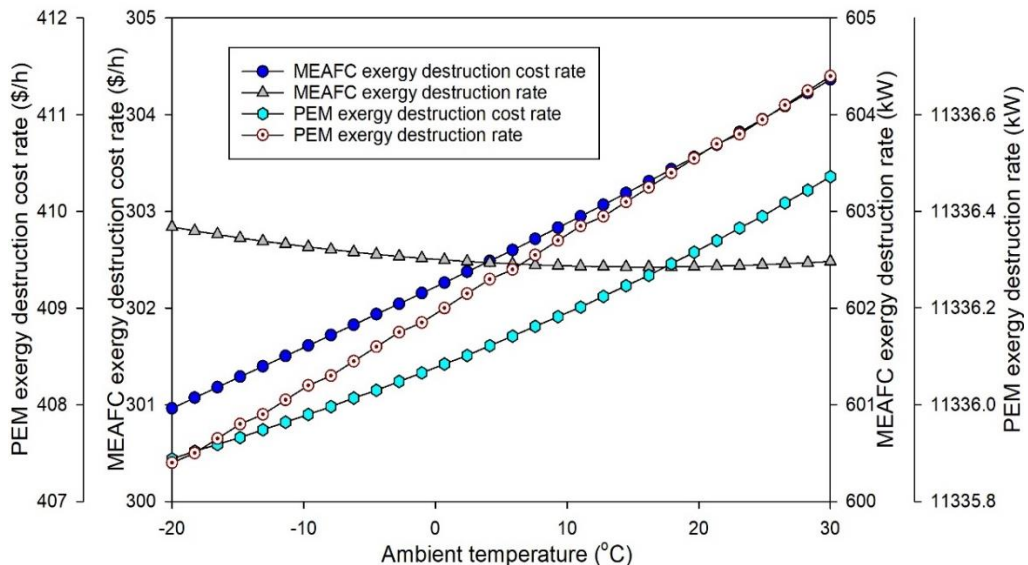


Fig. 6.85 Effects of changes in the ambient temperature on the exergoeconomic performance of MEAFC and PEM subsystems of System 2

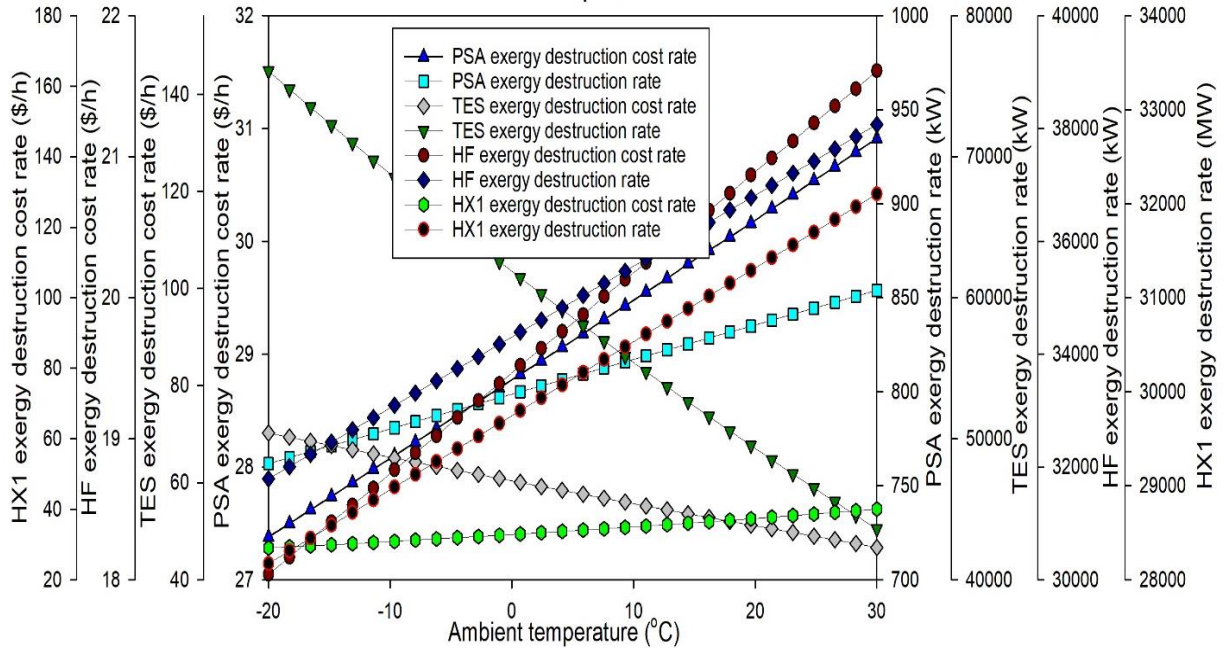


Fig. 6.86 Effects of changes in the ambient temperature on the exergoeconomic performance of different subsystems of System 2

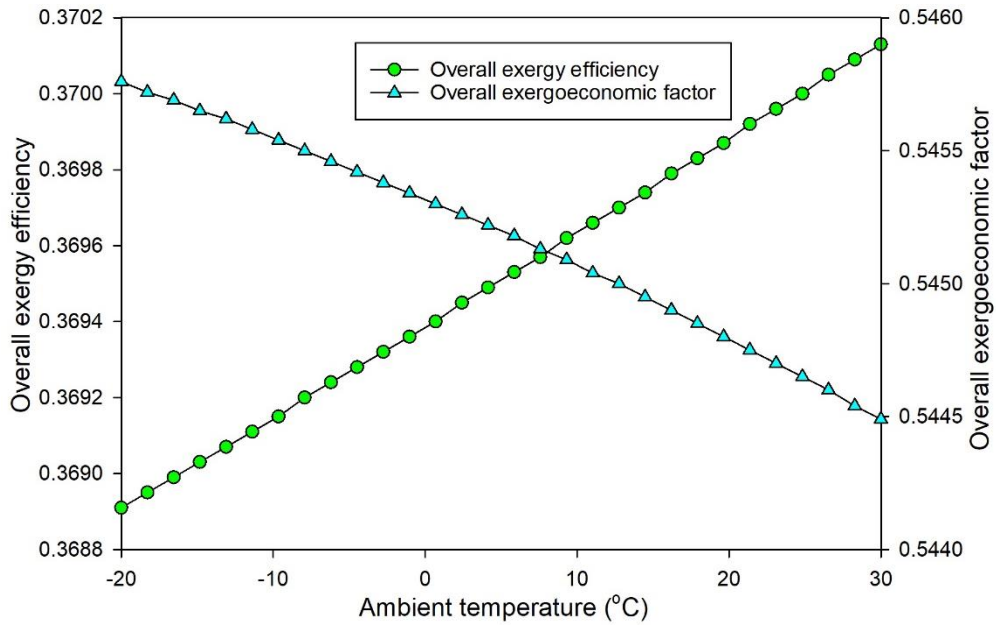


Fig. 6.87 Effects of changes in the ambient temperature on the overall exergoeconomic performance of System 2

As the solar radiation intensity changes during system operation, it is important to study how different subsystems responds to variations in solar intensities. This sensitivity analysis is presented in Figs. 6.88-6.90. Fig. 6.88 shows the effects on the REC, HX1, TES

and HX1 subsystems. The HX1 subsystem is observed to have a decreasing trend in the cost rate of exergy destruction rate while the rate of exergy destruction attains higher values at higher solar intensities.

The rate of exergy destruction reaches a peak value at a solar intensity of 0.4 kW/m^2 for some subsystems followed by a decrease in exergy destruction with a rise in solar intensity. The rate of exergy destruction in the HF increases from 12481 kW to 62407 kW as the solar intensity rises from 0.2 kW/m^2 to 1 kW/m^2 . The TES subsystem is observed to have a continuously increasing trend in the rate of exergy destruction.

The effects of varying solar intensities on the exergoeconomic performances of turbines T1-T3 are depicted in Fig. 6.89. The exergy destruction rates are observed to have an overall decreasing behavior with rising solar intensity while the cost rates of exergy destruction are observed to have varying trends. The cost rate of exergy destruction in T1, for instance, rises until a solar intensity of 0.45 kW/m^2 is reached. After this value, the cost rate of exergy destruction of T1 entails a decreasing trend. Thus, the operating conditions under design operation should be investigated during system design to determine which parameters provide optimal performances.

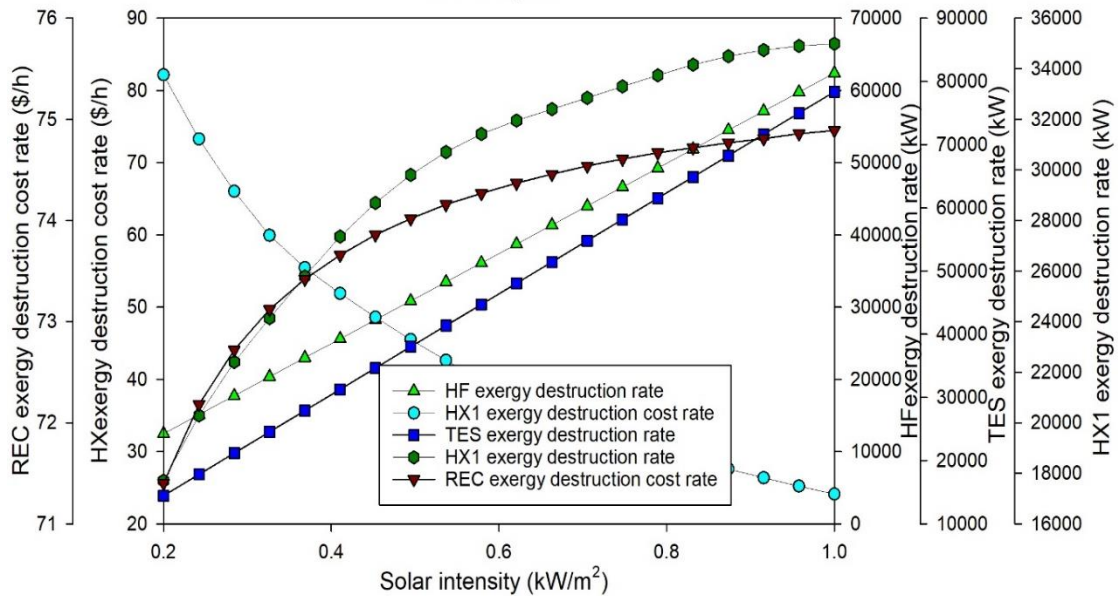


Fig. 6.88 Effects of changes in the solar intensity on the exergoeconomic performances of different subsystems of System 2

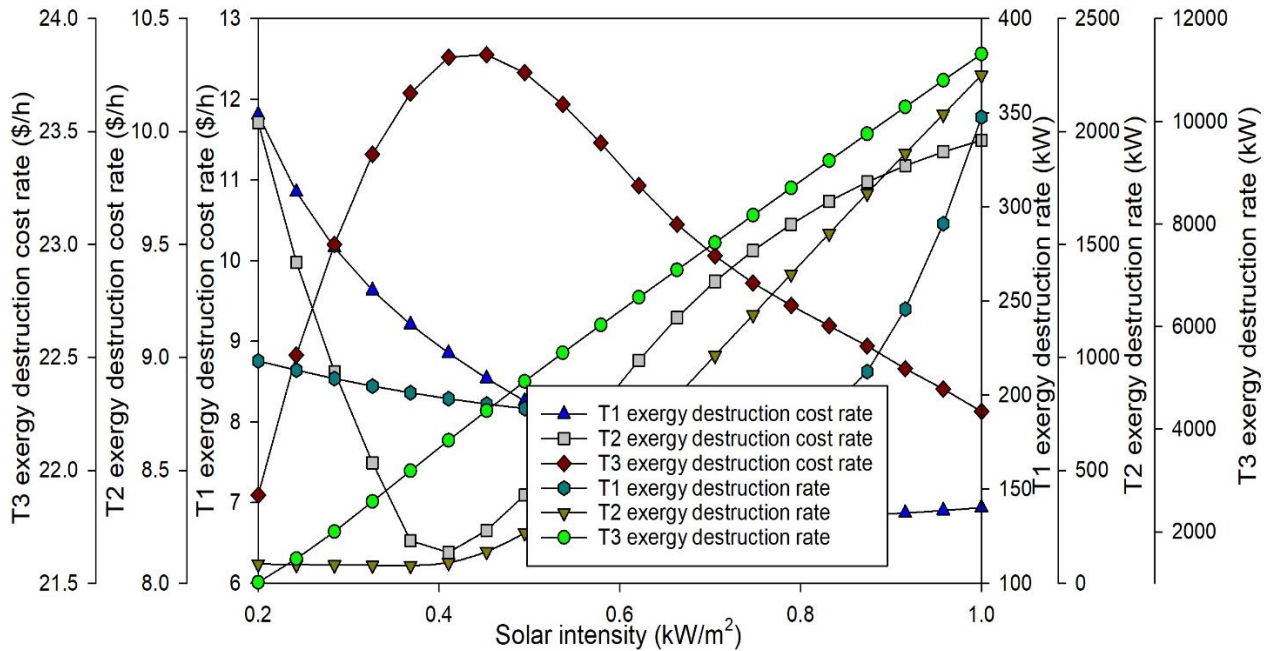


Fig. 6.89 Effects of changes in the solar intensity on the exergoeconomic performances of turbines T1-T3 of System 2

The overall exergoeconomic performance variation of System 2 under varying solar intensities is depicted in Fig. 6.90. Higher solar radiation intensities are found to provide better overall performances. The total cost rate of exergy destruction decreases and the energy efficiency, overall exergoeconomic factor and exergy efficiency are found to rise as the solar intensities increase. As the solar intensity increases from 0.2 kW/m² to 1 kW/m², the total cost rate of exergy destruction decreases from a value of 13509 \$/h to 11888 \$/h respectively.

The exergy efficiency rises from 38.9% to 40.9% and the overall energy efficiency increases from 38.4% to 39.7% for the same change in solar intensity. The overall exergoeconomic factor of the system is observed to rise from 52.9% to 57.5%. A change in the trends is observed after a solar intensity of 0.8 kW/m². The decreasing trend associated with the total exergy destruction cost rate entails a sudden drop in the cost rates after this solar intensity value.

The increasing trend observed in the overall exergoeconomic factor is observed to entail a considerable rise after a solar intensity of 0.8 kW/m². This can be attributed to the higher outputs from the solar-based plant at higher solar intensities. As the amount of output rises,

the associated unit costs of commodities decrease. Hence, resulting in a drop in the overall exergy destruction cost rates.

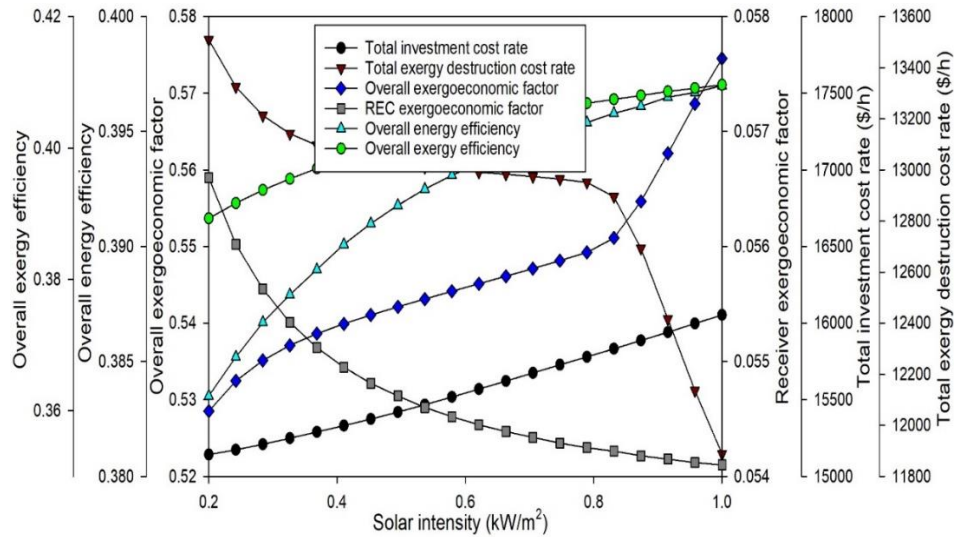


Fig. 6.90 Effects of changes in the solar intensity on the overall exergoeconomic performance of System 2

Thus, during system design and component sizing of solar-based systems, optimization studies should be performed to determine most suitable parameters that would aid in achieving high overall as well as subsystem performances. The interest rate considered in the exergoeconomic analysis can change depending on the economic conditions as well as national policies. Thus, the effects of varying interest rates on the economic performances of major subsystems and overall system for System 2 are shown in Figs. 6.89 to 6.91.

As can be observed from Fig. 6.91, the WT cost rate of exergy destruction entails comparatively higher values that increase with rising interest rates. For instance, WT cost rate of exergy destruction is 6519 \$/h if the interest rate is set at 5%. Nevertheless, when the interest rate rises to 20%, the WT cost rate increases to 16684 \$/h. The EAS subsystem also entails comparatively higher cost rates of exergy destruction. At an interest rate of 5%, for example, the exergy destruction cost rate for the EAS is evaluated to be 3705.4 \$/h, which rises to 9482.7 \$/h at a higher rate of 20%.

Fig. 6.92 shows the effect interest rate has on major components of the solar power generation subsystem. HX1 entails comparatively higher cost rates for exergy destruction. At the low interest rate of 5%, this component is associated with a cost rate of 32.9 \$/h,

which rises to 84.2 \$/h at the high interest rate of 20%. The changes in the overall exergoeconomic performance of System 2 with varying interest rates are shown in Fig. 6.93. Although, the total cost rates of investment as well as exergy destruction rise considerably with increasing interest rates, the exergoeconomic factor entails a minor effect. For instance, as the interest rate rises from 5% to 20%, the overall exergoeconomic factor rises from 56.9% to 56.9%.

The total investment cost rate rises from 13214 \$/h to 33816 \$/h. Similarly, the total exergy destruction cost rate rises from 11047 \$/h to 28272 \$/h for the same rise in interest rate. Hence, during the development and cost analysis of a given energy system, it is suggested to incorporate the effects of interest rate in economic planning. The system lifetime considered for the exergoeconomic analysis also effects the results obtained.

The sensitivity analysis performed for different system lifetimes is shown in Figs. 6.94-6.96. Significant effects are observed on the cost rates of system components. The rate of cost of exergy destruction for the WT subsystem, for instance, drops from 21440 \$/h at a lifetime of 10 years to 4685 \$/h for a lifetime consideration of 30 years as depicted in Fig. 6.92. The EAS cost rate of exergy destruction drops from 12728.3 \$/h to 2560.2 \$/h for the same change in system lifetime. The effect of system lifetime on the economic performance of the power generation subsystem based on solar energy is showed in Fig. 6.95.

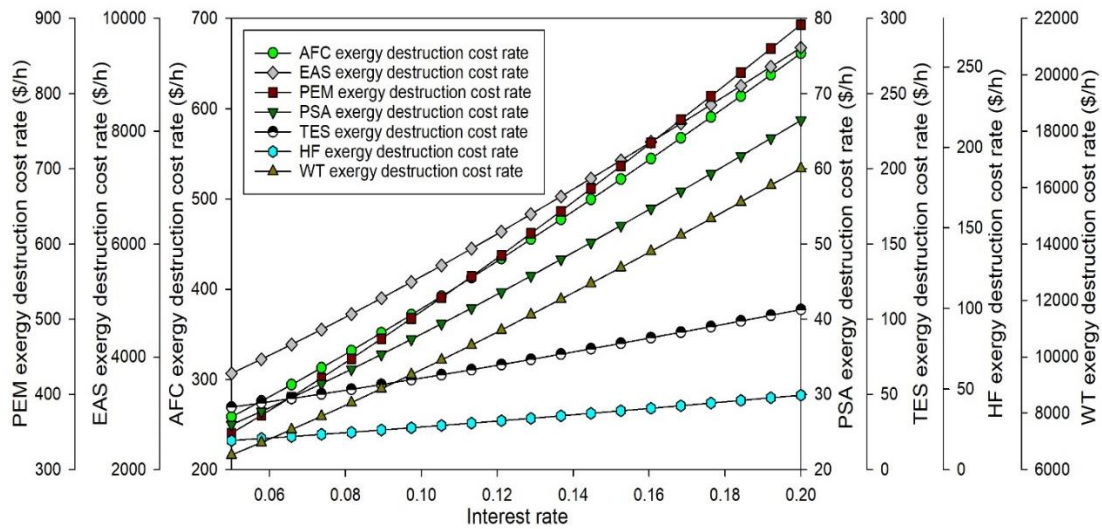


Fig. 6.91 Effect of interest rate on the exergoeconomic performance of different subsystems of System 2

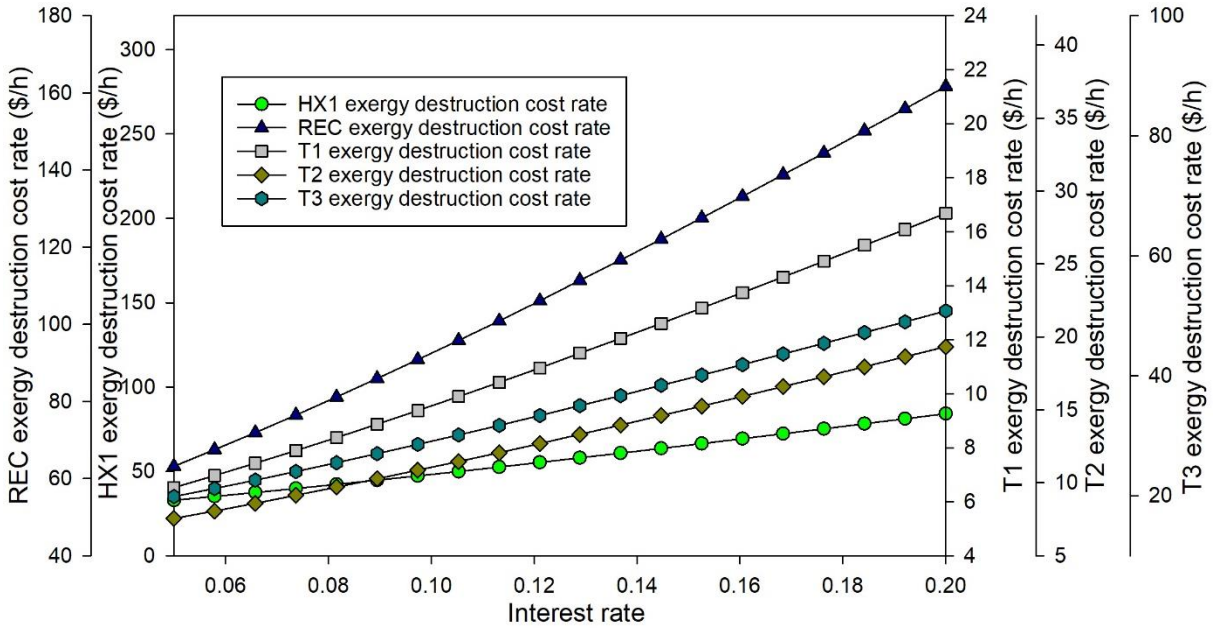


Fig. 6.92 Effect of interest rate on the exergoeconomic performance of steam turbines in System 2

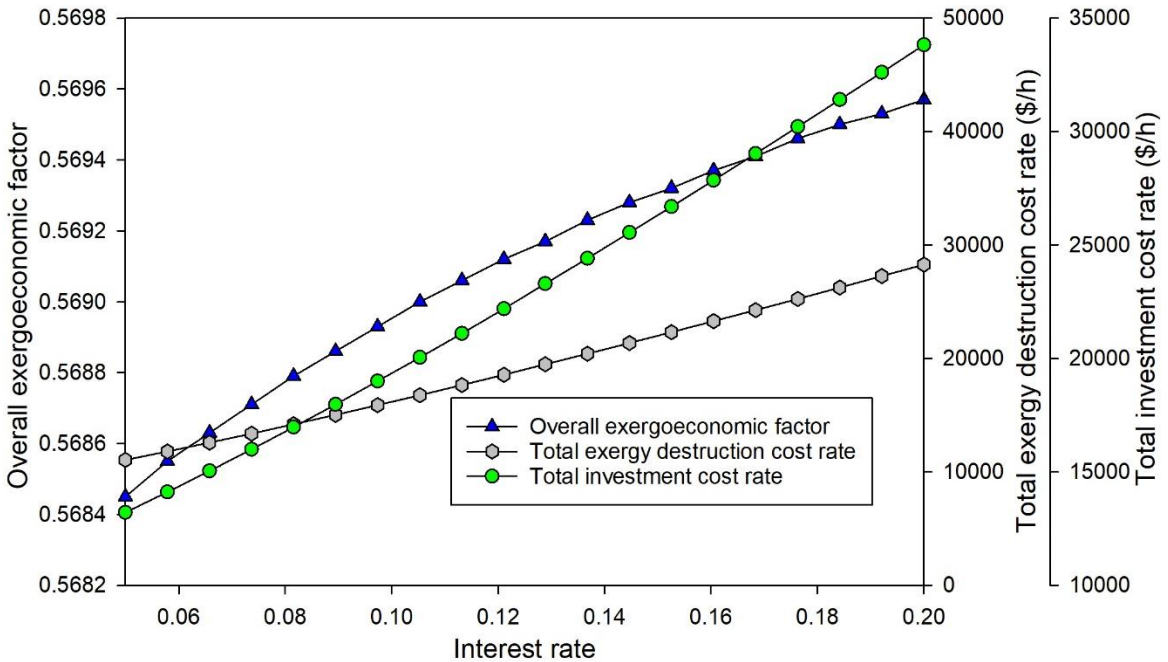


Fig. 6.93 Effect of interest rate on the overall exergoeconomic performance of System 2

The HF subsystem entails comparatively higher cost rates, which has a rate of cost of exergy destruction of 64.1 \$/h at a low lifetime of 10 years. This drops to 12.1 \$/h at a system lifetime of 30 years. The exergy destruction cost rate in turbine T3 entails a decrease

from 70.5 \$/h at a system lifetime of 10 years to 13.3 \$/h at a system lifetime of 30 years. The rate of cost of exergy destruction in HX1 is observed to decrease from 116.7 \$/h to 22.0 \$/h for the same change in system lifetime.

The REC subsystem entails a decrease in the exergy destruction cost rate from 224.2 \$/h to 42.3 \$/h. The effect of system lifetime on the overall exergoeconomic performance is depicted in Fig. 6.96. The overall exergoeconomic factor is observed to increase and the rates of cost of investment as well as exergy destruction are found to drop considerably. The rate of cost of investment, for instance, reduces from 40538 \$/h to 10045 \$/h for an increase in system lifetime from 10 years to 30 years.

The rate of cost of exergy destruction of System 2 decreases from 37018 \$/h to 7809 \$/h. However, the overall exergoeconomic factor increases from 52.3% to 56.3% for the same change in system lifetime. Therefore, longer system lifetimes should be targeted when possible, considering better economic performances that can be attained. Nevertheless, the lifetimes of different major subsystems may vary depending on their operational quality and higher quality equipment can aid in achieving longer system lifetimes

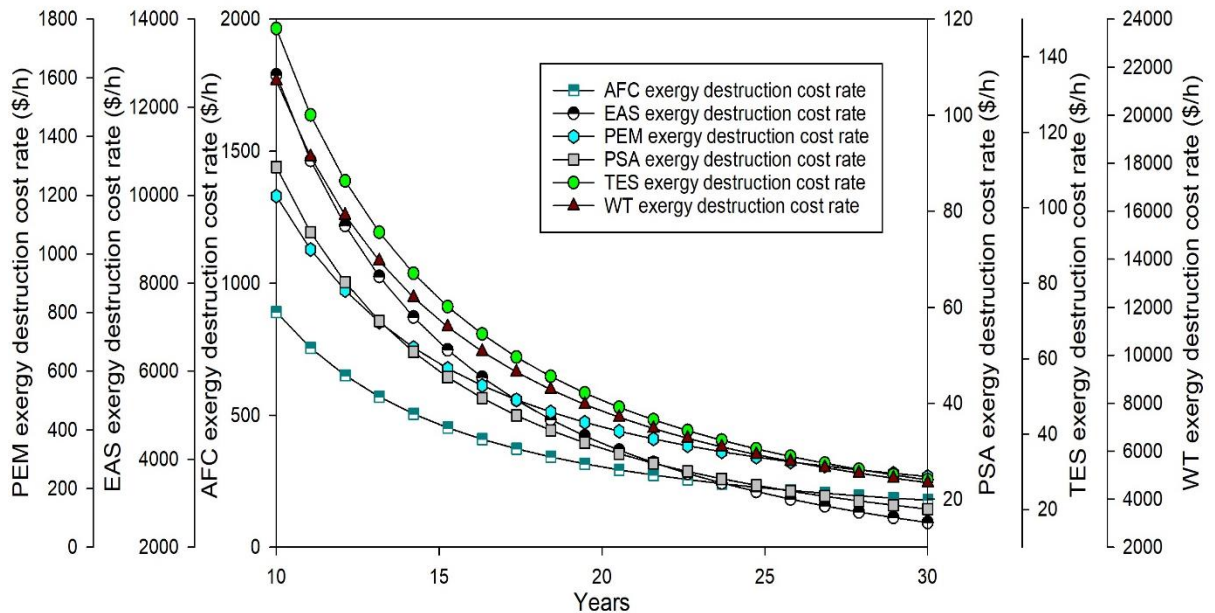


Fig. 6.94 Effect of system lifetime on the exergoeconomic performance of different subsystems of System 2

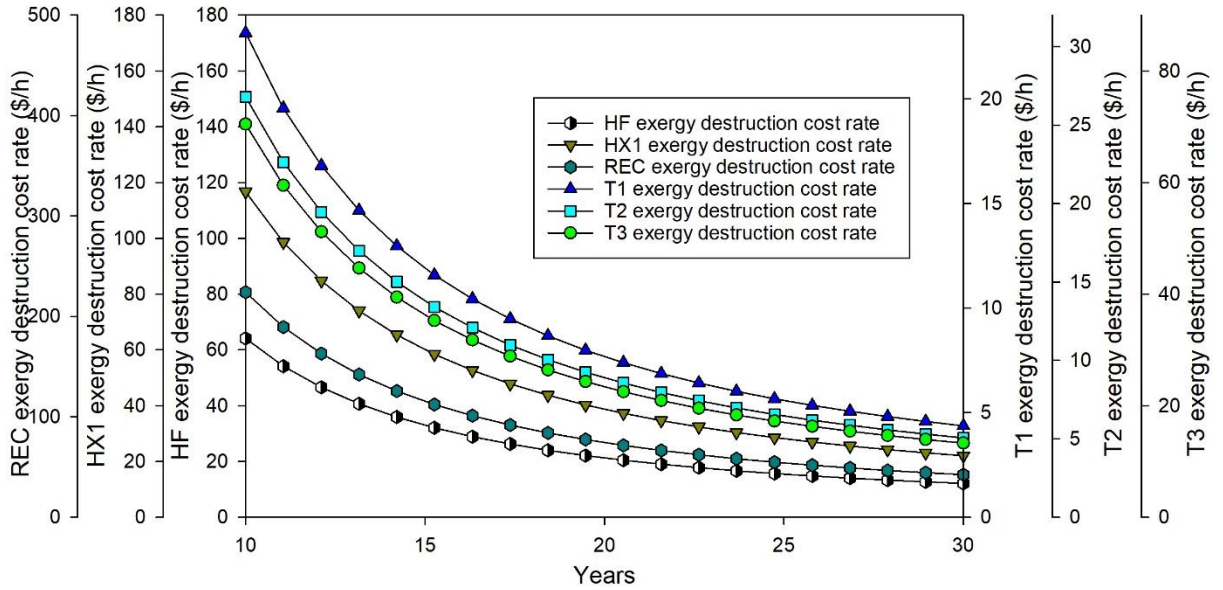


Fig. 6.95 Effect of system lifetime on the exergoeconomic performance of solar-based power generation subsystem in System 2

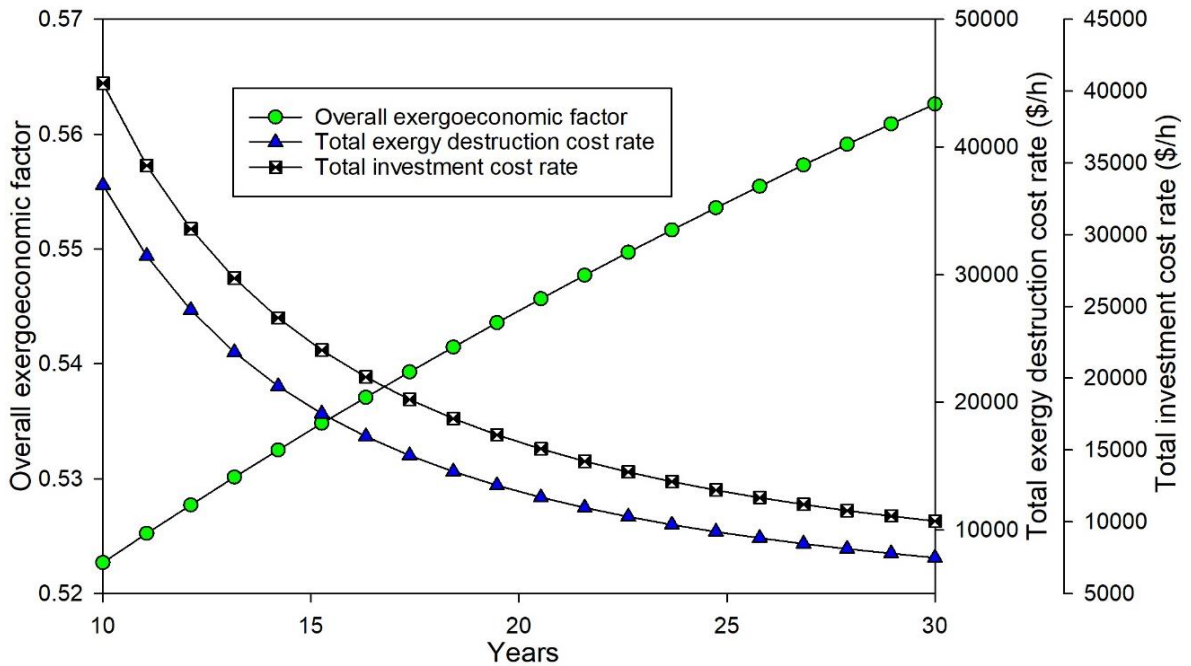


Fig. 6.96 Effect of system lifetime on the overall exergoeconomic performance of System 2

Wind speeds are variable and effect the exergoeconomic performance of the system. Thus, it is important to analyse how the system responds to different wind speeds. This is depicted in Figs. 6.95-6.97 where major subsystems effected are studied. When the wind speed rises,

the power input supplied to the PEM and EAS subsystems also rises resulting in higher production of hydrogen as well as ammonia. This also leads to higher exergy destruction rates in these subsystems as can be observed from Fig. 6.97. The PEM subsystem, for example, entails an increase from 1957 kW to 38811 kW in the rate of exergy destruction when the speed is raised from 5 m/s to 15 m/s.

The rate of cost of exergy destruction in the PEM subsystem also rises from 287.3 \$/h to 972.1 \$/h for the same change in wind speed. The effect of wind speed on the exergoeconomic performance of the PSA subsystem is shown in Fig. 6.98. The PSA subsystem entails a rise from 193.8 kW to 2586 kW in the rate of exergy destruction for the same increase in wind speed. The corresponding rise in the rate of cost of exergy destruction is found to be from a value of 28.4 \$/h to 64.8 \$/h. The overall exergoeconomic performance as a function of wind speed is shown in Fig. 6.99. The exergoeconomic factor is observed to increase from 41.8% to 57.9%. The rate of cost of total exergy destruction also rises. It is thus recommended to consider these factors during system design to ensure majority of system operation entails low operational costs as well as high exergoeconomic performances.

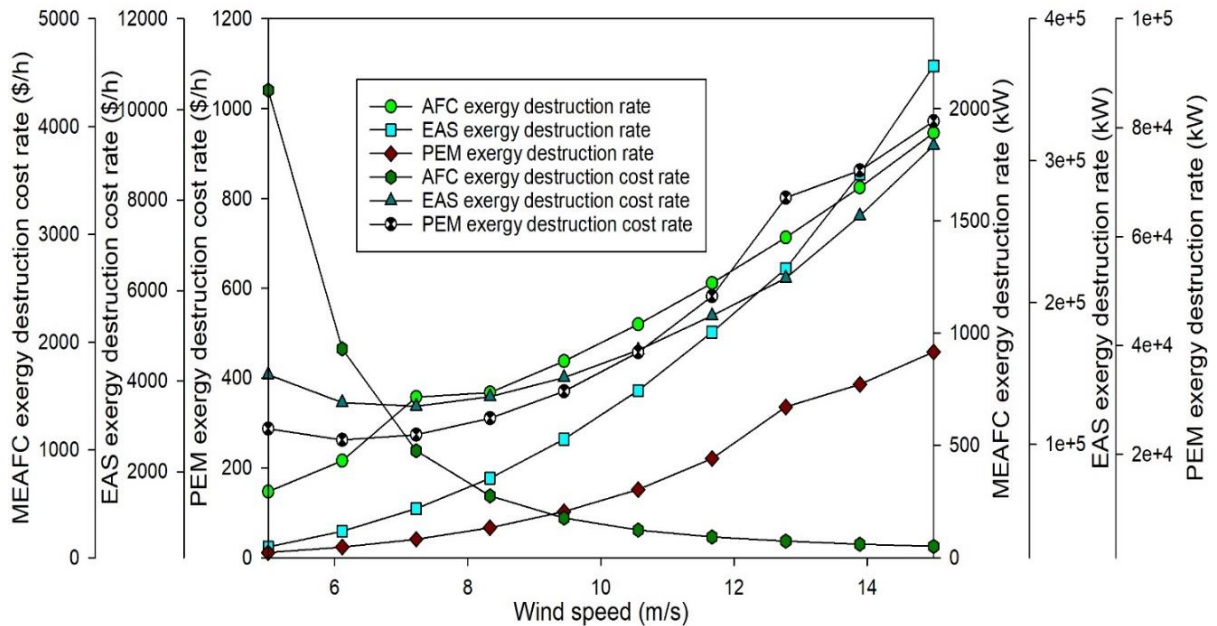


Fig. 6.97 Effect of wind speed on the exergoeconomic performance of PEM, EAS and MEAFC subsystems of System 2

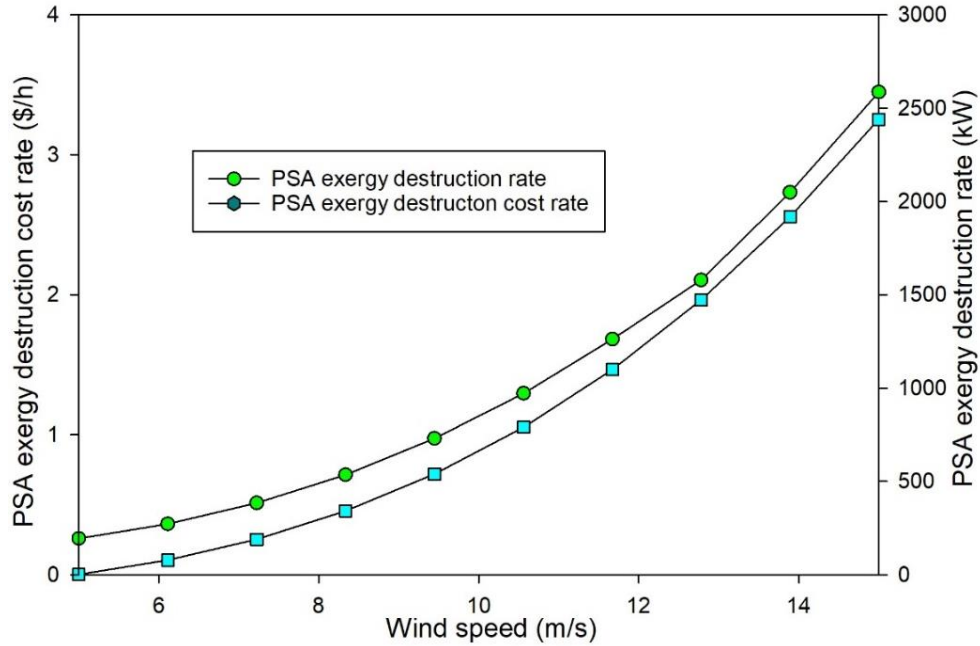


Fig. 6.98 Effect of wind speed on the exergoeconomic performance of PSA subsystem is System 2

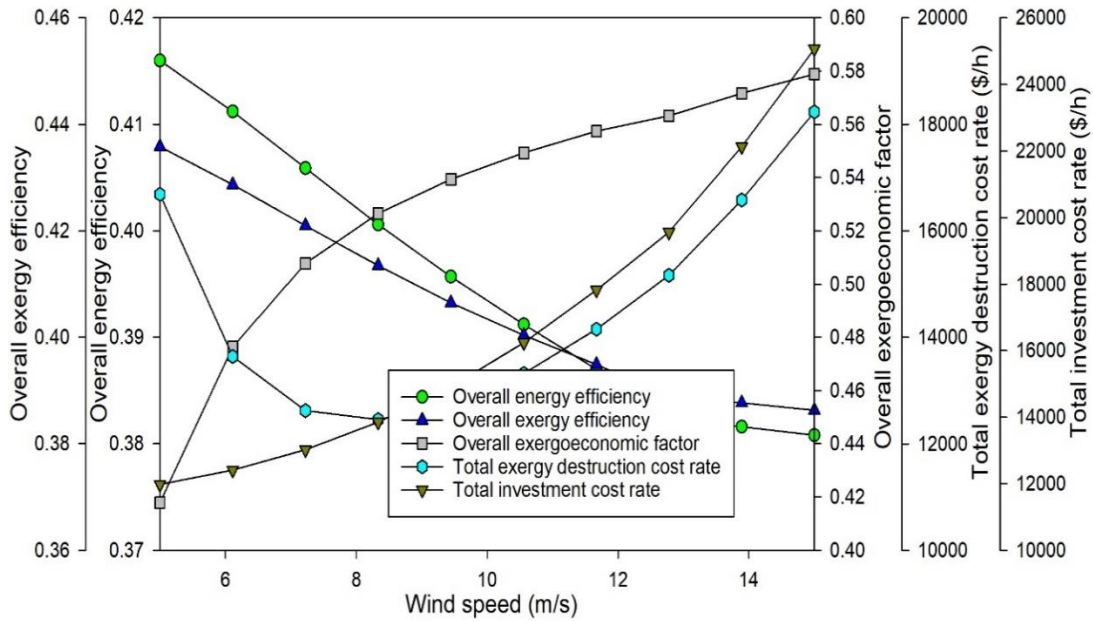


Fig. 6.99 Effect of wind speed on the overall exergoeconomic performance of System 2

The effects of varying PEM temperatures on the exergoeconomic performance of the overall system as well as associated subsystems are depicted in Figs. 6.100-6.101. The PEM temperature is varied from 10°C to 80°C and the effects on the exergy destruction rates as well as corresponding exergy destruction cost rates are investigated. Higher PEM

temperatures are found to result in lower exergy destruction rates as well as exergy destruction cost rates in the electrolysis subsystem.

For instance, the exergy destruction rate in the PEM subsystem decreases from 11710 kW to 9935 kW as the temperature is raised from 10°C to 80°C. The corresponding exergy destruction cost rate decreases from 423.5 \$/h to 359.3 \$/h for the same temperature change. The cost of exergy destruction rate in the EAS, however, is observed to entail an increasing trend with rising PEM temperatures. The exergy destruction cost rate in the EAS subsystem increases from 4320.8 \$/h to 4502.3 \$/h. However, the MEAFC exergy destruction cost rate entails a decreasing trend where the cost rate reduces from 305.6 \$/h to 297.5 \$/h respectively.

The effect of PEM temperature on the overall exergoeconomic performance of the system is depicted in Fig. 6.101. Higher PEM temperatures are found to provide better exergoeconomic performances. The overall exergoeconomic factor, for example, increases from 57.1% to 57.2% as the PEM temperature is raised from 10°C to 80°C. The overall energy and exergy efficiencies are found to entail increases from 39.3% to 39.5% and 40.3% to 40.6% respectively.

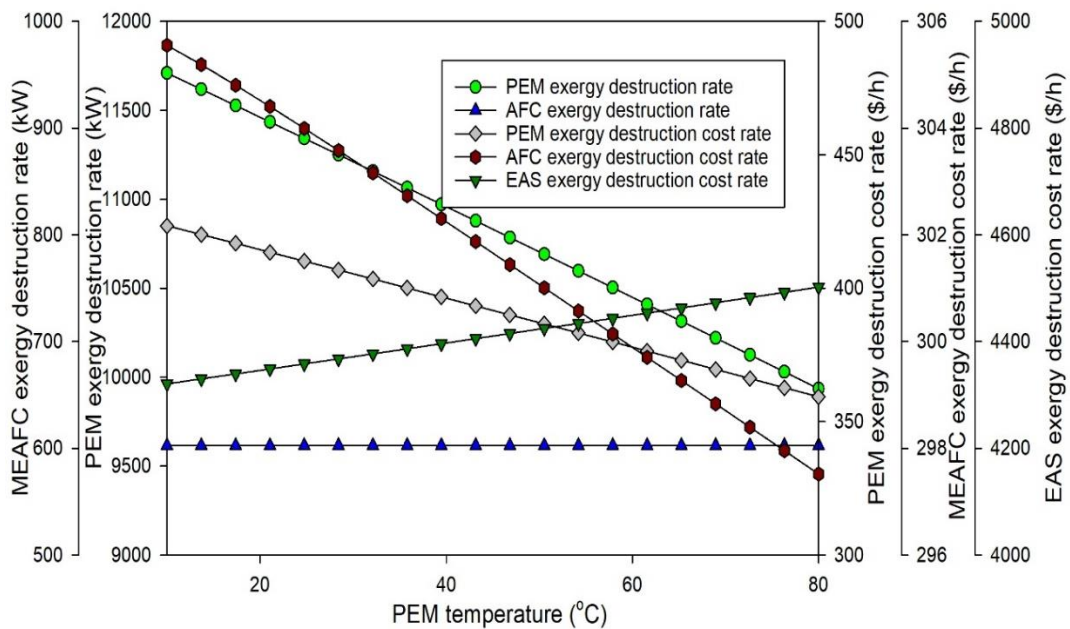


Fig. 6.100 Effect of PEM temperature on the exergoeconomic performances of different subsystems of System 2

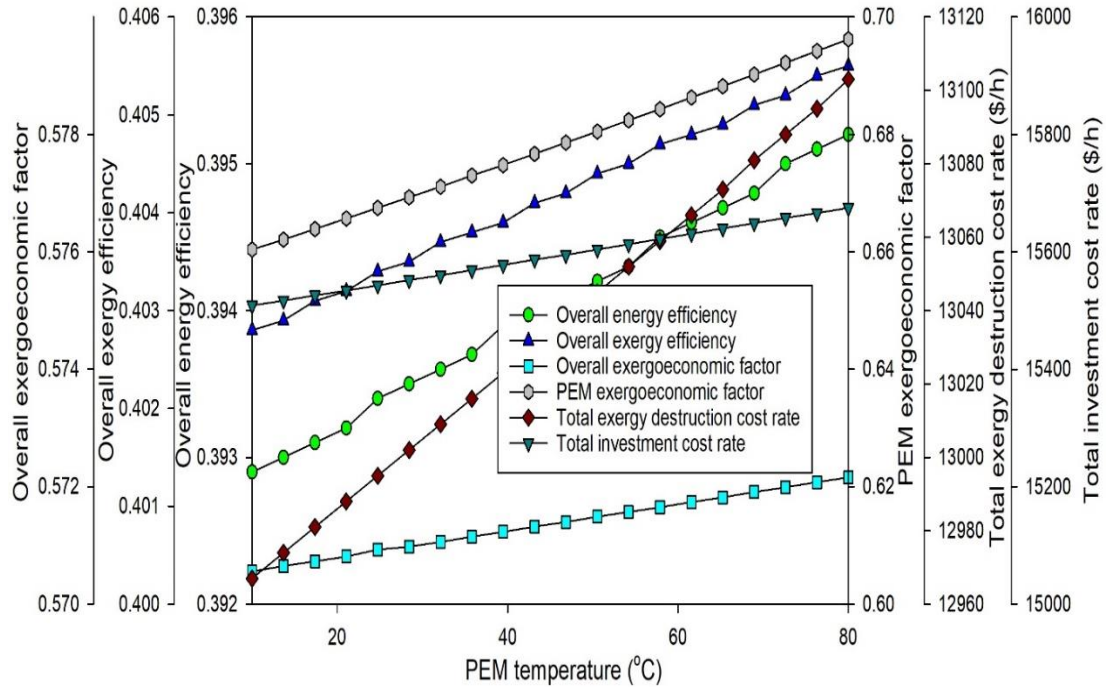


Fig. 6.101 Effect of PEM temperature on the overall exergoeconomic performances of System 2

The sensitivity analysis performed to study the effect of isentropic efficiency of mechanical system components including pumps, compressors and steam turbines on the system performances are shown in Figs. 6.102-6.104. The exergoeconomic performances of PSA and HX1 are shown in Fig. 6.102 as a function of the isentropic efficiency. Although the rate of exergy destruction as well as cost for HX1 rises with increasing isentropic performances, the PSA subsystem is observed to have a decreasing behavior with increasing isentropic efficiencies that is favorable for overall performance of the system.

The effect on the performance of steam turbines T1-T3 is shown in Fig. 6.103. Utilizing higher isentropic efficiency turbines provide considerable improvements to the exergoeconomic performances. The rate of exergy destruction in T3, for example, is found to be 14.9 MW at an isentropic efficiency of 65%. Nevertheless, this decreases considerably to 6.3 MW when the isentropic efficiency is raised to 85%. Similarly, the rate of cost of exergy destruction in T3 drops from 71.1 \$/h to 23.4 \$/h for the same rise in isentropic performance. The overall system performances also enhance with rising

isentropic efficiencies. The exergoeconomic factor, for instance, varies from 52.8% to 54.5% as the isentropic efficiency is raised from 65% to 85%.

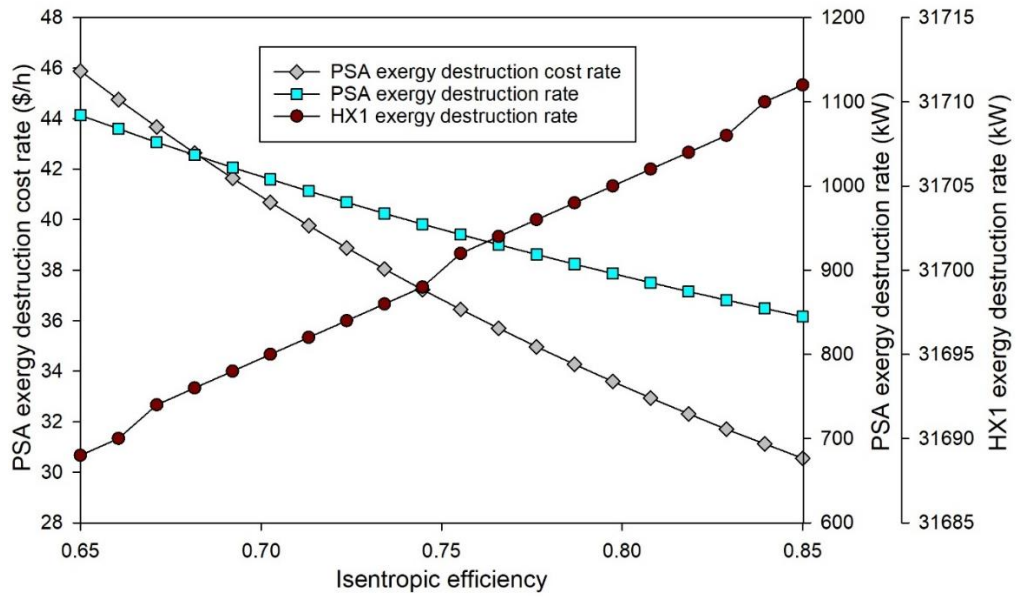


Fig. 6.102 Effect of isentropic efficiency on the exergoeconomic performances of PSA and HX1 in System 2

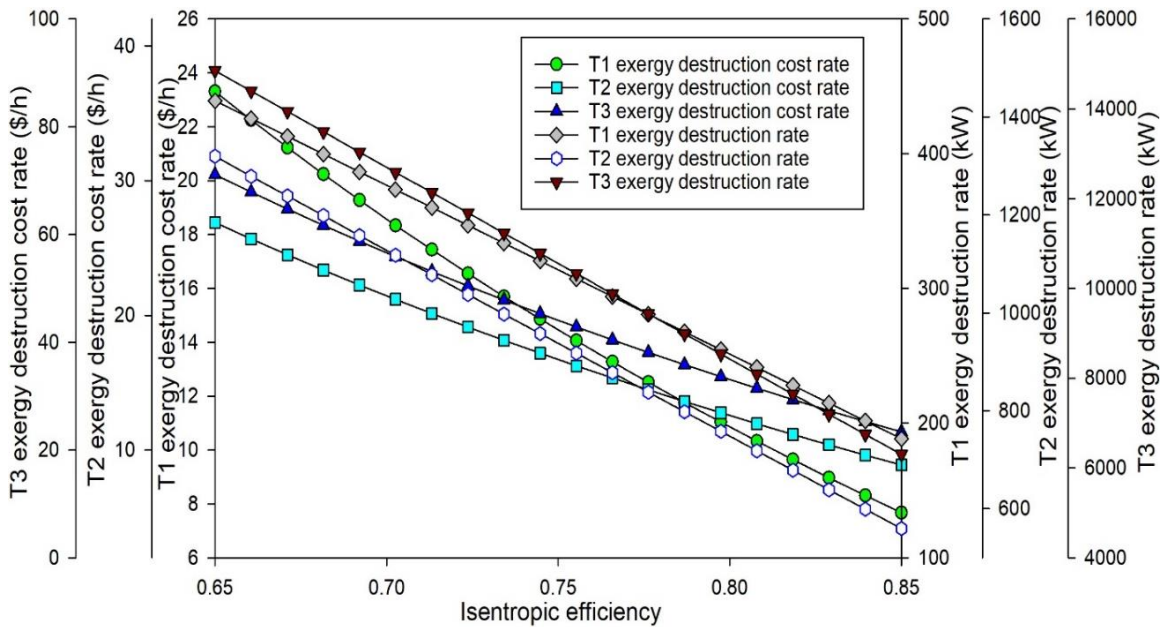


Fig. 6.103 Effect of isentropic efficiency on the exergoeconomic performances of steam turbines in System 2

6.5.3 System 3 exergoeconomic analysis results

The results of the exergoeconomic analysis of System 3 are presented in this section. The exergoeconomic performance of the overall system as well as different subsystems is discussed through different parametric studies. The effect of ambient temperature on the exergoeconomic performances is shown in Figs. 6.104-6.106. The effects on ADR and REC subsystems are shown

in Fig. 6.104. Exergoeconomic performance of the REC subsystem entails a decreasing trend with increasing ambient temperatures. The rate of exergy destruction in the REC, for instance, increases from 32341 kW to 38750 kW as the ambient temperature rises from -20°C to 30°C. The rate of cost of exergy destruction in the subsystem is observed to increase from 18.9 \$/h to 23.2 \$/h. Fig. 6.105 shows the effect of ambient temperature on different subsystems.

The exergy destruction rates of the HF, PSA and HX1 subsystems are found to entail an increasing trend with rising ambient temperatures. However, the exergy destruction rate in the TES is found to decrease with the same rise in temperature. For an ambient temperature of -20°C, the TES entails an exergy destruction rate of 84.3 MW. This is observed to decrease to 74.6 MW as the ambient temperature rises to 30°C.

As shown in Fig. 6.106, the exergoeconomic factor of the overall system decreases with rising ambient temperature. The overall exergoeconomic factor, for example, drops from 48.9% at a temperature of -20°C to 47% at a temperature of 30°C.

However, the overall exergy efficiency slightly rises from 46.2% to 46.3% for the same temperature change. Thus, the ambient temperature can affect the system performance and should be considered during system design.

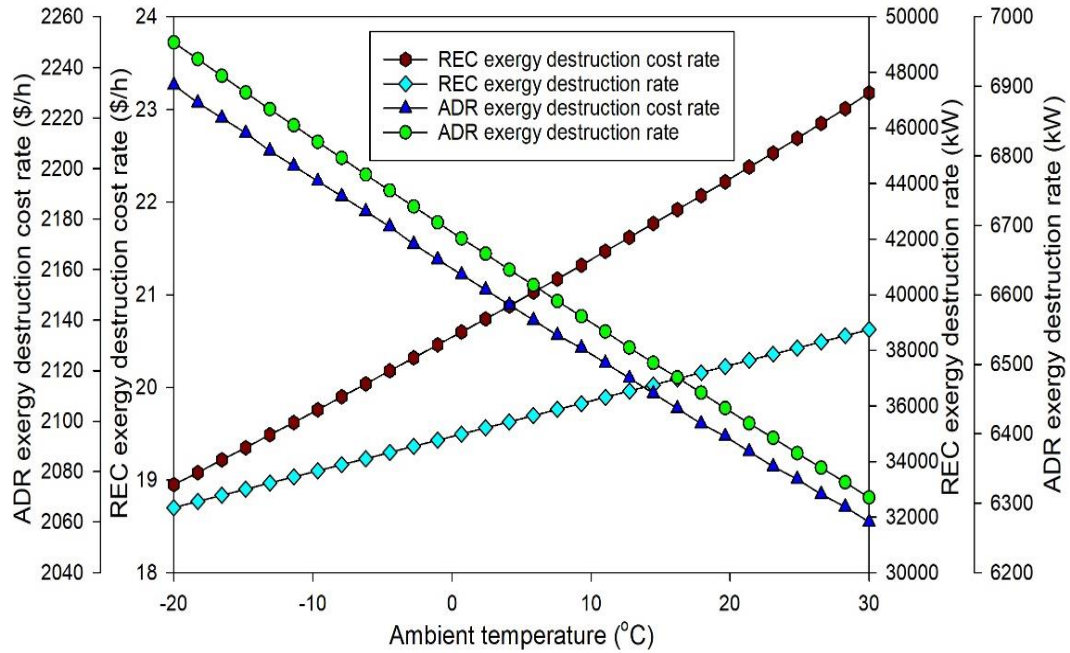


Fig. 6.104 Effect of ambient temperature on the exergoeconomic performances of ADR and REC subsystems in System 3

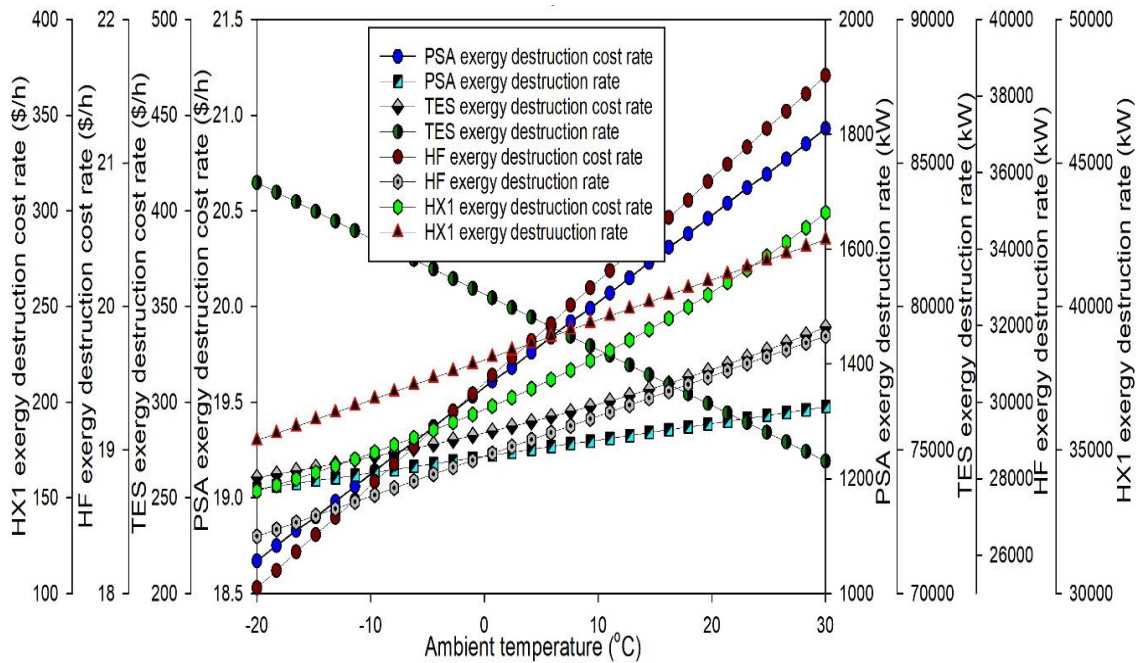


Fig. 6.105 Effect of ambient temperature on the exergoeconomic performances of different subsystems in System 3

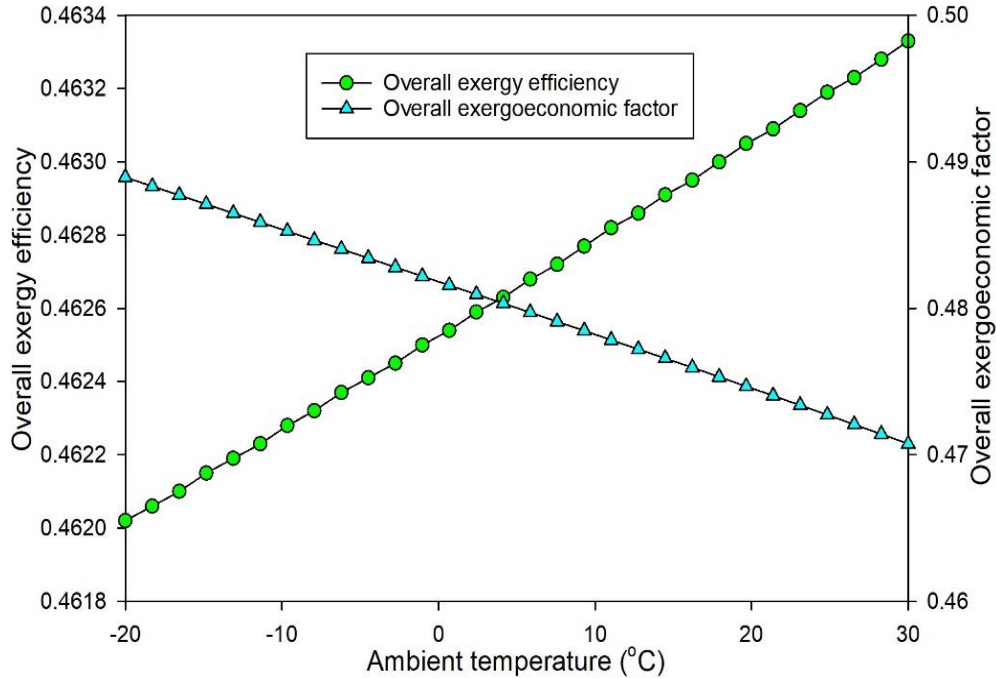


Fig. 6.106 Effect of ambient temperature on the overall exergoeconomic performance of System 3

Solar intensity variations are inherent with solar-based energy systems. Thus, it is important to analyse the thermodynamic as well as the economic performance of the developed system under different solar intensities. Fig. 6.107 shows the effects of solar intensity on major subsystems. A decreasing trend is found to be associated with the cost rate of exergy destruction rate in HX1. For instance, the cost rate decreases from 459.2 \$/h at a low solar intensity of 0.2 kW/m² to 186.6 \$/h at a high intensity value of 1 kW/m². However, the rate of exergy destruction in the HF increases from 12.5 MW to 62.4 MW for the same change in solar intensity.

The TES, HX1 and REC subsystems have an increasing trend in the rate of exergy destruction. The overall exergoeconomic performance of System 3 as a function of the solar intensity is depicted in Fig. 6.108. Although the overall exergoeconomic factor is observed to rise with increasing solar intensities, the overall efficiencies entail a decreasing trend. The total cost rates of exergy destruction are also observed to decrease as the solar intensities are raised. The total exergy destruction cost rate, for instance, decreases from 14741 \$/h to 14415 \$/h as the solar intensity rises from 0.2 kW/m² to 1 kW/m². However, the overall exergoeconomic factor rises from 46.9% to 47.4% for the same change in solar

intensity. Thus, it is essential to perform system optimization considering different solar radiation intensities to determine the optimal operating parameters at varying intensity levels.

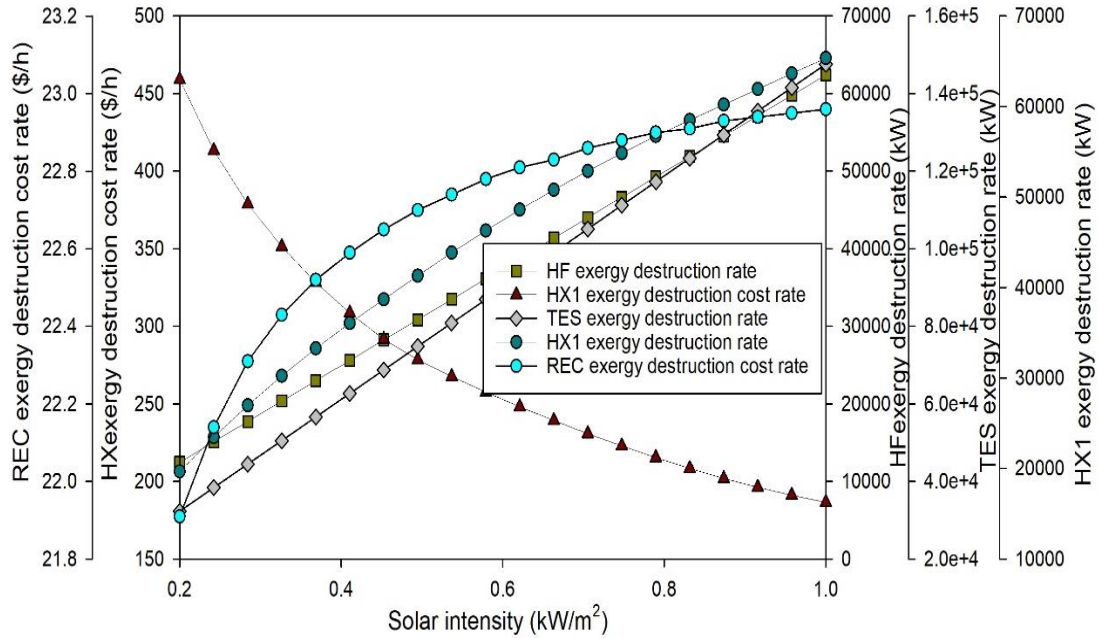


Fig. 6.107 Effect of solar intensity on the exergoeconomic performance of different subsystems of System 3

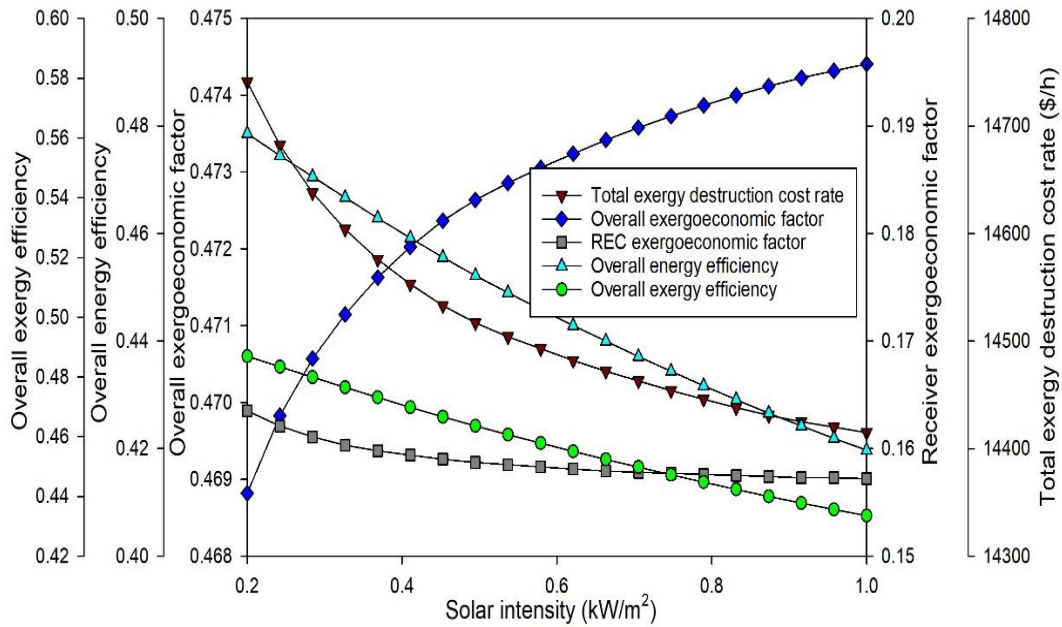


Fig. 6.108 Effect of solar intensity on overall exergoeconomic performance of System 3

The heliostat efficiency is an important system parameter that effects the overall thermodynamic as well as economic performance of the developed system. Fig. 6.109 depicts the effects of heliostat efficiency on exergoeconomic performances of different subsystems. An increasing trend is observed in the TES, HX1 and REC subsystems in terms of their exergy destruction rates as well as cost rates of exergy destruction.

For instance, the exergy destruction rate and the associated cost rate of HX1 is observed to rise from 38.5 MW and 222 \$/h to 47.5 MW and 252.8 \$/h respectively as the heliostat efficiency is raised from 60% to 80%. However, the overall energy and exergy efficiencies increase with rising heliostat efficiencies although the overall exergoeconomic factor decreases as depicted in Fig. 6.110.

This rising exergy destruction rates as well as the decreasing overall exergoeconomic factor can be attributed to the higher production of useful outputs via solar energy utilization. As the heliostat efficiency increases, higher energy inputs to the system result in the operation of different subsystems at higher output capacities. Thus, leading to higher exergy destruction rates.

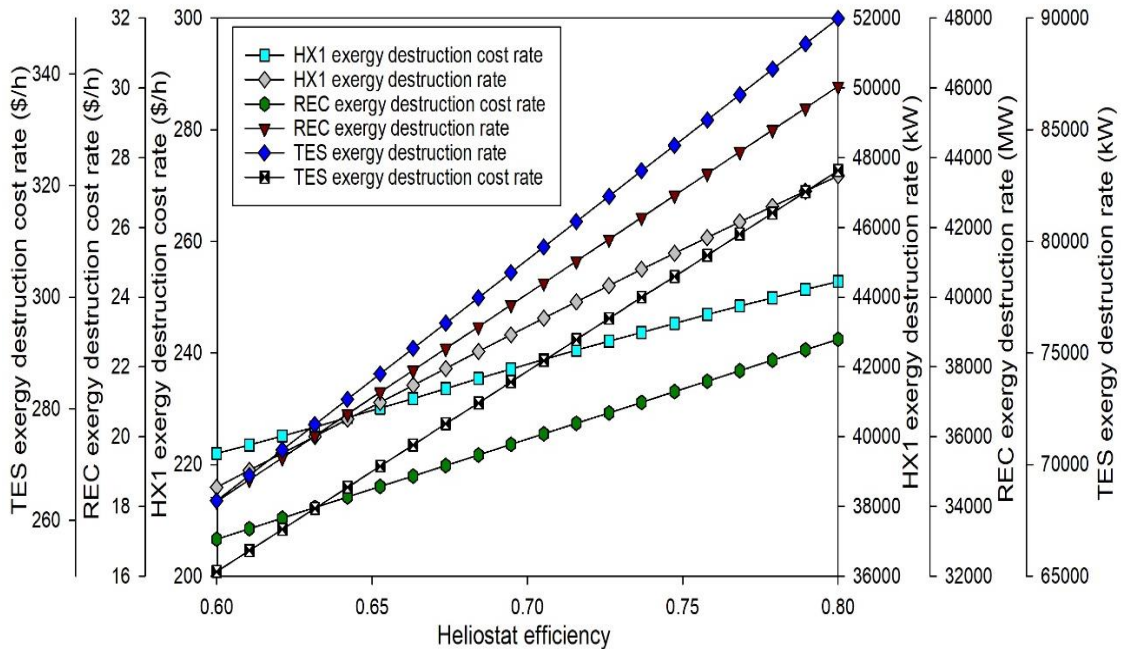


Fig. 6.109 Effect of heliostat efficiency on the exergoeconomic performance of major subsystems of System 3

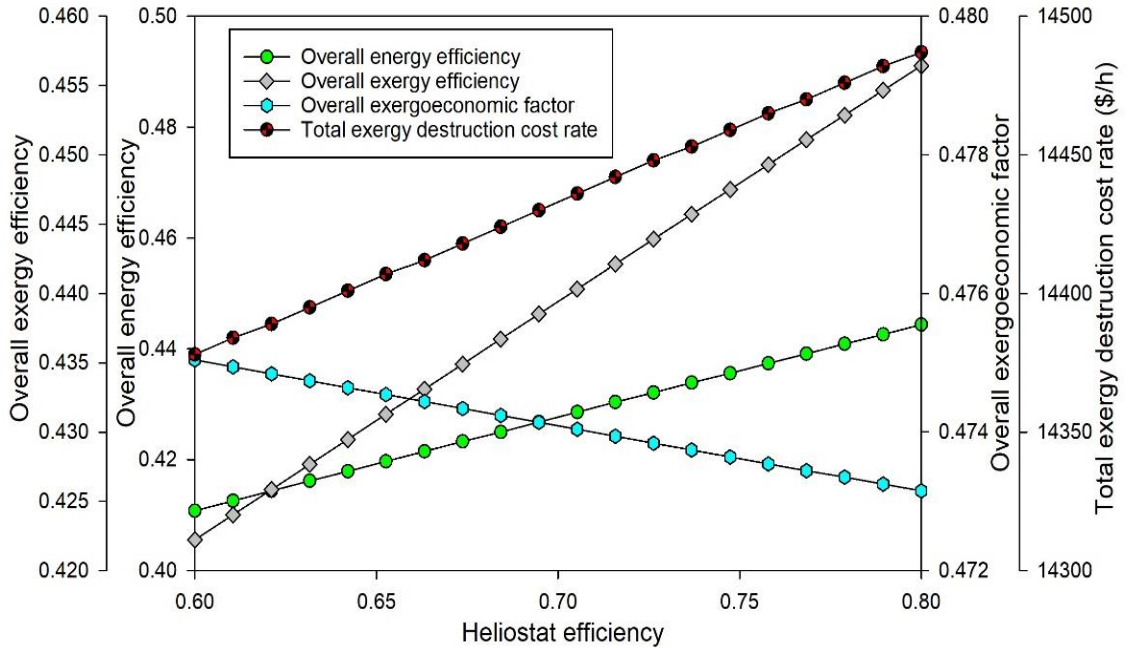


Fig. 6.110 Effect of heliostat efficiency on the overall exergoeconomic performance of System 3

As the interest rate varies depending on different economic factors, it is important to analyse the economic performance of the system under varying interest rates. Figs. 6.111 to 6.113 depict the effects of varying interest rates on the economic performances of System 3. As depicted in Fig. 6.111, the cost rate of exergy destruction entailed with the WT subsystem has a comparatively higher rise with an increase in the interest rates. For instance, as the interest rate rises from 5% to 20%, the cost rate of exergy destruction in the WT subsystem rises from 6519 \$/h to 16684 \$/h.

The ASR subsystem is associated with a rise from 151 \$/h to 386.5 \$/h in the cost rates of exergy destruction for the same rise in interest rate. Fig. 6.112 depicts the effect of interest rate on major components of the solar-based subsystem. The ADR is associated with comparatively higher cost rates of exergy destruction. For instance, as the interest rate rises from 5% to 20%, the exergy destruction cost rate in the ADR increases from 1765 \$/h to 4517 \$/h. The HX1 is observed to have a comparatively higher cost rate for exergy destruction that rises from 214.9 \$/h to 550.1 \$/h for the same increase in interest rate.

The changes in the overall exergoeconomic performance of System 2 with varying interest rates are shown in Fig. 6.113. Although, the total cost rates of investment as well as exergy

destruction rise considerably with increasing interest rates, the exergoeconomic factor entails a minor effect. The total investment cost rate rises from 11060 \$/h to 28306 \$/h.

Similarly, the total exergy destruction cost rate rises from 12316 \$/h to 31518 \$/h for the same rise in interest rate. Therefore, as the results depict, it is essential to consider the variations in interest rates in the economic planning as well as system design of energy systems.

System lifetime also effects the exergoeconomic results as shown in Figs. 6.114-6.116. Considerable variations are found to occur in the exergy destruction cost rates of different system components. For instance, the exergy destruction cost rate of the WT subsystem decreases from 21440 \$/h to 4685 \$/h when the system lifetime is raised from 10 to 30 years as depicted in Fig. 6.114.

The ASR cost rate of exergy destruction drops from 498.3 \$/h to 108.2 \$/h for the same change in system lifetime. The effect of lifetime on the exergoeconomic performance of solar-based subsystems is showed in Fig. 6.115. The exergy destruction cost rate of HX1 decreases from 762.7 \$/h to 143.9 \$/h as the lifetime is raised by 20 years.

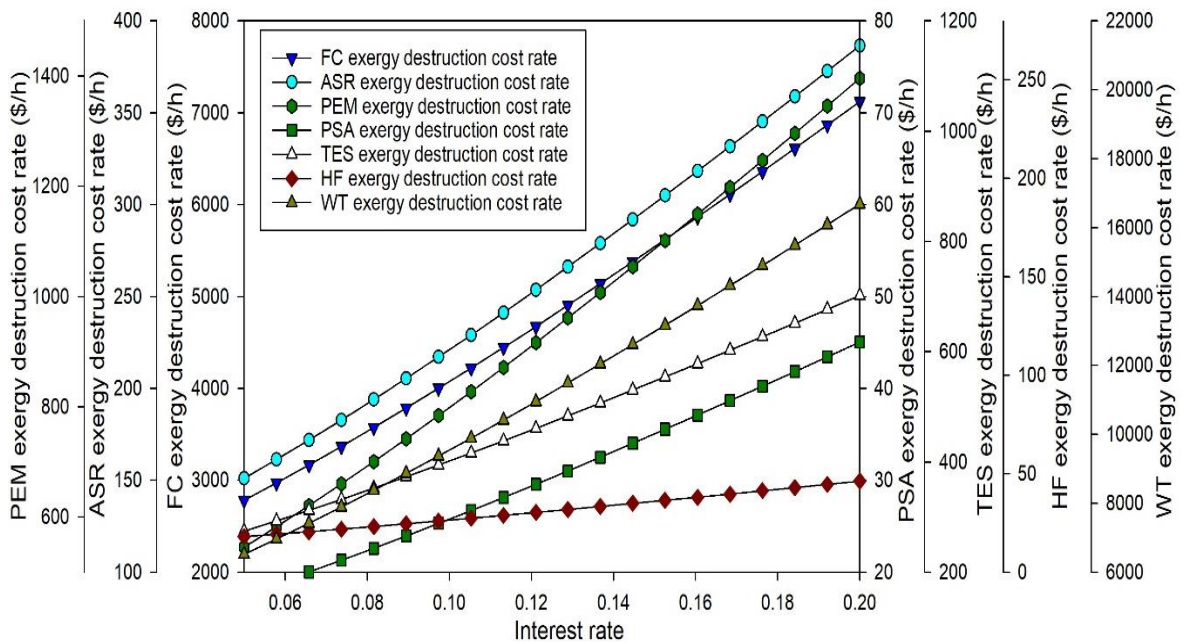


Fig. 6.111 Effect of interest rate on the exergoeconomic performance of different subsystems of System 3

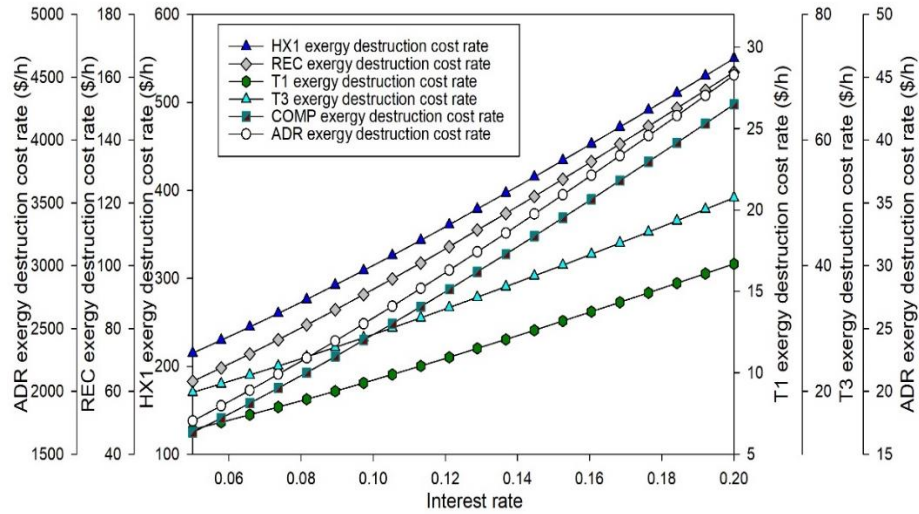


Fig. 6.112 Effect of interest rate on the exergoeconomic performance of solar-based subsystems of System 3

The effect of system lifetime on the overall exergoeconomic performance of System 3 is depicted in Fig. 6.116. The total investment as well as exergy destruction cost rates are found to decrease considerably with rising system lifetimes. For an increase in the system lifetime from 10 to 30 years, the total investment cost rate decreases from 37088 \$/h to 7813 \$/h. Similarly, the exergy destruction cost rate of the overall system decreases from 40699 \$/h to 8812 \$/h for the same change in system lifetime. However, the overall exergoeconomic factor decreases marginally from 47.7% to 46.9%.

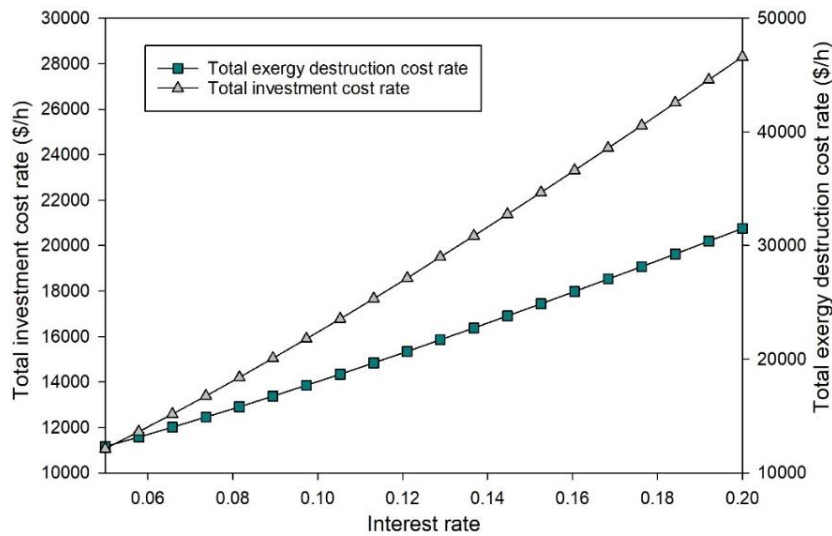


Fig. 6.113 Effect of interest rate on total investment and exergy destruction cost rates of System 3

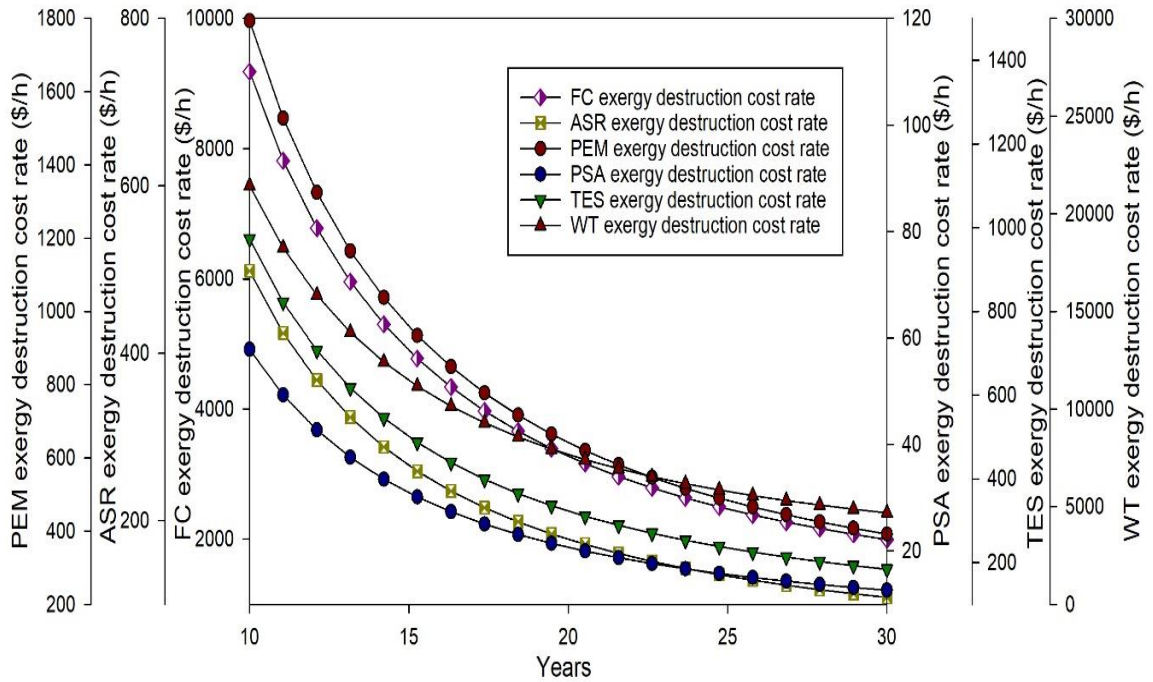


Fig. 6.114 Effect of system lifetime on the exergoeconomic performance of different subsystems of System 3

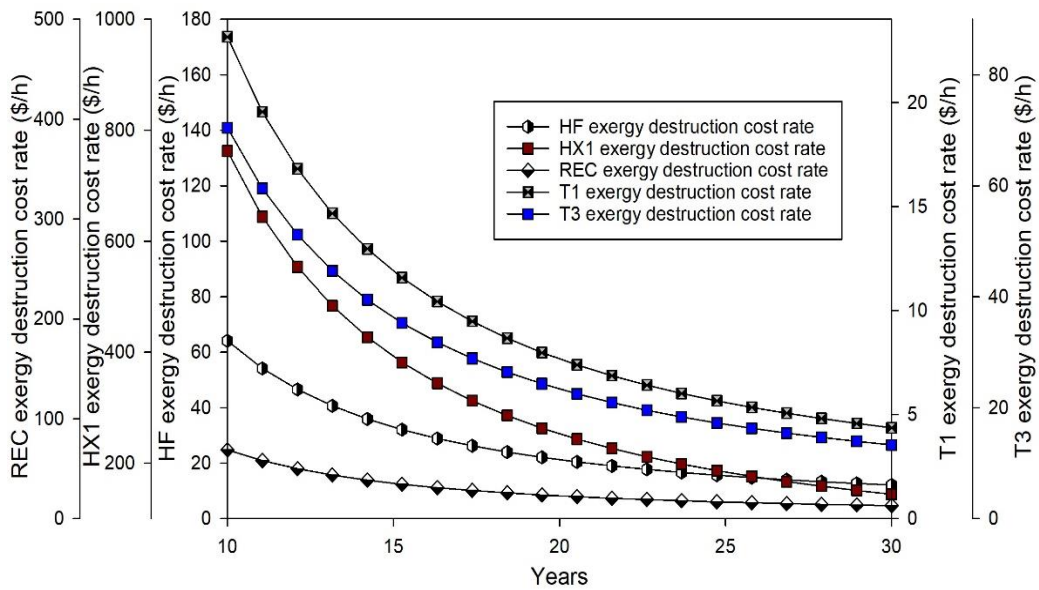


Fig. 6.115 Effect of system lifetime on the exergoeconomic performance of solar-based subsystems of System 3

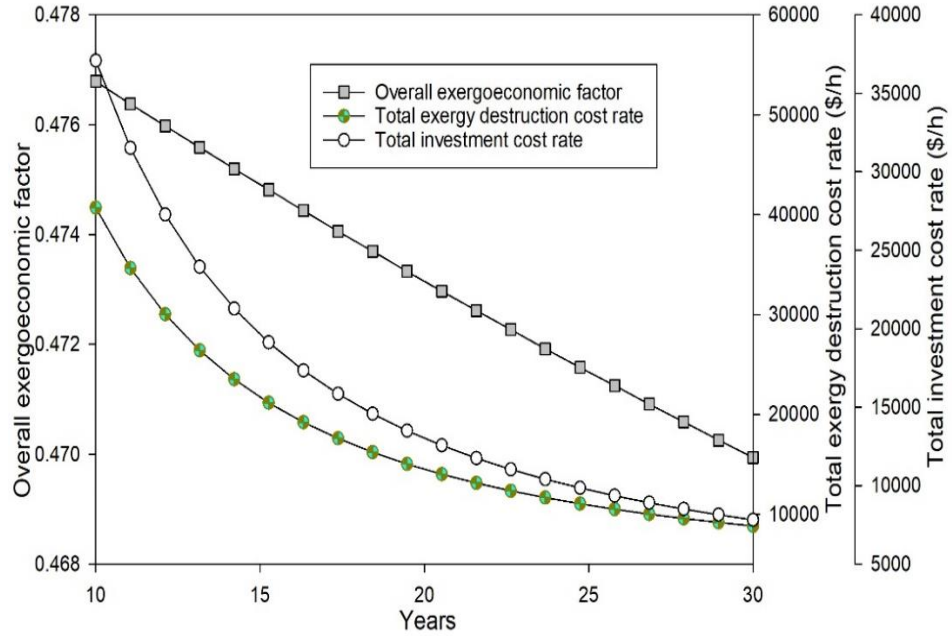


Fig. 6.116 Effect of system lifetime on the overall exergoeconomic performance of System 3

The effect of wind speed on the exergoeconomic performance of System 3 is depicted in Figs. 6.117-6.119. The PEM subsystem is found to entail an increasing trend in the exergy destruction rate up to a wind speed of 10 m/s. As the wind speed is raised further, the cost rate decreases with rising wind speeds.

The exergy destruction rate in the PEM subsystem rises continuously with increasing wind speeds. This can be attributed to the decrease in the ASR exergy destruction cost rate with rising wind speeds.

The FC subsystem entails an increasing trend in the exergy destruction rate with rising wind speeds. However, at higher wind speeds, the exergy destruction cost rate associated with the FC subsystem decreases with rising wind speeds.

The ADR subsystem is observed to have a decreasing trend in the exergy destruction cost rate with rising wind speeds. However, the PSA subsystem entails an increasing trend in both the exergy destruction rate as well as the cost rate of exergy destruction.

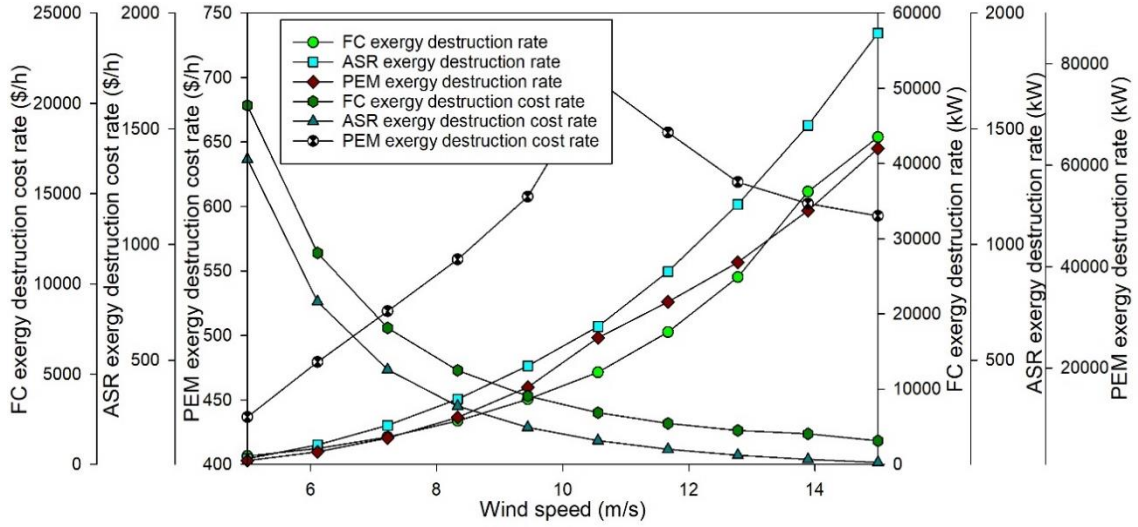


Fig. 6.117 Effect of wind speed on the exergoeconomic performance of PEM, ASR and FC subsystems of System 3

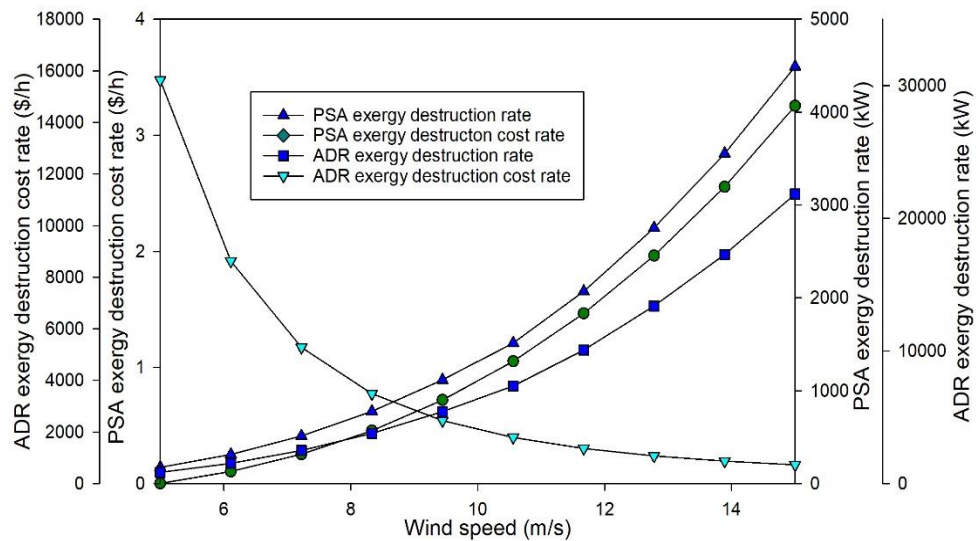


Fig. 6.118 Effect of wind speed on the exergoeconomic performance of PSA and ADR subsystems of System 3

At higher wind speeds, the total cost rate of exergy destruction decreases and the overall exergoeconomic factor rises. Both the overall energetic as well as the exergetic efficiencies are found to rise with increasing wind speeds. Hence, the developed system is found to provide more favorable thermodynamic as well as economic performance under high wind speeds.

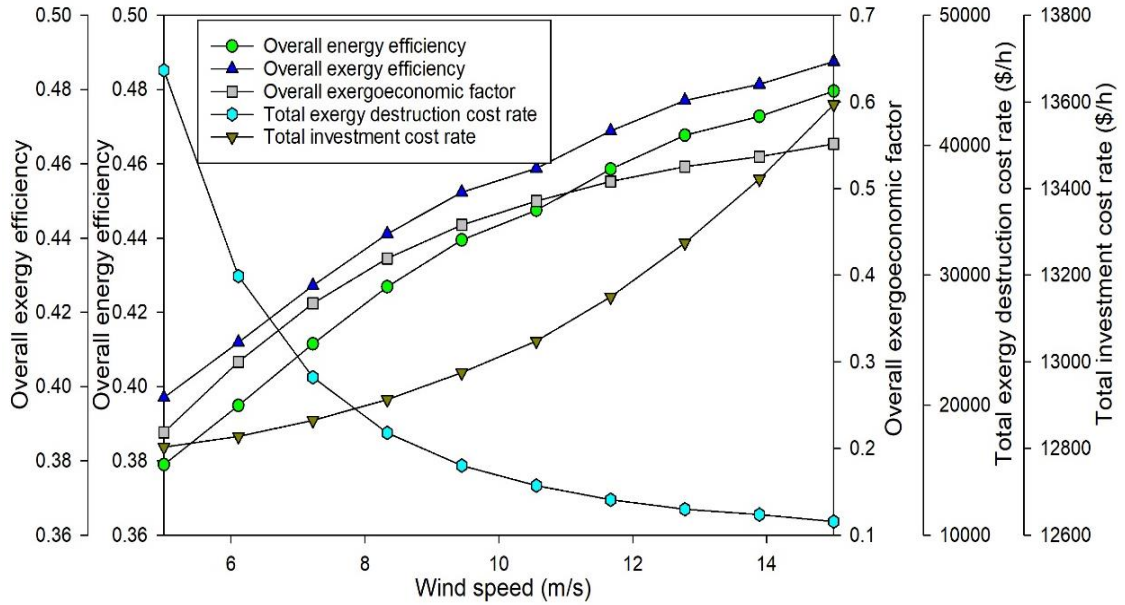


Fig. 6.119 Effect of wind speed on the overall exergoeconomic performance of System 3

The effects of PEM temperature on the exergoeconomic characteristics of the overall system are shown in Fig. 6.120. The overall energy as well as exergy efficiencies of the overall system are observed to increase with rising PEM temperatures. The total cost rate of exergy destruction in the overall system is also observed to entail a decreasing trend with rising PEM temperatures. This can be attributed to the decrease in the polarization losses in the electrolysis cells. As the temperature rises, the efficiency of the electrolyser is enhanced. Hence, this leads to higher hydrogen production rates with lower power input requirements.

As the rates of exergy destruction decrease, the costs associated with exergy destruction in the system also drop. Thus, it is recommended to utilize higher PEM temperatures for the attainment of higher system performances. Nevertheless, conventional electrolyzers do not support temperatures of more than 80°C owing to membrane damage. Thus, suitable PEM temperatures should be chosen that provide optimal system performances.

The effect of isentropic efficiency on the exergoeconomic performance of major subsystems of System 3 are depicted in Fig. 6. 121. The turbine exergy destruction rates are found decrease considerably when the isentropic efficiency rises. This can be attributed to the decrease in the irreversibilities with the usage of higher isentropic efficiency devices.

As the amount of irreversibilities decrease, the entropy generation and thus the exergy destruction rate also drop. Hence, it is recommended to utilize higher isentropic efficiency turbines to attain higher exergoeconomic performances.

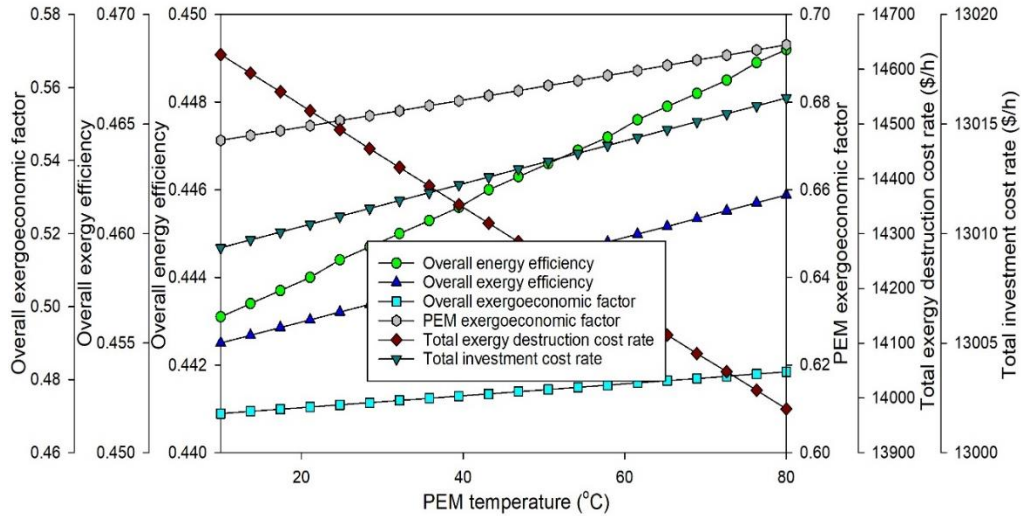


Fig. 6.120 Effect of PEM temperature on the overall exergoeconomic performance of System 3

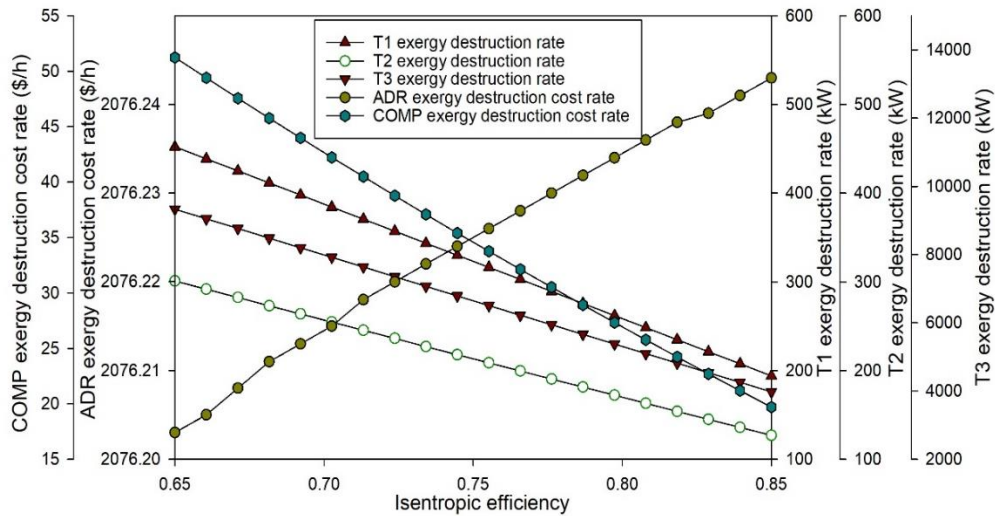


Fig. 6.121 Effect of isentropic efficiency on exergoeconomic performance of major subsystems

6.6 Multi-objective optimization results

This chapter presents the results of multi-objective optimization of the developed systems. Different configurations of solar intensities as well as wind speeds are considered. The $H_{sol}H_{wn}$ configuration denotes the system operation under a high solar intensity of 1 kW/m^2

and a high wind speed of 15 m/s. Next, the $H_{sol}L_{wn}$ configuration represents the combination of a high solar intensity value and a low wind speed of 5 m/s. The $L_{sol}H_{wn}$ configuration represents the system operation under a low solar intensity of 0.2 kW/m^2 and a high wind speed value of 15 m/s. The combination of average values of solar intensity (0.6 kW/m^2) as well as wind speeds (10 m/s) is denoted by $M_{sol}M_{wn}$. The pareto frontier solutions for the three systems under different configurations are presented, and the values of decision variables at a given optimal point in the pareto frontier are evaluated. Each point in the pareto frontier represents an optimal operation point and the point to be chosen for system design depends on the available budget and required overall efficiency.

6.6.1 System 1 multi-objective optimization results

The multi-objective optimization results for System 1 under the $H_{sol}H_{wn}$ configuration is depicted in Fig. 6.122. The Pareto frontier solution considering this configuration depicts the optimal combinations of the overall exergy efficiency and total cost rates of the system. The overall exergy efficiency is maximized while the total cost rate of the system is minimized. An increasing trend is observed as expected between the overall exergy efficiency and total cost rate.

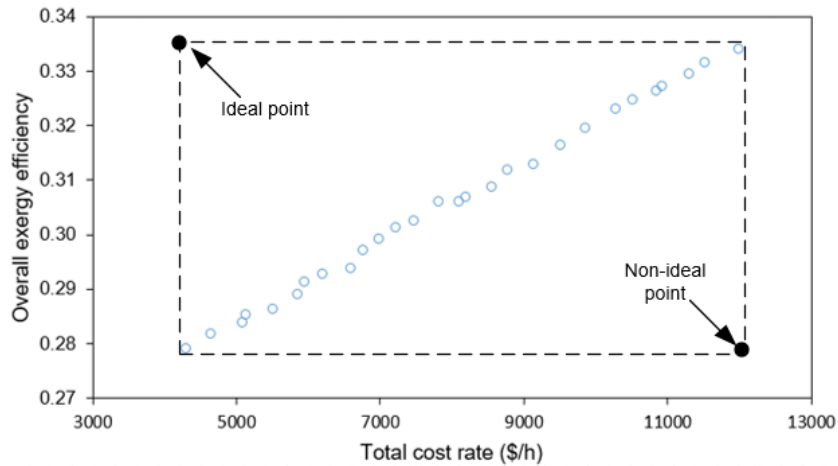


Fig. 6.122 Pareto frontier for System 1 under high solar radiation and high wind speed ($H_{sol}H_{wn}$) configuration

As the overall exergy efficiency is aimed to maximize, the total cost rate of the system also attained higher corresponding values. Similarly, when the total cost rate of the system is minimized, the overall exergy efficiency of the system also attained lower values. As

depicted in the figure, the ideal optimal point entails the top-left corner that would correspond to least costs and highest efficiency. The non-ideal point is labelled on the bottom right corner corresponding to the maximum cost and least efficiency. The operational point to be chosen depends on the type of application, available budget, targeted overall exergy efficiency, etc. In the present study, an exemplary optimal point is chosen from the pareto frontiers and the decision variables are evaluated at these configurations.

The values of decision variables of System 1 at an exemplary point are found that provide overall exergy efficiency of 29.2% and a total cost rate of 6067.9 \$/h. These are provided in Table 6.3. The minimum value of interest rate is obtained at the optimal point that signifies its importance in determining the overall economic performance of a given energy system.

The PV efficiency is observed to entail nearly the maximum value considered for the decision variable. This denotes the importance of developing and utilizing high-efficiency solar PV panels, which can aid in providing optimal exergetic as well as economic performances for System 1. An average PEM temperature of 50.4°C is obtained for the chosen optimal operation point. The operational current density of the AFC subsystem is found to be 60.8 A/m². The Pareto frontier solution considering the H_{sol}L_{wn} configuration for System 1 is depicted in Fig. 6.123.

The operation point considered entails a total cost rate of 13234 \$/h and a corresponding overall exergy efficiency of 17.6%. The lower overall exergy efficiency obtained at the optimal operation point for this configuration can be attributed to the higher portion of solar PV-based electricity generation. At low wind speeds and high solar intensities, the majority of the power generation is associated with the PV farm. As the PV farm, entails lower efficiencies than wind-based power generation, the overall system efficiency also entails a lower value as compared to the configuration with a higher wind speed.

The total cost rate of the system is higher owing to higher rates of exergy destruction costs in the system. Hence, the operation point considered under this configuration shows that comparatively lower system efficiencies as well as higher cost rates will be associated with system operation. However, these can be improved through the development of PV panels

entailing higher efficiencies. The Pareto frontier solution for System 1 under the $L_{sol}H_{wn}$ configuration is depicted in Fig. 6.124. The optimal point considered entails an overall exergy efficiency of 37% and a corresponding total cost rate of 6335.1 \$/h.

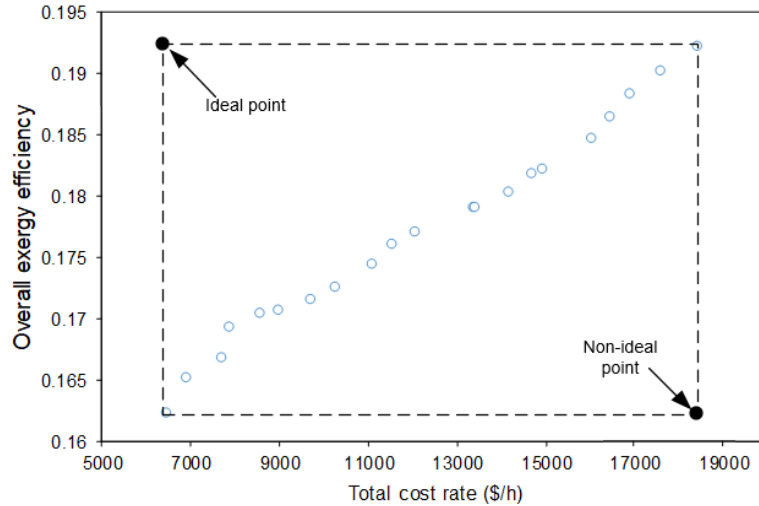


Fig. 6.123 Pareto frontier for System 1 under high solar radiation and low wind speed ($H_{sol}L_{wn}$) configuration

The higher overall exergy efficiency obtained as compared to other configurations can be attributed to the higher portion of wind-based power generation. At higher wind speeds and lower solar intensities, the majority of the power generation arises from the wind farm. As the wind-based power generation entails higher efficiencies as compared to the PV farm, the optimal point entails a higher overall exergy efficiency as compared to other configurations. The wind-based power generation subsystem also entails lower exergy destruction rates as well as exergy destruction cost rates. Thus, when the majority of system operation relies on wind-based power generation, the total cost rates are also lower due to lower rates of exergy destruction.

The Pareto solutions for System 1 under the $M_{sol}M_{wn}$ configuration is shown in Fig. 6.125. The operational point considered provides an overall exergy efficiency of 24.7% and a total cost rate of 7088.1 \$/h. The PEM temperature obtained entails a value of 44.2°C. As average portions of both, solar and wind-based power generation are associated with this configuration, the overall exergy efficiency is lower than the $L_{sol}H_{wn}$ configuration and higher than the $H_{sol}L_{wn}$ configuration.

Lower ambient temperatures are found to be favorable for optimal system performances. Maximum system lifetimes as well as minimum interest rates are also found to be common with all optimal configurations. Maximum values of the decision variable associated with the PV efficiency are also found to be common in all optimal configurations of System 1.

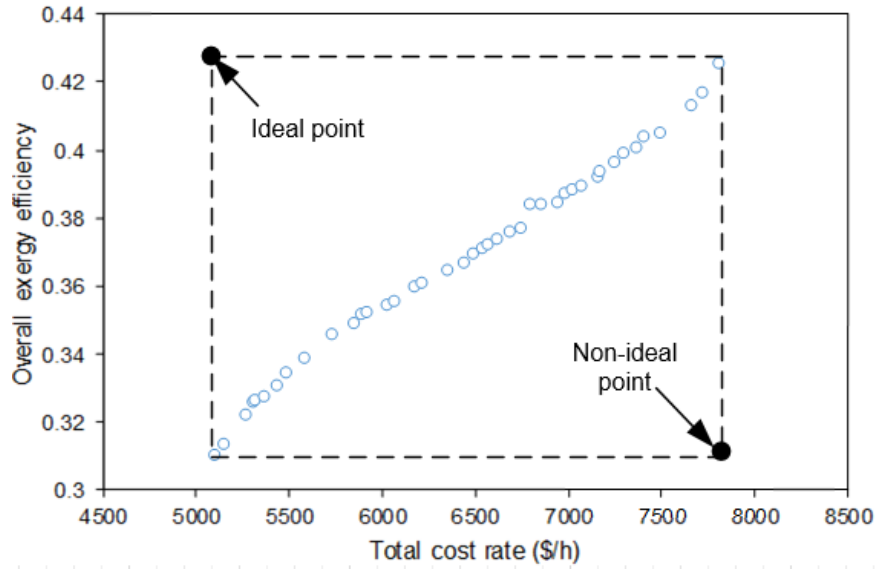


Fig. 6.124 Pareto frontier for System 1 under low solar radiation and high wind speed ($L_{sol}H_{wn}$) configuration

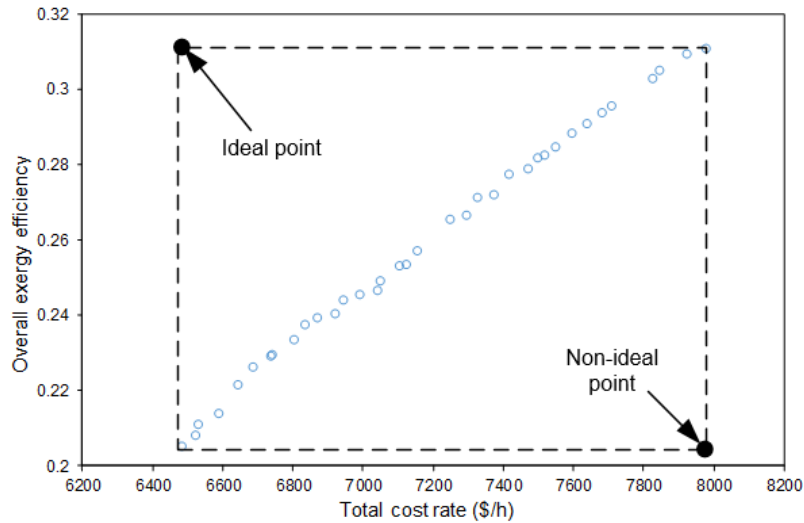


Fig. 6.125 Pareto frontier for System 1 under medium solar radiation and medium wind speed ($M_{sol}M_{wn}$) configuration

Table 6.3 Values of decision variables and objective functions for system 1

	Configuration			
	H_{sol}H_{wn}	H_{sol}L_{wn}	L_{sol}H_{wn}	M_{sol}M_{wn}
Total PV area (m ²)	1004121	1026607	1508844	1036258
Isentropic efficiency (%)	84.0	85.0	83.0	79.0
Wind turbine area (m ²)	2039	2013	2036	2122
Interest rate (%)	5.1	5.0	5.0	5.4
Ambient temperature (°C)	-11.6	-12.2	-19.6	-19.9
AFC operating temperature (°C)	60.8	28.8	13.6	20.1
PEM operating temperature (°C)	50.4	16.3	64.1	44.2
PV efficiency (%)	19.0%	19.1%	19.7%	20.0%
Operational lifetime (years)	30.0	29.7	29.9	29.8
AFC current density (A/m ²)	60.8	30.1	57.9	24.3
Overall exergy efficiency (%)	29.2	17.6	37.0	24.7
Total cost rate (\$/h)	6067.9	13234.0	6335.1	7088.1

6.6.2 System 2 multi-objective optimization results

The Pareto frontier solution for System 2 under the H_{sol}H_{wn} configuration is depicted in Fig. 6.126. The operation point chosen provides a total cost rate of 9385.5 \$/h and a corresponding overall exergy efficiency of 42.0%. The primary difference between the optimal operational points obtained for System 2 as compared to System 1 entails the utilization of the solar-tower based power generation technique. As System 2 also includes the utilization of available waste heat rejected from the steam turbine-based power generation cycle, higher overall efficiencies are obtained.

Under the H_{sol}H_{wn} configuration, the heliostat field area obtains a value of 372128 m² at the chosen optimal point. The MEAFC and EAS temperatures are found to be 220.8°C and 203.9°C under optimal conditions. However, a lower PEM temperature of 14.7°C is obtained at the optimal point. Nevertheless, similar to System 1, the minimum interest rate values as well as maximum system lifetimes are obtained for optimal system performance. High values of the heliostat efficiency are obtained for all configurations. The Pareto frontier solutions under the H_{sol}L_{wn} configuration are shown in Fig. 6.127. The overall

exergy efficiency is found to be 51% and the corresponding total cost rate is evaluated as 4503.3 \$/h at the chosen point. The higher overall exergy efficiency and as well as lower total cost rates obtained can be attributed to the lower portion of wind-based system operation for System 2.

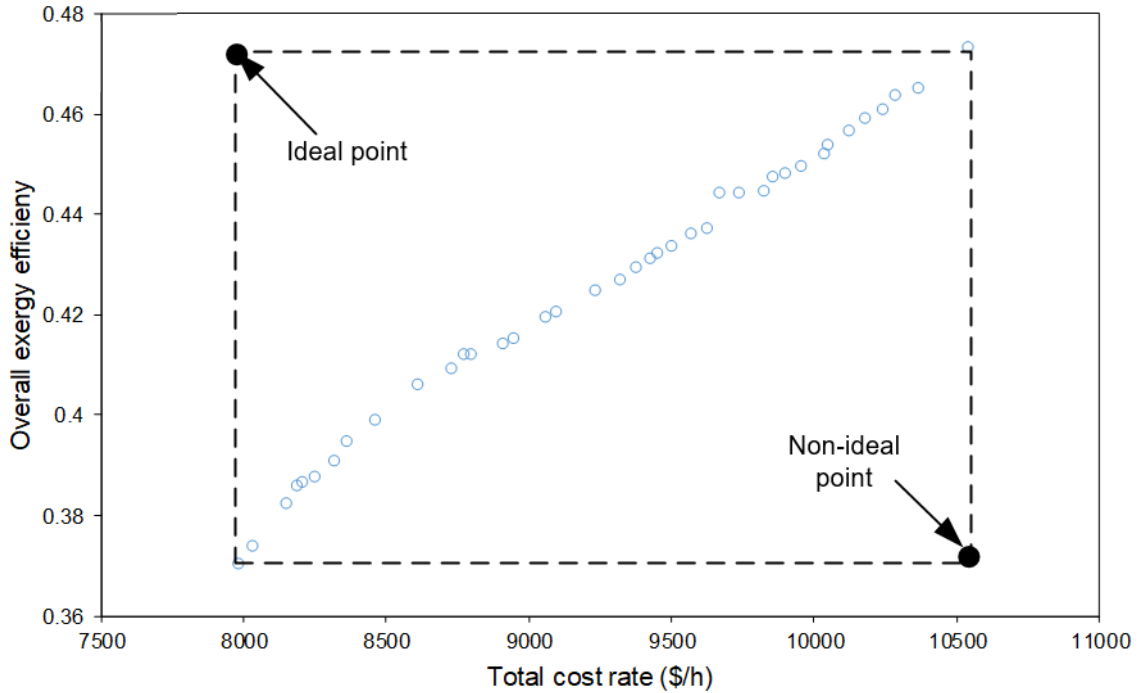


Fig. 6.126 Pareto frontier for System 2 under high solar radiation and high wind speed ($H_{sol}H_{wn}$) configuration

The solar-based system operation in System 2 includes both the production of electrical power as well as useful heat output. Hence, higher the solar-based portion of system operation, higher are the overall exergy efficiencies. The MEAFC operating temperature obtained at the chosen point of this system configuration has a value of 268.4°C and the EAS operating temperature is 226.3°C. A higher PEM temperature of 31.4°C is obtained under this system operation configuration. Nevertheless, a lower heliostat field area of 282766 m² is obtained for the $H_{sol}L_{wn}$ configuration.

The Pareto solutions under the $L_{sol}H_{wn}$ configuration for System 2 are depicted in Fig. 6.128. The overall exergy efficiency at the chosen operation point is found to be 39.1%. The corresponding total cost rate is determined to be 8730.8 \$/h. The comparatively lower overall exergy efficiency obtained for the $L_{sol}H_{wn}$ configuration as compared to $H_{sol}H_{wn}$ or

$H_{sol}L_{wn}$ configurations can be attributed to the lower solar-based system operation. Under lower solar-based system operation, both lower solar-based power output as well as useful heat output are associated with the operation of System 2. Hence, this leads to lower overall exergy efficiencies at the optimal point under this configuration. The total cost rate is also found to be higher for this configuration owing to the higher contribution of wind-based system operation. Higher exergy destruction rates as well as exergy destruction cost rates are associated with this optimal operation point.

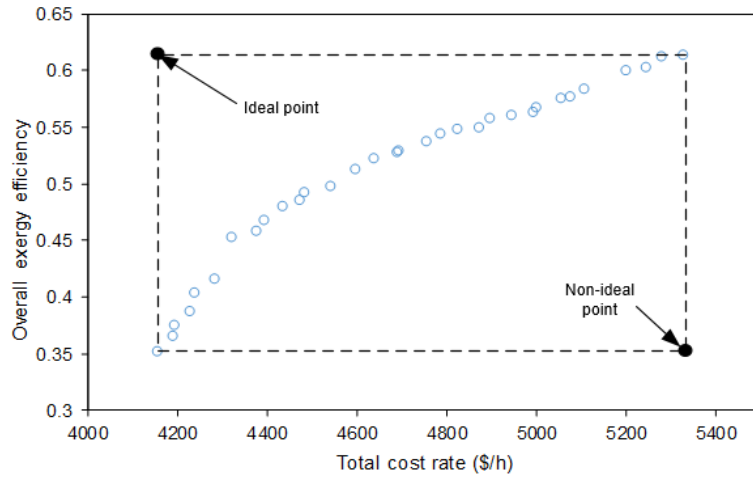


Fig. 6.127 Pareto frontier for System 2 under high solar radiation and low wind speed ($H_{sol}L_{wn}$) configuration

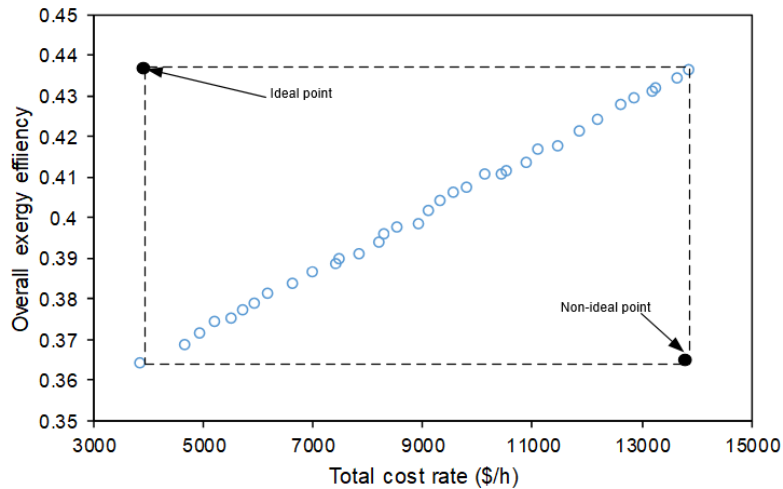


Fig. 6.128 Pareto frontier for System 2 under low solar radiation and high wind speed ($L_{sol}H_{wn}$) configuration

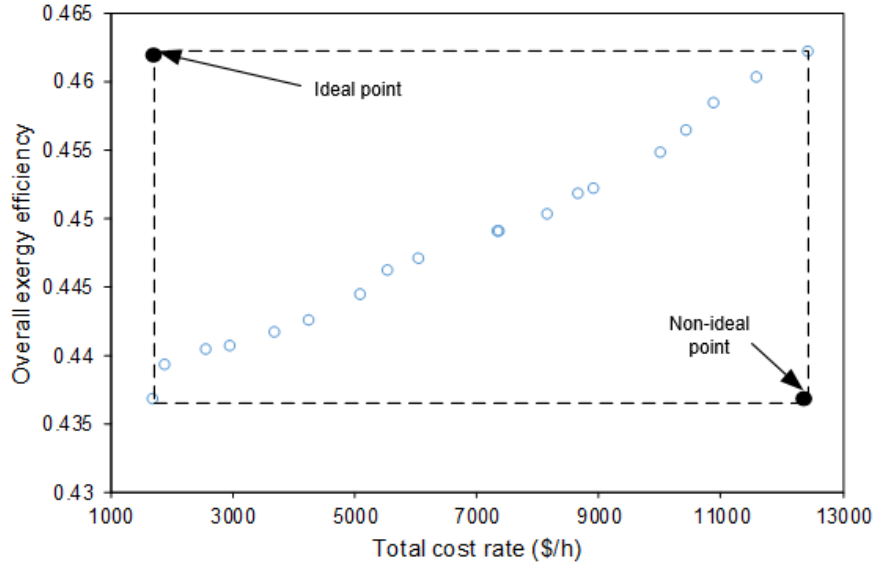


Fig. 6.129 Pareto frontier for System 2 under medium solar radiation and medium wind speed ($M_{sol}M_{wn}$) configuration

Table 6.4 Values of decision variables and objective functions for system 2

	Configuration			
	$H_{sol}H_{wn}$	$H_{sol}L_{wn}$	$L_{sol}H_{wn}$	$M_{sol}M_{wn}$
Heliostat field area (m ²)	372128	282766	853154	370426
Isentropic efficiency (%)	72	65	76	69
Wind turbine area (m ²)	2002	2090	2010	2086
Interest rate (%)	5.0	5.0	5.1	5.0
Ambient temperature (°C)	6.8	2.2	9.3	7.0
MEAFC operating temperature (°C)	220.8	268.4	213.5	227.6
EAS operating temperature (°C)	203.9	226.3	232.7	253.2
PEM operating temperature (°C)	14.7	31.4	12.5	21.4
Heliostat efficiency (%)	79	80	78	79
Operational lifetime (years)	29.3	30	29.9	29.8
Overall exergy efficiency (%)	42.0	51.0	39.1	44.6
Total cost rate (\$/h)	9385.5	4503.3	8730.8	6007.2

The optimal operation point chosen for System 2 under the $M_{sol}M_{wn}$ configuration comprising of medium levels of both solar intensities as well as wind speeds is found to have an overall exergy efficiency of 44.6%. The corresponding total exergy destruction cost rate entails a value of 6007.2 \$/h. The exergy efficiency under medium level inputs of solar intensities and wind speeds is found to be higher than the $L_{sol}H_{wn}$ as well as $H_{sol}H_{wn}$

configurations at the chosen points. This is attributed to the higher portion of solar-based system operation that results in higher System 2 performance as described earlier.

The heliostat field area of 370426 m² is obtained under this configuration at this operation point. A wind turbine swept area of 2086 m² is obtained. Next, an MEAFC temperature of 227.6°C and an EAS temperature of 253.2°C is obtained at the chosen point for the M_{sol}M_{wn} configuration. Nevertheless, although different system configurations are considered, the system lifetime entails the maximum possible values as a decision variable.

The interest rate entails the minimum decision variable values for the system configurations considered. Maximum decision variable values of the heliostat efficiencies are obtained for different configurations considered signifying the importance of having higher heliostat efficiencies for optimal performance of System 2.

6.6.3 System 3 multi-objective optimization results

The results of multi-objective optimization of System 3 are depicted in Figs. 6.130-134. The Pareto frontier solution for System 3 under the H_{sol}H_{wn} configuration is depicted in Fig. 6.130. The operation point chosen under this configuration has a total cost rate of 4955.5 \$/h and a corresponding overall exergy efficiency of 48.8%. Under this configuration, the optimal heliostat field area is 206719 m². The FC and PEM operating temperatures are 34.4°C and 64.1°C under optimal conditions respectively. Nevertheless, similar to earlier results, minimum interest rates and maximum lifetimes are obtained at the optimal operation point. High heliostat efficiencies are inherent to the optimal points at all configurations.

The Pareto frontier solution for the L_{sol}H_{wn} configuration is shown in Fig. 6.132. The overall exergy efficiency has a value of 39.7% and the corresponding total cost rate is evaluated as 8298.7 \$/h at the chosen operational point. The lower overall exergy efficiency as well as higher total cost rates are attributed to the lower contribution of wind-based power generation. The FC operating temperature is found to be 21.2°C and the PEM operating temperature is 52.6°C. However, a lower turbine inlet pressure of 12338 kPa is obtained under this system operation configuration.

A slightly higher heliostat field area of 230747 m² is obtained. Next, the Pareto solutions under the H_{sol}L_{wn} configuration for System 3 provide an overall exergy efficiency is found to be 50.2% under a chosen operation point. Moreover, the corresponding total cost rate is found to be 4503.8 \$/h. The comparatively higher overall exergy efficiency obtained for this configuration as compared to other configurations can be attributed to the higher wind-based system operation.

The total cost rate is also found to be lower for this configuration owing to the higher contribution of wind-based system operation. The system components operated with wind energy entail higher operation under this configuration owing to higher wind-based power output. Lower exergy destruction rates as well as exergy destruction cost rates are associated with this optimal operation point. Hence, System 3 is found to provide more favorable performances under higher levels of wind speeds and corresponding low levels of solar intensities.

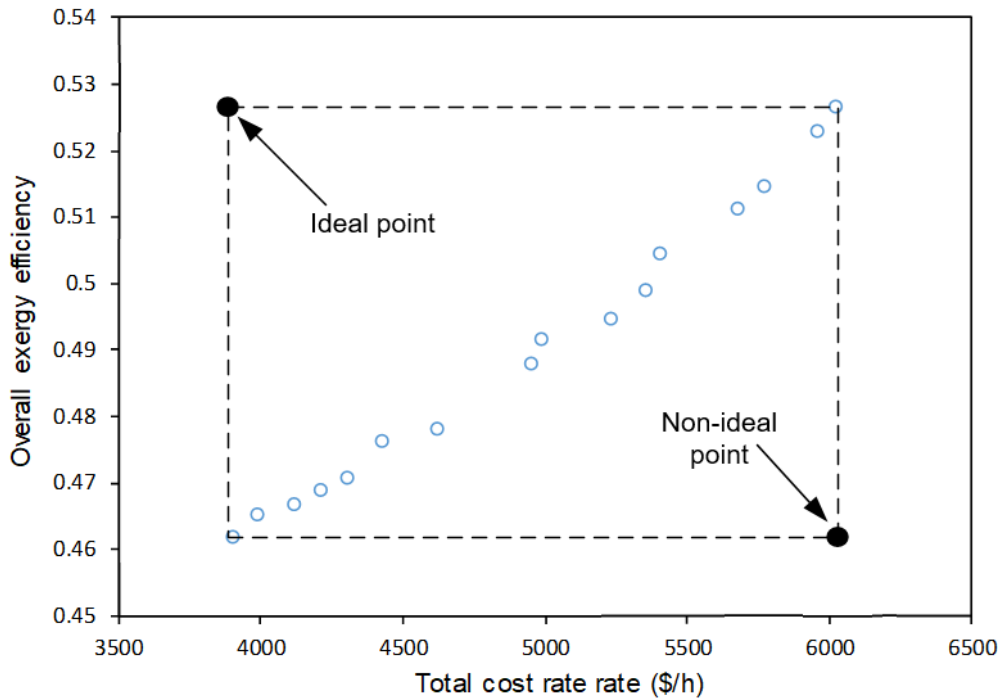


Fig. 6.130 Pareto frontier for System 3 under high solar radiation and high wind speed (H_{sol}H_{wn}) configuration

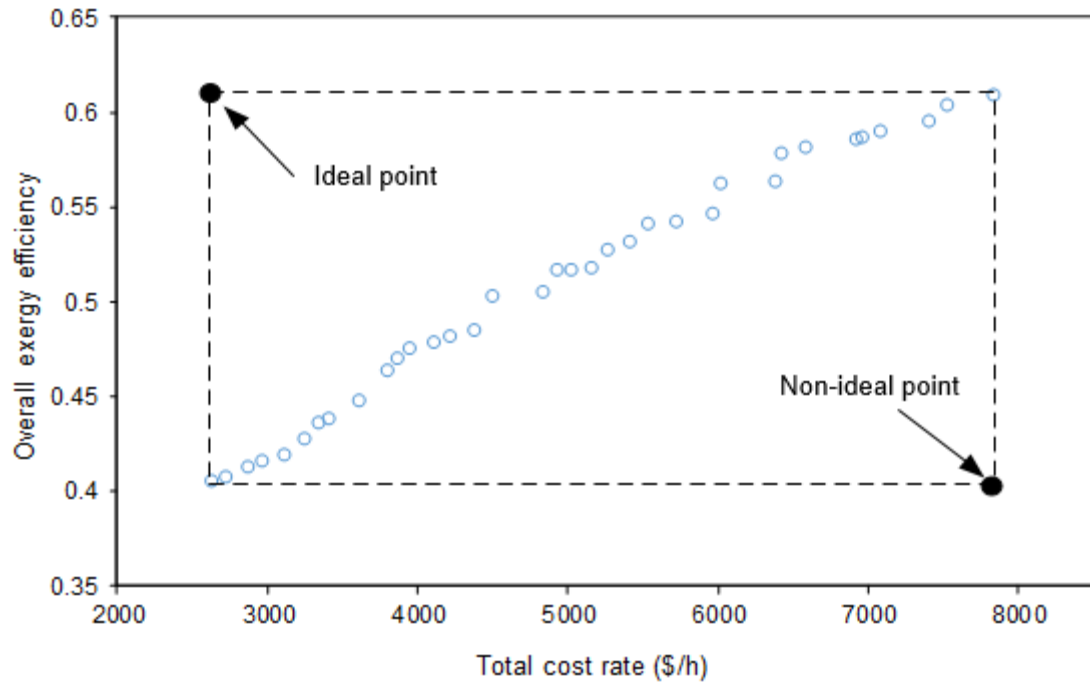


Fig. 6.131 Pareto frontier for System 3 under high solar radiation and low wind speed ($H_{sol}L_{wn}$) configuration

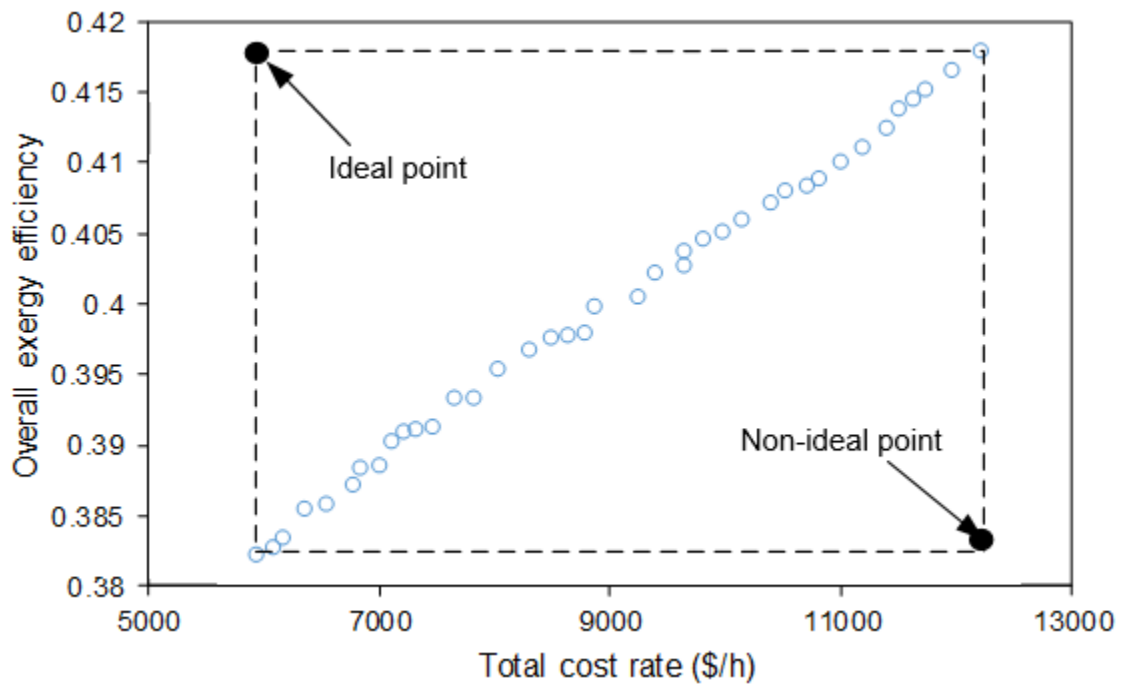


Fig. 6.132 Pareto frontier for System 3 under low solar radiation and high wind speed ($L_{sol}H_{wn}$) configuration

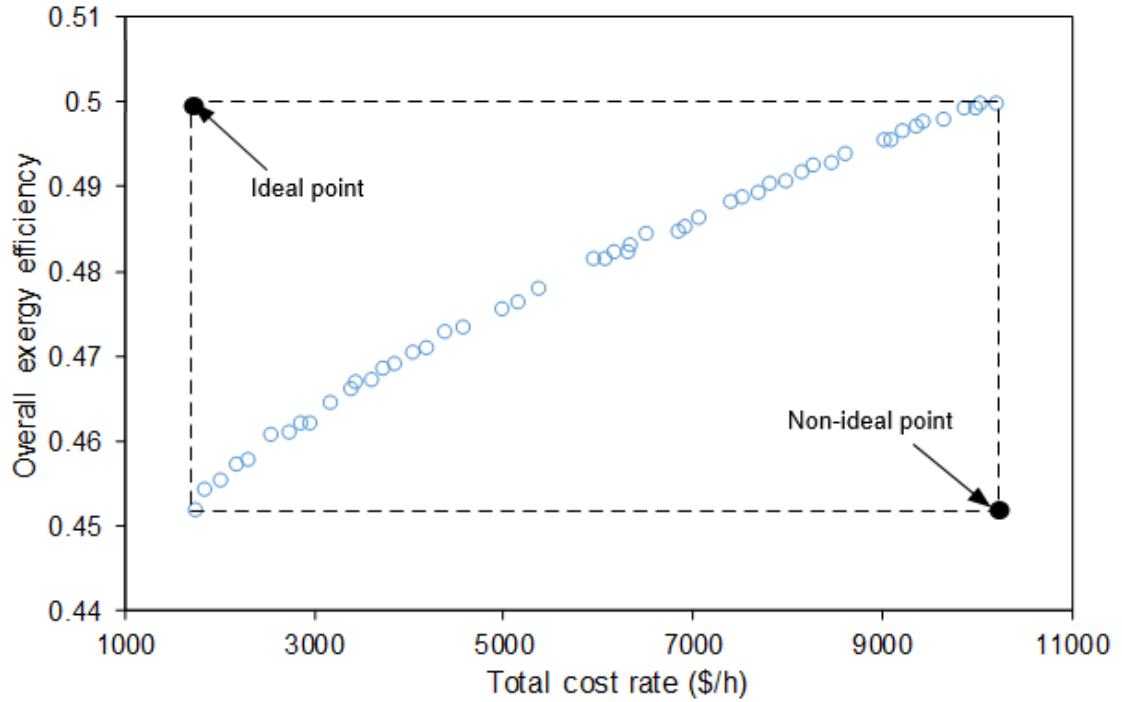


Fig. 6.133 Pareto frontier for System 3 under medium solar radiation and medium wind speed ($M_{sol}M_{wn}$) configuration

Table 6.5 Values of decision variables and objective functions for system 3

	Configuration			
	H_{sol}H_{wn}	L_{sol}H_{wn}	H_{sol}L_{wn}	M_{sol}M_{wn}
Heliostat field area (m ²)	206719	230747	270891	221247
Isentropic efficiency (%)	68	69	67	67
Wind turbine area (m ²)	2015	2031	2005	2021
Interest rate (%)	5.0	5.0	5.1	5.0
Ambient temperature (°C)	18.5	26.7	-10.5	15.6
FC operating temperature (°C)	34.4	21.2	48.8	35.2
Turbine inlet pressure (kPa)	17452	12338	11769	14493
PEM operating temperature (°C)	64.1	52.6	78.8	79.9
Heliostat efficiency (%)	79	77	79	79
Operational lifetime (years)	29.9	30	29.9	30
Overall exergy efficiency (%)	48.8	39.7	50.2	47.6
Total cost rate (\$/h)	4955.1	8298.7	4503.8	4978.8

The operating conditions considered for System 3 under the $M_{sol}M_{wn}$ configuration entailing medium levels of both solar intensities as well as wind speeds are found to provide an overall exergy efficiency of 47.6%. The corresponding exergy destruction cost rate is

found to be 4978.8 \$/h. The optimal exergy efficiency under this configuration is found to be higher than the $H_{sol}L_{wn}$ configuration owing to the higher contribution of wind-based system operation. An optimal heliostat field area of 221247 m² is found under this configuration and a wind turbine swept area of 2021 m² is found.

An FC temperature of 35.2°C and PEM temperature of 79.9°C are obtained at this operational point. However, although different system configurations are considered, the system lifetime entails the maximum values of decision variables. Similarly, the interest rate entails the minimum decision variable values for all configurations investigated. Maximum limits of the heliostat efficiencies are reached for each configuration denoting the significance of utilizing heliostats with higher efficiencies to obtain better system performances. It is recommended to conduct a life cycle analysis of the present system considering different stages of life cycles. The system optimization can then be expanded to include different metrics to investigate which optimal conditions provide lower life cycle costs as well as higher life cycle efficiencies. An overall comparison of the three developed systems under $M_{sol}M_{wn}$ configuration is provided in Table 6.6.

Table 6.6 Comparison of overall exergy efficiencies and associated costs of the developed systems

	System 1	System 2	System 3
Overall exergy efficiency	24.7	44.6	47.6
Hydrogen production cost (\$/kg)	7.5	7.1	6.6
Ammonia production cost (\$/kg)	1.5	1.7	1.2
Total cost rate (\$/h)	7088.1	6007.2	4978.8

System 3 is found to provide higher overall exergy efficiency as well as lower total cost rate under the $M_{sol}M_{wn}$ configuration. The hydrogen production cost is evaluated to be \$6.6/kg while the ammonia production cost is found as \$1.2/kg. Comparatively higher total cost rate and lower overall exergy efficiency is found for System 1. The total cost rate is determined to be 7088.1 \$/h that corresponds to a hydrogen production cost of \$7.5/kg and an ammonia production cost of \$1.5/kg. The comparatively lower performance of System 1 can be attributed to the usage of PV panels that are associated with comparatively low efficiencies, which lead to lower overall exergy efficiencies and higher total cost rates.

CHAPTER 7 : CONCLUSIONS AND RECOMMENDATIONS

In this chapter, the major outcomes, results and findings obtained from this thesis are briefly described. Based on these findings, recommendations for future studies are provided.

7.1 Conclusions

In this thesis, integrated solar and wind energy-based energy systems are developed for clean production of electricity, hydrogen and ammonia. Three new integrated energy systems are developed utilizing ammonia as a medium to store energy. Direct ammonia fuel cells are utilized for clean power generation via electrochemical ammonia oxidation through the utilization of alkaline electrolytes. A new multi-bed catalyst reactor is developed and investigated experimentally for ammonia synthesis and performance improvement in comparison with a conventional catalyst-based reactor is determined.

The primary findings obtained from the multi-bed ammonia synthesis reactor developed and investigated are summarized as follows:

- The multi-bed reactor results in an increase of 32.1% in ammonia production as compared to the single conventional catalyst reactor at a pressure of 700 kPa.
- At an operating pressure of 800 kPa, a rise of 40.2% is observed in ammonia synthesis as compared to the results obtained for conventional single catalyst reactor described earlier.
- The experimental energy efficiency is found to be 9.1% and the exergy efficiency entails a value of 9.9% for the multi-bed reactor at a pressure of 800 kPa.
- The experimental efficiency values denote the absence of recycling and considerably higher efficiency values are obtained when recycling of unreacted gases is considered in the integrated solar and wind energy-based systems.
- The ruthenium as well as wustite-based catalysts utilized in the multi-bed reactor are found to have considerably higher surface areas as compared to the conventional iron oxide-based ammonia synthesis catalyst, resulting in higher yields of ammonia.

The primary findings obtained from the analysis of System 1 are summarized as follows:

- The peak daily ammonia production reaches 5067.9 kmol across the year and the maximum daily hydrogen production is found to be 11650.4 kmol.
- The maximum energy discharge capacity of the AFC subsystem is found to be 43.5 MWh associated with high solar and wind energy availability.
- The peak daily exergy destructions of 175.6 MWh and 272.4 MWh are found to be associated with the ammonia synthesis and the hydrogen production subsystems.
- The energy efficiency of the overall system is found to entail a peak value of 29.3%. The corresponding overall exergy efficiency is evaluated to be 30.0%.

The major results derived from System 2 analyses are as follows:

- The maximum daily ammonia production is evaluated to be 3204.7 kmol across the year and the corresponding daily hydrogen production is 5634.4 kmol.
- The MEAFC energy discharge capacity is found to be 47.5 MWh at the peak value associated with high solar and wind energy availability. The peak daily heating output amount reaches a value of 761.8 MWh.
- The overall energy efficiency is found to be 51.1% and the overall exergy efficiency is evaluated to be 52.7% at the peak value

The primary findings obtained from System 3 analyses are summarized below:

- The highest daily ammonia production is found to be 5767.4 kmol and the peak daily hydrogen production is 9943.8 kmol.
- The peak daily heating output amount reaches a value of 754.5 MWh and the RC energy discharge time capacity is found to be 2.7 hours at the peak value associated with high solar availability.
- The overall energy efficiency is found to be 57.8% and the overall exergy efficiency is evaluated to be 60.5% at the peak value.
- The least overall energy efficiency across the year is found to be 48.5% and the least overall exergy efficiency is evaluated as 49.5%.
- Comparatively higher performances are obtained for System 3 owing to the utilization of effective waste heat recovery techniques.

7.2 Recommendations

Considering findings obtained from this thesis, the following recommendations are provided for future studies:

- The environmental performance of the developed systems should be investigated through life cycle assessment studies. Although during the operational phase, no environmentally detrimental emissions are emitted, it is essential to investigate the life cycle environmental impacts considering different stages of life cycles associated with several subsystems included.
- The exergoenvironmental analysis of the developed systems should also be performed to link the exergetic performances with their respective environmental performances.
- Different combinations of both high and low cost catalysts should be investigated for ammonia synthesis in the multi-bed reactor and their performances should be investigated at varying operating parameters.
- New electrochemical catalysts should be developed for electrochemical ammonia oxidation that can enhance the performances of direct ammonia fuel cells. Both low cost catalysts such as nickel and iron oxide, as well as high cost catalysts such as rhenium and iridium should be investigated.
- The performance of the developed systems should be investigated with integration to different applications such as urea and methanol production. The capture and conversion of CO₂ emissions into useful commodities via clean production of hydrogen through the developed systems should be considered.
- Pilot plants should be developed for the proposed systems to investigate their experimental performances and to determine which system components have the highest energy and exergy losses.
- Scale-up analysis should be performed on the developed systems to determine the system parameters required for implementing the energy systems in large-scale applications.
- Life cycle costing should be performed on the proposed energy systems to determine the costs associated with different stages of the life cycle.

REFERENCES

1. International Energy Agency (IEA), Data and statistics, 2019. Available at: <https://www.iea.org/data-and-statistics>.
2. International Energy Agency (IEA), Global Energy and CO₂ Status Report, 2019. Available at: <https://www.iea.org/reports/global-energy-and-co2-status-report-2019>.
3. International Energy Agency (IEA), Total Primary Energy Supply (TPES) by source, 2016. Available at: <https://www.iea.org/statistics/>.
4. International Energy Agency (IEA), Global Energy & CO₂ Status Report, 2018. Available at: <https://www.iea.org/geco/emissions/>.
5. International Energy Agency (IEA), Future of Hydrogen, 2019. Available at: <https://www.iea.org/reports/the-future-of-hydrogen>
6. I. Dincer and C. Zamfirescu, Sustainable Energy Systems and Applications, 2012. Springer US.
7. A. Valera-Medina, H. Xiao, M. Owen-Jones, W.I.F. David and P.J. Bowen, Ammonia for power, Progress in Energy and Combustion Science 69 (2018) 63-102.
8. Yara Fertilizer Industry Handbook. 2017. Available from <http://yara.com/investor-relations/reports-presentations/>.
9. Y. Bicer and I. Dincer, Assessment of a Sustainable Electrochemical Ammonia Production System Using Photoelectrochemically Produced Hydrogen under Concentrated Sunlight. Sustainable Chemistry and Engineering 5 (2017) 8035-8043.
10. USGS Mineral Commodity Summaries. 2019. Available from: <https://www.usgs.gov/centers/nmic/mineral-commodity-summaries>.
11. Environmental Protection Agency (EPA), Source assessment: Synthetic Ammonia production, 2004. Available from: <https://cfpub.epa.gov/si/sipublicrecordReport.cfm?Lab=ORD&dirEntryID=38326>.
12. Ammonia Industrial Efficiency Technology Database; Measures. Available from <http://ietd.iipnetwork.org/content/ammonia#key-data>.
13. International Energy Agency. Energy Technology Perspectives 2012. Energy Technol. Perspect, 2012. OECD Publishing, FRANCE. doi:10.1787/energy_tech-2012-en.
14. Kool A, Marinussen M, Blonk H. LCI data for the calculation tool Feedprint for greenhouse gas emissions of feed production and utilization. GHG Emissions. N, P K Fertilizer Production, Gravin Beatrixstraat, 2012. 34:2805.
15. G. Wang, A. Mitsos and W. Marquardt, Conceptual Design of Ammonia-Based Energy Storage System: System Design and Time-Invariant Performance. American Institute of Chemical Engineering 63 (2017) 1620-1637.
16. A. Hasan and I. Dincer, Development of an integrated wind and PV system for ammonia and power production for a sustainable community. Journal of Cleaner Production 231 (2019) 1515-1525.
17. Y. Bicer and I. Dincer, Performance assessment of electrochemical ammonia synthesis using photoelectrochemically produced hydrogen. International Journal of Energy Research 41 (2017) 1987-2000.
18. A. Sanchez and M. Martin, Optimal renewable production of ammonia from water and air. Journal of Cleaner Production 178 (2018) 325-342.

19. M. Matzen, M. Alhajji and Y. Demirel, Technoeconomics and Sustainability of Renewable Methanol and Ammonia Productions Using Wind Power-based Hydrogen. *Advanced Chemical Engineering* 5 (2015) 3-5.
20. P. H. Pfromm, Towards sustainable agriculture: Fossil-free ammonia. *Journal of Renewable and Sustainable Energy* 9 (2017) 034702.
21. M. Al-Zareer, I. Dincer and M.A. Rosen, Transient thermodynamic analysis of a novel integrated ammonia production, storage and hydrogen production system. *International Journal of Hydrogen Energy* 44 (2019) 18214-18224.
22. L. Ye, R. N. Luke, R. B. Alcantara and E. Tsang, Reaction: Green Ammonia Production. *Chem* 3 (2017) 712-714.
23. U. B. Shahid, Y. Bicer, S. Ahzi and A. Abdala, Thermodynamic assessment of an integrated renewable energy multigeneration system including ammonia as hydrogen carrier and phase change material energy storage. *Energy Conversion and Management* 198 (2019) 111809.
24. R. Gordon, Production of ammonia from air and water. U.S Patent: US20110243828A1, 2010.
25. R. Javaid and T. Nanba, Effect of reaction conditions and surface characteristics of Ru/CeO₂ on catalytic performance for ammonia synthesis as a clean fuel, *International Journal of Hydrogen Energy* (2020) Accepted: In press.
26. J. Armijo and C. Philibert, Flexible production of green hydrogen and ammonia from variable solar and wind energy: Case study of Chile and Argentina, *International Journal of Hydrogen Energy* 45 (2020) 1541-1558.
27. N. B. Esteves, A. Sigal, E. P. M. Leiva, C. R. Rodríguez, F.S.A. Cavalcante, L.C. de Lima, Wind and solar hydrogen for the potential production of ammonia in the state of Ceará – Brazil, *International Journal of Hydrogen Energy* 40 (2015) 9917-9923.
28. A.M.O. Mohamed, Y. Bicer, Development and assessment of concentrated solar energy driven ammonia synthesis from liquefied natural gas, *International Journal of Hydrogen Energy* (2020) Accepted: In Press.
29. K. Verleysen, D. Coppitters, A. Parente, W. Paepe, F. Contino, How can power-to-ammonia be robust? Optimization of an ammonia synthesis plant powered by a wind turbine considering operational uncertainties, *Fuel* 266 (2020) 117049.
30. C.F. Guerra, L. R. Bozo, E.Vyhmeister, M.J. Caparros, J. L. Salazar, C. C. Jul, Technical-economic analysis for a green ammonia production plant in Chile and its subsequent transport to Japan, *Renewable Energy* 157 (2020) 404-414.
31. A. Sanchez, M. Martin, Scale up and scale down issues of renewable ammonia plants: Towards modular design, *Sustainable Production and Consumption* 16 (2018) 176-192.
32. A. Allman, P. Daoutidis, Optimal scheduling for wind-powered ammonia generation: Effects of key design parameters, *Chemical Engineering Research and Design* 131 (2018) 5-15.
33. O. Osman, S. Sgouridis, A. Sleptchenko, Scaling the production of renewable ammonia: A techno-economic optimization applied in regions with high insolation, *Journal of Cleaner Production* 271 (2020) 121627.
34. J. Tallaksen, F. Bauer, C. Hulteberg, M. Reese, S. Ahlgren, Nitrogen fertilizers manufactured using wind power: greenhouse gas and energy balance of community-scale ammonia production, *Journal of Cleaner Production* 107 (2015) 626-635.

35. E. Morgan, J. Manwell, J. McGowan, Wind-powered ammonia fuel production for remote islands: A case study, *Renewable Energy* 72 (2014) 51-61.
36. M. J. Palys, A. Kuznetsov, J. Tallaksen, M. Reese, P. Daoutidis, A novel system for ammonia-based sustainable energy and agriculture: Concept and design optimization, *Chemical Engineering and Processing - Process Intensification* 140 (2019) 11-21.
37. U. Shahid, Y. Bicer, S. Ahzi, A. Abdala, Thermodynamic assessment of an integrated renewable energy multigeneration system including ammonia as hydrogen carrier and phase change material energy storage, *Energy Conversion and Management* 198 (2019) 111809.
38. Y. Bicer, I. Dincer, Exergoeconomic analysis and optimization of a concentrated sunlight-driven integrated photoelectrochemical hydrogen and ammonia production system, *International Journal of Hydrogen Energy* 44 (2019) 18875-18890.
39. S. Licht, B. Cui, B. Wang, F.F. Li, J. Lau and S. Liu, Ammonia synthesis by N₂ and steam electrolysis in molten hydroxide suspensions of nanoscale Fe₂O₃. *Science* 345 (2014) 637-640.
40. K. Kim, C. Yoo, J. Kim, H. C. Yoon and J. Han, Electrochemical synthesis of ammonia from water and nitrogen catalyzed by nano-Fe₂O₃ and CoFe₂O₄ suspended in a molten LiCl-KCl-CsCl electrolyte. *Journal of Chemical Engineering* 33 (2016) 1777-1780.
41. J. Yang, W. Weng and W. Xiao, Electrochemical synthesis of ammonia in molten salts. *Journal of Energy Chemistry* 43 (2020) 195-207.
42. Y. Bicer, F. Khalid, A.M.O. Mohamed, M. Al-Breiki, M. M. Ali, Electrochemical modelling of ammonia synthesis in molten salt medium for renewable fuel production using wind power, *International Journal of Hydrogen Energy* 45 (2020) 34938-34948.
43. R. Zhao, H. Xie, L. Chang, X. Zhang, X. Zhu, X. Tong, T. Wang, Y. Luo, P. Wei, Z. Wang and Xuping Sun, Recent progress in the electrochemical ammonia synthesis under ambient conditions. *EnergyChem* 1 (2019) 100011.
44. J. R. Gomez, J. Baca, F. Garzon, Techno-economic analysis and life cycle assessment for electrochemical ammonia production using proton conducting membrane, *International Journal of Hydrogen Energy* 45 (2020) 721-737.
45. A. A. Wahedi, Y. Bicer, Development of an off-grid electrical vehicle charging station hybridized with renewables including battery cooling system and multiple energy storage units, *Energy Reports* 6 (2020) 2006-2021.
46. C. Casallas, I. Dincer, Assessment of an integrated solar hydrogen system for electrochemical synthesis of ammonia, *International Journal of Hydrogen Energy* 42 (2017) 21495-21500.
47. A. Sanchez, L. M. Gil, M. Martin, Sustainable DMC production from CO₂ and renewable ammonia and methanol, *Journal of CO₂ Utilization* 33 (2019) 521-531.
48. V. Kyriakou, I. Garagounis, A. Vourros, E. Vasileiou, M. Stoukides, An Electrochemical Haber-Bosch Process, *Joule* 4 (2020) 142-158.
49. D. Chisalita, L. Petrescu, C. Cormos, Environmental evaluation of european ammonia production considering various hydrogen supply chains, *Renewable and Sustainable Energy Reviews* 130 (2020) 109964.
50. H. Zhang, L. Wang, J. V. Herle, F. Marechal, U. Desideri, Techno-economic comparison of green ammonia production processes, *Applied Energy* 259 (2020) 114135.

51. C. Chen, Y. Liu, H. Aryafar, T. Wen and A. S. Lavine, Performance of conical ammonia dissociation reactors for solar thermochemical energy storage. *Applied Energy* 255 (2019) 113785.
52. K. Lovegrove, A. Luzzi, I. Soldiani and H. Kreetz, Developing ammonia based thermochemical energy storage for dish power plants. *Solar Energy* 76 (2004) 331-337.
53. M. Zhou, Y. Wang, Y. Chu, Y. Tang, K. Tian, S. Zheng, J. Chen and Z. Wang, Ammonia as an environmentally benign energy carrier for the fast growth of China. *Energy Procedia* 158 (2019) 4986-4991.
54. Y. Wang, S. Zheng, J. Chen, Z. Wang and S. He, Ammonia (NH₃) Storage for Massive PV Electricity. *Energy Procedia* 150 (2018) 99-105.
55. G. Wang, A. Mitsos and W. Marquardt, Conceptual Design of Ammonia-Based Energy Storage System: System Design and Time-Invariant Performance. *American Institute of Chemical Engineering* 63 (2017) 1620-1637.
56. J. Ikaheimo, J. Kiviluoma, R. Weiss, H. Holttinen, Power-to-ammonia in future North European 100% renewable power and heat system. *International Journal of Hydrogen Energy* 43 (2018) 17295-17308.
57. Qi. Ma, R. Peng, L. Tian, G. Meng, Direct utilization of ammonia in intermediate-temperature solid oxide fuel cells, *Electrochemistry Communications* 8 (2006) 1791-1795.
58. G. Meng, C. Jiang, J. Ma, Q. Ma, X. Liu, Comparative study on the performance of a SDC-based SOFC fueled by ammonia and hydrogen, *Journal of Power Sources* 173 (2007) 189–193.
59. M. Liu, R. Peng, D. Dong, J. Gao, X. Liu, and G. Meng. Direct liquid methanol-fueled solid oxide fuel cell, *Journal of Power Sources* 185 (2008) 188–192.
60. Z. Limin, C. You, Y. Weishen, L. I. N. Liwu, A Direct Ammonia Tubular Solid Oxide Fuel Cell, *Chinese Journal of Catalysis* 28 (2007) 749–751.
61. Q. Ma, J. Ma, S. Zhou, R. Yan, J. Gao, G. Meng, A high-performance ammonia-fueled SOFC based on a YSZ thin-film electrolyte, *Journal of Power Sources* 164 (2007) 86–89.
62. G. G. M. Fournier, I. W. Cumming, and K. Hellgardt. High performance direct ammonia solid oxide fuel cell. *Journal of Power Sources* 162 (2006) 198–206.
63. A. Fuerte, R. X. Valenzuela, M. J. Escudero, and L. Daza. Ammonia as efficient fuel for SOFC. *Journal of Power Sources* 192 (2009) 170–174.
64. L. Pelletier, A. McFarlan, and N. Maffei. Ammonia fuel cell using doped barium cerate proton conducting solid electrolytes. *Journal of Power Sources* 145 (2005) 262–265.
65. N. Maffei, L. Pelletier, J. P. Charland, and A. McFarlan. An intermediate temperature direct ammonia fuel cell using a proton conducting electrolyte. *Journal of Power Sources* 140 (2005) 264–267.
66. N. Maffei, L. Pelletier, J. P. Charland, and A. McFarlan. An ammonia fuel cell using a mixed ionic and electronic conducting electrolyte. *Journal of Power Sources* 162 (2006) 165–167.
67. N. Maffei, L. Pelletier, and A. McFarlan. A high performance direct ammonia fuel cell using a mixed ionic and electronic conducting anode. *Journal of Power Sources* 175 (2008) 221–225.

68. Q. Ma, R. Peng, Y. Lin, J. Gao, and G. Meng. A high-performance ammonia-fueled solid oxide fuel cell. *Journal of Power Sources* 161 (2006) 95–98.
69. L. Zhang and W. Yang. Direct ammonia solid oxide fuel cell based on thin proton-conducting electrolyte. *Journal of Power Sources* 179 (2008) 92–95.
70. J. C. Ganley, An intermediate-temperature direct ammonia fuel cell with a molten alkaline hydroxide electrolyte, *Journal of Power Sources* 178 (2008) 44–47.
71. J. Yang, H. Muroyama, T. Matsui, and K. Eguchi, Development of a direct ammonia-fueled molten hydroxide fuel cell, *Journal of Power Sources* 245 (2014) 277–282.
72. Lan and S. Tao, Direct Ammonia Alkaline Anion-Exchange Membrane Fuel Cells, *Electrochemical and Solid-State Letters* 13 (2010) B83.
73. S. Suzuki, H. Muroyama, T. Matsui, and K. Eguchi, Fundamental studies on direct ammonia fuel cell employing anion exchange membrane, *Journal of Power Sources* 208 (2012) 257–262.
74. Ref 3000 Gamry Potentiostat, Gamry Instruments. Available at: www.gamry.com.
75. FMA1700A/1800A Series electronic gas mass flowmeters. Available from http://www.omega.com/pptst/FMA1700A_1800A.html.
76. J. A. Duffie and W.A. Beckman, *Solar Engineering of Thermal Processes*, 2006, 3rd Edition, N. J: Wiley.
77. RETScreen Clean Energy Management Software, Natural Resources Canada, Available at: <https://www.nrcan.gc.ca/energy/retscreen/7465>.
78. M. Ni, M.K.H. Leung and D.Y.C. Leung, Energy and exergy analysis of hydrogen production by a proton exchange membrane (PEM) electrolyzer plant, *Energy* 49 (2008) 2748-2756.
79. C. W. Skarstrom, Oxygen Concentration Process, U.S Patent: US3237377A, 1960.
80. ASPEN Plus Simulation software V10, Aspen Tech, Available from: <https://www.aspentech.com/en/products/engineering/aspens-plus>
81. J. Gómez-Hernández, P.A. González-Gómez, J. V. Briongos and D. Santana, Influence of the steam generator on the exergetic and exergoeconomic analysis of solar tower plants, *Energy* 145 (2018) 313-328.
82. H. Feng, G. Tao, C. Tang, Y. Ge, L. Chen and S. Xia, Exergoeconomic performance optimization for a regenerative closed-cycle gas turbine combined heat and power plant, *Energy Reports* 5 (2019) 1525-1531.
83. G. Bonforte, J. Buchgeister, G. Manfrida and K. Petela, Exergoeconomic and exergoenvironmental analysis of an integrated solar gas turbine/combined cycle power plant, *Energy* 156 (2018) 352-359.
84. F. A. Al-Sulaiman, Exergoeconomic analysis of ejector-augmented shrouded wind turbines, *Energy* 128 (2017) 264-270.
85. A. R. Elbar, M. S. Yousef, H. Hassan, Energy, exergy, exergoeconomic and enviroeconomic (4E) evaluation of a new integration of solar still with photovoltaic panel, *Journal of Cleaner Production* 233 (2019) 665-680.
86. P. Ahmadi, I. Dincer, M. A. Rosen, Multi-objective optimization of a novel solar-based multigeneration energy system, *Solar Energy* 108 (2014) 576-591.
87. Z. Hou, X. Wei, Xi. Ma, X. Meng, Exergoeconomic evaluation of waste heat power generation project employing organic Rankine cycle, *Journal of Cleaner Production* 246 (2020) 119064.

88. S. Zhou, X. Liu, Y. Bian, S. Shen, Energy, exergy and exergoeconomic analysis of a combined cooling, desalination and power system, *Energy Conversion and Management* 218 (2020) 113006.
89. Y. Bicer, I. Dincer, Exergoeconomic analysis and optimization of a concentrated sunlight-driven integrated photoelectrochemical hydrogen and ammonia production system, *International Journal of Hydrogen Energy* 44 (2019) 18875-18890.
90. J. Oyekalea, M. Petrollese, F. Heberleb, D. Brüggemannb, G. Cau, Exergetic and integrated exergoeconomic assessments of a hybrid solarbiomass organic Rankine cycle cogeneration plant, *Energy Conversion and Management* 215 (2020) 112905.
91. M. Ezzat, I. Dincer, Exergoeconomic analysis and optimization of a new hybrid fuel cell vehicle, *International Journal of Hydrogen Energy* 45 (2020) 5734-5744.
92. A. Abusoglu, M. Kanoglu, Exergoeconomic Optimization of a Diesel-engine-powered Cogeneration Plant, *Energy & Fuels* 23 (2009) 1977-1989.
93. S. Alharbi, M. L. Elsayed, L. C. Chow, Exergoeconomic analysis and optimization of an integrated system of supercritical CO₂ Brayton cycle and multi-effect desalination, *Energy* 197 (2020) 117225.
94. E. Acıkkalp, H. Aras, A. Hepbasli, Advanced exergoeconomic analysis of a trigeneration system using a diesel-gas engine, *Applied Thermal Engineering* 67 (2014) 388-395.
95. M. A. Rosen, I. Dincer, Exergoeconomic analysis of power plants operating on various fuels, *Applied Thermal Engineering* 23 (2003) 643-658.
96. F. S. Silva, J. A. Matelli, Exergoeconomic analysis and determination of power cost in MCFC-steam turbine combined cycle, *International Journal of Hydrogen Energy* 44 (2019) 18293-18307.
97. H. Liu, J. Sui, W. Han, Z. Wang, N. Zhang, Operation strategy of interconnected combined cooling, heating, and power systems based on exergoeconomic analysis, *Journal of Cleaner Production* 245 (2020) 118822.
98. S. Sayadi, G. Tsatsaronis, C. Duell, Exergoeconomic analysis of vehicular PEM (proton exchange membrane) fuel cell systems with and without expander, *Energy* 77 (2014) 608-622.
99. X. Zhang, R. Zeng, T. Du, Y. He, H. Tian, K. Mu, X. Liu, H. Li, Conventional and energy level based exergoeconomic analysis of biomass and natural gas fired polygeneration system integrated with ground source heat pump and PEM electrolyzer, *Energy Conversion and Management* 195 (2020) 313-327.
100. E.R. Morgan, Techno-economic feasibility study of ammonia plants powered by offshore wind, Ph.D. dissertation, University of Massachusetts, 2013.
101. G. Glatzmaier, Developing a cost model and methodology to estimate capital costs for thermal energy storage, 2011, National Renewable Energy Laboratory Technical Report.
102. R. Turton, R. C. Bailie, W. B. Whiting, and J. A. Shaeiwitz, Analysis, synthesis and design of chemical processes. Pearson Education, 2008.
103. I. Dincer and O. Siddiqui, *Direct Ammonia Fuel Cells*. 2020. Amsterdam: Elsevier. ISBN: 978-0-12-822825-8.
104. L. Czekajlo and Z. L. Bielun, Wustite based iron-cobalt catalyst for ammonia synthesis, *Catalysis Today* 286 (2017) 114-117.

Appendix

Copyright Permission

This thesis similarity is entirely due to the six published works of the candidate that are derived from this thesis. Consequently, equations, crucial information, notations, and illustrations that could not be revised without losing important essence of the work have been maintained. Thesis similarity with each of these published works is listed below:

Paper 1: O. Siddiqui and I. Dincer, Development of a sustainable energy system utilizing a new molten-salt based hybrid thermal energy storage and electrochemical energy conversion technique, *Sustainable Energy Technologies and Assessment* 42 (2020) 100866.

Similarity: 3%

Paper 2: O. Siddiqui and I. Dincer, A new solar energy system for ammonia production and utilization in fuel cells, *Energy Conversion and Management* 208 (2020) 112590.

Similarity: 3%

Paper 3: O. Siddiqui and I. Dincer, Design and transient analyses of a new renewable energy system for multigeneration of power, heat, hydrogen and ammonia, *Journal of Cleaner Production* 270 (2020) 112502.

Similarity: 3%

Paper 4: O. Siddiqui and I. Dincer, Development and performance evaluation of a direct ammonia fuel cell stack, *Chemical Engineering Science* 200 (2019) 285-293.

Similarity: 1%

Paper 5: O. Siddiqui and I. Dincer, Investigation of a new anion exchange membrane-based direct ammonia fuel cell system, *Fuel Cells* 18 (4) 379-388.

Similarity: 1%

Book: I. Dincer and O. Siddiqui, *Direct Ammonia Fuel Cells*. 2020. Amsterdam: Elsevier. ISBN: 978-0-12-822825-8.

Similarity: 1%